Formation, atomic structure, and electronic properties of GaSb quantum dots in GaAs

vorgelegt von
Diplom-Physiker

Rainer Timm
aus Kiel

Von der Fakultät II – Mathematik und Naturwissenschaften
der Technischen Universität Berlin
zur Erlangung des akademischen Grades

Doktor der Naturwissenschaften
– Dr. rer. nat. –

genehmigte Dissertation

Promotionsausschuss:

Vorsitzender:	Prof. Dr. Erwin Sedlmayr
Berichter:	Prof. Dr. Mario Dähne
Berichter:	Prof. Dr. Dieter Bimberg

Tag der wissenschaftlichen Aussprache: 14. Dezember 2007

Berlin 2007

D 83

Abstract

GaSb quantum dots (QDs) in a GaAs matrix exhibit a type-II band alignment with a strong hole localization and only weakly Coulomb-bound electrons, making these structures very promising for application in optoelectronic and especially charge storage devices. However, comparatively little has been known yet about the atomic structure of capped GaSb/GaAs QDs, as it results from the initial growth of GaSb nanostructures and structural changes upon subsequent GaAs overgrowth.

In this work, cross-sectional scanning tunneling microscopy and spectroscopy are used for the first time to study the shape, size, strain, chemical composition, and electronic properties of capped GaSb/GaAs QDs at the atomic scale. By evaluating such structural results on a variety of nanostructures built using different epitaxy methods and growth conditions, details on the underlying QD formation processes can be revealed.

A cross-over from flat quantum wells (QWs) to optically active QDs can be observed in samples grown by metalorganic chemical vapor deposition (MOCVD) with increasing amount of GaSb, including self-assembled Sb accumulations within a still two-dimensional layer and tiny three-dimensional GaSb islands probably acting as precursor structures. The QWs consist of significantly intermixed material with stoichiometries of maximally 50% GaSb, additionally exhibiting small gaps filled with GaAs. A higher GaSb content up to nearly pure material is found in the QDs, being characterized by small sizes of up to 8 nm baselength and about 2 nm height. In spite of the intermixing, all nanostructures have rather abrupt interfaces, and no significant Sb segregation in growth direction is observed.

This changes completely when molecular beam epitaxy (MBE) is used as growth method, in which case individual Sb atoms are found to be distributed over several nm above the nanostructures. Massive group-V atomic exchange processes are causing this strong intermixing and Sb segregation during GaAs overgrowth. In combination with the large strain inherent to GaSb/GaAs QDs, this segregation upon overgrowth is assumed to be the reason for a unique structural phenomenon: All MBE-grown QDs, independent of the amount of deposited GaSb, exhibit a ring structure, consisting of a ring body of high GaSb content and a more or less extended central gap filled with GaAs. These rings have formed in a self-assembled way even when the initial GaSb layer was overgrown considerably fast and continuously by GaAs, without any growth interruption or annealing step after partial capping. Depending on the exact growth conditions, some rings are found to be rather flat, while others exhibit an outer shape of a truncated pyramid with {111} side facets, in both cases showing lateral extensions typically ranging between 10 nm and 20 nm, inner diameters of in average around 40% of the outer ones, and densities of 5 to 9×10^{10} cm^{-2}. Hole localization energies of ~ 0.3 eV for the flat and ~ 0.4 eV for the somewhat higher ring-shaped QDs are obtained, with a type-II conduction band offset amounting to about 0.1 eV.

The observed results, which are extensively discussed in the context of literature data, reveal many new aspects of the atomic structure and allow a detailed and consistent understanding of the formation of GaSb/GaAs QDs.

Zusammenfassung

GaSb Quantenpunkte (QP) in GaAs zeichnen sich durch eine Typ-II-Bandkantenanpassung mit einer hohen Lokalisierungsenergie der Löcher aus, was sie vielversprechend für die Verwendung in optoelektronischen Bauelementen und insbesondere Halbleiter-Speichern macht. Trotzdem ist bisher vergleichsweise wenig über die atomare Struktur von vergrabenen GaSb/GaAs QP bekannt, die sich beim Überwachsen von freistehenden QP ergibt.

Diese Arbeit beinhaltet die erstmalige Untersuchung vergrabener GaSb/GaAs QP mittels Rastertunnelmikroskopie und -spektroskopie an Querschnittsflächen, wobei die Form, Größe, Verspannung, chemische Zusammensetzung und elektronischen Eigenschaften der QP auf atomarer Ebene bestimmt werden. Durch die Auswertung entsprechender Ergebnisse für eine Vielzahl unterschiedlich hergestellter Nanostrukturen lassen sich zahlreiche Rückschlüsse auf die zu Grunde liegenden QP-Wachstumsprozesse ziehen.

Anhand von Proben, die mit metallorganischer Gasphasenepitaxie (MOCVD) gewachsen wurden und unterschiedliche Mengen an GaSb enthalten, lässt sich der Übergang von flachen Quantengräben zu optisch aktiven QP nachvollziehen, der über selbstorganisierte Sb-Ansammlungen innerhalb von flachen Schichten und winzige drei-dimensionale GaSb-Inseln als Vorstufen der QP verläuft. Während die Quantengräben deutlich durchmischt sind und außerdem kleine Lücken aufweisen, ist der GaSb-Anteil der QP höher, teilweise bis fast 100%. Mit Basislängen von bis zu 8 nm und Höhen von etwa 2 nm sind die QP allerdings noch sehr klein. Alle Nanostrukturen weisen relativ abrupte Grenzflächen und keine nennenswerte Sb-Segregation in Wachstumsrichtung auf.

Dies ändert sich allerdings völlig, wenn Molekularstrahlepitaxie (MBE) als Wachstumsmethode verwendet wird: Umfangreiche Austauschprozesse zwischen Gruppe-V-Atomen sind die Ursache für eine hier beobachtete starke Durchmischung und Sb-Segregation beim Überwachsen, die zusammen mit der hohen Verspannung von GaSb/GaAs QP als Ursache für einen weiteren, besonderen Effekt angenommen wird: Alle mit MBE hergestellten QP – unabhängig von der GaSb-Materialmenge – weisen die Form eines Ringes auf, der aus Material mit einem hohen GaSb-Anteil besteht und eine mehr oder weniger ausgedehnte, durchgehende Lücke aus reinem GaAs umschließt. Diese Ringe bilden sich selbstorganisiert während des Wachstumsprozesses, auch wenn hier die GaSb-Schichten schnell und ohne Unterbrechung mit GaAs überwachsen wurden. Je nach genauen Wachstumsbedingungen werden sowohl flache Ringe gefunden als auch solche, deren äußere Form in etwa einem Pyramidenstumpf mit {111}-Seitenflächen entspricht. In beiden Fällen variiert die laterale Ausdehnung etwa zwischen 10 nm und 20 nm bei inneren Ringdurchmessern von im Durchschnitt etwa 40% der äußeren, und es werden Dichten von 5 bis 9×10^{10} cm^{-2} beobachtet. Die Lokalisierungsenergien der Löcher betragen ~ 0.3 eV in den flachen und ~ 0.4 eV in den höheren Strukturen, wobei ein Typ-II-Leitungsbandkantenversatz von etwa 0.1 eV ermittelt wird.

Die beobachteten Ergebnisse, deren Konsistenz mit Literaturdaten ausführlich diskutiert wird, offenbaren viele bisher unbekannte Aspekte der atomaren Struktur und ermöglichen ein detailliertes Verständnis der Entstehung von GaSb/GaAs QP.

Contents

HERR, mein Gott,
wie sind deine Werke so groß und viel!
Du hast sie alle weise geordnet,
und die Erde ist voll deiner Güter.

Psalm 104, 24

Chapter 1

Introduction

The development of semiconductor devices [1] has fundamentally changed the scientific and technological world over the last decades, which therefore are also called the "semiconductor age" or "information age". Besides Si crystals, which are predominantly used in the broad field of information technology, semiconductor heterostructures [2] like GaAs and other III-V material systems have become important for high-speed applications and optoelectronics [3], including the large area of semiconductor lasers [4–7].

A general and very impressive trend in the progress of semiconductor devices is the miniaturization of the structures to generally achieve a better performance and to decrease the power consumption and the production costs, often illustrated by Moore's Law, saying that the number of components per integrated circuit doubles every two years [8].

Semiconductor nanostructures and especially quantum dots (QDs) [2, 9] can be regarded as the end of miniaturization, or as the perfection of miniaturized structures, as they use single charge carriers for device performance [3, 10–13]. Even more, as typical QD sizes are in the regime of the de Broglie wavelength of their charge carriers, these nanostructures reveal fundamentally new physics as compared with bulk semiconductors, being dominated by quantum effects [2, 3, 14–17]. In addition to these electronic effects inherent to QDs, also their structures and possible formation exhibit unique possibilites in device fabrication as they can be grown in a self-assembled way [2, 9, 18–25].

Obviously, this self-assembled growth of nanostructures and especially QDs is not that straightforward as in Fig. 1.1, but is an interplay of different complex processes, many of which are still not completely understood [2, 9, 26–36]. Thereby the atomic structure of the QDs – i.e. their size, shape, and chemical composition, which result from the growth and overgrowth processes – is crucial for their electronic properties [37–43].

FIGURE 1.1: The author of this work during his first experiments on three-dimensional growth, still on a macroscopic scale.

Most research and application development on III-V semiconductor QDs have been concentrated on the InAs/GaAs material system. Comparatively few studies on GaSb QDs in GaAs can be found [44–62], although these structures are very promising both for fundamental physical effects and for special devices. GaSb/GaAs nanostructures exhibit a staggered type-II band alignment, meaning that only for holes a strong confinement exists at the GaSb, with localization energies of up to 450 meV [63, 64], while electrons are only weakly localized by Coulomb binding in the surrounding GaAs [44, 65–77]. Thus, rather low electron-hole recombination energies result, which have led to the realization of room temperature GaSb QW lasing [78, 79] and QD photoluminescence emission [55, 56] at the technologically important wavelength of 1.3 μm. Probably even more important will be the application of GaSb/GaAs QDs for charge storage devices [63, 80–83], as the strong hole confinement and the long exciton lifetime resulting from the type-II band alignment principally enable charge storage times in the QDs of up to years. Regarding the growth mechanisms of GaSb nanostructures in GaAs including intermixing and segregation effects, the interface with the different group-V elements Sb and As is an additional challenge for epitaxy, as under typical growth conditions it is much easier to change the group-III element, while abrupt interfaces are difficult to achieve between GaSb and GaAs [55, 69, 84]. Thus the rather poor supply of high-quality structural data on GaSb/GaAs QDs in literature may probably not be due to lacking interest in this system, but can rather more be explained by the difficulties inherent to the stable growth of GaSb nanostructures in GaAs.

Scanning tunneling microscopy (STM) [85–90] is a well-suited tool for the investigation of semiconductor nanostructures, as it is able to resolve the size, shape, inherent strain, and chemical composition of QDs with atomic resolution [3, 24, 25, 32, 91–103]. Especially in combination with scanning tunneling spectroscopy (STS), also electronic properties of the sample like the surface local density of states can be analyzed [104–110]. Thus, a detailed structural and electronic knowledge can be achieved, which is essential for understanding the underlying physical effects of QD growth.

Quantum dots need to be capped for nearly all applications in order to protect the nanostructures against ambient conditions and to even establish device performance like luminescence. As such an overgrowth process significantly changes the atomic structure of the QDs [29, 35, 36, 111–118], an atomically resolved structural characterization after the capping process is crucial for modeling and improving the QD properties and therewith the final device performance. This requirement can be fulfilled by employing cross-sectional STM (XSTM), as in this case the capped sample is cleaved and the cleavage surface of the QDs is investigated by STM [36, 119–133].

Although STM can generally be considered as a non-destructive characterization method, the scanning tip nevertheless interacts with the sample surface by its electric field [107, 134–138]. Therefore a detailed understanding of this interaction and the involved STM contrast mechanisms is crucial for quantitatively evaluating electronic sample properties from XSTM and especially XSTS data.

This work focuses on XSTM data on GaSb/GaAs QDs, presenting results on nanostructures grown under various growth conditions using both metalorganic chemical vapor deposition (MOCVD) and molecular beam epitaxy (MBE), and discussing details on the formation, atomic structure, and electronic properties of the QDs.

In the first part, a short overview is given on QDs in general, including their growth and structural properties as well as electronic states, and especially on GaSb/GaAs QDs with their band alignment, reported structural data, and possible applications (chapter 2). This

is followed by an introduction into (X)STM and STS, covering several operation modes that have been applied in this work and also the contrast mechanisms which are relevant for the (110) cleavage surface (chapter 3). The experimental STM setups used here are sketched in chapter 4, as are the main preparation steps of the XSTM experiment itself.

The main part of the work covers the XSTM results and their discussion, separated into structural data on MOCVD-grown (chapters 5-7) and MBE-grown samples (chapters 8-10) as well as results on electronic properties mainly derived from STS data (chapter 11). The structural variety in MOCVD-grown samples covers the range from a flat GaSb quantum well (QW) over a QW near the critical thickness of dot formation and possible QD precursor structures up to small, but optically active GaSb/GaAs QDs (chapter 5). Thus – after introducing and discussing a method used to evaluate the chemical composition of the nanostructures from the variation of the local lattice constant (chapter 6) – the onset and a possible pathway of QD formation is analyzed in chapter 7.

Larger GaSb/GaAs QDs could be observed in the MBE-grown samples, but – very astonishingly – all these QDs, formed within a rather broad range of growth conditions, exhibit a ring-like structure (chapter 8). Extensive exchange processes of the group-V atoms As and Sb are found to be typical for the MBE-grown samples, resulting in strong Sb segregation, as shown in chapter 9. This segregation, together with the large strain of the nanostructures, is obtained to be the main driving force for the formation of rings. A model of the transformation of initially compact free-standing GaSb QDs into ring structures upon GaAs overgrowth is presented in chapter 10, together with the analysis of the atomic shape of the ring-like QDs and an outlook on new quantum mechanical effects that can be assumed at such nm-sized rings.

Having understood many details on QD growth in the GaSb/GaAs material system, and after the discovery and explanation of the unique ring-formation, chapter 11 will focus on the special electronic properties of GaSb/GaAs structures, i.e. the type-II band alignment: A specific contrast observed in the XSTM images of the nanostructures as well as the appearance of current and conductance images can be explained in the context of this band alignment. With this knowledge, the type-II conduction band offset and also the hole localization energy can even quantitatively be evaluated from STS spectra for the GaSb/GaAs nanostructures.

Finally, both structural and electronic results will be summarized in chapter 12, thereby comparing MOCVD- and MBE-grown structures and distinguishing between general trends and details that rely on specific growth conditions. Thus, important effects and challenges for the growth as well as promising perspectives for the application of GaSb/GaAs QDs will be concluded.

Part I

Theoretical and experimental background

Chapter 2

Quantum dots

Semiconductor nanostructures, meaning structures with sizes in the nanometer regime, are of large importance, not only for the industrial purpose of miniaturizing and modifying electronic devices to increase their performance and decrease their costs and consumption of resources, but also because of their inherent change of physical properties due to nanoscale quantum effects [3, 9]. Although being solid crystals and of the same material as conventional bulk structures, semiconductor nanostructures like the so-called "quantum dots" (QDs) behave more like single atoms and differ significantly from the macroscopic crystal [2, 14].

Some main consequences of the reduced dimensionality of nanostructures are described in the first part of this chapter, followed by preparation processes and main properties of the zero-dimensional QDs. Finally, GaSb QDs in GaAs, the material system chosen for this work, will be highlighted.

2.1 Low-dimensional semiconductors

Crystal semiconductors are usually described as a periodic system consisting of a broad amount of interacting atoms, being characterized by an electronic bandstructure with an energy gap between the filled valence band and the empty conduction band [139, 140]. However, if the size of the structure is decreased at least in one dimension down to the range of the de Broglie wavelength of the charge carriers, the free motion of the carriers within the crystal (according to the bandstructure) is disturbed and the carriers get confined in this dimension. The de Broglie wavelength is

$$\lambda = \frac{h}{p} = \frac{h}{\sqrt{2\, m_{eff}\, k_B T}} \tag{2.1}$$

and depends on the effective mass of the charge carrier m_{eff} and the temperature T [141]. At room temperature the de Broglie wavelength is in the range of 30 nm for electrons in GaAs [9]. Thus, GaAs-based nanostructures have typical sizes of some tens of nm or below.

The simplest model structure of a quantum mechanically confined system is a particle in a box or so-called "quantum well" (QW) with infinitely high barriers in one dimension. In actual quantum wells built using semiconductor heterostructures, the finite barrier height leads to confined states only for carrier energies smaller than the barrier potential, for larger energies the carriers can propagate [1, 14].

A further reduction of dimensionality leads to the creation of so-called "quantum wires" (confinement within two directions) [1] and finally quantum dots with a confinement in all three dimensions [9].

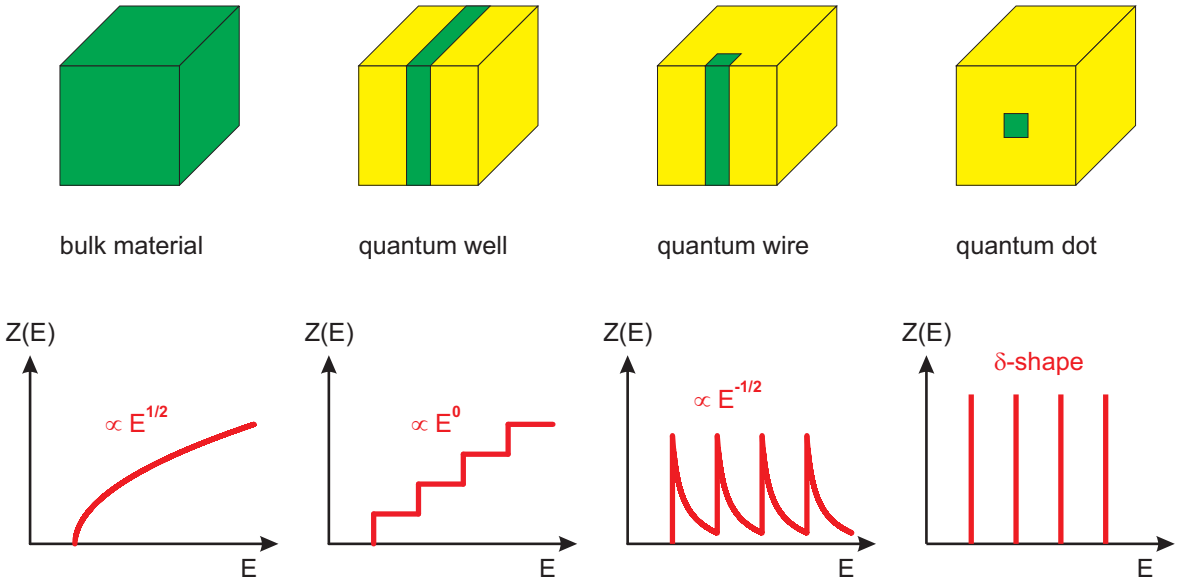

FIGURE 2.1: Spatial confinement of semiconductor structures and corresponding electronic density of states.

Among many material properties which are altered by the spatial and electronic confinement, the electronic density of states (DOS) has a strong significance for many possible applications. The change of the DOS as a function of energy with reduced dimensionality is shown in Fig. 2.1. In bulk semiconductors the DOS increases with increasing energy separation from the band edges according to $E^{1/2}$. In QWs the possible energies are quantized in one direction, therefore the DOS behaves like a step function (E^0 dependence). The quantization in two directions for quantum wires leads to a DOS variation according to $E^{-1/2}$, and ultimately for quantum dots the possible energies are completely quantized, corresponding to a δ-like DOS at discrete energies [142]. Due to these quantized energy states QDs are also denoted as "artificial atoms" [143], and especially this energy quantization has made QDs a fascinating system for studying fundamental physics and an outstanding system for new electronic and optoelectronic devices [17, 144, 145].

2.2 Epitaxy of quantum dots

The method of choice to create semiconductor nanostructures with high crystal quality and very few structural defects is epitaxial growth [9, 146], depositing individual atoms in crystalline layers on a given substrate. Some elementary processes taking place during epitaxy are sketched in Fig. 2.2, including adsorption or chemisorption of precursor molecules with subsequent dissociation, diffusion of the atoms on the substrate, partial desorption off the substrate, and finally incorporation at energetically preferable places like steps and terraces or as a new nucleus. The exact underlying physics of epitaxial growth are much more complex, already for homoepitaxy with substrate and epitaxial layers being of the same material (see for example [147] and references therein), and even more for heteroepitaxy using different materials, which is necessary for QD growth [2, 9, 26]. Depending on the chosen experimental conditions, the growth can be governed more by thermodynamics or more by surface kinetics.

The growth of semiconductor heterostructures and QWs using epitaxy has been known for more than 30 years by now [149–154] and is meanwhile well established. The formation of QDs within the semiconductor crystal, however, is even more complex and demanding

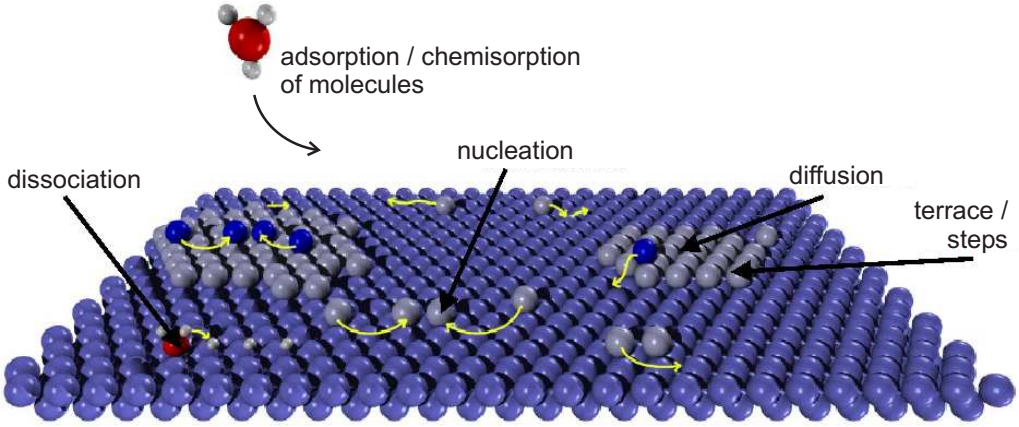

FIGURE 2.2: Elementary processes at the growth surface during epitaxial growth, taken from [148].

than heterostructure growth. One possibility to create QDs is post-growth structuring by lithography and chemical etching (see for example [155, 156]), the more direct way is the self-assembled formation of QDs via the Stranski-Krastanow growth mode [9, 23, 157]. A combination of both methods is the deposition of the QD material onto substrates which were previously patterned by lithography [158] or additional growth steps [159, 160].

2.2.1 Stranski-Krastanow growth

For heteroepitaxy near the thermodynamical equilibrium, there are three possible growth modes: If a complete wetting of the substrate by the deposited material is energetically favorable, i.e., if the energy of the substrate surface $\sigma_{substrate}$ is larger than the sum of the energies of the epilayer surface plus the interface $\sigma_{epilayer} + \sigma_{interface}$, the film-like Frank-van der Merve growth occurs, labelled after F. C. Frank and J. H. van der Merwe [161], Fig. 2.3(a). This is mainly the case for materials with no or only a very small lattice mismatch. However, it is also possible that such film formation is energetically unfavourable, $\sigma_{epilayer} + \sigma_{interface} > \sigma_{substrate}$, leading to the formation of islands according to the Volmer-Weber growth (Fig. 2.3(b), after M. Volmer and A. Weber [162]).

In combination of both modes, islands can evolve on top of a thin wetting layer (WL), called Stranski-Krastanow (SK) growth (Fig. 2.3(b), after I. N. Stranski (working at TU Berlin from 1945–1953) and L. Krastanow [163]). This SK growth can occur especially in material systems with a considerable lattice mismatch – like 4.2% for Ge on Si, 7.2% for InAs on GaAs, or 7.8% for GaSb on GaAs [164] – when the increasing strain in the growing epilayer can induce an inversion of the energetic situation.

The critical thickness of the deposited material, after which the transition from two-

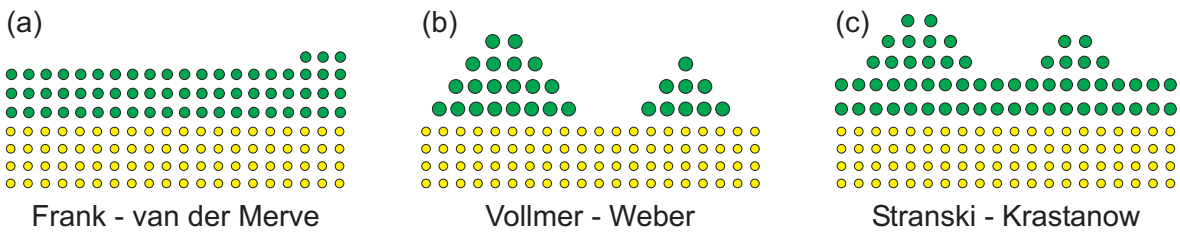

FIGURE 2.3: Schematic diagram of the three growth modes for heteroepitaxy on an atomic scale. The sizes and distances of the different atoms are not drawn to scale.

dimensional (2D) to three-dimensional (3D) growth occurs, depends on the growth conditions, but is mainly determined by the lattice mismatch and the elastic constants of the material system [19, 27, 28, 165, 166]. Thereby the island formation is characterized by pseudomorphic growth, meaning that the lateral positions of the atoms within the islands can be slightly shifted in respect to those of the WL and the bulk crystal, but the crystal lattice and symmetry are continued, each island atom is located at a lattice site defined by the underlying crystal. With proceeding deposition, the size of the islands increases, until the strain gets too large for continuing this pseudomorphic growth even in the islands. At this stage dislocations may form to reduce the strain energy [20], disturbing the crystal lattice and therewith the electronic and optical properties of the nanostructures.

Within the large and complex parameter range of epitaxial growth, only small windows exist and have to be explored for each material system for the self-assembled SK growth of QDs. Moreover, the QD density, shape, stoichiometry and size critically depend on the chosen growth parameters [18, 167–169].

2.2.2 Molecular beam epitaxy

The first self-assembled QDs have been grown using molecular beam epitaxy (MBE) [18]. This growth method is schematically shown in Fig. 2.4: The whole setup is situated within an ultrahigh vacuum (UHV) chamber serving as growth reactor. Within this reactor, the mounted sample substrate can be heated to the desired growth temperature. All growth components are evaporated from individually heatable effusion cells which are placed adjacent to the sample surface. Thus, the partial pressures of the different materials, which determine the chemical nature of the epitaxial film and the growth rate, are given by the geometry and the temperature of the effusion cells. For exact conditions and for enabling a fast change of the deposited material in heteroepitaxy, the effusion cells are equipped with shutters.

In many MBE reactors, the partial pressures can directly be measured by a mass spectrometer or an ion gauge in the beam, in others the growth rate can be controlled by a quartz-crystal oscillator. The surface structure of the evolving epitaxial layer can *in situ* be monitored by reflection high energy electron diffraction (RHEED), which shows the geometry

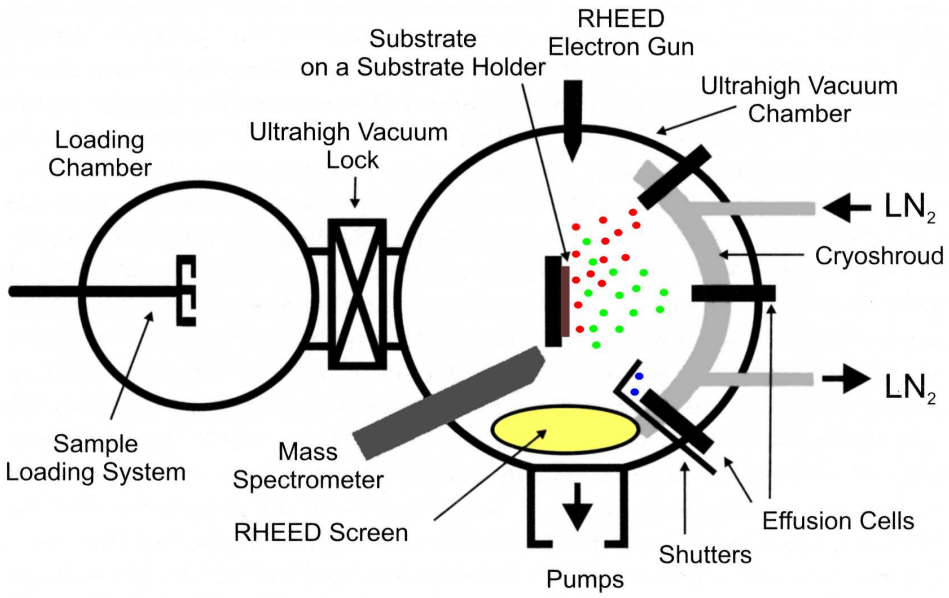

FIGURE 2.4: Schematic diagram of an MBE setup, adapted from [170].

of the surface reconstruction in reciprocal space, characterized by specific spots [26, 171, 172]. The layer by layer growth of a semiconductor film results in an oscillating surface roughness and therewith an oscillating RHEED signal e.g. of the specular reflex, allowing to count the deposited atomic layers directly. When QD growth sets in, the pattern changes from a spotty appearance to a streaky one due to the reduced periodicity [172].

The growth of III-V semiconductors can be controlled by the flux of the group-III atoms: Because the group-V atoms cannot stick on the substrate surface without the presence of group-III atoms, they are typically offered abundantly in the reactor, while the group-III flux governs the growth rate [9]. The ratio of group-V to group-III atoms (often called "V/III-ratio" which should be much larger than one) and the substrate temperature determine which kind of possible surface reconstructions appears [173–176]. Therefore it is much easier to change the group-III element during growth, like switching from GaAs to InAs, than the group-V element, like changing between GaAs and GaSb. In the latter case, As and Sb atoms form a permanent background within the reactor which needs some time to decline [177] and which can influence the stability and stoichiometry of the growth surface [55, 69].

Additionally important for the growth of As compounds is the possible existence of As as As_4 or As_2 molecules within the beam: Direct evaporating of metallic As usually produces As_4 tetramers, while a special cracker unit can be used to split the As_4 into As_2 molecules, which can be easier and faster dissociated and incorporated at the growth surface [26, 171, 176].

Typical growth rates of MBE are in the range of 0.01 to 1 monolayers per second (ML/sec), implicating an often time-consuming but very precise growth method. The necessary use of UHV conditions enables various characterization methods to study the grown structures either simultaneously during growth (like RHEED) or as an additional analysis step but without breaking the vacuum and contaminating the sample [like scanning tunneling microscopy (STM)]. One challenge in MBE chamber design is to avoid too much material being deposited somewhere in the chamber apart from the sample while securing identical growth conditions on the whole substrate.

Introdutions and technical details of MBE can be found in many textbooks (like e.g. [9, 26, 140, 170, 171]), theoretic approaches especially to island nucleation in GaAs growth are for example given by Kratzer et al. [30, 178, 179].

2.2.3 Metalorganic chemical vapor deposition

The other broadly used method for the self-assembled growth of QDs is metalorganic chemical vapor deposition (MOCVD) [43, 167, 168, 180, 181], shown schematically in Fig. 2.5: In this case, all or most of the growth components are extracted from metalorganic precursors by the use of a carrier gas which also transports the gaseous material to the heated sample substrate where it decomposes and gets incorporated [9, 26]. Gaseous precursors can easily be mixed with the carrier gas, but in the case of liquid or solid precursors special so-called "bubblers" are used in which the carrier gas flows through the precursor and dissolves the desired material. Group-III and group-V elements are transported separately and get mixed directly in the reactor to prevent pre-reactions. A homogeneous distribution of the growth components within the carrier gas and a laminar gas flux above the sample substrate are crucial for a uniform sample growth.

Due to the requirement of the carrier gas, which is usually nitrogen or hydrogen, the MOCVD reactor typically operates at pressures between 20 and 500 mbar (1 mbar = 100 Pa), where lower pressures are chosen if abrupt heterointerfaces are desired [183]. Nevertheless, the carrier gas has to be very clean in order to prevent contamination of the grown layers. These conditions inhibit the use of several *in situ* characterization methods which are known from MBE growth taking place in UHV, decreasing the possibility to directly control the growth.

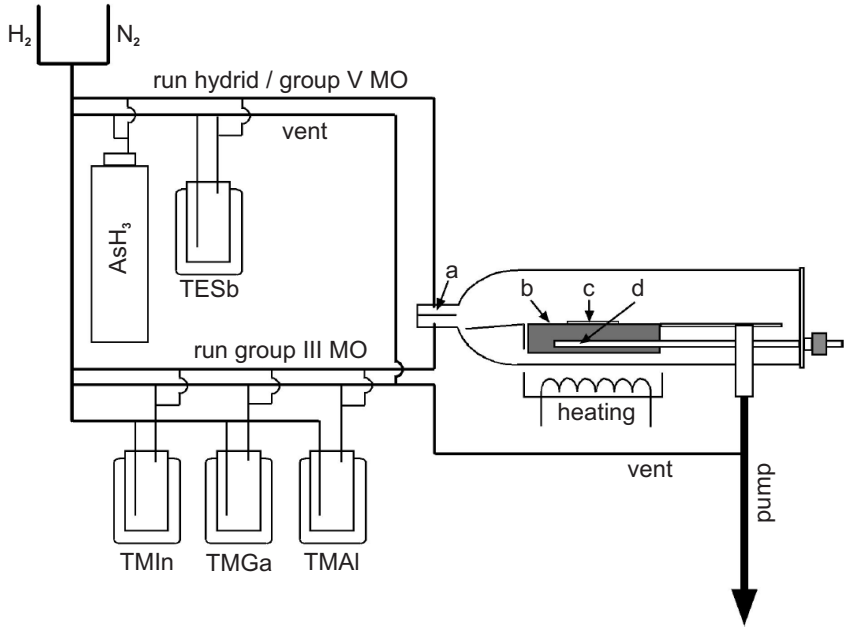

FIGURE 2.5: Schematic diagram of the MOCVD setup used for growing samples described in this work, from [182]. (a) Gas inlet, (b) susceptor, (c) substrate, (d) thermocouple.

On the other hand, growth can proceed significantly faster than in MBE, with typical growth rates in the range of 0.1 to 10 ML/sec.

The growth rate and composition of the sample is determined by the substrate temperature and the partial pressures of the individual growth components, which can be directly controlled by gas valves for each precursor line. Similar to the MBE-growth mentioned above, for the group-V elements significantly more material is supplied than can be incorporated, so that the group-III flux limits the growth process. The dependance of the growth rate on the temperature, however, is more complex in MOCVD, showing a different behavior in different temperature regimes [182, 183], which is beyond this short introduction.

For most components of III-V semiconductors like e.g. In, Ga, Al, As, or Sb, several metalorganic precursors are available, respectively, and the best choice of precursors for QD growth is a field of wide discussion [184–191]. For the samples studied in this work, trimethylgallium [TMGa, $Ga(CH_3)_3$] or triethylgallium [TEGa, $Ga(C_2H_5)_3$] and trimethylaluminium [TMAl, $Al(CH_3)_3$] were used for the group-III elements, triethylantimony [TESb, $Sb(C_2H_5)_3$] as Sb precursor, and the gaseous arsine (AsH_3) for As [51, 182, 192, 193]. Although the latter gets more and more displaced by the less toxic tertiarbutylarsine ($C_4H_9AsH_2$) as standard As precursor [182, 193], it was found that arsine is still superior for GaSb/GaAs growth.

2.3 Structural and electronic properties of quantum dots

Quantized tunable electronic states are the unique characteristics of semiconductor QDs. These electronic properties crucially depend on the QD size, shape and stoichiometry. Therefore, the exact knowledge and controllability of structural properties of QDs is essential both for understanding the underlying physics and for enabling and improving (new) QD applications [2, 3, 37, 194].

The structure of QDs is often analyzed for free-standing ones by local probes like STM or atomic force microscopy (AFM), yielding information on typical shapes, density, size distribu-

tion, and evolution of QDs and on the structure of the surrounding WL [24, 31–33, 91, 96, 195–201]. However, for nearly all applications QDs have to be overgrown by a cap layer in order to protect them and especially to establish the spatial and electronic confinement. This capping process essentially alters the nanostructures, changing their stoichiometry, strain distribution, shape, and size [35, 111–116, 202, 203]. Thus, it is not sufficient to analyze QDs on the growth surface, but the structural details of overgrown QDs need to be known for understanding the overgrowth process and for modeling the electronic properties of capped QDs.

2.3.1 Shape of free-standing quantum dots

Free-standing QDs usually have a pyramidal shape with a symmetry resembling the surface symmetry of the host material [24, 31, 33, 36, 197, 204, 205]. On typical (001) growth surfaces, QDs thus exhibit the shape of a pyramid with a polygonal base, a (110) and a ($\bar{1}$10) symmetry plane, and a clear apex. However, the simple and often used model comprising a four-sided pyramidal shape is strictly speaking only observed for small (Si)Ge islands on Si(001) [99, 206] and for InAs QDs on GaAs(001) in a very small, initial stage [33].

Actual QD shapes are more complex, as can be seen in Fig. 2.6, showing an example of the first atomically resolved STM data on InAs/GaAs QDs, obtained by Jacobi et al. [24, 25, 31, 176]. The authors were able to unambiguously identify the dominating side facets of the QD with the high-indexed {137} facets using their specific surface structure [33]. These facets form an angle against the (001) surface of only 24°, resulting in a relatively flat QD shape with a low aspect ratio, defined as the ratio between height and base diameter. The anisotropy of the shape is underlined by height profiles along the two symmetry axes of the QD, shown in Fig. 2.6(b).

With encreasing QD size, this flat structure becomes unfavorable due to strongly increasing strain of the lattice-mismatched material, and a shape evolution towards steeper structures occurs, described in detail by Jacobi et al. in Refs. [31, 33, 36]. Two examples of this evolution are displayed in Fig. 2.7: The QD shown in the STM image (a), together with

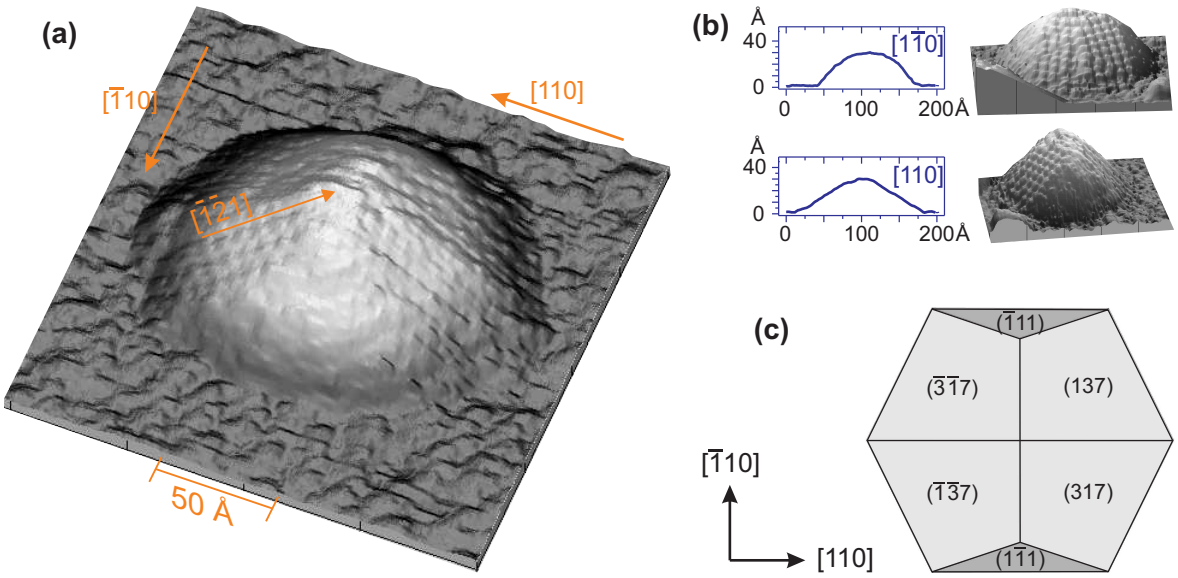

FIGURE 2.6: Structure of a free-standing InAs/GaAs QD, from [24], [36], and [207]. (a) STM image, taken at V_T = -2.75 V and I_T = 0.15 nA. (b) Profiles of the [1$\bar{1}$0]-and [110]-direction, respectively, with corresponding STM images. (c) Structural model of the QD shown in (a) with Miller indices of the side facets.

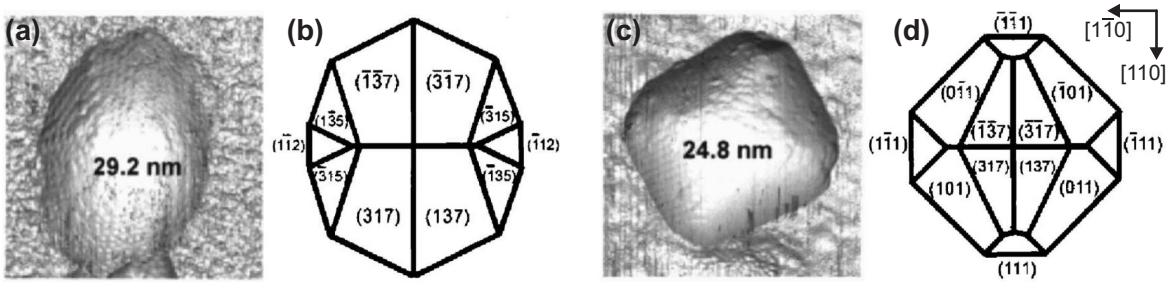

FIGURE 2.7: Structure of larger InAs/GaAs QDs, from [33]. (a) STM image of a "hut"-shaped QD with (b) corresponding structural model. (c) STM image of a "dome"-shaped QD with (d) corresponding structural model.

a sketch of its structure (b), is still dominated by {137} facets, but several steeper facets have additionally emerged at two sides. In the STM image (c), a steeper and more compact QD can be seen, with its structure sketched in (d): Now, the structure is dominated by {101} facets, forming an angle of 45° against the (001) surface, and only the small top area of the QD is still characterized by the flatter {137} facets.

Costantini et al. have first shown that this transition from a flat to a steep shape with increasing QD volume seems to be universal, as it occurs not only in the InAs/GaAs material system, but also for Ge/Si, exhibiting much larger QDs, but with a comparable shape evolution [32, 101, 198, 208]. In both material systems the QD structures are sometimes also called "hut" for the flat one and "dome" for the steep one. Such a shape transition had already theoretically been predicted by Daruka et al. [209], and Kratzer et al. have succeeded in theoretically modeling the transition between atomic shapes observed experimentally [34, 210].

The main driving force for the formation of QDs according to the SK growth mode, for the shape evolution of free-standing QDs, and also for structural changes upon overgrowth is the strain due to the lattice-mismatch between QD and host material. During WL growth the material has to adopt the lateral lattice constant of the host matrix and can only partly compensate this by an increased lattice constant in growth direction, leading to cumulative strain with increasing WL thickness. This situation changes in the QD, where only the bottom interface is defined by the material underneath, while towards the top also the lateral lattice constant can increase for strain relaxation [2, 3, 9].

A quantitative analysis of the strain field in QDs is difficult to obtain. A possible experimental method is x-ray diffraction under grazing incidence, combining the reciprocal space mapping of x-ray diffraction with surface sensitivity, as has been demonstrated by Kegel et al. [195, 196]. Alternatively, the strain distribution can be theoretically simulated, which is also essential for precise calculations of electronic QD properties [3, 41, 92, 211–214], and which has also been performed for uncapped QDs [215].

Examples of both calculated results and x-ray measurements are presented in Fig. 2.8, displaying (a) the calculated trace of the strain tensor as a direct measure of the strain in a single InAs QD and the GaAs(001) matrix underneath [215], and (b) the measured lateral lattice parameter in free-standing InAs QDs also on GaAs(001) [195]. It should be noted that a pyramidal QD shape with a sharp peak was assumed for the calculation [Fig. 2.8(a)], while the summit of the experimentally observed QD is slightly rounded (b). Comparing both data, it can nicely be seen that the increasing lattice parameter towards the apex of the QD, as shown in Fig. 2.8(b), leads to a decrease of the strain, as indicated in (a). The strain is maximum, however, at the bottom edges of the QD, and also the GaAs matrix underneath is influenced.

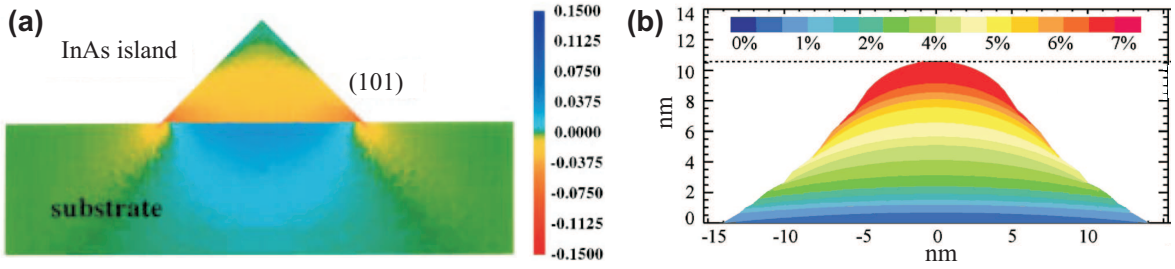

FIGURE 2.8: Strain within an uncapped InAs/GaAs QD: (a) Calculated trace of the strain tensor for the (010) cross section through an idealized QD, from [16, 215]. (b) Deviation of the lateral lattice parameter from that of GaAs, experimentally obtained from grazing-incidence x-ray diffraction on free-standing QDs, adapted from [196].

2.3.2 Changes of the quantum dot shape upon overgrowth

During overgrowth of the formerly free-standing QDs with the host material, the strain distribution changes drastically, as the QD is forced to fit into the surrounding host matrix. As a consequence, the region of the sharp summit of the pyramid, which possessed hardly any strain in free-standing QDs due to the increased lattice constant, gets strongly compressed and becomes a very unfavorable place for the QD material. The result is a truncation of the QD pyramid upon overgrowth [35], coming along with steeper side facets like {101} or {111} [36, 118].

Obviously, no direct three-dimensional imaging of capped QDs is possible, but two-dimensional projections and cross sections of the QD shape can be obtained, e.g. by cross-sectional STM (XSTM). A cross section through a typical, large InAs/GaAs QD grown in the same MBE reactor under similar conditions as the free-standing QDs shown in Figs. 2.6 and 2.7 is presented in Fig. 2.9(a). The flat (001) top face of the truncated pyramid is evident, and also the side facets are significantly steeper than the {137} facets discussed above.

Several authors have studied the initial capping of QDs and report drastical shape changes and material redistribution already during the first few MLs of overgrowth [29, 111, 114, 115, 117, 202, 203]. Just recently, the shape transition from free-standing to capped QDs was studied step-by-step using AFM and *in-situ* STM. The complex process of shape transition was divided into two successive regimes, namely an initial, fast strain-driven material transfer, leading to QD shapes near thermodynamical equilibrium, which upon further capping was followed by kinetically limited surface diffusion [35]. Not only the shape, but also the stoichiometry of the QDs can get rearranged upon overgrowth, especially for larger structures:

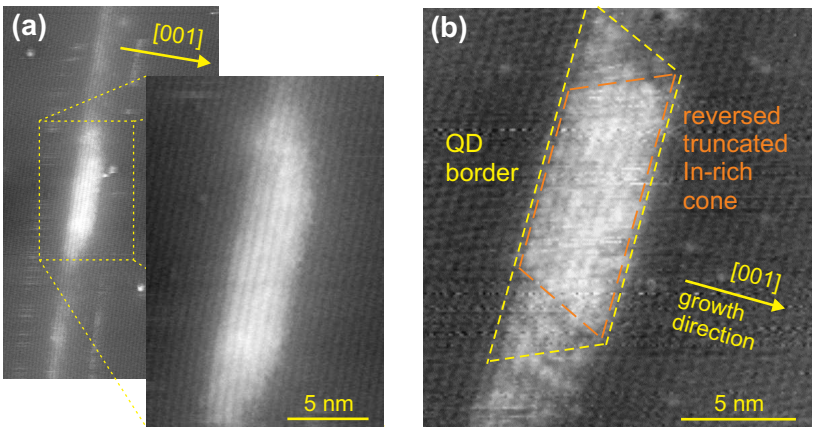

FIGURE 2.9: Cross sections through different capped QDs, obtained by XSTM. (a) InAs/GaAs QD grown by MBE. (b) InGaAs/GaAs QD, grown by MOCVD: The shape of the QD (yellow) and an In-rich central region (red) are indicated.

Liu et al. first reported a nonuniform chemical composition of $In_{0.5}Ga_{0.5}As$/GaAs QDs, obtaining an In-rich core characterized by an inverted-cone shape [95]. Similar results have been observed by several groups [100, 216–218], and also theoretical considerations support this inverted pyramid-like In composition [219]. An example of a nonuniform In distribution, here having the shape of a reversed truncated cone [100], is shown in Fig. 2.9(b).

Beyond such material redistributions within the QDs, additional effects can happen under special growth conditions: Firstly, when QDs are only thinly or partially overgrown prior to a long growth interruption or annealing step, a complete dissolution of the QDs can occur, often accompanied by the formation of a second WL. Such a dissolution has been experimentally observed [125, 220, 221] and theoretically predicted [222]. Also a partial dissolution of formerly sane QDs was found, leading to the existence of nanoholes within or beside the QDs [36, 118, 127, 132].

Secondly, a growth interruption after only partial overgrowth of existing QDs can also lead to a redistribution of material from the top center of the QD towards the surrounding growth surface, resulting in ring-like structures. Such quantum rings were first described by García, Lorke et al. [202, 223–227] and were obtained also by other groups in the InAs/GaAs system [228–231] as well as in other material systems of III-V [60, 232, 233], II-VI [234], and Si-Ge [235–237] semiconductors. Recently these quantum ring structures found considerable interest because of the possibility of persistent currents and quantized magnetic fluxes under external magnetic fields [77, 224, 238–242].

2.3.3 Energy states and wavefunctions in quantum dots

The electronic confinement of a QD is schematically sketched in Fig. 2.10(a): The QD material (InAs) has a smaller bandgap than the host material (GaAs), leading to an electronic band offset for both valence band (VB) and conduction band (CB) at the interface between the two materials. The bandgaps of the bulk materials at room temperature are $E_g = 1.42$ eV for GaAs and $E_g = 0.35$ eV for InAs [164]. However, it is too simplified to regard the QD material as bulk InAs, actually the situation at the QD is an interplay between the properties of the GaAs host material and quantized states, leading to confined ground and excited states for electrons and holes within the GaAs bandgap and to resonant electron and hole states in the GaAs CB and VB, respectively.

According to the structure of the QD, different wavefunctions exist for both electrons and holes at distinctive energies, respectively, ranging from the ground state up to excited states of higher order with different symmetries, as illustrated in Fig. 2.10 (b,c). Overviews on calculated QD states regarding their energies and the shapes of their probability density can, for example, be found in Refs. [37, 39, 41, 42, 211]. Stier et al. have also shown that the electron ground state is mainly of *s*-like symmetry, while the hole ground state is strongly *p*-like [37, 211]. Additionally, due to the larger effective masses of the holes compared to the electrons, the confinement energy and the energetic distance between excited states are larger for electrons than for holes, too, as can be seen in Fig. 2.10(b).

Both the distribution of electron and hole states and their absolute energies strongly depend on the structure of the QDs, which is also displayed in Fig. 2.10(b). This dependence is evident from simulations [37, 39, 42, 240] and is as well confirmed by experimental results [13, 244–246]. Thereby not only the pure size and shape of the quantum box influences the electronic states, but also the strain distribution [16, 41, 211] and the stoichiometry [38, 40, 247, 248] of the QDs. Thus, an exact knowledge of these structural parameters is essential for simulating the electronic details of QDs [43], and, even more, the ability of reproducibly adjusting size, shape and stoichiometry of QDs enables one to tune the energetic properties of the grown nanostructures and possible devices.

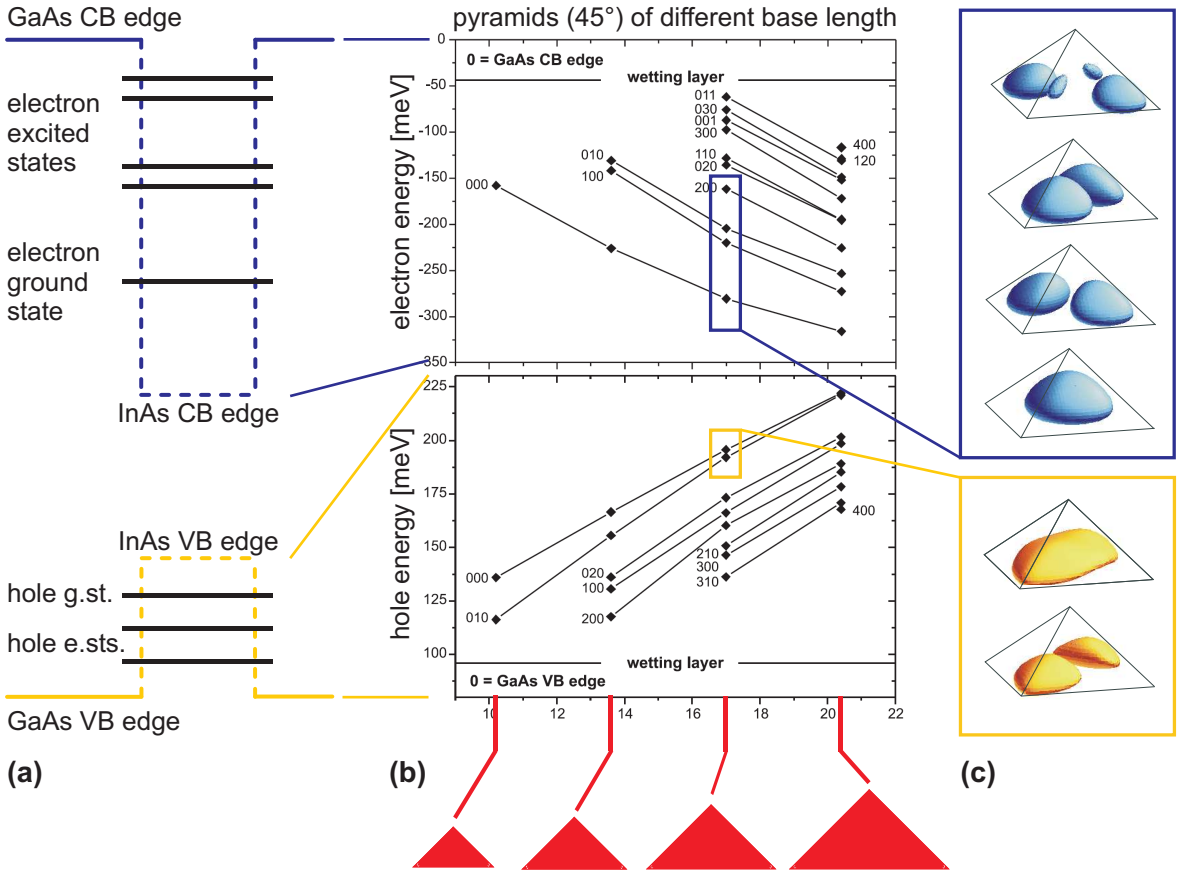

FIGURE 2.10: (a) Schematic energy diagram of an InAs/GaAs QD. (b,c) Calculated energies and wavefunctions of confined states for pyramidal InAs/GaAs QDs of different size. Adapted from [211] and [243].

The spatial and electronic confinement of single charge carriers in QDs embedded in a semiconductor crystal enable a large variety of new applications. Of special importance is the formation of a confined electron-hole pair, a so-called exciton, and its recombination under emission of a photon of the corresponding energy, as this process opens the wide area of nano-optoelectronics [3]. The emission wavelength of an optical device based on QDs is determined by their quantized energies, resulting in very sharp luminescence peaks [15, 17, 21, 142, 143, 249]. This narrow linewidth, possible photoluminescence and lasing wavelengths covering the whole visible spectrum and the technologically important near infrared, very low threshold current densities, and very fast electronic processes are some of the advantages of applying QDs for light emitting diodes (LEDs) and in particular for lasers [6, 7, 17, 250–252].

2.4 GaSb/GaAs nanostructures

Compared to InAs/GaAs QDs, which are most common for III-V semiconductor nanostructures, GaSb QDs in GaAs are much less intensively studied. The structural parameters are similar, with a GaSb bulk lattice constant of 0.610 nm compared to 0.606 nm of InAs, resulting in a GaSb/GaAs lattice misfit of 7.8% at similar elastic moduli [164]. A comparison of these lattice constants of the GaAsSb system with those of other III-V heterostructures can be found in Fig. 2.11. However, the electronic properties are completely different, because not only the absolute bandgap of bulk GaSb, 0.75 eV at room temperature, is significantly

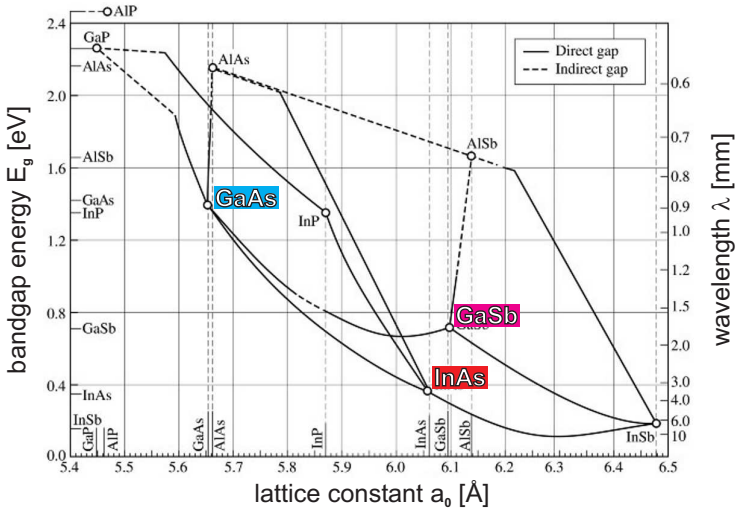

FIGURE 2.11: Bulk lattice constants, bandgap energies, and corresponding luminescence wavelengths of various binary and ternary III-V semiconductors, adopted from [253].

larger than the InAs value [164], but the band alignment of GaSb/GaAs nanostructures has a specific, staggered appearance, leading to distinctive physical effects and a new class of promising applications.

2.4.1 Type-II band alignment

Many material systems like the common InAs/GaAs quantum dots build a so-called "type-I" band alignment, meaning that both electrons and holes are confined within the nanostructure, as sketched in Fig. 2.12(a). However, there are also systems forming a staggered or so-called "type-II" band alignment with only one sort of charge carriers being confined [2]. GaSb/GaAs represents such a type-II alignment, exhibiting a strong confinement for holes but a repulsive potential for electrons [44], as shown schematically in Fig. 2.12(b). Just when a hole is confined within the QD but no corresponding electron is present due to the energetically unfavorable GaSb CB offset, the system gets charged, leading to a local band bending and a weak Coulomb attraction for electrons in the GaAs surrounding the QD [44, 66, 69, 71, 72, 75]. This situation is sketched in Fig. 2.12(c).

The exact band alignment and especially the CB offset of GaSb/GaAs QDs and QWs are still under discussion [44, 67, 68, 75–77] and depend strongly on the strain [44, 75, 77] and the chemical composition of the often alloyed GaSb or $GaAs_{1-x}Sb_x$ nanostructures in GaAs [47, 57]. A strong hole confinement, however, is evident for GaSb/GaAs QDs: Using capacitance-voltage (CV) and deep level transient spectrocsopy (DLTS), Geller et al. obtained hole localization energies around 450 meV and charged QDs containing up to 15 holes each [63, 64, 80].

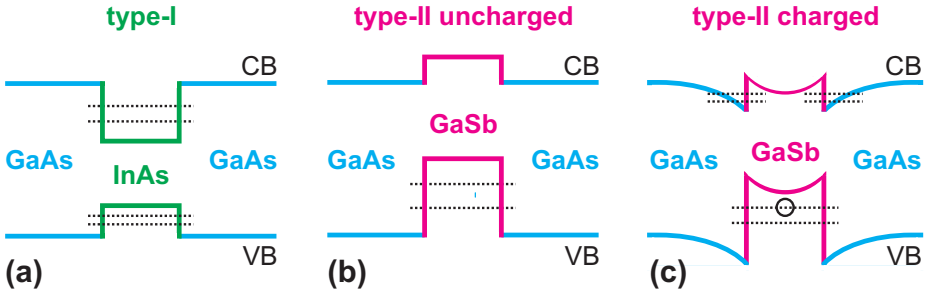

FIGURE 2.12: Schematic band alignment of type-I and type-II nanostructures.

In a classical model considering the staggered type-II band alignment, holes confined within the QD GaSb material and electrons in the surrounding GaAs matrix are spatially separated, leading to only weak Coulomb interaction. Quantum mechanically, however, there is a partial spatial overlap between the hole and electron wavefunctions as they decline exponentially in the classically forbidden regions. Thus, a recombination of electrons and holes is possible, but with a strongly reduced probability compared to type-I QDs. This combination of the staggered band alignment, a strong hole confinement, and the low electron-hole recombination probability leads to two important consequences for the physics and applications of GaSb/GaAs nanostructures: Firstly, extraordinary long exciton lifetimes can be achieved [47, 66, 254, 255]. Secondly, the recombination energy of holes confined in the QD and electrons in the CB of the surrounding matrix is considerably low, in principle it can be even smaller than the bandgap of bulk GaSb [see Fig. 2.12(c) for illustration] [55, 56].

2.4.2 Literature data on GaSb quantum dot structure

First data on GaSb/GaAs quantum dots, grown by MBE, were published in 1995 by Hatami et al. in a cooperation of the Technische Universität Berlin, the Max-Planck-Institut für Mikrostrukturphysik in Halle, Germany, and the Ioffe Physical-Technial Institute in St. Petersburg, Russia [44]. They concluded a nearly square-based pyramidal QD shape, finding an average lateral size of 22 nm and a density of about 4×10^{10} cm^{-2}. Extended optical studies explored the carrier dynamics of these QDs using photoluminescence (PL), photoluminescence excitation (PLE) and cathodoluminescence spectroscopy, confirming the type-II band alignment by an observed blueshift of the QD luminescence with increasing excitation energy [47]: This blueshift can be explained by the spatial separation between holes and electrons, leading to the formation of an increasing dipole layer and an increased band bending at the QD interfaces with increasing carrier density and thus to a larger energy separation between confined hole states in the QD and Coulomb-bound electron states in the neighboring GaAs [65]. The optical results were shortly later confirmed by results from Sun, Kroemer, and coworkers at the University of California at Santa Barbara, USA [66]. In the same group, details of the band alignment were studied by Rubin et al. using ballistic electron emission microscopy [67].

A large step towards the understanding of GaSb growth and QD formation was done by the group around Bennett, Shanabrook, and Whitman at the Naval Research Laboratory in Washington D.C., USA, intensively studying the growth of III-Antimonides on GaAs by MBE. Using transmission electron microscopy (TEM), atomic force microscopy (AFM) and *in-situ* STM, they observed several stages of the QD formation process, ranging from flat 2D GaSb layers over small QDs of 15 nm lateral size, larger QDs with in average 28 nm diameter and 3.2 nm height up to large, relaxed GaSb islands containing dislocations [45, 46, 256, 257]. For an enhanced understanding of the growth surface they also studied the atomic reconstructions of GaSb(001) by STM [258]. The type-II nature of their QDs was confirmed by PL measurements [65], and DLTS studies revealed the strong hole confinement with activation energies of 400 meV and more [70].

Some more specific QD structures were grown by Suzuki, Arakawa, and coworkers at the University of Tokyo, Japan: After studying general optical and structural properties of GaSb/GaAs QDs and especially the influence of the amount of deposited material, obtaining QD sizes from about 26 nm diamter with 6.2 nm height to 32 nm diameter with 9.5 nm height [48, 69, 255], they grew the first stacked GaSb QD layers [49]. By suppressing the effect of intermixing of As and Sb during the overgrowth process, they were able to produce GaSb QDs with a PL peak at the technologically important wavelength of 1.3 μm [56]. Studies on Sb/As exchange reactions during GaSb QD growth and overgrowth are also published by

Silveira, Garcia and Briones from the Instituto de Microelectrónica de Madrid, Spain [50].

All GaSb QD structures discussed above were grown by MBE, today still being the dominant growth method for GaSb/GaAs nanostructures. The first publication on intentionally obtained 3D GaSb structures grown on GaAs by MOCVD was given by Bozek et al. from Warsaw University, Poland. However, they deposited 20 ML or more of GaSb and obtained large islands which most probably contained many crystal defects, showing no photoluminescence or carrier confinement [259]. Even earlier, Graham et al. from the University of Oxford, UK, had observed the unwanted formation of islands of several 100 nm size when they intended to grow thick flat GaSb films on GaAs [185, 186]. Large, relaxed GaSb/GaAs islands were also grown by Kinder, Subekti and Goldys at Macquarie University in Sydney, Australia [260, 261].

Some years later the latter group produced the first real GaSb QDs using MOCVD, published by Motlan et al. [52]. They obtained QDs of about 40 nm average width and 5 nm height at a density of 1.6 $\times 10^{10}$ cm^{-2}, investigated with AFM, TEM, and scanning electron microscopy (SEM), but also large islands of more than 100 nm size. Also stacked multilayer structures were studied optically and structurally, showing a vertical ordering of the QDs [61, 262]. Using PL spectroscopy, Motlan and Goldys found a seperation between their QD and WL PL peaks of 0.3 eV, which is about twice as large as the corresponding value reported for MBE-grown GaSb QDs. They suggested a systematically different intermixing at the WL for MOCVD and MBE growth to be the reason [74, 263]. A blueshift of the PL peak with increasing excitation energy, as already known from MBE-grown samples, confirmed the type-II band alignment also for the MOCVD-grown GaSb QDs.

MOCVD was also used at the Technische Universität Berlin by Müller-Kirsch and coworkers in the group of Bimberg to grow GaSb/GaAs QD structures with typical sizes of 26 nm width and 3.5 nm height [51, 264]. At smaller amounts of GaSb deposition, prior to the formation of distinctive QD structures, stoichiometric fluctuations of a strongly intermixed GaAsSb QW have been observed by high-resolution transmission electron microscopy (HRTEM). Antimony-rich regions within this layer of about 10 nm lateral extension have been found to exhibit QD confinement [71, 73, 265]. The QD evolution with increasing GaSb deposition and the influence of growth interruptions prior to overgrowth were intensively studied using AFM and TEM [51, 182, 264, 265], finding that a correct length of the growth interruption is crucial for QD formation. A combination of GaSb and InAs QDs in GaAs was also successfully demonstrated: Taking InAs QDs as stressors, GaSb QDs could be grown on top with a very high QD density of 1×10^{11} cm^{-2} [53], which could not yet be achieved in the pure GaSb/GaAs system. From PL spectroscopy measurements the type-II band alignment could be confirmed and many-particle effects and state filling in GaSb/GaAs QDs were explored [71–73]. Also the DLTS and capacitance-voltage measurements mentioned above were performed in this group [63, 80], demonstrating the feasibility of GaSb QDs as storage media, as will be shown in more detail in the next chapter. Calculations of the band structure motivated by the optoelectronic results complete the GaSb QD research of this group [75].

During the last three years, several other groups have published individual results on GaSb/GaAs QDs: The effect of a growth interruption prior to QD overgrowth was studied by Luo et al. at the Chinese Academy of Sciences in Beijing, China [54]. Yamamoto et al. at the Communications Research Laboratory in Tokyo, Japan, introduced a new growth method when they irradiated the GaAs growth surface by Si atoms prior to GaSb deposition in order to increase the QD density [58]. Promising are the works of Nakai et al. at the University of Electro-Communications in Tokyo, Japan, obtaining QDs with a very narrow PL linewidth of 67 meV [59] and of Kobayashi et al. at the University of Tokyo, Japan, demonstrating the self-assembled formation of either GaSb QD or quantum ring structures on GaAs, depending

on the growth parameters [60]. Balakrishnan, Huffaker, and coworkers at the Center of High Technology Materials in Albuquerque, New Mexico, USA, have compared SK growth of coherently strained GaSb QDs with the formation of GaSb islands upon a growth mode characterized by laterally propagating interfacial misfit dislocations [62, 266]. Finally, detailed studies on the initial deposition of GaSb on GaAs and the onset of QD formation have been performed by Farrer, Ritchie, and coworkers at the University of Cambridge, UK, for MBE growth [55] and by Pitts, Watkins, and coworkers at the Simon Fraser University in Burnaby, Canada, for MOCVD growth [57].

Although the investigation of GaSb/GaAs nanostructures has increased during the last years, the number of institutions being involved with GaSb QD growth and structural characterization is still concise, as the map shown in Fig. 2.13(a) illustrates, without necessarily being exhaustive. The main structural and some optical results on GaSb QDs of the publications mentioned above are summarized in Table 2.1.

In conclusion, GaSb/GaAs QDs have been grown over the last ten years using both MBE

year	growth method	deposited GaSb	GaSb QDs width	GaSb QDs height	GaSb QDs density $\times 10^{10}$	characterized with	PL energy QD	PL energy WL	reference
		[ML]	[nm]	[nm]	[cm^{-2}]		[eV]	[eV]	
1995	MBE	4	22 ± 4		4	TEM x-ray	1.09	1.23	[44, 47]
1995	MOCVD	20	200	100	0.04	SEM, STM			[259]
1996	MBE	1.4	80 ± 7	10	0.4	AFM	1.32		[66]
1996	MBE	2.5	∼15			TEM			[46]
		3.0	28 ± 4	3.2 ± 0.9	1	AFM	1.13	1.27	[45, 256]
		3	33 ± 4	5 ± 1.3	1–2	AFM	1.14		[70]
1997	MBE		50	5		STM			[67]
1998	MBE	2.5	32 ± 5	9.5	0.26	AFM			[48, 69]
		2.8	28 ± 6	6.7	0.75				
		3.1	26 ± 6	6.2	1.2		1.1	1.3	
1998	MOCVD	2	∼100	15		AFM			[260]
1999	MBE	1.1	30		9.5	SEM			[267]
		45		3.0					
		55		0.38					
2001	MOCVD		38 ± 2	5 ± 0.3	1.55	AFM	1.08	1.40	[52, 263]
2001	MOCVD	∼2	10			HRTEM	1.10	∼1.4	[71, 73]
		4.5	26	3.5	3	TEM	1.06	1.40	[51, 264]
2003	MBE	5	31 ± 5	7.2 ± 0.8	2.2	AFM	1.01	1.38	[55]
2004	MBE	3.0	30–45	6–8	1	AFM	0.9	1.28	[56]
2004	MBE	2.0	80	14	0.2	AFM	1.12	1.41	[58]
2004	MBE	3.5	50–70	2	0.5	AFM	1.2	1.28	[60]
2004	MBE	3–4	30	12	1	STEM	1.09	1.41	[59]
2005	MOCVD	3.8	44	5	1.5	AFM	1.11	1.32	[61]
2006	MBE	3	10	5	3	AFM, TEM	1.2		[62]

TABLE 2.1: Overview on reported structural data on GaSb/GaAs QDs and corresponding PL energies, arranged by publication time and workgroups of the authors.

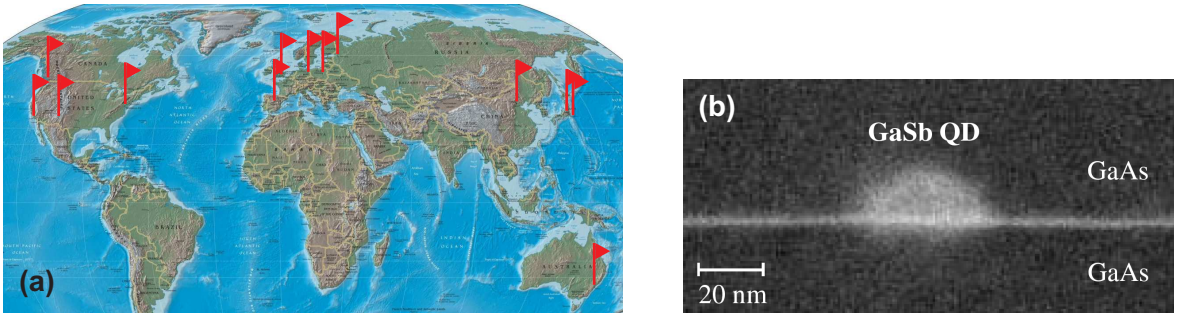

FIGURE 2.13: (a) Places of GaSb/GaAs QD growth and structural characterization worldwide (world map from [268]). (b) Structure of a GaSb/GaAs QD, imaged with cross-sectional STEM, from [59].

or MOCVD. Typical published QD sizes are in the range of 25 to 40 nm width and 3 to 7 nm height, with a roughly pyramidal shape and densities of typically 1×10^9 to 4×10^{10} cm^{-2}. However, to my knowledge the best structural image of a GaSb QD obtained yet is the one shown in Fig. 2.13(b), aquired by Nakai et al. using cross-sectional scanning transmission electron microscopy (STEM) in a high-angle annular dark field mode, and no structural data with atomic resolution has been available yet — with the exception of the XSTM data presented in this work.

2.5 Applications of GaSb quantum dots

Due to the all in all comparatively low interest in GaSb QDs during the last decades and to the still existing difficulties in growing high quality GaSb structures, no commercial devices based on GaSb/GaAs QDs are available yet. Nevertheless, several very promising approaches have been published, mainly in the fields of long-wavelength luminescence and in particular charge storage.

2.5.1 Storage devices

Due to the large hole confinement and large exciton lifetimes, GaSb QDs are very promising for charge storage devices on a nanometer scale. The charging and charge emission of GaSb QDs has been studied in detail by CV spectroscopy and DLTS [63, 70, 80], and a hole retention time at room temperature of about 1 μs for a single hole with a ground state energy of 450 meV has been obtained, which is five orders of magnitude larger than for InAs/GaAs QDs [63].

The principal idea how to use GaSb QDs as single charge storage device is illustrated in Fig. 2.14, based on a concept of Geller, Marent, and Bimberg [82, 83, 269]. The device structure consists of a semiinsulating GaAs substrate, followed by a highly p-doped GaAs contact layer and another p-doped GaAs layer. Onto this, the GaSb QDs are grown, sandwiched between thin undoped GaAs layers. After deposition of another p-doped GaAs layer, a highly n-doped GaAs cap layer completes the structure, which can be lithographically etched and contacted by metal evaporation [63, 81]. As a result, the GaSb QD is situated within the depletion zone of a p-n diode, as depicted for the VB in Fig. 2.14(a).

All necessary processes of charging and discharging the QDs can now be controlled by adjusting the voltage at the p-n junction: At sufficiently high reversed voltages, the band bending is so strong that the holes can tunnel out of the QD in a reasonably short time, as sketched in Fig. 2.14(b). For charging the QDs, on the other hand, a forward bias enables the charge carriers to reach the QD where the holes get trapped, shown in Fig. 2.14(c).

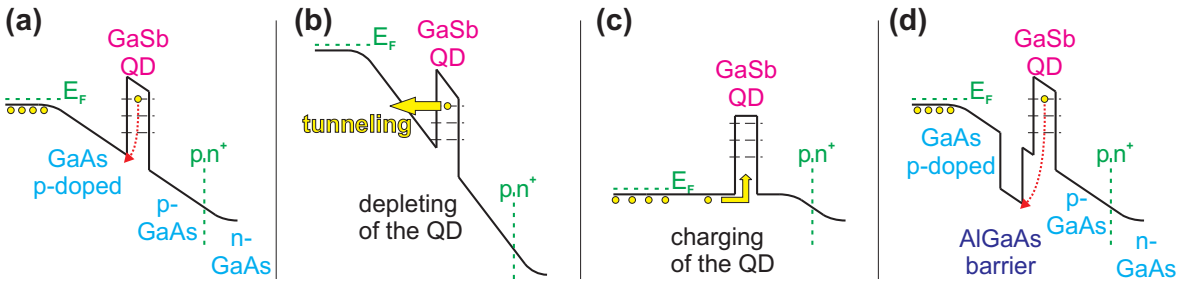

FIGURE 2.14: Schematic diagram of the VB of a GaSb QD embedded in a p-n-junction, used for charge storage. (a) Storage: The hole is confined. The red pointed arrow indicates the energy needed to overcome the emission barrier. (b) Discharging: Increasing the electrical field, the hole can tunnel out of the QD. (c) Charging: Decreasing the electrical field, holes can relax into the QD. (d) By using an additional AlGaAs layer, the emission barrier for confined holes gets enlarged.

These processes are already established from the DLTS measurements, thus the relevant time constants are well-known: Adjusting the diode voltage is extremely fast, and the relaxation process of the holes occurs within picoseconds. Thus, writing in such a QD-based charge storage device is even faster than in conventional dynamic random access memory (DRAM) devices [82]. Reading the stored information could be implemented in the same way as in conventional Flash storage devices by depositing a thin QW containing a 2D electron gas near the QD layer and measuring the current in this layer, getting influenced by the charge of the QDs.

Crucial for an application as storage device is the storage time of the QDs at room temperature. For InAs/GaAs QDs with an hole localization energy of 210 meV this storage time amounts to about 0.5 ns [270], and for Ge/Si QDs with 350 meV hole localization it is ~ 0.1 μs [271], in comparison to ~ 1 μs for GaSb/GaAs QDs. Recently, the emission barrier for holes in InAs/GaAs QDs was significantly increased by growing an $Al_{0.6}Ga_{0.4}As$ barrier closely underneath the QD layer: In this way, the hole localization energy could be extended to 560 meV and a storage time of about 5 ms was obtained [81]. By increasing the Al content in the AlGaAs buffer to 90%, corresponding to a hole localization of ~ 700 meV, even storage times in the range of seconds could be obtained in the latest experiments [82].

These results can be extrapolated for an intended structure using an AlGaAs barrier underneath a GaSb QD layer, as sketched in Fig. 2.14(d): For this structure, a hole localization energy of more than 1 eV is expected, corresponding to storage times of months up to years. Yielding such timescales, the proposed GaSb QD device could combine the storage times of nonvolatile Flash memories with the fast access and the durability of DRAM devices and exceed both conventional memories by very low electrical currents and extremely high storage densities.

2.5.2 Optoelectronics

For optoelectronic applications within the technologically important telecommunication area, lasing wavelengths of 1.3 μm or 1.55 μm are required as these are the values of least absorption and optical dispersion in fiber optics. In the InAs/GaAs system, QD emission or even lasing at these wavelengths has been achieved mainly by using additional complex strain reducing layers, often containing small amounts of antimony [272–277]. For GaSb/GaAs QDs, room temperature emission wavelengths of 1.3 μm have been obtained without the necessity of additional layers [55, 56], due to the low electron-hole recombination energy. However, special care had to be taken to prevent strong Sb-As exchange processes, for this reason the correct sequence of Ga, As, and Sb flux and intermitting growth interruptions is essential.

While lasing at 1.3 μm has already been established some years ago for GaAsSb/GaAs QW heterostructures in edge emitting lasers [78] as well as in vertical cavity surface emitting lasers [79], the device formation using GaSb/GaAs QDs is still on the way. One challenge is the luminescence intensity, which – due to the only partial overlap of electron and hole wave functions – is comparably low for GaSb QDs. Possible strategies to overcome this limitation and to increase the intensity could be using stacked QD layers [49, 61, 262] or the use of InAs QD stressors for an increased GaSb QD density [53]. If, in the latter case, the GaSb QDs are grown in close proximity or directly on an InAs layer, a combined band alignment can be expected with electrons confined in the InAs layer and holes confined in the GaSb QDs, leading to an even smaller recombination energy [182]. However, such a structure has not been realized yet.

Chapter 3

Scanning tunneling microscopy

Since its invention in 1982 by Binnig, Rohrer, Gerber, and Weibel [85, 86, 88], scanning tunneling microscopy (STM, also used for "scanning tunneling microscope") has revolutionized the characterization and description of crystal surfaces, enabling one to analyze topografic and electronic properties of surfaces with atomic resolution [89, 90, 278, 279].

The principle of STM is shown schematically in Fig. 3.1: A sharp metal probe tip is scanned over a conductive sample surface in close proximity but without physically touching it. When a bias voltage is applied, a tunneling current results which depends exponentially on the distance between the tip and the sample and also on the electronic potential of the surface. Thus, the topography of the sample can be imaged as well as local variations of electronic properties of the surface, induced for example by variations of the chemical composition. It should always be kept in mind that STM results represent an interaction between tip and sample properties. This is exemplarily sketched in Fig. 3.1 as sharp edges and interfaces of the sample surface appear rounded in the STM data due to the geometry of the probe tip.

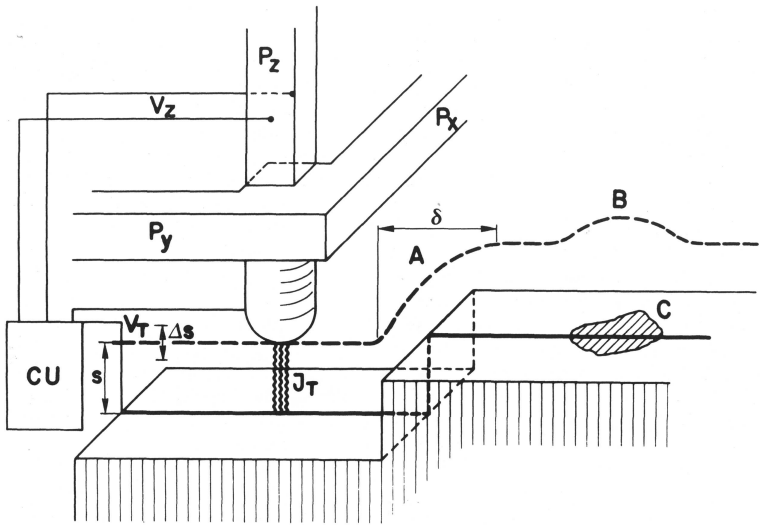

FIGURE 3.1: Operation principle of the STM, from [85]: A metal probe tip is scanned over a conductive sample in a distance s by a piezo tripod P_x, P_y, P_z. The tunneling voltage V_T is generated by a control unit CU, which also keeps the tunneling current I_T constant by adjusting the voltage of the z-Piezo V_Z. This regulation of the tip height Δs represents the STM signal (dashed line), which depends on the topography of the sample surface (A) as well as on local variations of the electronic or chemical composition (B, C). It is additionally influenced by the geometry of the probe tip, leading for example to an apparent broadening δ of actually sharp surface steps.

Although the theory and some possible applications of electron tunneling were quite well understood (see [89, 90] and references therein) and even vacuum tunneling of electrons from metal to metal was established already in 1971 [280], two large challenges had to be overcome by the realization of the first STM showing atomic resolution: The obtained tunneling currents are very small, typically in the 100 pA range, and are extremely sensitive to variations of the tip-sample distance, so that sensitive amplifiers and fast feedback electronics have to be used. To establish a stable tip-sample distance and to control the lateral tip position with atomic precision, a very precise positioning of the tip is crucial. This task can be coped with by piezo-ceramic actuators. Additionally, for atom-resolved surface studies very clean ultrahigh vacuum conditions and an enhanced vibration isolation are necessary. Once this preconditions were fulfilled [85, 281], STM soon proved its ability to resolve surface atomic structures [88, 279, 282–284] and also to analyze local electronic properties [104, 105, 107, 285, 286].

In this section, first some aspects on STM theory will briefly be introduced, followed by a presentation of the operational modes of STM used for this work. Then the special issues of cross-sectional STM (XSTM) are presented, enabling the characterization of capped nanostructures. As most III-V semiconductor heterostructures crystallize in the Zincblende structure, revealing a (110) cleavage surface in XSTM studies, finally the appearance of this surface and the mechanisms relevant to the generation of corresponding STM images are discussed.

3.1 Theory of STM

The underlying physical effect of STM is the quantum mechanical effect of tunneling. Its basic consequences for STM imaging can qualitatively be understood even in a simple one-dimensional model. The actual STM situation, however, the three-dimensional interaction between a probe tip and a sample surface, is much more complex; and its theoretical description goes far beyond the scope of this thesis. So only some implications of STM theory, which are directly relevant for the STM data of this work, will be mentioned here. For an extensive introduction textbooks like Refs. [89, 287, 288] are suggested.

3.1.1 One-dimensional tunneling

Tunneling from a metal tip through a vacuum barrier into a conductive sample (or vice versa) can, in a most simple case, be described by a one-dimensional model with a potential barrier of finite height, sketched in Fig. 3.2. An electron of energy E can classically not penetrate a barrier of the potential $V_0 > E$. In quantum mechanics, however, the electron can be described by the time-independent Schrödinger equation

$$\left(-\frac{\hbar^2}{2m}\frac{\partial^2}{\partial x^2} + V(x)\right)\psi(x) = E\,\psi(x) \tag{3.1}$$

with the potential $V(x) = V_0$ in the barrier between $x = 0$ and $x = s$ and $V(x) = 0$ elsewhere. This equation can be solved by electron wave functions

$$\psi(x) = \psi(0)\,\exp\left(-\kappa\, x\right), \quad \text{with}\,\kappa = \frac{\sqrt{2m\,(V-E)}}{\hbar}\,. \tag{3.2}$$

This solution implies a sinusoidal oscillation of the wave function in regions with $V(x) = 0$, where κ is imaginary, but an exponential decay of the probability density $|\psi(x)|^2$ within the barrier, where κ is real. Correspondingly, the electron can tunnel from the tip (or the sample) into the vacuum, where its probability density decays exponentially.

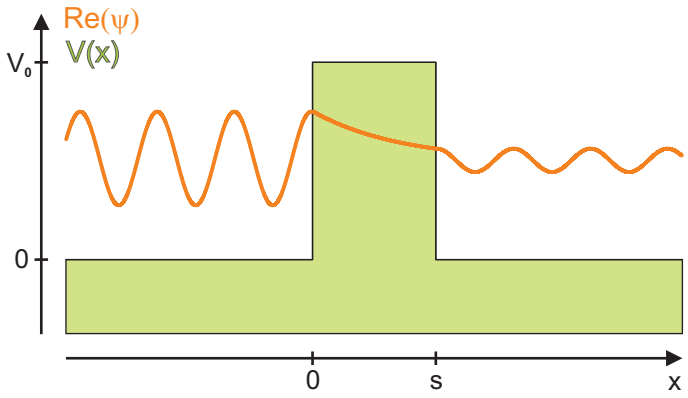

FIGURE 3.2: One-dimensional tunneling through a potential barrier.

Regarding a current density in front of and behind the potential barrier, the transmission coefficient through the barrier can be calculated straightforwardly (as it is carried out in typical textbooks like [141]). The current density behind the barrier results approximately to

$$j \propto e^{-2\,\kappa\, s}, \tag{3.3}$$

meaning that the tunneling current depends exponentially on the tip-sample distance, and also on the applied tunneling voltage V_T, as κ contains the electron energy $E = eV_T$.

3.1.2 Bardeen and Tersoff-Hamann approaches

Although the simple one-dimensional model can already explain the exponential behavior of the tunneling current, the actual tunneling situation at STM experiments is much more complex. A three-dimensional configuration has to be considered, with potentials of probe tip and sample surface which in general vary both spatially and temporally. The tunneling itself is not a straight-forward and unidirectional process, but is a transition of electrons and holes between tip and surface states, as the wavefunctions of tip and surface atoms partially overlap.

This situation can theoretically be described by quantum mechanical perturbation theory: The tip and the sample are first modeled as independent systems, and the tunneling process then corresponds to a transition of a charge carrier from a certain state of one system into a state of the other system [87, 89]. Considering tip states ψ_μ^t with energy E_μ^t and sample states ψ_ν^s with energy E_ν^s to solve the time-dependent Schrödinger equation, respectively, and regarding a tunneling voltage V_T being applied to the surface, the tunneling current results to

$$I \;=\; \frac{2\pi e}{\hbar} \sum_{\mu,\nu} f(E_\mu^t)\,[1 - f(E_\nu^s + eV_T)]\;|M_{\mu\nu}|^2\;\delta(E_\mu^t - E_\nu^s)\,, \tag{3.4}$$

with the Fermi-distribution $f(E)$ and the transition matrix element $M_{\mu\nu}$. Thereby the sum extends over all possible tip and sample states, while the delta-distribution restricts the current to elastic tunneling processes and the Fermi-distributions imply that tunneling can only occur from occupied into empty states. At room temperature and typical energy ranges of interest covering some eV, the Fermi-distribution comes close to a step function. When additionally the sum over discrete energies is replaced by an integral over all states in the tip and the sample, the tunneling current can approximately be written as

$$I \;=\; \frac{4\pi e}{\hbar} \int_0^{eV_T} \varrho_s\,(E_F - eV_T + \epsilon)\;\varrho_t\,(E_F + \epsilon)\,|M|^2\,d\epsilon\,. \tag{3.5}$$

Thereby ϱ_s and ϱ_t are the electronic density of states (DOS) of the sample surface and the tip, respectively. The transition matrix element M has to be evaluated for all tip and sample

states. For this, an approach based on Bardeen can be used, who parameterized it as an integral over an arbitrary plane $\vec{S}$ between the two subsystems [289]:

$$M_{\mu\nu} \;=\; -\frac{\hbar^2}{2m} \int \left(\psi_\mu^{t\,*}\, \nabla \psi_\nu^s \;-\; \psi_\nu^s\, \nabla \psi_\mu^{t\,*} \right) \cdot d\vec{S} \tag{3.6}$$

Therefore, the value of the matrix element is determined by the specific wave functions of both tip and sample and especially by the interaction between these wave functions.

A widely used approximation of the matrix element and the tunneling current goes back on the model of Tersoff and Hamann, developed shortly after the invention of STM [87, 278, 290]. In this model the tip is considered as a locally spherical potential well, including the assumptions that the tip is geometrically and electronically isotropic and that its contribution to the tunneling matrix element is dominated by wave functions with s-orbital shape. Under these restrictions, which resemble the ideal STM tip, equation 3.5 transforms into

$$I \;\propto\; \varrho_t \int_0^{eV_T} \varrho_{s,\,loc} \left(\vec{R}, E_F + \epsilon \right) d\epsilon \,. \tag{3.7}$$

The term $\varrho_{s,\,loc}\,(\vec{R}, E)$ means the local density of states (LDOS) of the sample surface for a certain energy E at the position $\vec{R}$ of the topmost atom of the probe tip, whereas the tip DOS ϱ_t is considered as constant. An exponential dependence of the current on the tip-sample distance is not directly evident in formula 3.7 any more, but it is still valid, at least approximately, as the sample LDOS typically decays exponentially in the vacuum. The tunneling voltage influences the current as upper limit of the energy integral.

It should be noticed that hardly any STM tip satisfies the assumption of an isotropic, locally and temporally invariant DOS, being necessary to obtain the expression 3.7. Instead, real STM images are very often affected by the tip geometry and changes of the geometric and electronic structure of the tip. The influence of different tip wave functions on the tunneling current and the STM images was studied by Chen [89, 291], including s and different p and d wave functions. He showed theoretically that for some surfaces the experimentally observed resolution and atomic corrugation amplitude can only be reached by STM tips with specific wave functions of higher angular momentum l.

Nevertheless, Eq. 3.7, called the Tersoff-Hamann approximation, is the most general and simple expression of the tunneling current, interpreting it as an energy integral over the sample LDOS at the position of the tip.

3.2 Operation modes of STM

STM can be performed in different ways, leading to real-space images of the sample surface containing different kind of information. Scanning tunneling spectroscopy can contribute additional electronic details, either for specific points or also in combination with a whole STM image. Those of the possible operation modes which have been used for this work will shortly be introduced in the following.

3.2.1 Constant current mode of STM

The most common way to obtain STM images is the constant current mode: When the tip is scanned over the sample surface, the resulting tunneling current is permanently measured by a control electronic, which compares it with a given reference value. A feedback loop adjusts the tip-sample distance by controlling the voltage of the z-piezo actuator so that the tunneling current is kept constant. This method has already been sketched in Fig. 3.1. A

stable, fast, and sensitive performance of this feedback loop is crucial for obtaining STM images in a reasonable time without damaging the tip or the sample surface.

Typical STM currents are about 50 pA to 100 pA for semiconductor samples and up to several nA for metals. The tip-sample distance depends on the chosen combination of tunneling voltage and reference current and is typically in the range of 1 nm. As a role of thumb, decreasing the tip-sample distance about 1 Å (1 Ångstrøm = 0.1 nm) increases the tunneling current by a factor of ten.

As the current is intended to be kept constant, the actual STM signal in this operation mode is the height adjustment of the tip above the surface. This signal could easily be understood as the direct topography of the sample surface, but that would be strongly simplified. Regarding the STM theory and the Tersoff-Hamann approximation (Eq. 3.7), the contour lines of the STM measurement or the areas of the same color in a grayscale or color picture represent areas of the same integrated LDOS of the sample at the position of the tip, evaluated for the energy integral from $E = E_F$ to $E = E_F + eV_T$.

Thereby electronic states with larger energies contribute stronger to the integral than states with smaller energies, as depicted in Fig. 3.3 for both polarities of the tunneling voltage: The decay of the sample LDOS into the vacuum barrier can in first order be approximated as exponentially with an energy dependence given by Eqs. 3.3 and 3.2. Accordingly, states with energies near the vacuum potential decay comparatively slow and contribute stronger to the tunneling current than states with small energies [287].

3.2.2 Tip-induced band bending

Although STM is a non-destructive method, meaning that ideally the sample surface is exactly the same before and after being scanned by the tip, it is important to notice that nevertheless the tip can significantly influence the STM images by the effect of tip-induced band bending (TIBB) [107, 134–137, 292, 293].

The tunneling regime of a metal tip in close proximity to the semiconductor sample surface, separated by the vacuum barrier, can be described as a metal–insulator–semiconductor junction, which – in the planar case – is well understood and described in appropriate textbooks (see [294, 295] for example). The exact band alignment of this junction is determined

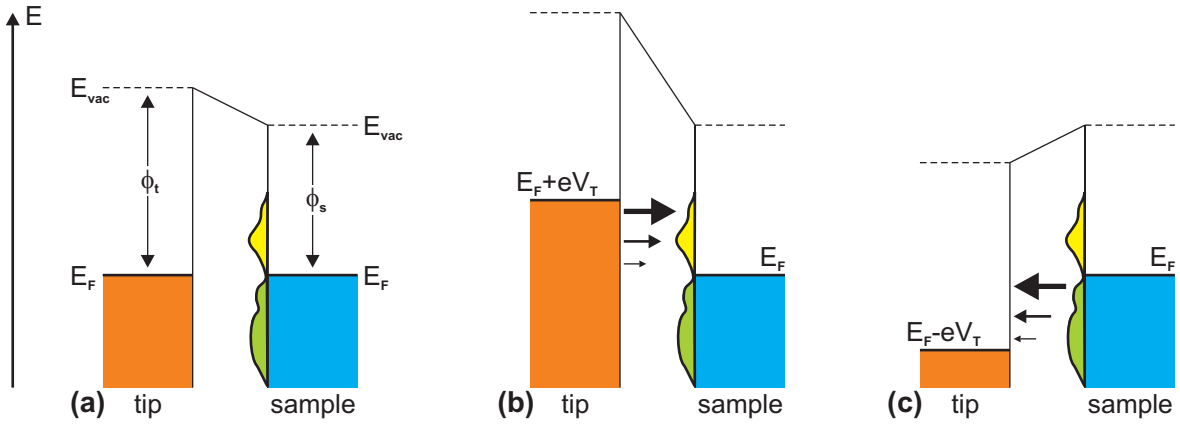

FIGURE 3.3: Tunneling between the tip (with work function ϕ_t) and the sample (with work function ϕ_s) through the vacuum barrier. An arbitrary sample LDOS is sketched with empty (yellow) and filled (green) states. The tunneling probabilities are indicated by black arrows (a) without applied voltage, where no tunneling current results, (b) for a positive sample voltage, and (c) for a negative sample voltage. Adapted from [287].

by the Fermi energies of tip and sample, the metal work function, the electron affinity and the doping of the semiconductor, and by the gap width [see Fig. 3.4(a)].

When a tunneling voltage is applied to the sample, the resulting electric field between the sample and the tip will induce a bending of the bands [Fig. 3.4(b-d)]. Such a bending can also occur without an applied voltage [Fig. 3.4(a)], when a strong doping or surface states of the sample cause additional charges at the surface, which will also induce an electric field, or just because of the band alignment due to the electron affinity [134, 296]. The electric fields are shielded both in the tip and the sample by space charges. In the metal, the high density of free electrons leads to a shielding of the fields within about 1 Å, so that the effect of band bending is negligable within the tip. In the semiconductor, however, the lateral extension of the space charge region depends on the available number of free charge carriers [296]: Strongly doped samples have a very small space charge region, while for intrinsic and very pure regions of semiconductors TIBB can even extend over several hundred nm. The band bending can easily amount to several eV for GaAs already at moderate tunneling voltages [107, 297], and especially in very pure samples a dominant influence of TIBB has been observed [298]. Additionally, the amount of TIBB depends on the width of the vacuum barrier, being the

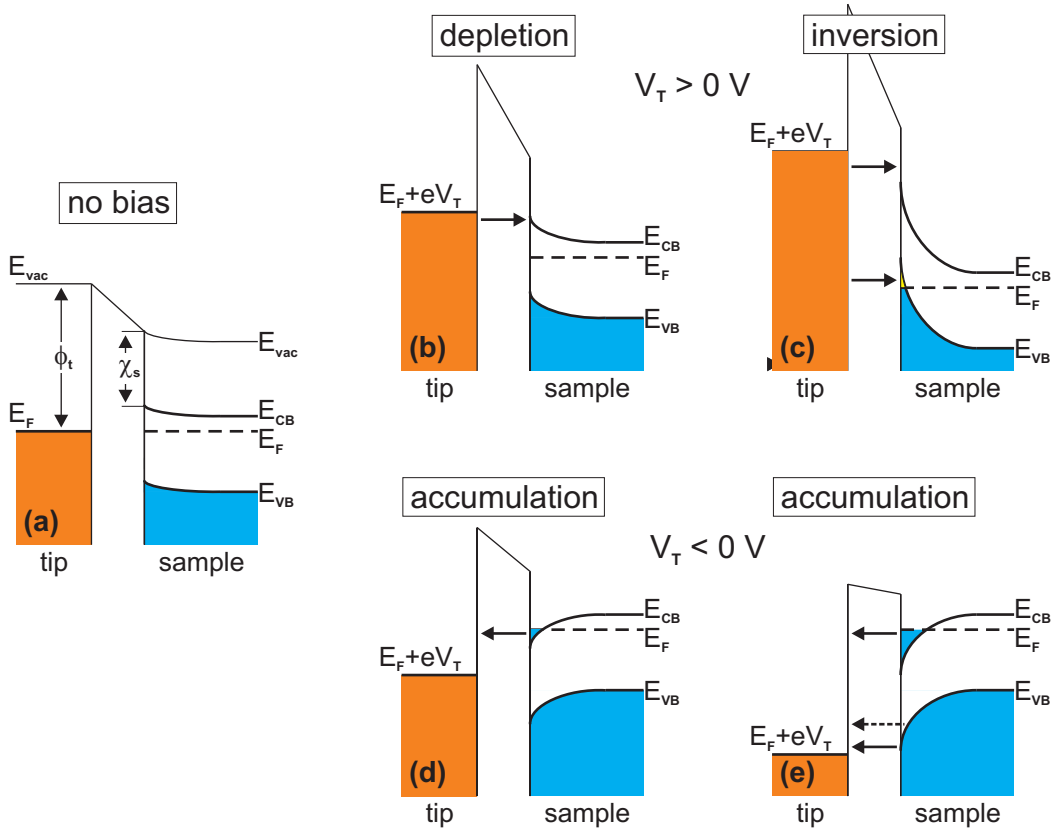

FIGURE 3.4: Schematic overview on typical regimes of tip-induced band bending at an n-type semiconductor: (a) No voltage applied, the band bending is determined by the tip work function ϕ_t, the sample electron affinity χ_s, the doping concentration, and the width of the vacuum barrier. No tunneling current is obtained. (b) Moderate positive sample voltage, the sample CB is depleted of electrons and tunneling into this CB occurs. (c) Large positive sample voltage, in spite of the n-type doping of the sample there are empty states in the VB at the surface (inversion), leading to additional tunneling. (d,e) Negative sample voltage, the CB is accumulated with electrons near the sample surface, leading to tunneling into the tip. (e) For larger negative sample voltages, also tunneling from the sample VB into the tip occurs.

tip-sample distance [134, 135].

As a consequence of TIBB, a tip-induced accumulation of electrons has been observed at the sample surface directly underneath the tip, leading to the formation of a two-dimensional electron gas [299] or even of so-called tip-induced QDs with zero-dimensional confinement of the accumulated electrons [136]. As the band bending is induced by the STM tip, the geometry of the tip strongly influences the lateral and spatial extension of the space charge zone in the sample [135, 299].

Depending on the polarity and amount of the applied tunneling voltage, different typical regimes of TIBB are occuring, which are labeled in literature with respect to the used type of doping, defining the majority charge carriers in the sample [107, 297]. Figure 3.4 sketches these regimes for a moderately n-doped sample, with electrons being the majority charge carriers: With no applied voltage, or for small positive and very small negative sample voltages, both the conduction band (CB) edge and valence band (VB) edge of the sample are bend upwards, so at the surface the CB is depleted of electrons. As additionally the Fermi energies of tip and sample are equal while no external bias is applied and are lying within the band gap of the sample, no tunneling current occurs (a).

The term depletion is also used to describe the situation at moderate positive sample bias, where the sample CB edge is below the Fermi energy of the tip and electrons can tunnel from the tip into the empty states of the sample (b). At large positive voltages also inversion may take place, meaning that the sample VB edge is shifted above E_F, and holes as minority charge carriers contribute to the tunneling current from the sample into the tip (c). However, it is still under discussion whether inversion actually occurs at GaAs or not [297].

A downward band bending is yielded with negative sample voltages (d): At moderate negative voltages the CB edge is shifted below E_F, resulting in an accumulation of electrons in the CB at the surface which can tunnel into the tip. For larger negative voltages (e) the Fermi energy of the tip is below the sample VB edge, and additional tunneling from filled VB states of the sample into empty states of the tip can occur. Such a tunneling from the sample VB for strong accumulation can also occur if the Fermi energy of the tip is still slightly above the VB edge, as in this case the electrons can additionally tunnel through the thin space charge region, leading to a correspondingly decreased current. The same argument is valid, too, for electron tunneling from the tip through the vacuum and through the thin space charge region into the CB at strong depletion.

3.2.3 Voltage-dependent imaging

As STM images represent the integrated LDOS of the sample at the tip, the applied tunneling voltage determines the energy range over which the integration is performed. This can have significant influence on the information stored in the images. As a general consequence, the energy range of the integral gets larger with increasing tunneling voltage, so that the reference current is reached for larger tip-sample distances. At such large distances, the sample LDOS will be less distinctive and corrugated, as early calculations of Tersoff et al. have shown [87, 290], displayed in Fig. 3.5(a). Thus, good atomic resolution can easier be achieved at lower voltages, although then the stability of the tunneling current often reduces as electronic effects gain in importance. Especially at STM studies on semiconductors care has to be taken when applying very low voltages, as obviously no or only very weak tunneling can occur within the bandgap, easily leading to a tip crash.

Beside the amount of the tunneling voltage, its polarity is of even larger significance, especially at semiconductors with a pronounced band structure. Depending on the tunneling polarity, either the filled or the empty states of the sample LDOS get imaged, as is sketched in Fig. 3.3(b,c). Feenstra et al. have impressively shown that for III-V semiconductors like GaAs

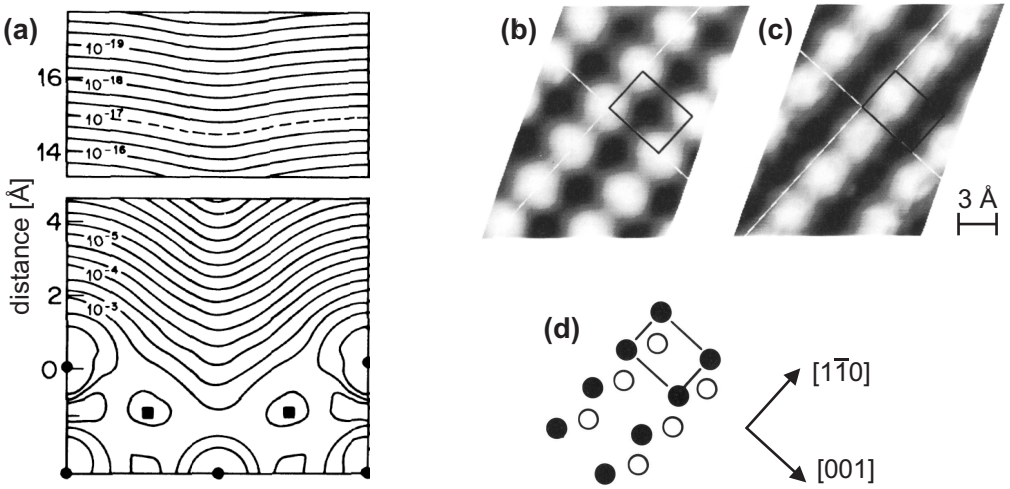

FIGURE 3.5: (a) Calculated LDOS of an Au(110) surface with (2x1) reconstruction, shown in the (1$\bar{1}$0) plane, from [87]. Positions of the Au nuclei are indicated by solid circles (in plane) and squares (out of plane). Contour lines of constant LDOS are plotted and labeled in units of a.u.$^{-3}$ eV^{-1}. (b,c) STM images of a GaAs (110) surface, aquired at sample voltages of (b) V_T = + 1.9 V, representing the Ga atoms, and (c) V_T = - 1.9 V, representing the As atoms. (d) A sketch of the GaAs (110) surface, containing both Ga (closed circles) and As atoms (open circles). The corresponding surface unit cell is also indicated in (b) and (c). Taken from [106].

the empty states are attributed to the group-III atoms and the filled states to the group-V atoms, so that either the Ga or the As atoms are seen in the STM images, depending on the bias polarity [106, 300]. The corresponding images are shown in Fig. 3.5(b-d), together with a sketch of the GaAs(110) surface and its unit cell.

In accordance with these and most other STM publications, in the following tunneling voltages will be designated regarding the sample, so a negative V_T means that the sample is negatively biased in respect to the tip, and vice versa.

3.2.4 Scanning tunneling spectroscopy images

While by decreasing the tunneling voltage the energy range of the LDOS integration can be limited, it is yet not possible to study the sample surface at one specific energy. A very elegant way to enable this is by using scanning tunneling spectroscopy (STS), meaning a continuous variation of the tunneling voltage.

Starting from STM theory and the Tersoff-Hamann approximation of the tunneling current (Eq. 3.7)

$$I \propto \varrho_t \int_0^{eV_T} \varrho_{s,loc}\left(\vec{R}, E_F + \epsilon\right) d\epsilon \,,$$

the integration of the LDOS over a certain energy range can be avoided if the tunneling current is differentiated in respect to the voltage:

$$\frac{dI}{dV} \propto \varrho_t \cdot \varrho_{s,loc}\left(\vec{R}, E_F + \epsilon\right) . \tag{3.8}$$

Thus the differential conductance dI/dV has to be obtained to directly study the LDOS of the sample at the position of the tip for a certain energy $E_F + eV_T$, so the variation of the tunneling current with varying bias voltage needs to be measured. This can experimentally be realized by using a lock-in amplifier: The given tunneling voltage is slightly modulated and the variation of the tunneling current per voltage modulation can then be measured.

Thereby the modulation amplitude and frequency have to be chosen in such a way that they do not interfere with the feedback loop of the STM. Then the conventional constant current STM image can be taken at the average tunneling voltage, and additionally the dI/dV-signal is obtained for every image pixel. As a result, two images are aquired simultaneously, namely the constant current STM image, often called topographic image, and an additional dI/dV-image, in the following called STS image. The first one represents the sample LDOS for energies integrated up to the tunneling voltage, while the latter shows the sample LDOS directly at the energy corresponding to the tunneling voltage.

In a further step, the tunneling voltage can not only be slightly modulated but strongly varied at each pixel of the image: Using this method, called current imaging tunneling spectroscopy (CITS), a common STM image is aquired in the constant current mode at a certain voltage, but at each pixel the feedback loop is opened, the voltage is ramped from the initial stabilization value over a large voltage range, and at various specific voltages during this ramp the corresponding current is measured. Thus, a data cube containing several images of tunneling currents at specific voltages is obtained within one scan. Due to the applied voltage ramp special care has to be taken to perform the measurement slowly enough to avoid decaying capacitive currents during data aquisition and fast enough to keep the time per image within reasonable limits.

The CITS method has first been developed to investigate different surface states of a Si(111) sample [285, 286]. But it is even more useful to study confined states of QDs, as it is possible to stabilize the tunneling feedback at sufficiently large voltages and at the same time studying the QDs at energies which lie within the band gap of the host material. In this way Grandidier et al. were able to distinguish between s- and p-like states of cleaved InAs/GaAs QDs from CITS images at different voltages [108]. Maltezopoulos et al. used the CITS method in combination with lock-in technique and obtained not only current but also dI/dV-images at various voltages, mapping the wave functions of single electrons in free-standing InAs QDs [110].

3.2.5 STS point spectra

Besides the possibility to aquire different kinds of images of two-dimensional sample surfaces at certain voltages, STS also enables one to obtain continuous tunneling spectra over the complete voltage range at specific positions on the surface, preferentially at points of special interest.

By varying the tunneling voltage and at the same time measuring the resulting current, local I–V-spectra can be taken, showing directly the dependence of the tunneling current on the applied voltage. By using the lock-in technique described above, also dI/dV–V-spectra can simultaneously be obtained.

Typical I–V- and dI/dV–V-spectra of GaAs are shown in Fig. 3.6, obtained by Feenstra et al. [107, 301, 302]. The intrinsic GaAs band gap can clearly be recognized as voltage region for which no tunneling current results, provided that no additional states, induced for example by dopant atoms, are present at the surface [Fig. 3.6(a)]. The more voltage is applied to the sample of either positive or negative polarity, the larger the tunneling current gets, as more states contribute to the energy integral of the current. Although the onsets of the valence band and conduction band are evident, the energy distance between them does not agree with the literature value of 1.4 eV. Generally, in I–V- and dI/dV–V-spectra the absolute energies especially of the band edges are often shifted due to TIBB, while the slope and characteristic peaks of individual bands of the sample's LDOS and also the energetic distances between distinct features within one band are well resembled [107, 134, 135].

If the local area of the GaAs sample contains dopant atoms, the Fermi energy is shifted

towards the VB or CB edge and the apparent band gap in the spectra is decreased, as an additional small conductivity is implied. Figure 3.6(b,c) shows this additional contribution of dopant-induced states for (b) p-type and (c) n-type doping, respectively, which can only be understood considering the effect of TIBB [107, 297, 301]: In the case of p-type doping, the Fermi energy is near or within the VB of the sample, and the holes are the majority charge carriers. At negative sample voltages electron tunneling out of the VB occurs (which can equally be described as hole tunneling into the depleted VB), but the corresponding curve in the spectra (b) is shifted towards positive voltages with respect to the intrinsic case (a) due to the shifted Fermi energy. For larger positive voltages electrons can tunnel into the CB, resulting in a strong current, but already at low positive voltages an additional small current can be observed, which is a doping-induced contribution: In this voltage regime TIBB leads to an accumulation of holes in the VB at the sample surface, leading to small electron tunneling into the VB (or hole tunneling out of the accumulated VB).

In the case of n-type doping, the Fermi energy is near or within the CB, and electrons are the majority charge carriers [Fig. 3.6(c)]. Correspondingly, the I–V-curves corresponding to electron tunneling out of the VB and into the CB are shifted towards negative voltages, and a doping-induced contribution of the tunneling current occurs for small negative voltages. This dopand component can be explained as tunneling of accumulated electrons from the CB of the sample due to TIBB (see also Fig. 3.4 for illustration). In the insets of Fig. 3.6(b,c) the

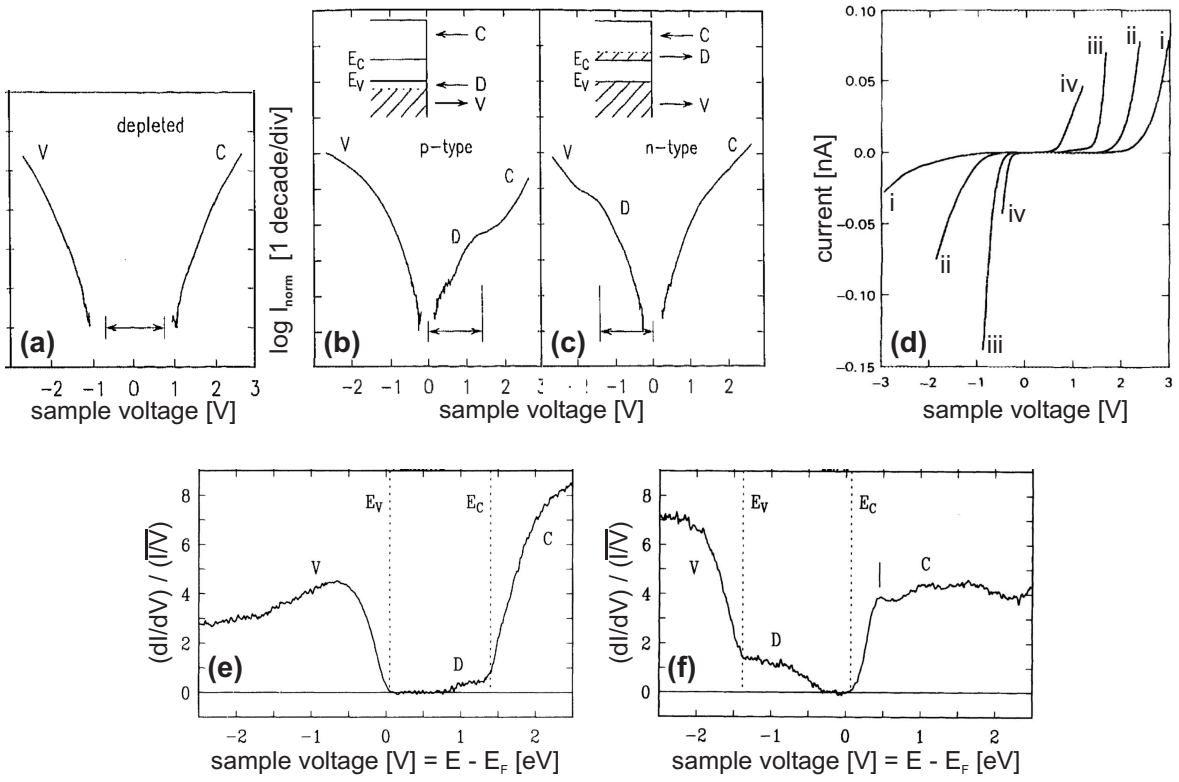

FIGURE 3.6: STS point spectra on GaAs(110): (a-c) I–V-spectra of GaAs pn-diode structures, plotted using a logarithmic I scale, aquired at (a) the depleted interface region, (b) a p-doped layer, and (c) an n-doped layer; from [301]. The insets of (b,c) sketch the tunneling from and into CB, VB, and dopant-induced states, respectively. (d) I–V-spectra of one p-doped GaAs layer, while the tip-sample distance is decreased by (ii) 1.2 Å, (iii) 3.2 Å, and (iv) 4.8 Å; from [107]. (e,f) Spectra of the normalized differential conductance over the tunneling voltage for (e) p-doped and (f) n-doped GaAs; from [302].

respective electron tunneling into CB and acceptor states and out of VB and donator states is depicted for p- and n-doped GaAs.

As the tunneling current is determined not only by the tunneling voltage, but varying also exponentially by the tip-sample distance, the slope of the I–V-spectra strongly depends on this distance, too. In Fig. 3.6(d) several I–V-spectra of the same GaAs layer are shown, taken at different tip-sample distances. This time the current is plotted on a linear scale. Besides the obvious increase of the current with decreasing distance, it should also be mentioned that a doping-induced contribution to the tunneling current can only be seen for small tip-sample distances, as in this case the effect of TIBB is stronger.

The measurement of the current is technically limited to a few orders of magnitude, because too large currents would destroy the tip or sample and too small currents cannot be resolved. Thus, only a small range of the actual I–V-characteristic can be obtained experimentally with one spectrum, especially for semiconductors with a considerable band gap.

This limitation can be overcome by performing STS point spectra using the variable gap mode, first introduced by Feenstra et al. [278, 303, 304]: In this mode, the tip-sample distance is changed as a function of the applied tunneling voltage. During the voltage ramp of the spectrum, the distance is decreased while the absolute value of the voltage is decreased, and increased again when the absolute value of the voltage is increased at the other polarity. Afterwards, the measured current has to be normalized by a function which includes the dependence on the distance. By this method, the dynamic range of the spectra can be increased by several orders of magnitude [302].

As described above, the dI/dV-signal is better suited to describe the sample LDOS than the tunneling current itself, therefore in many studies using STS point spectra also dI/dV–V-spectra are obtained, either by numerically differentiating the measured tunneling current, or by directly measuring the differential conductance by lock-in technique. These data, too, are influenced by the tip-sample distance, especially in the variable gap mode. A very elegant way to normalize the measured differential conductance is by dividing it through the absolute conductance, which eliminates the dependence on the distance. Additionally, this $(dI/dV)/(I/V)$-signal has been shown to directly represent a normalized sample LDOS, independent of the distance of the tip [105, 305, 306]. One modification has to be added for spectroscopic studies on semiconductors with a considerable band gap like GaAs: For such systems, the normalized conductivity diverges at the band edges for a division by (I/V) because the current approaches zero faster than the conductivity. To avoid this divergence, a broadened conductivity can be used for normalizing the differential conductance, resulting in a signal $(dI/dV)/(\overline{\mathrm{I/V}})$ [302]. Several methods for such a broadening are proposed and used in literature [278, 303, 307, 308]. Figures 3.6(e,f) show examples of $(dI/dV)/(\overline{\mathrm{I/V}})$–$V$-spectra of p- and n-doped GaAs, respectively [302]. In this spectra it can well be distinguished between intrinsic and dopant-induced tunneling, and the VB edge and CB edge can clearly be labeled.

3.3 Cross-sectional STM

STM imaging of semiconductor nanostructures is in most cases performed in a top view configuration, meaning that QDs are typically imaged at the (001) growth surface (see for example Refs. [19, 24, 29, 31, 32, 35, 91, 96, 109, 198, 309, 310]). Thereby only free-standing QDs or the initial stages of overgrowth can be investigated, but the structure of capped QDs, which are of much higher relevance for almost all kinds of applications, remains hidden.

This important information can be obtained when STM is performed in a cross-sectional configuration instead: In cross-sectional STM (XSTM) the sample is cleaved, and the cleavage

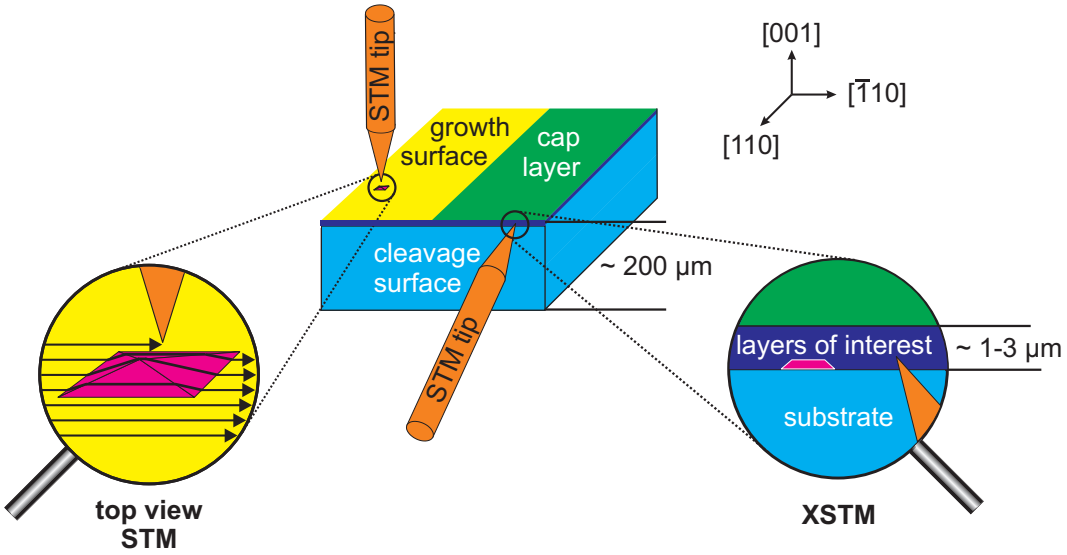

FIGURE 3.7: Comparison of STM in the conventional top-view configuration with cross-sectional STM, imaging a QD on the growth surface (top-view STM) or an overgrown QD (XSTM).

surface is scanned with the STM tip. In the case of QD investigations, the nanostructures can be completely capped during the initial growth, as it is done for optoelectronic or other applications, and the overgrown QDs are studied in cross section. This STM situation, compared with a conventional top view configuration, is shown schematically in Fig. 3.7. An additional benefit of XSTM is that the sample is typically cleaved in ultrahigh vacuum (UHV), yielding a clean and fresh investigated surface, indepedent of the history of the sample.

XSTM was first used to study semiconductor QDs, to my knowledge, by W. Wu and J. R. Tucker at the University of Illinois in Urbana, USA, in 1997 [119]. Within the following ten years, only a few scientific groups worldwide joined in this experimentally complex XSTM investigation on QDs. Among these are (in chronological order of the earliest publications) the groups of D. Stiévenard at the Institut d'Electronique et de Microélectronique du Nord in Lille Cédex, France [108, 120, 311], of R. S. Goldman at the University of Michigan in Ann Arbor, USA [94, 121, 312, 313], and the group of M. Dähne at the Berlin University of Technology, Germany [92, 93, 100, 103, 122, 125, 127, 131], in which this work was realized; further the groups of C. K. Shih at the University of Texas in Austin, USA [95, 123, 314], of P. M. Koenraad at the University of Technology Eindhoven, The Netherlands [97, 126, 128, 130, 133, 277, 315–318], and just recently the groups of E. Lundgren at Lund University, Sweden [129], A. Nakamura at Nagoya University, Japan [319], and W. W. Pai at the National Taiwan University [320].

Like all STM data also XSTM images contain structural and electronic information on the investigated sample. Remembering the tunneling current representing the integrated sample LDOS at the position of the tip, the topography of the sample will most directly influence the tip-sample distance and therewith the current, while the electronic properties of the sample surface and their local variations are contained within the LDOS. Beside these general considerations, there are also a structural and an electronic contrast mechanism specific for XSTM studies on cleaved QDs.

3.3.1 Structural contrast

Surface steps, adatoms, and other structural features within the cleavage surface can directly be observed in the XSTM images due to their structural image contrast. But even atomically

flat cleavage surfaces will significantly contribute to the structural contrast if they contain a cross section through a strained QD: Self-assembled QDs achieved by the SK growth mode contain a lot of strain which is even increased upon capping (see also chapter 2.3). When such a QD is cleaved during the XSTM experiment, it can release a part of the strain energy by a structural relaxation at the cleavage surface, leading to a protrusion at the position of the QD and its surrounding. Such a protrusion typically amounts to a few Å in height at the QD, declining laterally within several nm [92, 93, 124].

3.3.2 Electronic contrast

The structural contrast of cleaved QDs in XSTM images is often increased by an electronic contrast, given by different band gaps and tunneling probabilities of chemically different materials and by the electronic confinement in nanostructures. This is illustrated in Fig. 3.8 for bulk GaAs (a), bulk GaSb (b), and for a GaSb/GaAs QD (c): At a negative sample voltage, which is considered in Fig. 3.8, the electronic states within the energy interval from E_F to $E_F + eV_T$, which contribute to the tunnling current, stem from the VB for the bulk material (a,b). The LDOS of the VB of bulk GaAs and GaSb increases in first approximation with $E^{1/2}$. Due to the smaller absolute band gap and the staggered type-II band alignment of GaSb, the resulting tunneling probability is larger for GaSb than for GaAs, leading to a retraction of the tip in constant current mode and to a brighter appearance. By this image contrast not only pure GaAs and GaSb can clearly be distinguished in XSTM images, but also intermixed GaAsSb material has its specific image contrast depending on the grade of alloying.

In the case of nanostructures, the existence of confined states plays a special role also for the image contrast: For GaSb QDs in GaAs, the GaSb electronic states have to satisfy the boundary conditions of the spatial confinement and the band gap of the host material. The resulting confined states, energetically placed above the position of the GaAs VB edge, are characterized by a δ-like LDOS [Fig. 3.8(c)]. In constant current STM imaging, the integrated LDOS of GaSb/GaAs nanostructures is similar to that of bulk GaSb, resulting in a similar electronic contrast. Using STS, however, individual confined states can in principle be distinguished in STS images or spectra [108, 110], provided that the energy separation between the states is larger than the thermal broadening, which at room temperature is about 25 meV.

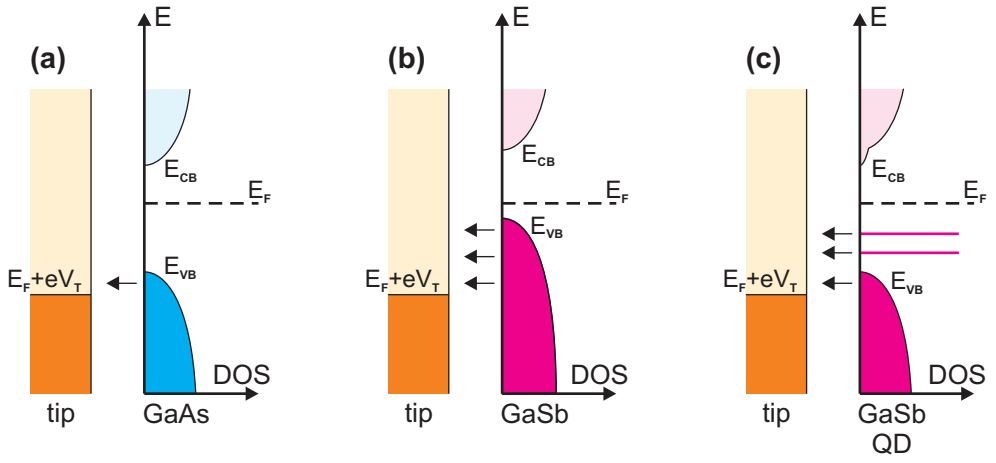

FIGURE 3.8: Electronic image contrast for (a) bulk GaAs, (b) bulk GaSb, and (c) a GaSb/GaAs QD. Contributions to the tunneling current for small negative sample voltages are indicated by arrows.

The differences regarding the band alignment, confined states, and the resulting LDOS are dominant at energies near the Fermi energy, corresponding to small tunneling voltages. Thus the electronic image contrast is of special significance at small tunneling voltages, as in this case a large fraction of the energy integral contributing to the tunneling current is affected. The structural image contrast, however, is given by the topography of the cleavage surface and is therefore comparatively independent of the tunneling voltage. So by varying the applied voltage in XSTM measurements it is possible to distinguish whether observed features are of structural or electronic nature, making XSTM an additionally powerful tool for studying capped nanostructures.

3.4 The zincblende (110) surface

Most III-V semiconductors, including GaAs, GaSb, and also InAs, crystallize in the zincblende structure. It consists of two fcc sublattices of group-III and group-V atoms, being separated from each other by a quarter of the diagonal of the cubic unit cell. The resulting structure is sketched in Fig. 3.9(a), the cubic lattice is plotted with respect to the group-V atoms.

Zincblende crystals can nicely be cleaved in one of the {110} planes [see Fig. 3.9(b)], because these planes are non-polar and contain the least density of unsaturated bonds, being the energetically most favorable among all possible crystal planes. As a consequence, the (110) surface has no reconstructions, meaning a rearrangement of atomic bonds, but shows a relaxation, a shifting of the atomic positions. Additionally, no surface states consist within the band gap of the bulk material for zincblende (110) surfaces, making them very suitable for an electronic characterization of the underlying material by STS.

Relaxation leads to a so-called buckling of the GaAs(110) surface, affecting mainly the atoms of the first surface layer and slightly those of the second layer, too [321–323]. It is displayed for GaAs in Fig. 3.9(c): In the surface layer, the Ga atoms are shifted into and the As atoms out of the crystal, resulting in a vertical height difference of about 0.7 Å. The lateral positions are also adjusted to maintain the Ga–As bond lengths. The complete relaxation results in a projected angle of the surface layer Ga–As bond of 27° to 30° (see [324] and references therein). Beside this geometric relaxation, the formation of double As dangling bonds at the relaxed GaAs(110) surface instead of an equal distribution of single unsaturated bonds at both the Ga and As atoms leads to a further energy reduction.

Looking at the GaAs(110) surface in top-view [Fig. 3.9(d)], atomic zig-zag-chains along $[1\bar{1}0]$-direction are the dominant feature, consisting of alternating Ga and As atoms. However, in STM images only either the Ga or the As atoms can be seen, depending on the polarity, as mentioned above [106, 300]. This effect is independent of the surface buckling, and it was explained by the empty states being attributed to the Ga atoms and the filled states to the As atoms. The exact distribution of electronic states to Ga and As atoms is very complex (see for example Refs. [325, 326]). At least at sufficiently small voltages, however, the main contribution to the tunneling current are – for the respective polarities – the empty dangling bonds of the Ga atoms and the filled dangling bonds of the As atoms.

It is also important to note that in STM data on zincblende {110} surfaces only every second atomic ML in the typical epitaxial growth direction is imaged: Regarding the [001]-direction, the topmost Ga and As atoms are alternately situated either in the (110) surface layer or in the second atomic layer, and at common STM conditions the imaging process is restricted to the surface atoms. (For exceptions at extreme conditions like very small tip-sample distances see for example [292, 327]).

A nearly perfect example image of a GaAs(110) surface can be seen in Fig. 3.9(e). It has been imaged by XSTM with a negative sample voltage, so the LDOS corresponding to the

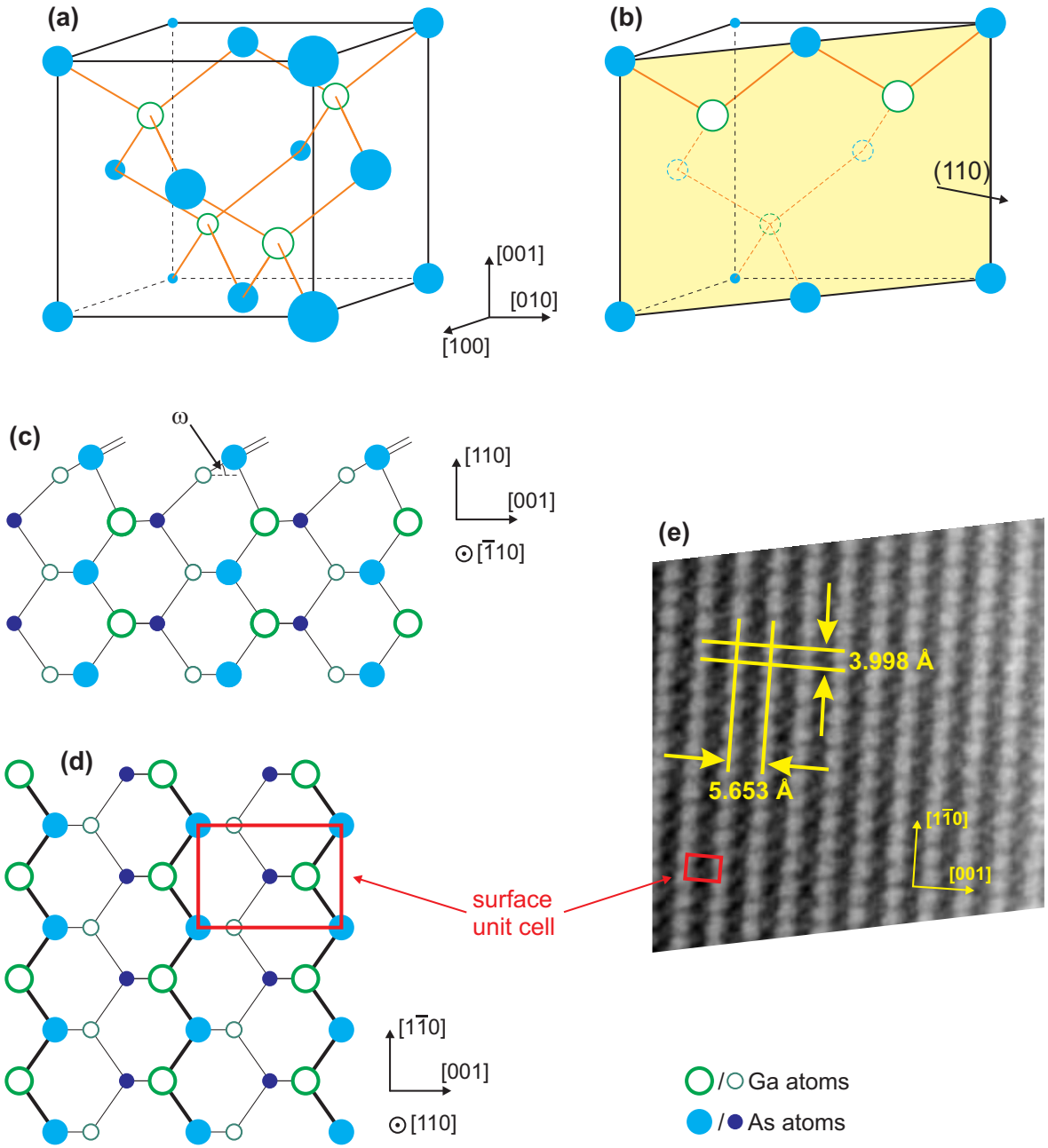

FIGURE 3.9: Atomic model of the zincblende structure, showing (a) a cubic unit cell, (b) the (110) cross section through this cell, and the (110) cleavage surface in (c) side-view and (d) top-view. The radius of the circles displays the position of the corresponding atoms regarding the respective line of sight. Buckling of the surface, with tilt angle ω, and the angles of the filled dangling bonds are considered in (c), according to Refs. [324, 326]. (e) XSTM filled state image of GaAs, representing the As atoms.

filled dangling bonds of the As atoms can be seen. The surface unit cell and the distances between neighboring surface As atoms are indicated, amounting in [001]-direction to the GaAs lattice constant $a = 5.65$ Å and in $[1\bar{1}0]$-direction to $a/\sqrt{2} = 4.00$ Å. These atomic constants are perfectly suited to calibrate the XSTM images. Such a calibration is principally necessary for each XSTM image, as perturbing effects like thermal drift, piezo non-linearity, and others may vary with time or depending on the image parameters. Unfortunately atomic

resolution is often given only within the [001]-direction, enabling one to determine the size of the investigated structures in one direction, but leaving an uncertainty of typically 10% to 20% regarding the exact shape. However, when atomic resolution is present in both directions, the aquired images can be corrected by lengthening or shearing them according to the measured angles and distances of the surface unit cell.

As mentioned above, the image contrast in STM images generally consists of a structural and an electronic part. This can well be understood at the atomistic level, too: Obviously, a surface step and also a protrusion of the surface at the position of a cleaved QD, producing a structural contrast, will influence the position of each individual atom; and different bulk electronic band structures of, for example, GaAs and GaSb correspond to different atomic bond characteristics and electronic states. But also the smallest possible variation of the sample, an exchange of a surface As atom by an Sb atom, varies the structural and electronic image contrast: Due to the larger bond length of GaSb compared with GaAs, the Sb atom will structurally slightly protrude out of the GaAs(110) surface, and also the dangling bond of a single Sb atom is very different to those of the neighboring As atoms, leading to a distinctive change of the sample LDOS. Imaging of single Sb atoms within the GaAs matrix will be analyzed in more detail in chapter 9.1. Extensive studies on XSTM imaging of GaAs(110) surfaces can be found for example in Refs. [327–330] for intrinsic GaAs and in [331–335] for GaAs surfaces with single dopant atoms.

Chapter 4

Experimental setup

Two different home-built STM systems have been used for the XSTM studies of this work. The principal setup of these chambers, including the use of ultrahigh vacuum (UHV), sample preparation stages, data aquisition and processing, and the STM design, are shortly presented in the following, while details on the mechanical and electronic setup of the STM chambers can be found elsewhere [124, 336–339]. The procedures used until now for tip and sample preparation will be introduced as well as an extensive future tip preparation stage. Finally the process of sample cleaving and positioning the STM tip at the nanostructures will be highlighted, together with some typical structural aspects of the cleavage surface.

4.1 The STM chambers

The MOCVD-grown GaSb/GaAs samples studied within this work were examined in a more universal kind of STM system, being used for XSTM studies [92, 100, 124, 127, 221] as well as for growth and top-view STM characterization [340, 341]. For the MBE-grown samples another STM was used, which was directly designed for XSTM measurements on semiconductor samples [103, 124, 131, 132, 338, 342]. Both STM setups equally consist of two coupled UHV chambers, respectively, one of which contains the STM itself, while the other one can be used for tip or additional sample preparation and storage. All chambers contain several pump stages and pressure gauges and have especially be designed for the intended STM work.

4.1.1 UHV conditions

In order to keep and preserve atomically clean sample surfaces, excellent UHV conditions are crucial: At a pressure of about 1×10^{-6} mbar (1 mbar = 100 Pa), each atom of the surface is on the average hit by one residual gas atom per second [295], so even at very good UHV conditions of less than 1×10^{-10} mbar adsorbates could have reached the complete surface within less than three hours. Fortunately the sticking probability of such residual gas adsorbates on III-V semiconductor (110) surfaces is very low: The experiments described here are typically carried out at pressures $p < 5 \times 10^{-11}$ mbar, enabling good XSTM conditions for about one to two weeks until the cleavage surface is significantly contaminated.

Such pressures are routinely reached by a combination of diaphragm, turbomolecular, titanium sublimation, and ion getter pumps. The absence of water molecules is of special importance, therefore the whole system has to be baked out at at least 100°C for several days after venting. In order to avoid mechanical vibrations as well as Ti contamination of the sample, only ion getter pumps are used to maintain the UHV during STM measurements.

4.1.2 The universal STM chamber

The more universal STM system was developed in 1995 by T. Kalka [337] and further enhanced in several steps later on by C. Preinesberger [336], H. Eisele [124], and S. Becker [343]. The STM unit itself is suspended by soft springs in the STM chamber, mechanically isolating it from the surrounding, whereupon vibrations are additionally reduced by eddy current damping. Twelve backup tips can be stored within the STM chamber, as it is necessary to exchange damaged or insufficient tips from time to time during the experiment. A preparation stage for heating the tips by electron bombardment under an applied electrical field (as described in section 4.2.1) is included. Five samples can be stored in the preparation chamber, attached by a UHV valve, where they are cleaved and transferred into the STM using a magnetic transfer.

A challenge of STM instrumentation is to exactly position and move the tip in close proximity to the sample surface, combined with a desired large range of motion. These requirements of a coarse movement including the tip-sample approach as well as the scan movement of the tip are here fulfilled by a walker unit carrying the scanning tip, shown in Fig. 4.1(a) together with the sample. This walker unit consists of a copper block, mounted on three crossed pairs of shear piezos with sapphire balls underneath. It stands on a polished steel plate and moves as a slick-and-slide motor when a saw tooth voltage is applied to the shear piezos. Inside the copper block a sectorized tube piezo is mounted, carrying a magnet which holds the STM tip, isolated by a thin glass and contacted by a gold platelet. The xy scan movement of the tip can be accomplished by applying a high voltage to specific sectors of the tube piezo, bending it into the respective direction, while the z positioning of the tip is obtained by compressing or extending the piezo tube.

The bias voltage is applied to the sample, while the tunneling current is measured at the tip. An *in-situ* preamplifier, which converts the tunneling current into a voltage by a factor 10^8 VA^{-1}, is situated directly above the STM unit, minimizing electronic pickup. The completely home-built control unit of the STM consists of three parts, including the main control electronics, a high-voltage amplifier supplying the scan piezo, and another high-voltage unit which controls the approach of the walker. All three parts are addressed by

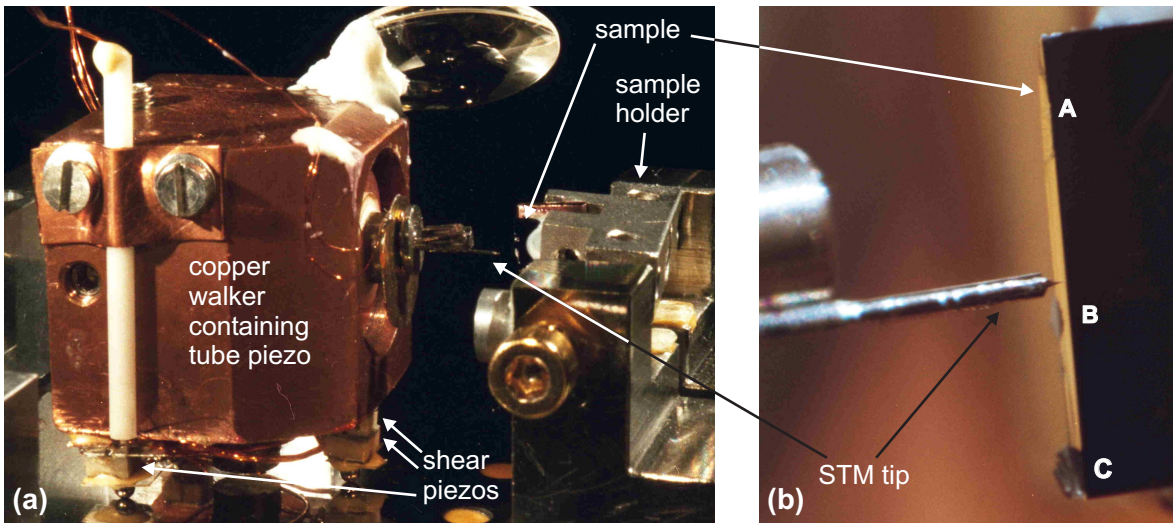

FIGURE 4.1: (a) The STM unit: A copper walker, standing on pairs of shear piezos on top of a steel ball, contains a tube piezo which holds the tip at its end by a magnet, opposite to the sample screwed on the sample holder. (b) The STM tip near the cleavage surface (gleaming brightly orange) of the sample (with the growth surface appearing dark), photographed through the optical microscope.

a personal computer. A non-commercial software, written by M. Dähne and T. Kalka, is used [344], controlling STM operation and enabling STS images and point spectra. Image processing was performed employing another home-built software, written by S. Becker [345].

Before the STM imaging can be performed and governed by the feedback electronic and the software using the constant current mode, the tunneling contact has to be established by bringing the tip and the sample together very closely without touching each other. The last few μm of this approach can be performed automatically by repeatedly moving the whole walker and stretching the scan tube piezo until a tunneling current is measured. As this procedure is rather slow, for a fast initial positioning of the tip opposite the sample cleavage surface, including the lateral adjustment, the slick-and-slide motor of the walker is controlled manually. This is enabled by an *ex-situ* optical microscope with long working distance (Leica M 420 with apozoom 1:6 lens), allowing an optical access to the cleavage surface and the walking STM tip. A view through the optical microscope is shown in Fig. 4.1(b), where (from right to left) a sample with the cleavage surface and the tip mounted to a tip holder can be seen.

4.1.3 The XSTM/XSTS chamber

To improve and facilitate the experimental conditions for XSTM studies, a new system was built in 2001 by H. Eisele [124], with additional contributions from M. Ternes [338], Ch. Hennig [346], A. Lenz [347], L. Ivanova [348], J. Grabowski [349], F. Streicher [350], and in the frame of this work. While the principal setup of the STM system is similar to that of the universal STM chamber described above, many details are optimized for specific needs of XSTM and XSTS experiments.

An overview image of the XSTM system can be seen in Fig. 4.2. The STM unit itself is

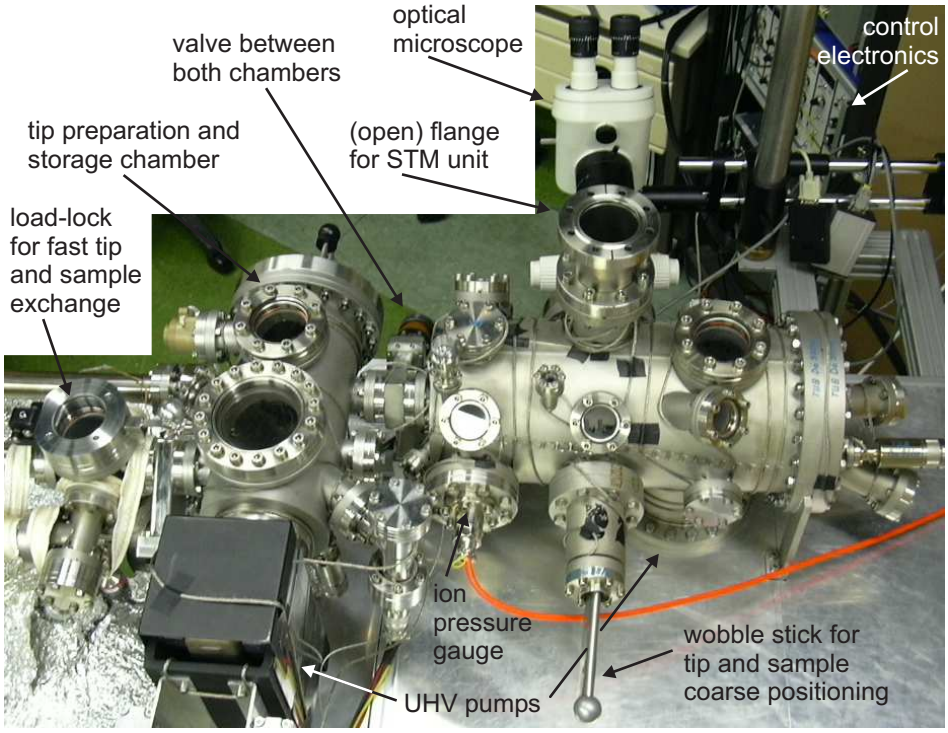

FIGURE 4.2: Look from above on the XSTM chamber (the STM unit itself is temporarily taken out) and the attached preparation chamber.

located centrally within the larger STM chamber, enabling a more direct and ample access, both optically by the external microscope (also a Leica M 420 with apozoom 1:6 lens) and mechanically by a wobble stick used for tip and sample exchange. Five backup tips can be stored within the STM chamber, while an additional storage for 32 tips and the tip heating stage are located within the preparation chamber, enabling the preparation of fresh tips without polluting the vacuum in the STM chamber. Four samples can also be stored in the preparation chamber. Additionally, tips and samples can be exchanged via a loadlock coupled to the preparation chamber without destroying the vacuum.

The STM unit, shown in Fig. 4.3, is suspended at the STM flange of the chamber by springs. It is designed as a very stiff and compact unit, which in combination with rather soft springs results in a high stability against external vibrations, assisted by eddie current damping. In this setup, three crossed piezo pairs with steel balls glued on top are mounted firmly to the STM unit. The sample holder made of copper lies on top of these balls, completing the inertial walker, which enables the coarse positioning and tip-sample approach by a slick-and-slide motor. A sectorized tube piezo carrying the tip and performing the scan movement is mounted directly on the STM unit. The tunneling current is measured at the tip and converted into a voltage by an *in-situ* amplifier mounted to the STM unit with a factor of 10^8 VA^{-1}, while the bias voltage is applied to the sample via contacts at the steel balls of the walker.

A commercial SPM 1000 Control System from RHK Technology was used, consisting of an SPM 100 Rev. 8 control electronic and the associated SPM 32 software, which was recently exchanged by the Windows-based XPMPro^{TM} software, running on a personal computer. All STM imaging and STS spectroscopy were performed by this control system, whereas an additional home-built high-voltage amplifier was used to actuate the walker for coarse positioning and approach of the sample. For an improved control of this approach by hand using the optical microscope, two mirrors have been attached to the STM unit, enabling an optical access of the tip-sample system from different perspectives. Besides the RHK software, also the WSXM freeware tool [351] was used for image processing.

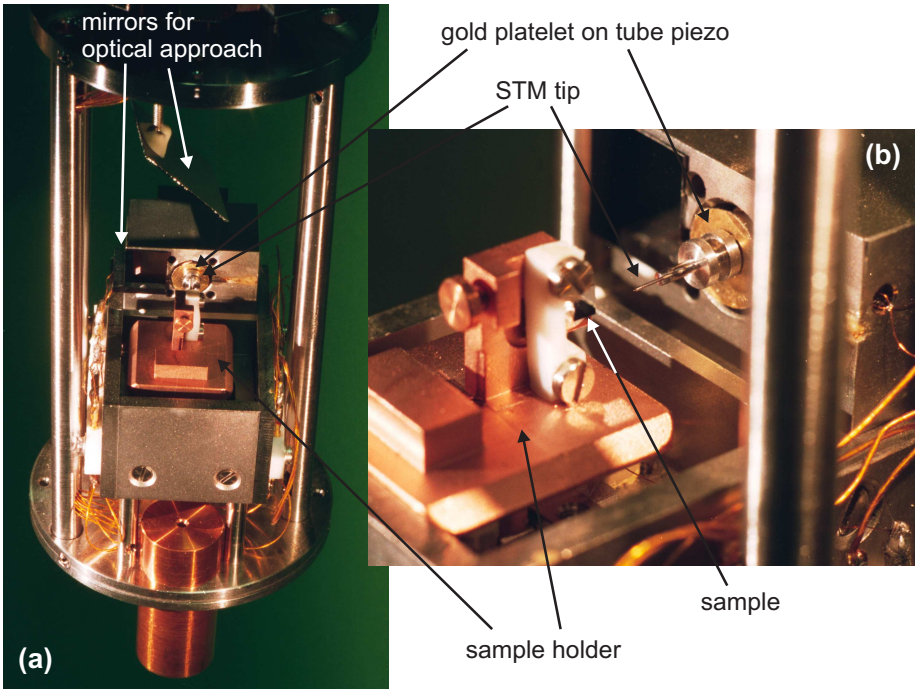

FIGURE 4.3: Photographs of (a) the compact and stiff XSTM unit, which contains, magnified in (b), the sample holder standing on shear piezos and the tip held on a tube piezo by magnets.

4.2 The XSTM experiment

Although the XSTM measurements themselves are rather challenging, implying high requirements on the accuracy of electronic and mechanical components as well as the UHV conditions, and also time consuming, the preparation steps necessary for setting up new tips and samples are comparatively straightforward.

A short overview of the preparation steps for tips and samples used here is presented in the following, while more detailed descriptions of this procedure [339] or of STM tip preparation in general [352–354] can be found elsewhere. The aim of sample preparation (besides contacting it) is to receive a good cleavage surface. The cleavage process, forming the basis of any XSTM experiment, and the remaining steps until finally the nanostructures can be imaged with STM are outlined in the last part of this section.

4.2.1 Tip preparation

The quality of the probe tip is crucial for all STM experiments, therefore care has to be taken in the preparation of the tips. At flat surfaces also rather blunt or irregularly shaped tips can lead to good atomic resolution due to the strong exponential dependence of the tunneling current on the tip-sample distance. But as the partly relaxed QDs protrude out of the cleavage surface and strongly influence the local electronic properties, well defined tips with a sufficiently small radius of curvature are necessary to resolve the nanostructures and to avoid multiple tip effects. Additionally, STM tips generally need to be mechanically stable, though easy to prepare, chemically inert at the experimental conditions, conductive with a possibly uniform DOS around the Fermi energy, and made of material of an affordable price.

Forming a good compromise between these requirements, electrochemically etched W tips are used here, prepared as follows: Starting with a 0.25 mm thick polycrystalline tungsten filament, this wire is firstly annealed under nitrogen atmosphere to heal possible defects and cleaned with isopropanol before it gets etched. Using sodium hydroxide at a concentration of 10% as electrolyte, a voltage is applied between the tungsten wire and a steel cathode, so that the tungsten gets oxidized [355]. The porous tungsten oxide (WO_4) drops down, shielding the lower part of the wire and enhancing the etching process close to the interface between electrolyte and air, which forms a meniscus around the wire. Finally, the bottom part of the intersected wire falls down, leaving a sharp, tapered end at the opposite part of the wire. Now the etching current has to be stopped immediately by a fast electronic, as otherwise this sharp end would get blunt again [352, 356]. Evenly tapered W tips with a radius of curvature of much less than a μm can routinely be obtained by this procedure. A typical tip can be seen in the scanning electron microscopy (SEM) images of Fig. 4.4, obtained using a JEOL JSM-5410 SEM.

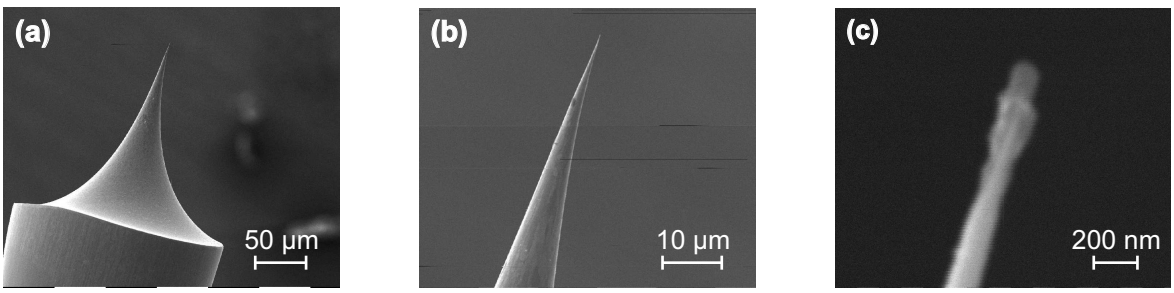

FIGURE 4.4: Scanning electron micrographs of an etched W tip for STM: (a) The initial tungsten wire and the tapered tip, (b) the sharp end of the tip, and (c) at large magnification the oxide layer and some contamination around the sharp tip can be seen.

As a result of the etching process, a several nm thick oxide layer is covering the sharp tip [Fig. 4.4(c)], which would severely obstruct a stable tunneling current. Therefore the tips are heated *in-situ* prior to the STM experiment by electron bombardment, removing the predominant part of the oxide [89, 357]. This is achieved by placing the tip opposite to a W filament within UHV (in the STM or the preparation chamber), applying a high voltage of about 350 V between the negatively biased filament and the tip, and increasing a heating current through the filament until an emission current to the tip in the range of 1 mA is established, which then lasts for some minutes.

4.2.2 Outlook: Improved tip preparation and characterization

Within STM imaging, sudden changes in the appearance of the surface or the nanostructures or in the resolution occur from time to time. Such phenomena are rather common for STM experiments [358] and also occured in the measurements described here. They can be explained by small structural changes of the tip geometry [359] which can significantly influence the electronic states of the tip like localized surface states [291].

Although the used STM tips have a macroscopically sharply tapered shape, at their very end they usually consist of several microtips, being separated by several nm [358]. Usually the strong dependence of the tunneling current on the tip-sample distance selects only one of these microtips, but small local structural or electronic changes of one of the microtips can alter this choice, leading to a strongly different appearance of the STM image, as shown in Fig. 4.5. Changes of the electronic properties of the tip are hardly to avoid upon tunneling spectroscopy, when the voltage applied to the tip is repeatedly changed over a large range, sometimes also at high frequency.

To overcome these obstructions and increase the structural and electronic tip quality and reliability, an additional UHV chamber containing a strongly improved tip preparation stage was designed for the XSTM chamber and is currently under construction. It combines the preparative step of ion sputtering with characterization possibilities by measuring the field emission current or taking field ion microscopy images. A short introduction into these methods and a description of the new chamber are given in appendix A. By using this enhanced preparation stage very sharp and defined tips will be created which can then be transferred into the STM without breaking the UHV.

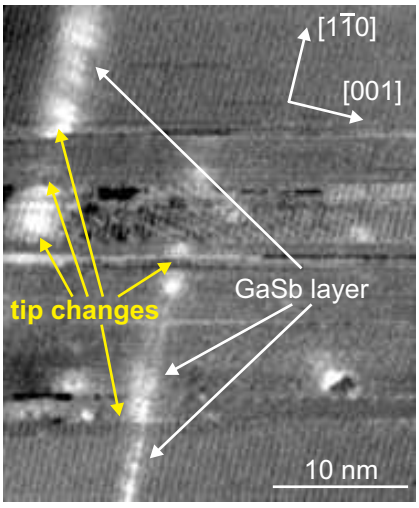

FIGURE 4.5: STM filled state image of a GaSb layer in GaAs. Due to several changes of the tip, the layer seems to jump and change its appearance. Repeating the image, it was proven that those apparent structural changes are not real.

4.2.3 Sample preparation

The samples studied in this work have been grown on industrial GaAs(001) 2 inch wafers, or on fragments of those, with a typical thickness of 400 to 550 μm. Samples of such rather large thicknesses are difficult to cleave, often resulting in many large steps on the cleavage surface or completely irregular cleaves. Therefore they are thinned mechanically to about 150 to 200 μm, which has turned out to be sufficiently thin for good cleavage, though still thick enough to prevent too frequent damages during preparation and handling.

The thinned samples are cut to pieces of about 4 mm $\times$ 5 mm with edges along the [110]- and [1$\bar{1}$0]-directions and are provided with a notch of 1 to 2 mm length

along $[1\bar{1}0]$ for (110) cleavage planes or along [110] for $(\bar{1}10)$ cleavage planes: Starting from the position of this notch, the cleavage of the sample will take place later on. After cutting, the samples are glued on small copper plates and contacted with indium, enabling an Ohmic back contact of the sample. The copper plates can then be screwed into the sample holder in such a way that a part of the sample including the notch is protruding.

As the surface investigated by STM will be created upon cleaving within UHV, no elaborate cleaning of the samples is necessary. Nevertheless, when the samples are transferred into the UHV chamber through a loadlock, they should get outgased by heating the loadlock for several hours, as otherwise the fresh cleavage surface will get contaminated by mobile adsorbates from the sample surface or the sample holder.

4.2.4 Sample cleavage and finding the nanostructures

When the designated sample and enough tips are readily prepared and the base pressure of the STM chamber is below about 5×10^{-11} mbar, the XSTM experiment can be started by cleaving the sample. For this purpose the protruding part of the sample must be cleaved off the mounted and back-contacted part, so that the small notch prepared *ex-situ* will proceed throughout the whole sample, yielding a (110) cleavage surface. In the universal STM setup this has to be realized by pressing the sample against a fixed rod of the preparation chamber, while in the XSTM setup the protruding part of the sample can directly be hit by a wobble stick.

After a successful cleave, the sample is positioned within the STM unit and the tip is approached. While the distance between tip and sample (z direction) and the horizontal position of the tip relative to the cleavage surface (x direction) can precisely be changed by the walker, the height of the tip (y direction) can only coarsely be adjusted by manually pushing or pulling the tip on the gold platelet at which it is held by a magnet. Depending on the quality of the cleavage surface, more or less large areas are suitable for the XSTM measurement. A macroscopically good cleavage surface can be seen in Fig. 4.1(b), imaged through the optical microscope which is used for controlling the coarse approach: The top end of the cleavage surface (A) is rough as it was notched externally. At the very bottom the cleavage surface also contains many irregular steps (C), but the large region between appears macroscopically flat and is well suited for XSTM investigation. The bright feature protruding behind the cleavage surface (B) is a small piece of the glue with which the sample is mounted to the copper plate beneath.

Once the tip has approached the sample at an appropriate position and tunneling is established, it is still a long way to the desired nanostructures. While the cleavage surface has a thickness of 150 to 200 μm (which is already challenging for tip positioning), only the outmost 1 to 3 μm consist of epitaxially grown layers containing the QDs of typically 10 to 30 nm size. These relations can be compared, for illustration, to an object with the size of a cherry pit (the QD) within a football pitch (the cleavage surface). The scan range of the STM is about 1×1 μm^2 (one step of a football player). It can be extended by adding an offset voltage to the piezos, reaching about 5 μm, which can cover the width of the epitaxial layers, but only a very small fraction of the cleavage surface.

Therefore a special strategy was developed to find the epitaxial layers [124, 338, 339] (based on ideas from Refs. [360, 361]), without losing too much time by scanning large areas of the cleaved wafer, and without damaging the tip by running into a large surface step or scanning across the edge of the cleavage surface: Starting at the position of the initial approach, the tip is retracted, moved several walker steps along [001] growth direction, and extended again until tunneling. This procedure is repeated until a tunneling current fails to appear, indicating that the tip was moved across the edge of the sample. From this position,

only a few steps have to be moved backward to be within the area of interest, where the nanostructures can then be searched for by large STM overview images.

Along the way from somewhere on the wafer over the epitaxially grown buffer layers to the nanostructures, the appearance of the GaAs surface often changes in an astonishingly systematic manner, displayed in Fig. 4.6: The GaAs (110) cleavage surface typically consists of large terraces intersected by surface steps of 1 or 2 ML height running along $[1\bar{1}0]$- or $[2\bar{2}1]$-direction, as can be seen in Fig. 4.6(b), taken at the original GaAs wafer but close to the epitaxially grown area. At the wafer further away from the strained layers, and under the influence of dopants and crystal impurities, the surface steps are sometimes less regular, shown in Fig. 4.6(a). But very often, the regularity and density of the surface steps strongly increases when the tip reaches the area of the strained heterostructures, until closely underneath the first wetting layer the structure suddenly changes. This change can – in good cases – lead to a very flat surface, but – in bad cases – also to large and steep hills, or it can reveal only few, but merged and correspondingly high steps or a change of the slope of the steps. The latter two cases can be seen in Fig. 4.6(c), which is taken at an epitaxially grown GaAs buffer, 200 nm underneath the first GaSb WL of the sample.

This changing character of the cleavage surface is due to the strain induced by the heterostructures, leading to locally inhomogeneous conditions during the cleave. On the one hand it can help as an assisting sign to find the nanostructures, but on the other hand it often hides the QDs in a strongly stepped surface dominating the image contrast. As the strain is largest at the heterostructures, large surface steps often form directly along a WL, making it impossible to analyze the embedded structures.

Such microscopic surface conditions of the epitaxially grown area cannot be seen macroscopically, so several approaches can be necessary, each at another position of the cleavage surface, until a suitable region for XSTM studies on the nanostructures is obtained. Once such a region is found and the used tip has proven to be of good quality, the measurement should not be unnecessarily interrupted. Therefore and due to the limited durability of an adsorbate-free surface the XSTM experiments are performed around the clock.

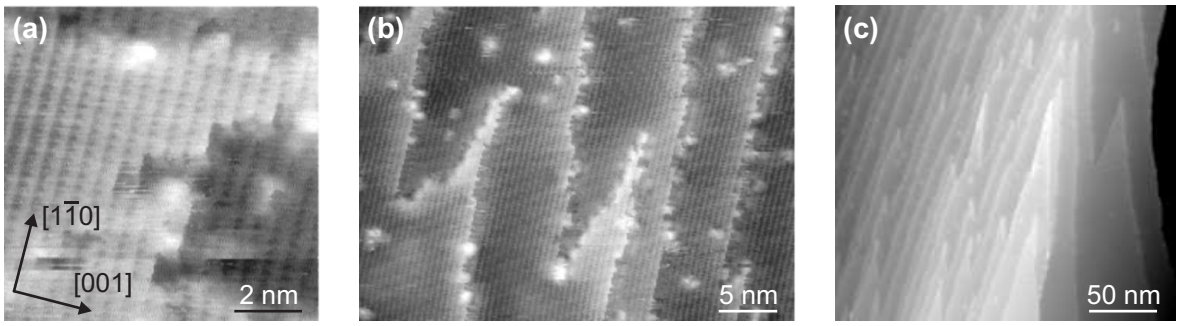

FIGURE 4.6: Appearance of the GaAs (110) cleavage surface with predominantly mono-atomic surface steps (a) at the n-doped wafer, (b) still at the wafer but near the epitaxially grown layers, and (c) at a buffer layer grown by MOCVD, 200 nm underneath a GaSb WL. The large step on the right side of image (c) has a height of 2.2 nm or 11 ML.

Part II

Results and discussion

Chapter 5

XSTM results on MOCVD-grown samples

A variety of samples containing GaSb nanostructures in GaAs has been examined within the context of this work. Not all attempts were effective, sometimes due to unexpected challenges during growth or during preparation of the samples, sometimes because some detail of the experimental setup did not work properly. However, several samples could successfully be studied, and thus a pool of nearly 2,500 XSTM images could be generated, aquired during more than 1,500 hours.

The data chosen for this thesis can be devided into those obtained from samples prepared by MOCVD and those from MBE-grown samples. Firstly, this is an easy classification to structure the large amount of data, which also is a chronological one because the MOCVD-grown samples have been grown and studied first and the MBE samples later. Secondly, the designs of the samples have changed with time, too, in such a way that the studied MBE-grown QDs generally contain more GaSb material than the MOCVD ones. Finally, as some of the obtained results can directly be related to the growth conditons or to effects which are typical for only one of both growth methods, this classification can also be helpful to discuss and understand the underlying physics.

According to this classification, firstly an overview over XSTM results on two MOCVD-grown samples containing three different GaSb/GaAs layers is given in this chapter, followed by a detailed analysis of the chemical composition and a discussion of the QD formation in chapters 6 and 7. Data on two MBE-grown samples containing another seven GaSb/GaAs layers with varying growth conditions and the resulting different QD structures are presented in chapters 8 to 10. Finally, in chapter 11 results on the electronic properties of both MOCVD- and MBE-grown GaSb nanostructures will be shown.

5.1 Sample structures

Both MOCVD-grown samples reported here were fabricated by Lutz Müller-Kirsch in the group of D. Bimberg at Berlin University of Technology [51, 71, 73, 264, 362]. They were grown in the same machine, which is an AIXTRON AIX-200 reactor with rotating susceptor, using hydrogen as carrier gas at a flow of about 5 l per minute and at a total pressure of 20 mbar [182, 265]. Epiready n-type GaAs(001) wafers were taken as substrates, with a nominal Si dopant concentration of $1.5 - 3.6 \times 10^{18}$ cm^{-3}.

Onto these substrates, heterostructures consisting of several undoped GaAs and AlGaAs buffer layers and the GaSb layers were grown using AsH_3 and TESb as precursors for the group-V elements and TEGa, TMGa, and TMAl as group-III precursors. For growth at

600°C or below, TEGa is used instead of the more common TMGa because of the limited dissociation of TMGa at lower temperatures [186].

The sample structures are finished by an n-doped cap layer of about 1.3 μm thickness with Si dopant concentrations of 1×10^{17} cm^{-3} for sample A and 2×10^{16} cm^{-3} for sample B, respectively. While the active layers are not intentionally doped in order to study preferably pure GaSb/GaAs nanostructures, an increased conductivity of the substrate by dopant atoms is crucial for stable tunneling conditions. Recently we observed that also the doping of the cap layer can be helpful to prevent too strong effects of tip-induced band bending [298]. The thickness of more than 1 μm of the cap layer has been chosen to prevent the STM tip at the cleavage surface beside the GaSb layers from reaching the edge of the sample.

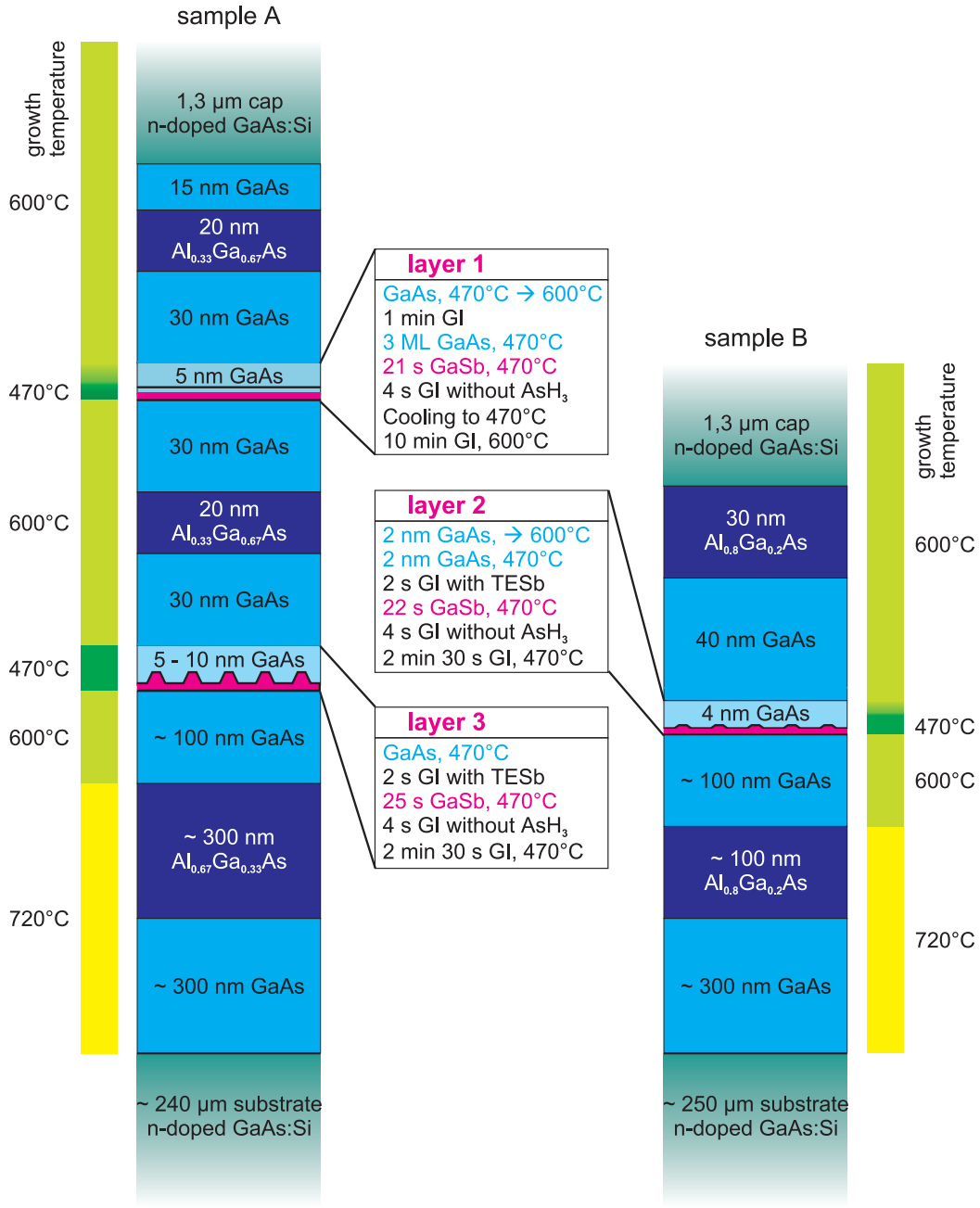

FIGURE 5.1: Comparison of detailed sample structures of the MOCVD-grown samples.

Detailed sample structures are shown in Fig. 5.1: In both samples, the epitaxial growth was started by thick buffer layers of GaAs and AlGaAs (about 300 nm GaAs and 300 nm $Al_{0.67}Ga_{0.33}As$ in sample A and 300 nm GaAs and 100 nm $Al_{0.8}Ga_{0.2}As$ in sample B, respectively), grown at 720°C, in order to heal possible crystal defects or impurities of the substrate and the interface and to obtain a flat growth surface. In XSTM experiments, AlGaAs layers are additionally helpful for finding the tiny nanostructures within the cleavage surface, as they act as marker layers.

After growth of these thick buffer layers, the temperature was decreased to 600°C in both samples and another 100 nm GaAs were deposited, followed by the first GaSb layer at 470°C. In sample A, this GaSb layer was overgrown with a sequence of 30 nm GaAs, 20 nm $Al_{0.33}Ga_{0.67}As$ and 30 nm GaAs, before another GaSb layer was grown, again followed by 30 nm GaAs, a 20 nm thick $Al_{0.33}Ga_{0.67}As$ marker, 15 nm GaAs, and finally the thick GaAs cap layer. The spatial separation between both GaSb layers is so large that they can be regarded as completely independent. Sample B contains only one GaSb layer, which is covered by 40 nm GaAs, a 30 nm thick $Al_{0.8}Ga_{0.2}As$ marker, and the thick GaAs cap layer.

Thus three GaSb/GaAs layers with different amounts of deposited GaSb material are existing within the two samples. The top layer of sample A is the one with least GaSb material, labeled "layer 1" in the following. "Layer 2" with a medium GaSb content is that of sample B, while the bottom layer of sample A is that containing most GaSb, labeled "layer 3". Prior to the growth of all three GaSb layers was a long growth interruption (GI) under AsH_3 pressure, lasting 10 min for layer 1 and $2\frac{1}{2}$ min for layer 2 and 3, respectively, in order to flatten the surface. After this, AsH_3 was switched off and another GI of 4 s took place, during which the arsine background in the reactor should decline [177, 182], before the TESb flux was switched on and GaSb was deposited.

After GaSb growth, layer 1 was immediately covered by 3 ML GaAs before a 1 min GI took place, while the deposition of layer 2 and layer 3 was followed by a GI of 2 s under TESb pressure for QD formation, before the next GaAs layer was grown. It has been found that such a GI is essential for the formation and increase of size of GaSb QDs, but that a longer GI time can already lead to a dissolution of formerly existing QDs or to a contamination of the QDs with rest gas molecules from the reactor [51, 182]. For all three GaSb layers, grown at 470°C, the first few nm of covering GaAs had the same growth temperature, respectively, and only after deposition of 3 to 5 nm GaAs, the temperature was raised again to 600°C.

The deposition times of the GaSb layers were 21 s for layer 1, 22 s for layer 2, and 25 s for layer 3. A nominal growth rate of $\sim$ 0.1 ML/s was chosen with a V/III ratio of 6, but it is not possible to derive the actual amount of deposited material from these parameters, because the initial MOCVD growth of GaSb on GaAs is strongly non-linear in time: It was observed that under similar growth conditions after 10 s deposition time no GaSb layer could be found at all and that generally the growth rate of the first ML GaSb on GaAs is much smaller than that of the following monolayers [182]. Thus the nominally small variations in deposition time of 21 s, 22 s, and 25 s result in a considerable difference of the amount of deposited GaSb material.

5.2 Overview of XSTM results

Overview images of the (110) cleavage surfaces of both samples are shown in Fig. 5.2. The three GaSb layers can clearly be seen in the images as thin stripes with a brighter image contrast, parallel to the atomic zig-zag chains in $[1\bar{1}0]$-direction. It should be noted that atomic resolution is only given in Fig. 5.2(b). The different appearance of layers 1 and 3 in sample A compared with layer 2 in sample B is due to the different tunneling polarities

of both XSTM images, this effect will be discussed in detail in section 11.1. All images of sample A were taken with a tunneling current of $I_T = 80$ pA, while the current used for imaging sample B was always $I_T = 100$ pA.

Common for all three GaSb layers are an inhomogeneous contrast, appearing a little brighter in some parts and less bright in others, and even discontinuities, i.e. small gaps within the stripes which look the same as the surrounding GaAs matrix.

The functionality of the AlGaAs layers as markers is obvious from the images: Firstly, these layers generally look darker than the surrounding GaAs due to a larger bandgap of AlGaAs and the resulting electronic image contrast (as mentioned in section 3.3.2). Secondly, they have an inhomogeneous appearance of darker and brighter areas given by an alloying and formation of Ga-rich and Al-rich regions [131, 363, 364]. Finally, the AlGaAs layers contain many white and black spots arising from adsorbates, as the AlGaAs(110) surface has a much higher sticking coefficient for rest gas atoms than the surrounding GaAs(110) surface [131].

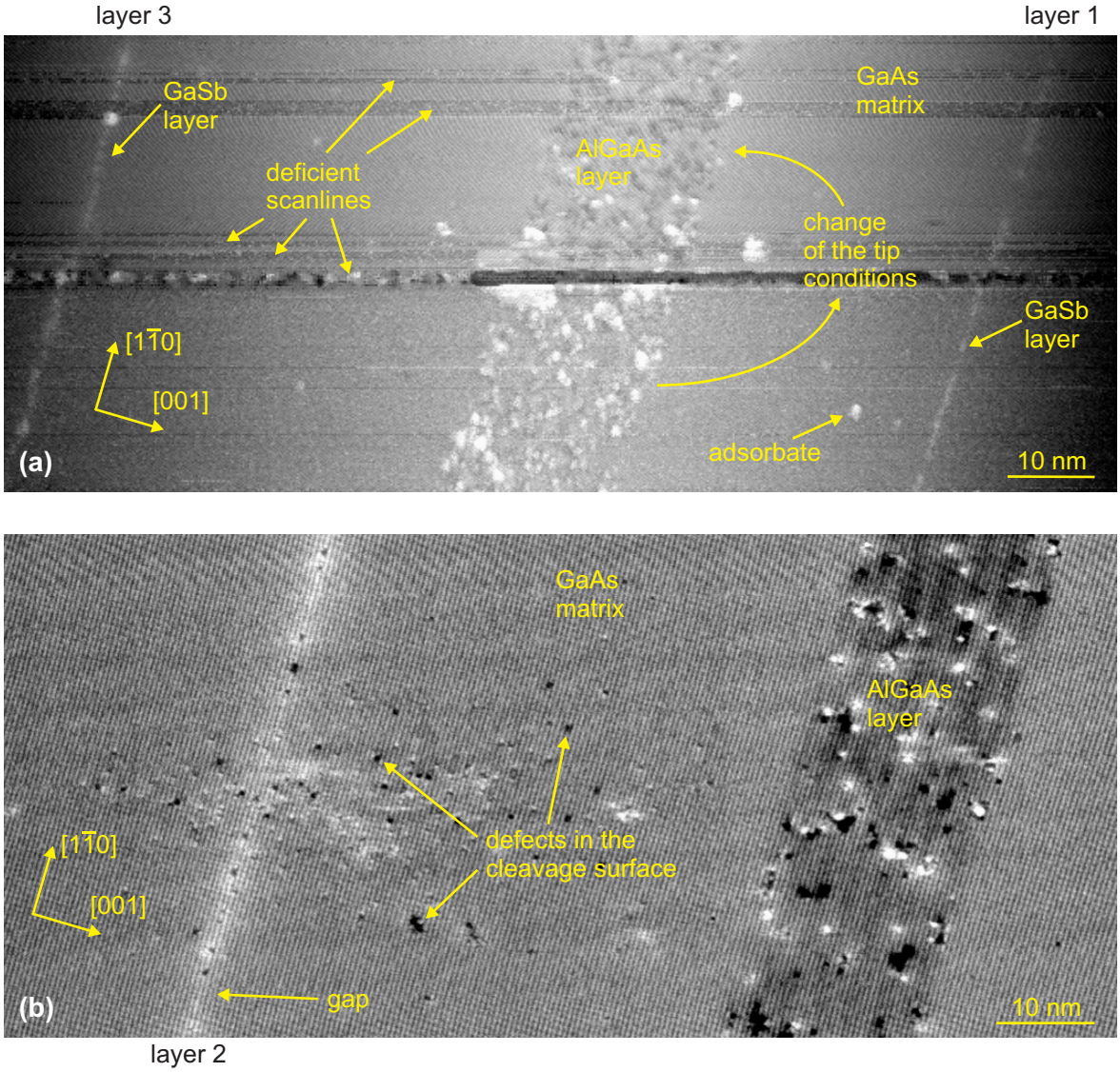

FIGURE 5.2: XSTM overview images of (a) sample A, containing GaSb layers 1 (on the right) and 3 (on the left), and (b) sample B, containing GaSb layer 2. Growth direction is from the left to the right. Sample voltages were chosen as (a) V_T = -3.5 V and (b) V_T = +2.4 V.

Significantly less adsorbates can be found on the GaAs surface.

In Fig. 5.2(a) also a typical artifact of XSTM images can be recognised: The image shows several deficient scanlines caused by an unstable tip. After a rather severe instability in the center of the image, in particular the AlGaAs layer looks different than before, with the former white spots of adsorbates becoming dark, which is a strong sign for a change of the electronic properties of the STM tip during the instability. Another STM artifact in this image is the fact that the left and right edges appear much darker than the central part, which can be explained by the non-linear scan movement of the tip over the considerably large overview image area: The tip on top of a tube piezo moves along a spherical surface instead of a plane, thus it is slightly closer to the sample in the center of the image than in the outer parts.

5.2.1 Layer 1: 21 s GaSb deposition

A more detailed view of layer 1 is shown in Fig. 5.3, which is an overlay of two XSTM images of partly overlapping areas of the cleavage surface. In this way, an extended region of the sample can be studied image by image.

GaSb layer 1 is characterized by a very thin extension in growth direction, the increased image contrast of the layer is mainly concentrated to one atomic chain. Within this thin layer, the contrast is strongly inhomogeneous, ranging from small gaps in the layer, which obviously consist of pure GaAs, over parts of the layer with an only weakly increased contrast up to parts with a much brighter appearance, which are often dominated by small bright spots with a lateral extension of only about one to three atoms. Thus, the layer is found to be strongly intermixed, consisting of GaAsSb with a strongly varying ratio between As and Sb atoms. Nevertheless, the term "GaSb layer" will be maintained in the following, keeping in mind that an uncertain amount of As is contained within this layer.

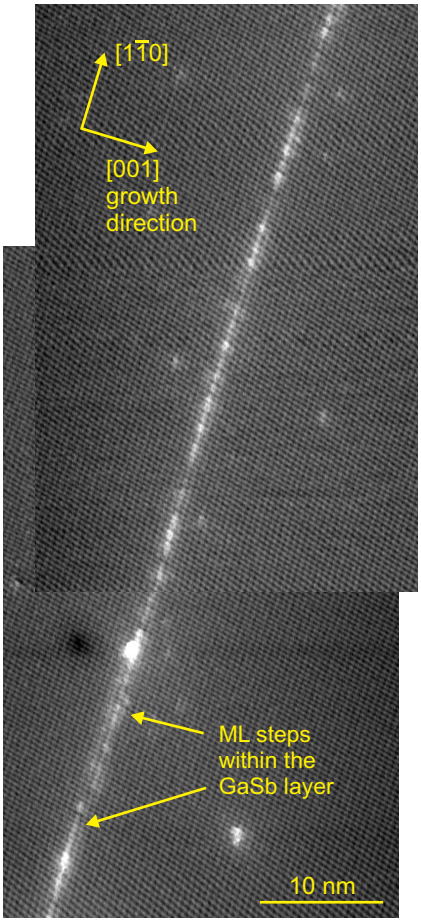

FIGURE 5.3: Overlapping XSTM filled state images of layer 1, aquired at V_T = -3.0 V.

It should be noted that the large white spot directly on the GaSb layer in the bottom part of the image in Fig. 5.3 is an adsorbate and not part of the layer itself. Additionally, the atomic zig-zag chains are clearly resolved in the image along the [1$\bar{1}$0]-direction, while the somewhat whinding lines perpendicular to these do not represent any real structures but are due to some electronic or mechanical oscillations.

Nevertheless, Fig. 5.3 is a typical image of layer 1, as this GaSb layer looks almost the same all over the investigated parts of the sample: There are no three-dimensional (3D) structures at all, thus this GaSb layer is a clear quantum well, and also its thin vertical extension of only one atomic chain with the inhomogeneous contrast and smaller or larger gaps, ranging up to 7 nm lateral extension, is everywhere the same.

One special feature can be observed in the bottom part of Fig. 5.3: Just at the bottom of the image, the QW is clearly situated at one atomic chain, then further up the contrast gets weaker but extends over a second

chain, and finally it is completely concentrated at the second chain. As the chains of the (110) surface represent only each second atomic ML (see section 3.4), this appearance can be explained by two ML steps of the QW due to steps on the (001) growth surface of the underlying GaAs layer.

5.2.2 Layer 2: 22 s GaSb deposition

GaSb layer 2, as shown in Fig. 5.4(a), presents an appearance which in many aspects is very similar to that of layer 1: Again, the thin layer exhibits several gaps of different lateral extensions, consisting of pure GaAs, and it has an inhomogeneous contrast with brighter and darker parts, standing again for an intermixed GaAsSb stoichiometry. However, the vertical extension of the layer appears to be a bit larger, covering about two atomic chains. It should be noted that Fig. 5.4(a) shows an excellent cleavage surface of the surrounding GaAs matrix, containing no adsorbates and also no segregated Sb atoms, dopant atoms or crystal defects.

Also this layer shows no 3D structures at all and is therefore considered a quantum well. However, within the intermixed QW, there are many structures like those shown in Fig. 5.4(b), which are completely flat, two-dimensional (2D) islands with a very bright contrast. Thus these islands have to consist of material with a significantly higher GaSb content than the residual QW. The lateral extension of these 2D islands varies strongly, the maximum of the size distribution is at about 4 nm, but also islands with up to 20 nm lateral size were observed, which is comparable with typical base lengths of QDs. The density of these 2D islands of $\sim$ 6 x 10^{11} cm^{-2} is very high.

5.2.3 Layer 3: 25 s GaSb deposition

In layer 3, finally, GaSb quantum dots can be observed, as shown in Fig. 5.5. The structure of the wetting layer is similar to that of the QWs of layers 1 and 2: Its vertical extension is concentrated to one or two atomic chains, but within this layer there are small gaps and the image contrast of the WL varies inhomogeneously, standing for an intermixed GaAsSb stoichiometry [Fig. 5.5(a)].

The flat WL, however, is interrupted by small QDs. These QDs have a significantly larger image contrast than the WL, as can be seen in Fig. 5.5(b), which cannot be explained by a

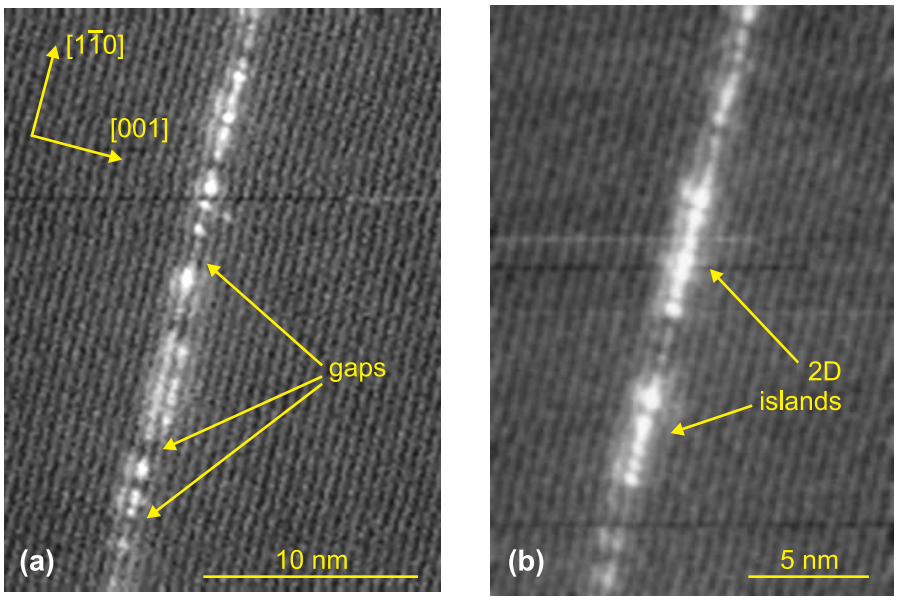

FIGURE 5.4: XSTM filled state images of layer 2, taken at V_T = -1.8 V. (a) A typical image of the GaSb QW, (b) flat two-dimensional GaSb-rich islands within the QW.

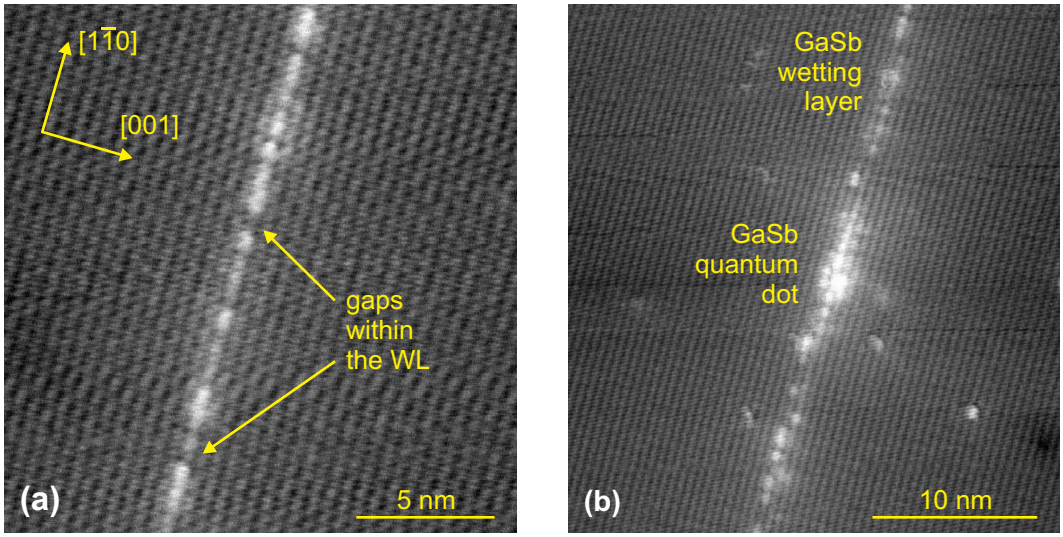

FIGURE 5.5: XSTM filled state images of layer 3, aquired at V_T = -2.3 V. (a) A typical image of the GaSb wetting layer, (b) overview image of a GaSb quantum dot.

purer GaSb stoichiometry of the QD alone. In fact, two additional effects are responsible for the bright appearance of the QD in the XSTM image: Firstly, the electronic image contrast (see also section 3.3.2) is increased by a higher tunneling probability from the electronic states of the QD [92]. Secondly, also the structural image contrast (see section 3.3.1) is affected by strain relaxation of the QD upon cleavage, leading to a local outward bending of the cleavage surface at the intersected QD [93, 97, 124] and underlining the significant amount of strain within the QD. It is notable that in the direct neighborhood of the QDs the WL seems to contain less GaSb material, being indicated by a decreased general contrast and larger gaps than in the residual WL.

A closer view of the QD shown in Fig. 5.5(b) is given in Fig. 5.6(a). In [001] growth direction, the bright contrast extends over four atomic chains, indicating that the height of the QD amounts to about 2 nm. The base length is around 8 nm, and the shape of the QD is rather flat with the largest lateral extension just at the base, similar to truncated pyramids. However, no exact structure can be identified due to the small extension and the contrast, which again is slightly inhomogeneous at the QD and especially at its borders, indicating an

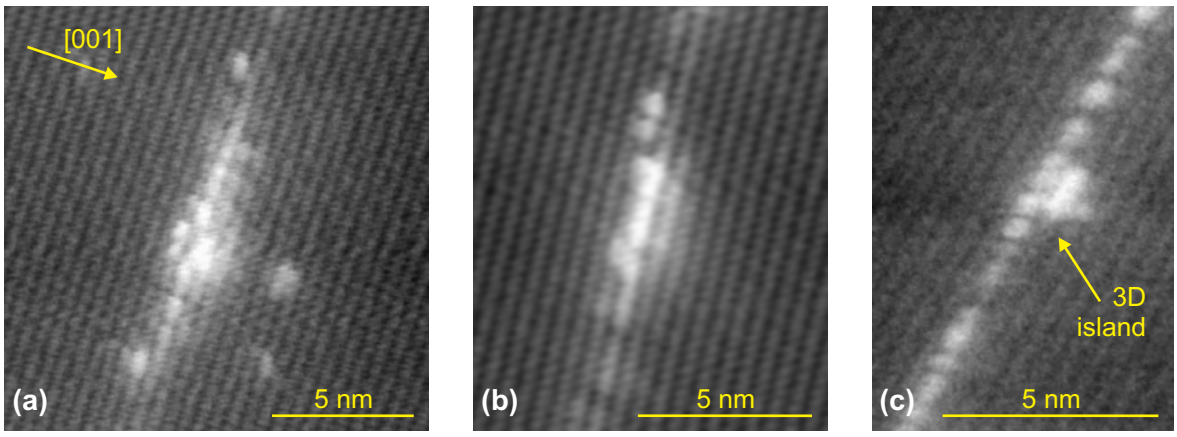

FIGURE 5.6: XSTM filled state close-view images of (a,b) GaSb quantum dots and (c) a tiny 3D GaSb island in layer 3, taken at (a,b) V_T = -1.6 V and (c) V_T = -3.3 V.

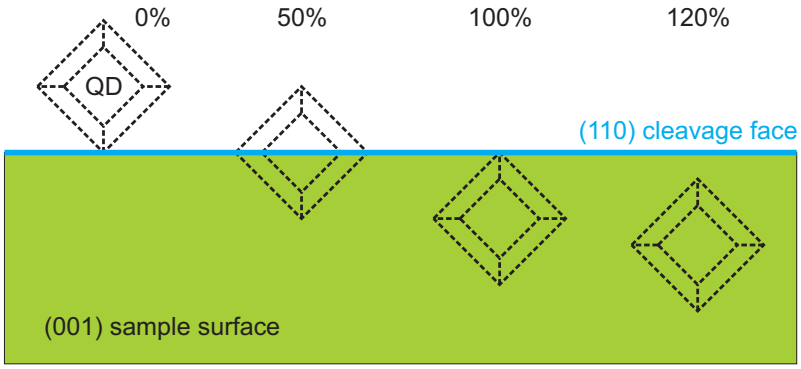

FIGURE 5.7: Sketch of differently cleaved QDs. The cleavage positions are indicated in regard to the QD extension in [110]-direction.

intermixed stoichiometry also for the QD. An even smaller QD is shown in Fig. 5.6(b), with a base length of about 4 nm and a height of two to three atomic chains, corresponding to ~ 1.5 nm. It should be noted that the smaller size of the structure shown in Fig. 5.6(b) can be due to a cleavage outside the center of the formerly larger QD (see also Fig. 5.7).

From the observed size of the QDs and the frequency of their occurence when scanning a larger area of GaSb layer 3, the QD density can be estimated as follows: QDs can randomly be cleaved upon sample cleavage at any position, as sketched schematically in Fig. 5.7, resulting in different cross sections in the XSTM image. If the cleavage position of the QD, indicated as percentage of its lateral extension, is somewhere between 0% (completely cleaved away) and 120% (20% of its diameter underneath the cleavage surface), it can be detected in the XSTM image due to the increased image contrast, which is influenced also by the strain of completely buried QDs [124]. Thus, the range of sight of the XSTM for QDs in [110]-direction is around 120% of the mean QD diameter, at least at good tunneling conditions and flat cleavage surfaces as it is the case here. In an area of $\Delta x \approx 1$ μm extension in $[1\bar{1}0]$-direction, studied image by image using small images with atomic resolution, three QDs were detected with a mean diameter of about 8 nm. Dividing this number of observed QDs through the lateral extension times the range of sight of $\Delta y \approx 120\% \times 8$ nm, the QD density results here to $\sim 3 \times 10^{10}$ cm^{-2}.

Besides such small, but distinctive quantum dots, tiny 3D island structures were observed in the WL. These islands are not only even smaller than the QDs, but they exhibit a qualitatively different nature, as can be seen in Fig. 5.6(c): The bottom atomic chain of the structure has exactly the same appearance as the surrounding WL, and the image contrast of the whole island does not significantly exceed that of the WL. This indicates that there is no electronic confinement and only little strain within this island, even the stoichiometry does not seem to differ from that of the intermixed WL. What remains outstanding for these islands is their three-dimensional shape, extending vertically over two to three atomic chains or 1.5 nm, with a lateral extension of only about 2.5 nm. The density of these islands can be estimated in the way described above to $\sim 5 \times 10^{10}$ cm^{-2}.

The GaAs matrix, likewise for layer 2, shows a nearly perfect cleavage surface with hardly any defects, dopant atoms, or segregated Sb atoms, as can be seen in Fig. 5.5(a).

5.3 Results from other characterization methods

Although XSTM is a very elaborate investigation tool for semiconductor nanostructures, comparing the obtained XSTM data with other structural or optical characterization methods is of course helpful.

5.3.1 Photoluminescence spectroscopy

Sample A, containing GaSb layers 1 and 3, has been studied by photoluminescence (PL) spectroscopy. These measurements were performed by Lutz Müller-Kirsch, using the 514 nm line of an Ar^+ laser as excitation source, a cooled Ge pin-diode for detection, a double-grating monochromator and a He cryostat [182]. A PL spectrum taken at a temperature of 10 K and with a moderate excitation density of 50 $W\,cm^{-2}$ is shown in Fig. 5.8.

Three peaks can clearly be distinguished within the spectrum: The most intensive peak arises from the GaAs matrix and has an energy of $h\nu = 1.52$ eV, corresponding to a wavelength of $\lambda = 820$ nm, in nice agreement with the GaAs band gap. The second peak with an energy of 1.37 eV or a wavelength of 906 nm can be identified with that of a two-dimensional layer, thus this peak can be associated both with the QW of layer 1 and the WL of layer 3, what also explains the asymmetric broadening of the peak. Finally, a third peak is obtained at an energy of 1.20 eV, corresponding to a wavelength of 1036 nm. This peak, which is evident but much less pronounced than the other two and strongly broadened, is assigned to the QDs of layer 3. Its broadness stands for a rather broad size distribution of the QDs, and its rather smooth transition to the WL peak corresponds to the small size of the QDs, the additionally found tiny 3D islands and to the inhomogeneity of the WL, because all these structural details impede a clearer separation between QD and WL photoluminescence. On the other hand, the existence of a QD PL peak confirms that the observed structures shown above are indeed QDs with an electronic confinement, in spite of their rather small size.

Comparing these results with other PL data on MOCVD-grown GaSb QDs found in literature [51, 71, 74], two trends are evident: Firstly, the QDs studied here have a larger PL energy, amounting to 1.20 eV compared with 1.13 eV [71], 1.12 eV [51], and 1.09 eV [74] for equal or similar temperature and excitation energy. Secondly, the separation between QD and WL peak of 0.17 eV here is smaller than the reported values of 0.23 eV [71], 0.24 eV [51], or 0.30 eV [74]. Both trends point out that the QDs studied here are smaller than those reported, leading to a weaker confinement within the QDs relative to the WL.

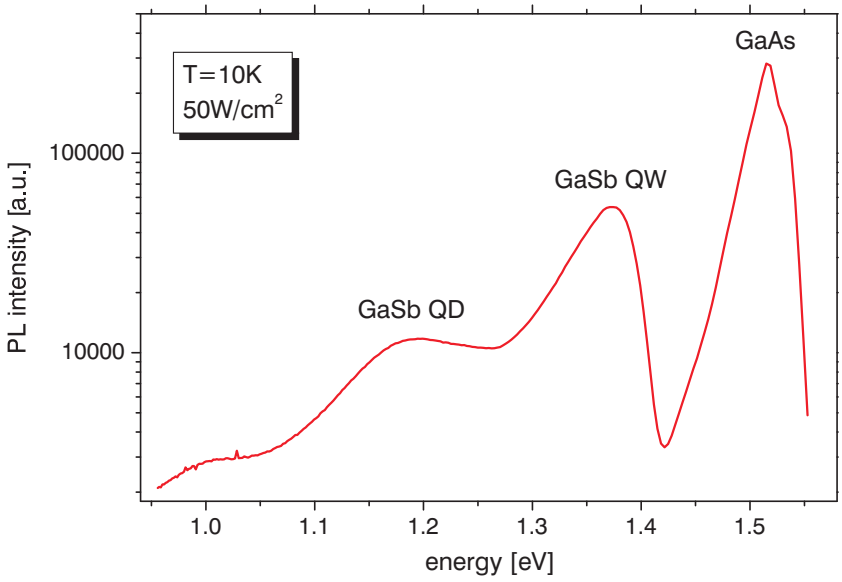

FIGURE 5.8: Photoluminescence spectrum of sample A, containing GaSb layers 1 and 3, taken at low temperatures and a moderate excitation density. Intensity peaks arising from the GaAs matrix, from the GaSb QW and WL, and from the GaSb QDs can be distinguished.

5.3.2 Transmission electron microscopy

For a sample that has been grown much earlier, but in the same MOCVD reactor and with similar growth parameters as GaSb layer 3, also transmission electron microscopy (TEM) was used for structural characterization. These measurements were done by Holm Kirmse and Ines Häusler at the Humbold University of Berlin, Institute of Physics, Chair of Crystallography, using a Hitachi H-8110 microscope [51, 365, 366].

Using dark-field TEM imaging in top-view geometry, QDs capped with 20 nm GaAs could be studied, as shown in Fig. 5.9(a). The (220) reflection was used for imaging, which is mainly sensitive to strain. Randomly distributed QDs with an isotropic shape and different sizes can be seen. A size distribution with a maximum at a QD diameter of 21 nm is obtained from the data, as shown in Fig. 5.9(b). This value is much larger than the XSTM data showing QDs with diameters between 4 and 8 nm. Though it has to be considered that the extensions obtained by top-view TEM represent rather the strain distribution in the QD layer than the actual QD size. However, the broadness of the size distribution over more than one order of magnitude is of larger significance, as this is at least partially maintained during overgrowth. The total QD density of about 3×10^{10} cm^{-2} agrees nicely with the value obtained for capped QDs by XSTM.

A more direct comparison is possible for cross-sectional TEM results on capped QDs. Figure 5.10(a) displays a composition-sensitive image using the (002) reflection, showing only weak variations of the GaSb layer contrast. From the coarse resolution of the TEM image, it cannot be concluded whether these variations stem from fluctuations within a QW or from flat QDs, but the absence of large QD structures observed in the equally grown XSTM sample is confirmed. When the same GaSb layer is imaged using the strain-sensitive (004) reflection, as shown in Fig. 5.10(b), a very different appearance is found: A flat WL contains structures comprising very different amounts of strain, partly reaching several nm into the surrounding GaAs matrix. While the bright feature in the center of Fig. 5.10(b) can only be assigned to a quantum dot, the weaker and smaller bright spots may arise from fluctuations within the WL or also from the tiny 3D islands observed by XSTM.

Beyond the potential of such conventional dark-field TEM images, the lateral resolution can be increased by using energy filtered high resolutional TEM, considering element-specific

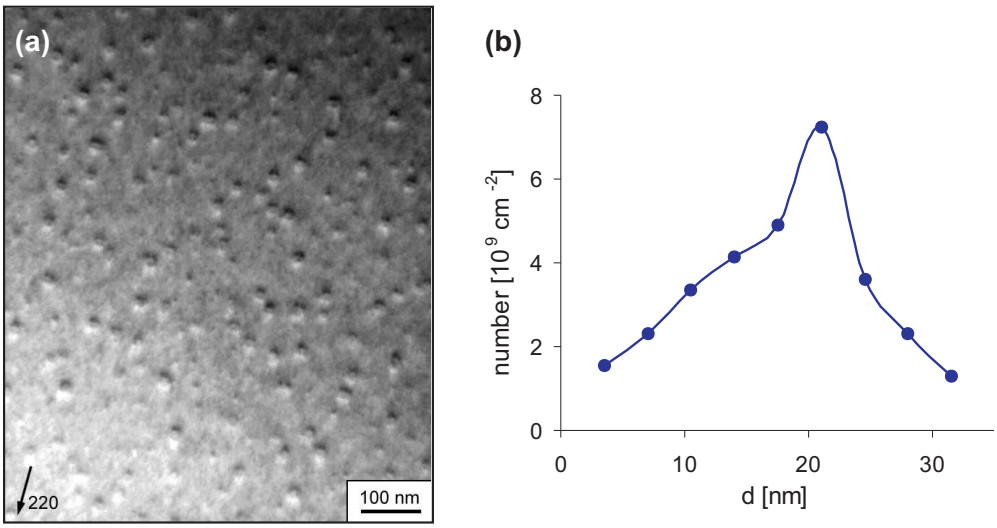

FIGURE 5.9: (a) Top-view dark-field TEM image of GaSb QDs on GaAs, using the strain-sensitive (220) reflection. (b) Size distribution of the QDs shown in (a).

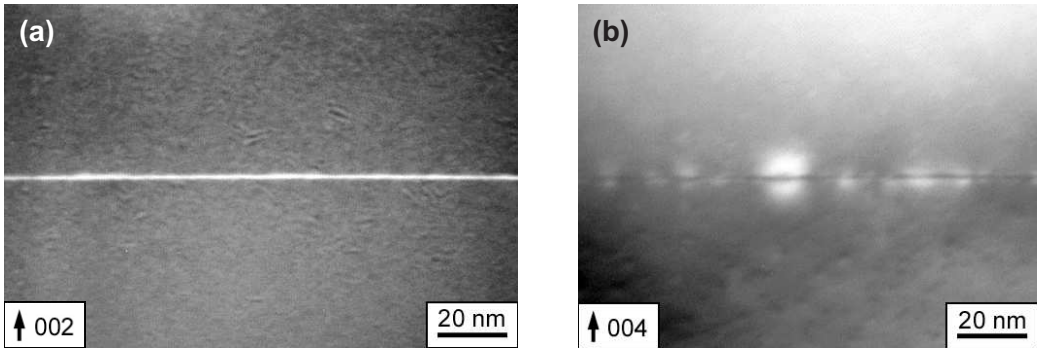

FIGURE 5.10: Cross-sectional TEM images of a GaSb/GaAs QD layer, using (a) the composition-sensitive (002) reflection and (b) the strain-sensitive (004) reflection.

electron energy losses: In Fig. 5.11(a), only the signal energetically corresponding to Sb is mapped, leading to a rather noisy image with an increased contrast at the GaSb layer.

For a quantitative analysis of the stoichiometry this method is strongly limited by lattice distortions and the thickness of the TEM specimen in the order of 10 nm [3, 366]. However, keeping in mind the statistical averaging over many atomic layers which is immanent to all TEM techniques, the extension of an increased Sb content can be obtained from signal profiles across the GaSb layer, as shown in Fig. 5.11(b,c) for a QD and the WL, respectively. A QD height of about 2.1 nm can be estimated, which agrees well with the XSTM result of 2 nm shown above. Also the observed WL thickness of about 0.9 nm confirms the XSTM data, showing an extension over one to two atomic chains.

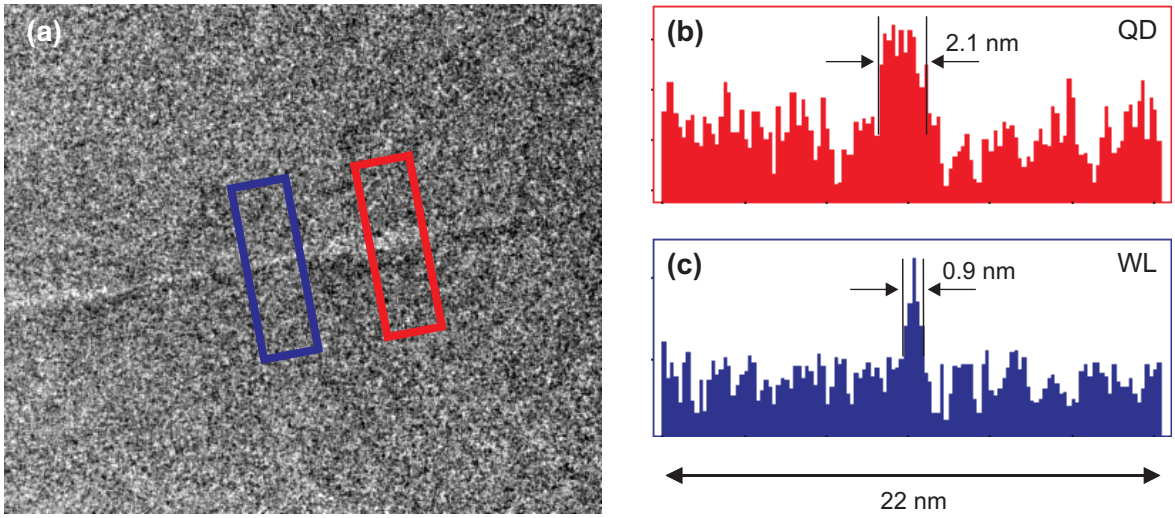

FIGURE 5.11: (a) Sb-sensitive energy-filtered TEM image of a GaSb/GaAs QD layer. The indicated areas are evaluated regarding their Sb content for (b) a QD (red) and (c) the WL (blue).

Chapter 6

Analysis of the chemical composition

As mentioned before, the XSTM image contrast is a first qualitative indication of the chemical composition of nanostructures. However, a more precise and quantitative knowledge of the local stoichiometry of quantum dots and wells is essential for understanding the growth and modeling the electronic and optical properties of the structures (see chapter 2.3).

For this purpose, a method has been developed (basically by H. Eisele [92, 124] and further by M. Dähne, A. Lenz [100], E. Lenz [367], and in the framework of this work) to evaluate the local lattice constant in XSTM images and compare the results with simulations of strain relaxation. By this method the chemical composition of cleaved nanostructures can be analyzed with typical errors of less than 5% for QWs and 10% for QDs.

6.1 Evaluation of the local lattice constant

During epitaxial growth of strained heterostructures, the lateral positions of the single atoms are predefined and the only direction into which the strain induced by lattice misfit can partly relax is the growth direction (see sections 2.2.1 and 2.3.1). Thus the local lattice constant in growth direction is a measure for the inherent strain and therewith for the chemical composition.

The method to evaluate this lattice constant is illustrated step by step in Fig. 6.1: First, a height profile has to be taken in [001] growth direction across the QD which is to be analyzed, performed here for the QD already shown in Figs. 5.5(b) and 5.6(a). In order to be independent of atomic positions or short-range fluctuations in $[1\bar{1}0]$-direction and for noise reduction, the height profile needs to be averaged in $[1\bar{1}0]$ over a few nm, typically over about 100 data points of the XSTM image. For this purpose, a homebuilt software tool written by S. K. Becker [345] has been used for this work. The area of the averaged height profile is indicated within the XSTM image in Fig. 6.1(a).

Within the height profile, shown as black line in Fig. 6.1(b), the atomic corrugation in [001]-direction can clearly be seen, but its amplitude is strongly exceeded by the steeply increased apparent height at the position of the QD, arising from the actual structural protrusion of the QD material and the increased electronic contrast. Additionally, the adsorbate that can be seen slightly above the QD in Fig. 6.1(a) also leads to a small peak in the height profile. In a next step, the pure atomic corrugation has to be isolated from these other influences. For this purpose, a background is evaluated from the measured height profile by averaging it over about one wavelength of the atomic corrugation. The resulting background, shown as blue line in Fig. 6.1(b), can then be subtracted from the height profile, obtaining

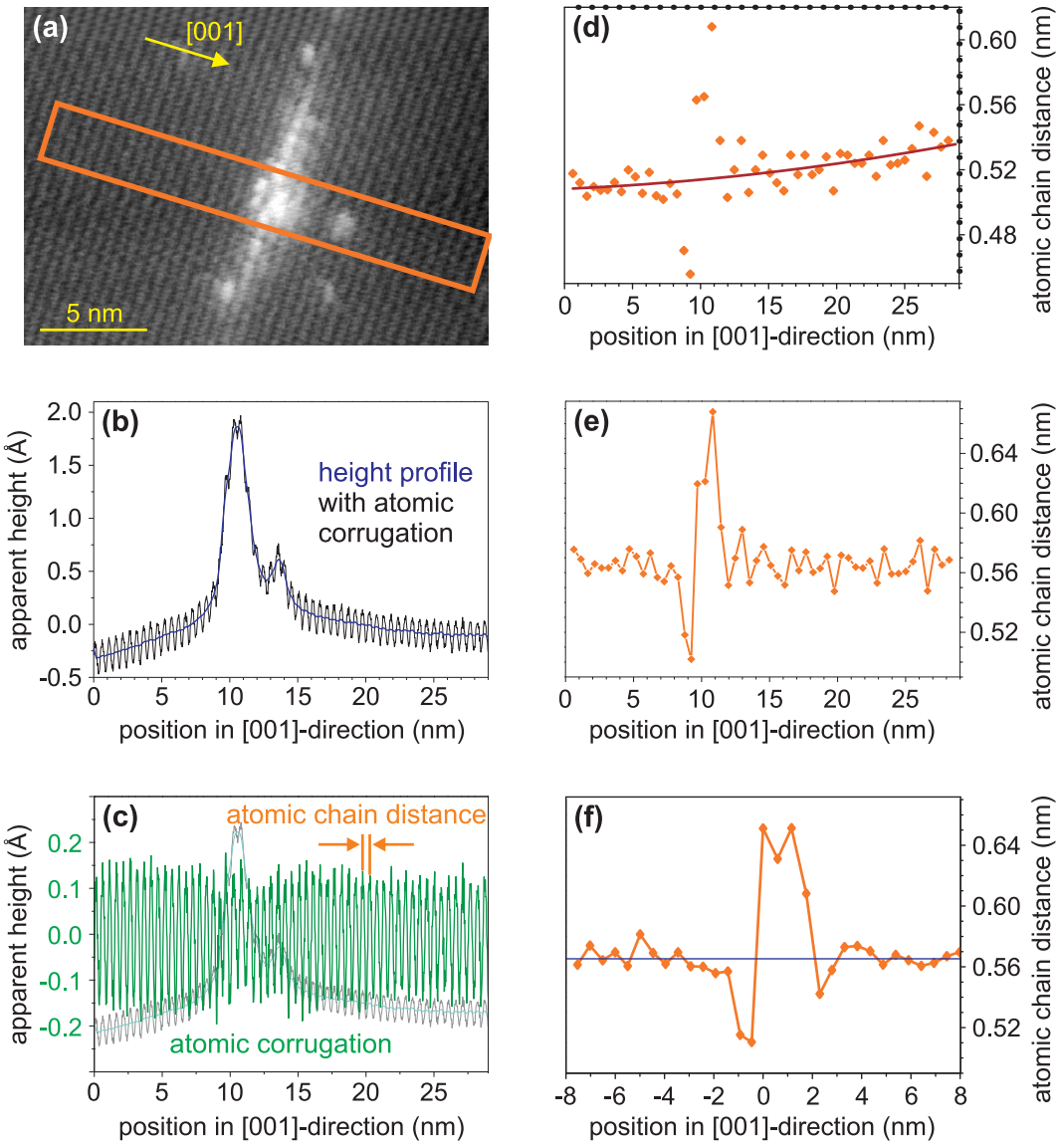

FIGURE 6.1: Procedure for evaluating the local lattice constant: (a) XSTM image with indicated averaging area of the height profile, (b) height profile across the QD, (c) atomic corrugation of the height profile, (d) atomic chain distances, (e) normalized atomic chain distances, (f) local lattice constant averaged from various XSTM images.

the atomic corrugation, as shown in 6.1(c). Each peak of this (green) corrugation curve corresponds to one atomic chain and is formed only by a few data points which are subject to electronic noise – it should be noted that the amplitude of the corrugation is only of the order of 0.1 Å = 10 pm. Therefore, every single peak has to be fitted with a Gaussian shape, so that the maxima of these Gaussian peaks represent the exact positions of the atomic chains along $[1\bar{1}0]$.

The therewith obtained distances between neighboring atomic chains, which resemble the distribution of the local lattice constant, are displayed in Fig. 6.1(d) as orange points: A maximum can clearly be seen at the position of the QD, but the plotted chain distance at the GaAs matrix is not constant but seems to increase homogeneously in average. This artifact of XSTM imaging is created by the nonlinear movement of the STM tip, resulting in a non-perfectly planar course as mentioned above (section 5.2), and by a nonlinearity of

the piezo properties themselves. It has to be corrected by normalizing the data: The plotted chain distances at the GaAs matrix several nm away from the QD are fitted linearily or quadratically, and this line of best fit [indicated in Fig. 6.1(d) as red curve] is normalized to 0.5653 nm, the literature value of the GaAs lattice constant at room temperature. By this way, also a calibration of the XSTM data is done.

Finally, the normalized atomic chain distance is obtained, as shown in Fig. 6.1(e). A sharp increase of the chain distance can clearly be seen at the position of the QD, extending over three to four atomic chains, agreeing nicely with a dot height of about 2 nm as already obtained from the visual inspection of the XSTM images.

In analogy to the enlarged lattice constant of the QD directly shown by the increased chain distance, the decreased chain distance observable directly underneath the QD – and to a less extent also above it – has to refer to a locally reduced lattice constant. It can be explained by a compression of the neighboring GaAs material by the highly strained QD.

It should be noted that it can be difficult to fit the maxima of the atomic corrugation correctly, especially at the steep flanks of the height profile at the bottom and top edges of the QD. This leads to rather large errors of the chain distance for the lowest and topmost chain of the QD. However, these errors compensate each other regarding the integral under the curve for the area of increased chain distance, corresponding to the total strain within the QD. For reducing the influence of these errors at the flanks of the QD region and for general noise reduction, the complete procedure of evaluating the local lattice constant can be repeated for different XSTM images of the same position, averaging the obtained data. Figure 6.1(f), for example, is achieved by averaging the results from five images of the same QD, and especially for the GaAs matrix the reduced statistical noise is evident.

The whole procedure of evaluating the lattice constant is time consuming already for one XSTM image. Therefore, a part of the chain distance results shown in this work is obtained using a software routine written by E. Lenz [367] for half-automatically performing the fitting and normalizing of the chain maxima. However, if the XSTM conditions are not ideal (i.e. only weak atomic resolution, electronic noise, or adsorbates, defects, or steps on the cleavage surface), the whole procedure remains challenging.

6.2 Comparison with strain simulations

Up to here, the local lattice constant was evaluated, which is an essential, but not sufficient step towards a determination of the local stoichiometry of the QD material: The relation between measured lattice constants and chemical composition is still missing. Such a relation can only be attained by simulating the strain corresponding to given stoichiometries.

A model for the strain relaxation for QDs and QWs upon cleavage has been developed by H. Eisele especially for the simulation of XSTM data [92, 93, 124]: The model is based on the continuum-mechanical theory of elasticity, which was modified to discrete atomic positions. The stress tensor is applied in a linear approximation, considering only next-neighbor atoms. The bulk lattice parameters and the linear elastic moduli of GaAs and GaSb are taken from Ref. [368]. For the simulation, a cuboid with the extensions of 48 nm in [001]- and $[1\bar{1}0]$-directions, respectively, and 24 nm in [110]-direction, resulting in 2.65×10^6 atoms, resembles the sample cleaved in [110]-direction. As a starting configuration, this model cuboid contains a GaSb or GaAsSb QW of defined thickness and stoichiometry within a GaAs matrix, arranged at the atomic positions of the GaAs zincblende structure. During the iterative simulation, only the five side facets are held fixed, while all atoms of the cleavage surface and inside the cuboid can relax according to strain energy minimization. Additionally, an offset of the atomic distances in growth direction is allowed to form at the GaSb layer. After several

thousand iteration steps, the variation of the atomic positions becomes negligible compared with the resolution of the XSTM.

As results of the simulation, both the structural relaxation of the GaSb material out of the (110) cleavage surface and the local lattice constant in [001] direction can directly be obtained from the calculated atom positions.

Alternatively to the method described here, also valence-force field theory can be applied to calculate strain in nanostructures [41, 213]. This atomistic approach, based on atomic potentials and the deformation of atomic bands, is superior concerning the material interfaces and strongly intermixed material, whereas continuum mechanics should be used to describe the interior of compositionally pure QDs [124, 211, 369].

For the simulation of XSTM data, also simpler analytical models are used to describe the strain and local lattice constant within cleaved nanostructures [97, 98, 217, 315, 317]. Although these models are much less precise, they can resemble the experimental findings at least qualitatively [98] and to some extent, especially with more complex enhancements to the model, also quantitatively [102]. However, all simple approaches lack atomic resolution in the zincblende configuration and are therewith principally limited regarding their preciseness.

Using the described model based on continuum elasticity, the experimentally obtained atomic chain distances could be compared with simulations of the local lattice constant: In Fig. 6.2(b) both the experimental data obtained from the QD shown in Fig. 6.2(a) and calculated values for a GaAsSb/GaAs QW with a thickness of one atomic chain (2 ML) and chemical compositions of $GaAs_{0.75}Sb_{0.25}$ and $GaAs_{0.5}Sb_{0.5}$, respectively, are displayed, together with the line corresponding to pure bulk GaAs. Now it can be seen directly that the GaSb content of the QD is mainly in the range of 50%, in nice agreement with the observed inhomogeneity in the image contrast.

While a simulation of a QD would need its exact three-dimensional shape and size as prerequisite which differs from dot to dot and mostly is not evident from two-dimensional XSTM images, simulating QWs leads to much more general results like the calculated lattice constants indicated in Fig. 6.2(b). Though, the difference of the local lattice constants regarding QDs and QWs need to be discussed: The compressive strain in the QD is significantly higher than in the QW, also influencing the surrounding host material, what can be seen by the strong undershoot of the measured chain distance at the two atomic chains just below the QD in Fig. 6.2(b), representing a compression of the two GaAs atomic chains underneath the QD. Above the QD a slightly smaller undershoot is expected, too, regarding the typical QD shape of a truncated pyramid with a smaller lateral extension at the top than at the bottom. However, the observed compression is much less pronounced above the dot

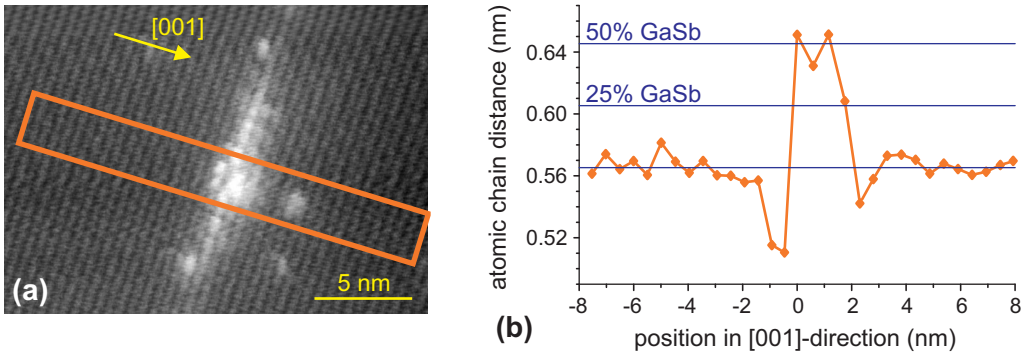

FIGURE 6.2: (a) XSTM image, the area for analyzing the chain distances is indicated, and (b) analyzed local lattice constant within the area shown in (a), compared with calculated values for $GaAs_{0.75}Sb_{0.25}$ and $GaAs_{0.5}Sb_{0.5}$ QWs.

material, indicating that the bottom interface of the QD is more abrupt than the top face. These undershoots within the chain distance profile and the larger strain in a QD compared to QWs lead to a small underestimation of the QD GaSb content when comparing it with the calculated QW values. However, this is partly compensated by another effect explained in the following section.

6.3 Local bending of the cleavage surface

Besides the atomic corrugation, the height profiles across a QD in XSTM images also show a considerable outward protrusion of QD material due to partial strain relaxation upon cleavage. Especially at tunneling voltages with a higher absolute value the contribution of the electronic contrast to the apparent height in XSTM images decreases, so that the structural contrast is dominating, showing the actual morpholgy of the cleavage surface (see section 3.3).

This structural relaxation gets evident in Fig. 6.3(a), displaying a height profile (green curve) across the GaSb QD of Fig. 6.2(a) and the corresponding outward protrusion (blue curve) without the atomic corrugation, obtained by averaging the green curve. The profile is taken from an XSTM image acquired at a relative high absolute voltage of V_T = -2.7 V. An outward relaxation of the QD material of about 1.5 Å can be obtained, implying a strong convex bending of the cleavage surface at the QD and a strong concave bending just underneath and above.

Now one has to consider that not the position of the atomic core is measured by STM, but the charge density which is mainly concentrated at the dangling bonds. More precisely, the "equipotential" surface of the integrated LDOS of the sample at the position of the tip is imaged, which is determined by different contributions of the surface atoms and dominated by the occupied and empty dangling bonds of the group-V and group-III atoms, respectively (for a more detailed view see for example Refs. [325, 326, 370]). When the sample surface is bended, the surface atoms and also the directions of their dangling bonds follow, at least partly, this bending. This situation is shown schematically in Fig. 6.3(b): All sketched atoms have equal distances in [001]-direction, but the surface is exaggeratedly bended in [110]-direction, assuming for illustration an outward protrusion which is ten times larger than the measured one shown in Fig. 6.3(a). For simplicity, the atomic dangling bonds are plotted perpendicular to the local surface, and due to the surface bending the dangling bonds increase their distance to each other at the center of the QD but move together below and above it. When the tip is scanned across the QD, the tunneling probability is largest at the positions directly above the dangling bonds, marked by red lines. Thus, the distance between neighboring atomic chains appears larger than it really is at the QD center and smaller underneath and above.

This effect gets additionally enlarged when the background is subtracted from the height profile in order to locate the maxima positions of the atomic corrugation, as described above, because in this case the peaks of the dangling bonds are regarded, as indicated by green lines in Fig. 6.3(b), and not their largest protrusion in [110]-direction (red lines). The background subtraction is nevertheless necessary for the chain distance analysis, as in most cases it is not possible to locate the positions of the atomic chains directly in the height profile at the steep flanks of the QD region.

It should be noted that only a large curvature of the surface bending significantly contributes to the derivation of the apparent chain distance, while at areas with a small curvature this effect is negligible and the local lattice constant is evaluated correctly. The latter case is given, for instance, at the flanks of the QD shown here and also at the center of larger QDs [92, 100, 118]. Additionally, the surface bending leads to enlarged apparent chain dis-

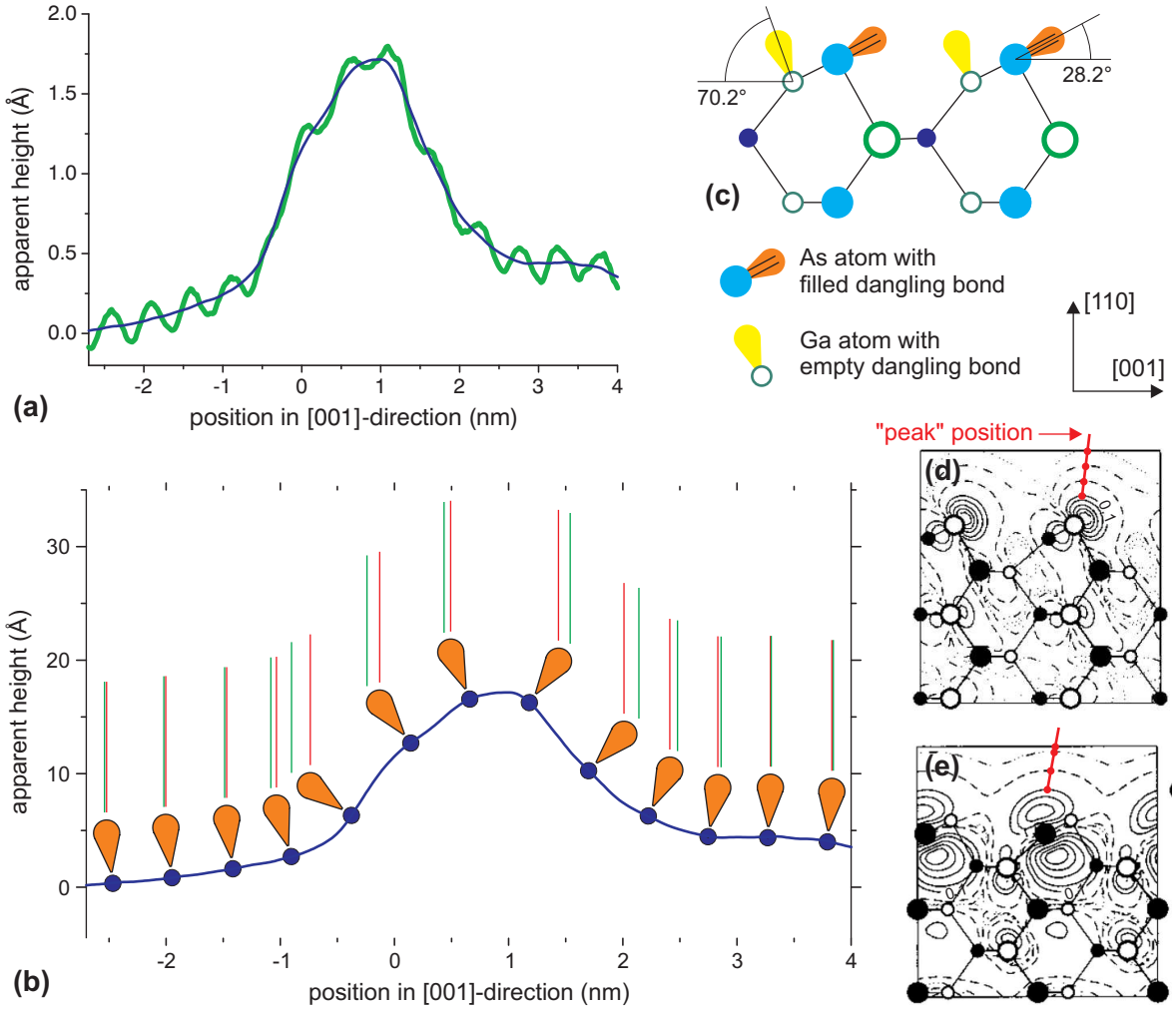

FIGURE 6.3: (a) Height profile (green curve) in growth direction across the GaSb QD shown in Fig. 6.2(a), and averaged over one wavelength of the atomic corrugation (blue curve). (b) Schematic drawing of the effect of surface bending on the apparent distances between neighboring atoms within the cleavage surface. The amount of the surface bending is strongly exaggerated for illustration, and the outlined atoms (blue) and their dangling bonds (orange) are only for illustration and not drawn to scale. The red lines indicate the apparent positions of the atoms looked from above, while the green lines indicate the peak positions of the dangling bonds. (c) Sketch of the GaAs(110) cleavage surface including buckling and the actual angles of the dangling bonds, according to Ref. [326]. (d,e) Calculated charge density distributions at occupied (d) and empty (e) dangling bonds at the (110) cleavage surface of a III-V zincblende semicondutor, taken from Ref. [326]. Equiprobability lines for different values of the probability density $|\Psi|^2$ are indicated.

tances directly at the QD but to reduced ones below and above the QD, so that both errors compensate each other when the chain distance is integrated over the complete QD region.

As mentioned above, the sketch of Fig. 6.3(b) is strongly exaggerated and not drawn to scale. Actual dangling bonds are not perpendicular to the local sample surface, but have an angle of 70° for empty states and 28° for filled states [326], as displayed in Fig. 6.3(c). Detailed calculations of the different contributions to the local charge density at the (110) cleavage surface of III-V zincblende semiconductors were performed by Ebert et al. [325] and Engels et al. [326]. Charge density distributions for occupied and empty dangling bonds are shown in Fig. 6.3(d,e), respectively, taken from Ref. [326]: For both kinds of dangling bonds

the equiprobability lines of the corresponding wavefunctions are plotted, showing that the idea of strongly localized dangling bonds is only valid for areas of high probability density $|\Psi|^2$. At the tunneling conditions of rather high absolute voltages and moderate currents used here, however, the STM tip does not get so close to the sample surface but images the equiprobability surfaces of rather low $|\Psi|^2$, which are much more delocalized, as can be seen by the dashed lines in (d) and (e). The surface bending can be expected to strongly modify the direction of the dangling bonds regarding the strongly localized part, while it should be of less influence on the comparably smoothly varying charge density distribution corresponding to low probability densities.

Although it is far beyond the scope of this work to exactly calculate the amount of the surface bending effects, at least a quantitative estimation can be performed as follows: From the experimental height profile a measured outward relaxation of the QD Δy of about 1.5 Å and an extension of the surface bending in [001] direction $4\Delta x$ of about 4 nm can be obtained. According to the geometric considerations sketched in Fig. 6.4, the radius of curvature of a homogeneous surface bending can be obtained from $r^2 - (r - \Delta y)^2 = \Delta x^2$, resulting here in

$$r = \frac{(\Delta x)^2 + (\Delta y)^2}{2\Delta y} = 3.4 \text{ nm} \quad . \tag{6.1}$$

The relevant length l of the filled As or Sb dangling bond is estimated to about 1.3 Å, which is in the range of the As and Sb atomic radii of 1.25 Å and 1.45 Å, respectively [371], and about half the GaAs covalent bond length of 2.45 Å [322]. Considering Fig. 6.3(d,e) and the discussion above, $l \approx 1.3$ Å also corresponds to the extension of the strongly localized charge density of the dangling bond, thus being a good upper limit of this error estimation. As a last parameter, the distance between neighboring atoms is needed, which is estimated to about $d_0 = 0.6$ nm being a rough average value for both GaAs matrix and GaSb QD material, also considering the variation of the distance due to the surface bending. Then the maximum effect of the surface bending on the apparent chain distance, according to the situation sketched in Fig. 6.4, results to

$$\Delta d = \frac{d_0}{r}\, l = 0.02 \text{ nm} \quad . \tag{6.2}$$

In conclusion, the effect of the surface bending on the measured chain distances can roughly be estimated to about 0.02 nm or 10% of the typical chain distance variations [see for example Fig. 6.2(b)]. Thus, the chain distances at the compressed GaAs matrix are actually about 0.02 nm larger than evaluated from the XSTM images, while at the QD itself they are up to 0.02 nm smaller. Remembering the underestimation of the GaSb content in the QDs resulting from the strain simulations – which may be of the same size or slightly larger depending on the exact QD structure –, both effects mainly compensate each other directly at the QD, where only a small underestimation remains. Directly below and above the

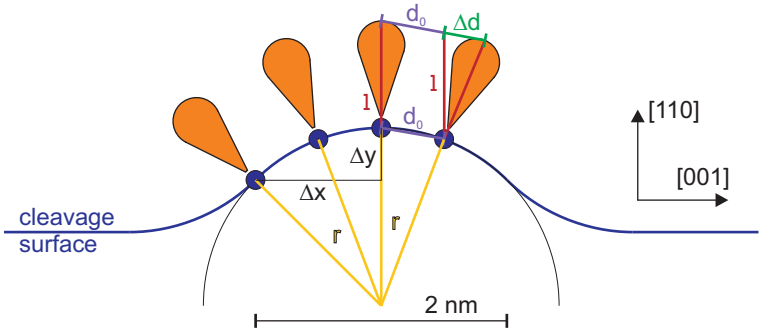

FIGURE 6.4: Schematic drawing of the geometrical situation at the bended cleavage surface, showing four surface atoms and their dangling bonds. The radius of curvature of the bended surface is indicated.

QD, however, both effects have the same direction, leading here to a significantly decreased apparent chain distance.

6.4 Stoichiometry of MOCVD-grown GaSb QDs

Coming back to the evaluation of the lattice constant with its corresponding Sb stoichiometry and considering the discussed corrections for the simulations and the surface bending, the chemical composition of the discussed QD can now be specified. Figure 6.5(a) displays the atomic chain distance across the center (orange line) and across the outer parts (green line) of the QD, as indicated in the XSTM image in the inset. For comparison, also the analyzed chain distances for the WL far away from any QD are shown (blue line).

Within the QD the chain distance varies between 0.63 nm and 0.67 nm, which is about 0.1 nm above the value of bulk GaAs. Considering the corrections discussed above, this value firstly has to be corrected by -0.02 nm due to the surface bending. On the other hand, for the same local lattice constant the actual GaSb content in a QD is about 20% higher than in a QW, which was considered in the simulations. With both effects partly compensating, the maximum GaSb content within the QD can be concluded to be 60% to 70%, with an error of about 10%. At the quantum dot center, the high GaSb content extends over three atomic chains and drops significantly at the topmost fourth chain. It should be noted that the slight reduction of the GaSb content at the second chain corresponds to a locally darker part of the QD in the XSTM image, indicating fluctuations of the chemical composition within the QD. At the outer parts of the quantum dot, the high GaSb content is kept only at one central chain, with two additional chains of moderate composition, again in good agreement with the XSTM image contrast.

Beside this intensively discussed QD, also purer GaSb material was observed in another QD, as already shown in Fig. 5.6(b). The stoichiometry analysis of this QD is displayed in Fig. 6.5(b), reaching a GaSb content of nearly 100%. Corresponding to the nearly pure GaSb material, also an increased local strain within this QD can be concluded from the increased compression of the GaAs matrix underneath, as compared with Fig. 6.5(a).

The analysis of the wetting layer yields that both its vertical extension and composition do not reach the values of the QDs: The stoichiometry shows a maximum GaSb content of nearly 50% for one atomic chain, with a second chain of only about 10%, corresponding to the XSTM images showing a strongly intermixed layer extending over one to two atomic chains.

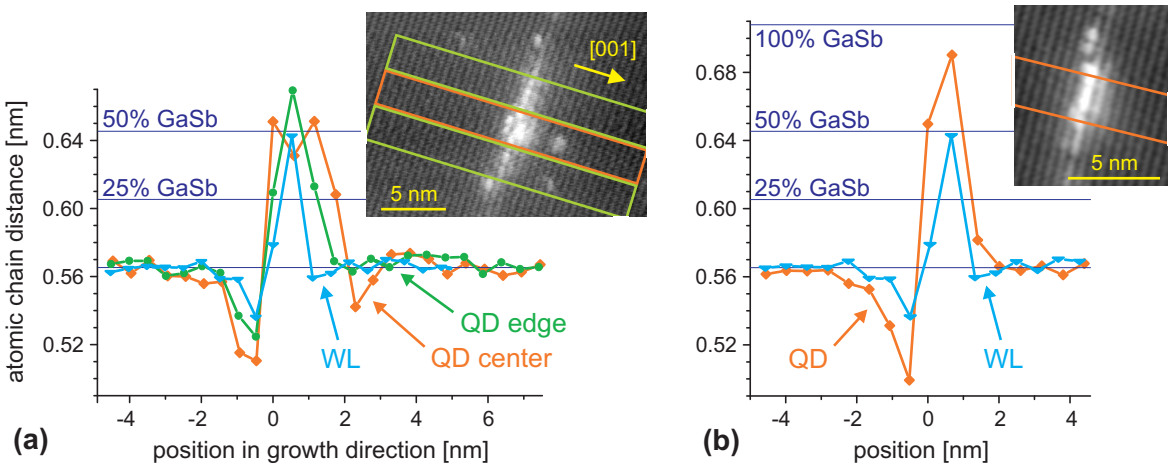

FIGURE 6.5: Analysis of the chemical composition of GaAsSb quantum dots.

Chapter 7

The onset and pathway of quantum dot formation

Comparing the XSTM data on different MOCVD-grown GaSb layers and knowing the tool to analyze their local stoichiometry, it is now possible to discuss the growth of GaSb nanostructures and especially the initial development of self-assembled quantum dots. In the first section of this chapter, the general growth mechanism of GaSb layers on GaAs will be highlighted in the context of earlier publications. Secondly, the GaSb content of the QWs and the WL will be evaluated, allowing conclusions on the cross-over from 2D to 3D growth and a comparison with the strongly varying literature data for the critical thickness of QD formation. The onset of this QD formation will finally be examined, introducing a possible pathway from quantum wells to quantum dots.

7.1 Gaps within the Sb layers: GaSb growth

All three MOCVD-grown GaSb layers studied here are not continuous, but are interrupted by smaller or larger gaps consisting of pure GaAs, as has been demonstrated in section 5.2 and the XSTM images shown there. These gaps are most pronounced in layer 1 with lateral extensions of up to 7 nm, but also in layer 2 many gaps are found with a maximum extension of 5 nm, and even the WL of layer 3 is interrupted. Typical examples of gaps are indicated in Fig. 7.1(a), imaged at layer 2. The gaps are randomly distributed over the layer, with typical distances between neighboring gaps of 2 to 15 nm and an average lateral extension of the gaps of 1.4 nm.

In order to ensure that a gap shows the same contrast in an XSTM image as the surrounding GaAs, at least the two topmost atomic layers have to consist of pure GaAs [372, 373]. This means that for a typical gap extension of 2 nm within a 1 nm thick WL, within an area of 10 surface unit cells and a volume of at least 20 group-V atoms no Sb but only As atoms may be found. Such a decomposition is too unlikely for a statistical fluctuation within an inhomogeneous GaAsSb layer, but has to be a systematic feature of GaSb growth. It should be noted, too, that such gaps are not common for intermixed InGaAs QWs or other III-V material systems.

However, this effect is consistent with results published by Bennett, Thibado et al. [45, 46, 257], who studied GaSb growth on GaAs(001): After depositing 1 ML GaSb on a c(4x4)-reconstructed GaAs(001) surface, they observed a network of 2D GaSb islands of 10 to 20 nm size and thin, 1 ML deep trenches, as shown in Fig. 7.1(b). Even when a second ML GaSb is deposited, this material grows predominantly on top of the existing islands, increasing their height but maintaining their diameter and preserving the trenches [46]. At

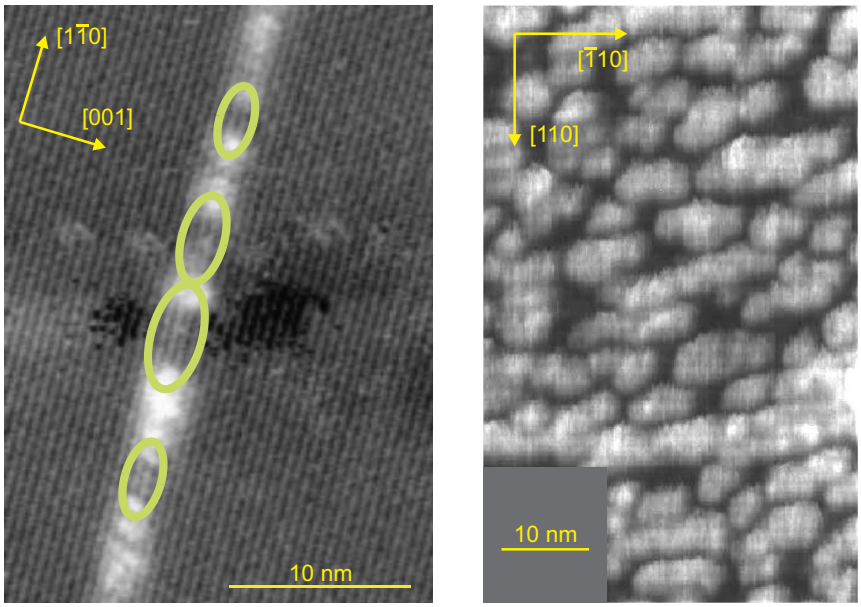

FIGURE 7.1: (a) XSTM image of GaSb layer 2, acquired at V_T = -2.0 V. Sb-free gaps within the layer are indicated. (b) Top-view STM image of a 1 ML thick GaSb layer on GaAs, taken from [46].

this point the growth is still of two-dimensional kind. Just upon depositing a third ML GaSb, three-dimensional growth sets in and quantum dots evolve in a self-assembled way.

Comparing these results obtained by top-view STM and the XSTM samples studied here, one can see that the initial structure of larger 2D GaSb islands and thin trenches in between remains conserved during dot growth: The observed gaps are the cross section of the initial trenches, getting filled with pure GaAs when the GaSb layers are overgrown.

It should be mentioned that in a later publication from the same group, Bennett et al. [257] report a transformation of the rather isotropic 2D island structure shown in Fig. 7.1(b) into a strongly anisotropic surface upon further GaSb deposition: The surface of the WL studied after deposition of 3.5 ML GaSb and accompanying QD growth is found to consist of thin 2D islands strongly elongated along the [$\bar{1}$10]-direction. Corresponding structures could not be found in the present XSTM images. However, due to the complete lack or the small size of the observed QDs, respectively, probably significantly less than 3.5 ML GaSb were deposited in all three layers studied by XSTM.

The discussed publications of Bennett, Thibado et al. are, to my knowledge, the only studies of GaSb/GaAs QD growth using top-view STM. Although the authors used MBE, their observed GaSb growth mode characterized by 2D GaSb islands interrupted by thin trenches seems to agree also with the MOCVD-grown samples studied here.

In the PL spectroscopy results on the QD sample, shown in section 5.3.1, a clear intensity peak which was related to a WL was obtained, indicating that the existence of gaps within the layer does not prevent the 2D electronic confinement inherent in QWs and WLs. This behavior agrees with an observation of Thibado et al., stating that the 2D islands form an interconnected network [46], which could explain the lateral mobility of charge carriers confined within the layer. Additionally, even if the 2D islands of the GaSb WL were actually separated by the thin trenches filled with GaAs, electron tunneling across these trenches could take place.

The gaps observed in the XSTM images show that the structure of the GaSb WL is significantly less homogeneous and continuous than that of WLs in the InAs/GaAs [3, 92, 100] or other material systems. Neverthelss, the Stranski-Krastanow growth mode, leading to the formation of QDs embedded in a WL as described in section 2.2.1, is confirmed – at least in a slightly modified case – also for the GaSb growth on GaAs studied here.

7.2 GaSb content of the quantum wells

The structures of the GaSb QWs of layers 1 and 2 and of the GaSb WL of layer 3, which have been presented in section 5.2, are compared in Fig. 7.2. Although they show the same general appearance, smaller differences between the three layers can be identified, with layer 1 being the thinnest and most inhomogeneous and layer 2 having the largest vertical extension.

For a more quantitative analysis of the GaSb content of these layers, their local lattice constants have been evaluated by the method described in chapter 6, resulting in the data shown in Fig. 7.3. Thereby typical areas of the XSTM images, containing parts of the layers with different GaSb composition and small gaps, too, were chosen for averaging and evaluating the chain distances, as can be seen in the insets of Fig. 7.3. Layer 1 exhibits the sharpest peak of increased chain distance, with the GaSb material being mainly concentrated to one atomic chain and a maximum GaSb content of 50%. In layer 2, in contrast, the maximum GaSb content reaches only about 27%, but in [001] direction the QW extends over slightly more than two atomic chains, with a smoother decay of the lattice constant at the top side of the layer. The chain distances of layer 3, finally, resemble more those of layer 1, showing an abrupt decrease at the top side. Layer 3 extends over two atomic chains, with chain distances corresponding here to 16% and 36% GaSb content, respectively.

In spite of the different extensions and maximum stoichiometries of the three layers, their total GaSb content, which can be evaluated from the chain distance analysis by integrating the curves over the area of increased GaSb content, amounts to 1 ML of pure GaSb for each of the three layers. Thus, the higher maximum content in one layer is balanced by the larger vertical extension of another. This result is important for understanding GaSb growth on GaAs: Layers 1 and 2 have been grown with nearly the same GaSb deposition time of 21 s for layer 1 and 22 s for layer 2, while at layer 3 GaSb was deposited at the same rate for 25 s. The fact that only layer 3 exhibits quantum dots agrees well with the observed identical GaSb content within the 2D layers, showing that the additional GaSb material of layer 3 was completely incorporated into the 3D structures. Therefore, layer 2 has been grown very close to the critical thickness of QD formation. The observed existence of Sb-rich 2D islands in layer 2 supports this result, as will be discussed in the next section. The intermixed stoichiometry of all three layers not exceeding 50% antimony, which leads to the relatively large vertical extension of 2 to 4 ML compared with only 1 ML total GaSb content, shows a

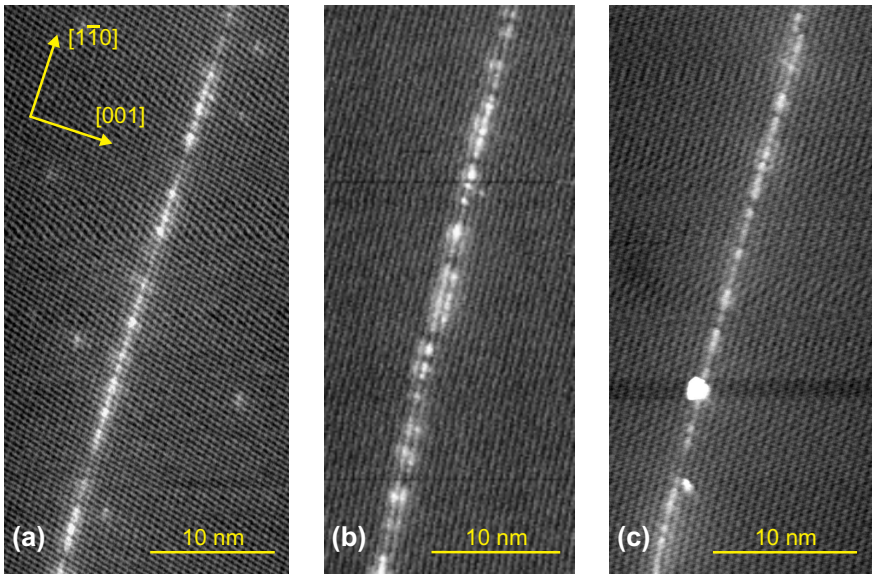

FIGURE 7.2: XSTM filled state images of the QWs of (a) layer 1, (b) layer 2, and (c) layer 3, acquired at (a,b) V_T = -3.0 V and (c) V_T = -2.3 V. The two bright spots at the QW in the bottom part of (c) are adsorbates.

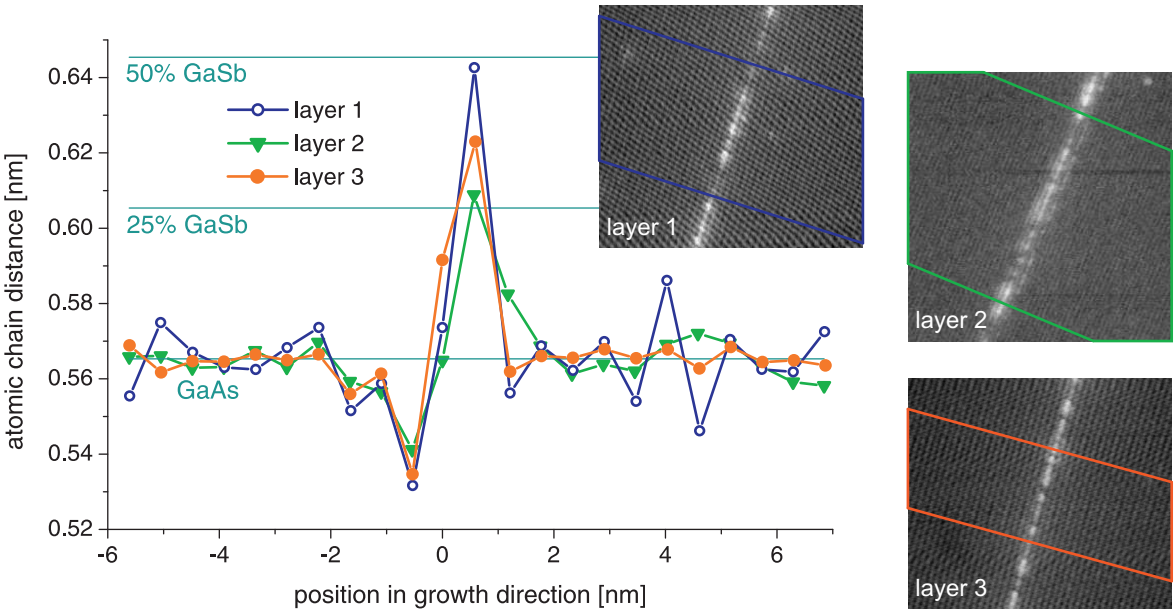

FIGURE 7.3: Evaluation of the local lattice constant of the MOCVD-grown GaSb layers, far away from any Sb-rich islands or QDs. Calculated values for $GaAs_{0.75}Sb_{0.25}$ and $GaAs_{0.5}Sb_{0.5}$ QWs are indicated. The areas for analyzing the chain distances in the XSTM images are shown as insets.

strong intermixing between Sb and As atoms.

Coming back to the exact characteristics of the analyzed chain distances, more details about the GaSb growth mechanisms can be revealed: The QW of layer 1 and the WL of layer 3 have the same total GaSb content and nearly the same variation of the lattice constant, except that in layer 1 the antimony is more concentrated in only one atomic chain. The growth parameters of these two layers differ regarding the GaSb deposition time, which has lead to the QD formation at longer deposition in layer 3, and regarding a growth interruption subsequent to GaSb deposition which only took place at layer 3. This 2 s growth interruption under TESb flux was chosen to give the deposited material enough time for QD formation [51, 182], and it also seems to have the effect of an additional intermixing of the deposited Sb atoms with the As atoms of the underlying GaAs matrix. Even stronger intermixing may have occured during overgrowth of the GaSb layers, but such intermixing should influence layers 1 and 3 to the same extent.

Layer 2 was grown with 22 s GaSb deposition time, slightly longer than layer 1, also followed by a 2 s growth interruption, equal to layer 3. However, the variation of the local lattice constant is considerably different to that of layers 1 and 3, although the remaining growth parameters were nominally the same. The sample containing layer 2 was grown in the same MOCVD chamber, but several months earlier than the sample with layers 1 and 3. Therefore, slightly different conditions of the reactor, such as an unintended As background pressure during GaSb growth, are supposed to cause the observed larger intermixing of layer 2.

All three chain distance curves shown in Fig. 7.3 show a significant undershoot just before they increase, standing for compressive strain within the GaAs matrix directly underneath the GaSb layers. However, a homogeneous quantum well does not compress the underlying material, because the strain in growth direction can completely relax by increasing the chain distance, in contrast to quantum dots with a locally enlarged strain [3, 124]. An apparently decreased chain distance can also be given by a concave surface curvature directly underneath the GaSb layer, as discussed in section 6.3. However, this effect cannot sufficiently explain the observed undershoot, as a QW undergoes only very small cleavage-induced relaxation as

compared with a QD [124], and because for homogeneous WLs studied in the InAs/GaAs material system, hardly any undershoot of the chain distances is present [100]. Thus the existence of locally compressed strain underneath all three GaSb layers studied here is a clear evidence for a laterally inhomogeneous composition of the layers, with fluctuations of the stoichiometry in $[1\bar{1}0]$ direction leading to fluctuations of the local strain.

Values of the critical thickness of deposited material upon which epitaxial growth changes from 2D to 3D (often called "critical thickness of dot formation"), which depend weakly on the growth parameters and essentially on the material system, vary strongly in literature for the GaSb/GaAs system [44, 46, 49–51, 55, 57, 59, 69, 182, 256, 260, 264, 267]. Almost all publications about MOCVD growth of GaSb QDs can, to my knowledge, be distributed to either Müller-Kirsch in the group of Bimberg at Berlin University of Technology in Germany [51, 53, 71, 73, 264, 265] or Motlan in the group of Goldys at Macquarie University in Sydney, Australia [52, 61, 74, 260, 262, 263]. Recently, also GaSb QDs grown by organometallic vapour phase epitaxy were published by Pitts from the group of Watkins at Simon Fraser University in Burnaby, Canada [57].

Müller-Kirsch reports a large critical thickness of dot formation of about 4 ML GaSb deposition [51, 264], obtained by growing several samples with varying GaSb deposition times and observing by AFM in which samples QDs have formed. For this evaluation, the GaSb growth rate has to be known which is a non-trivial issue as this growth rate can change dramatically with deposition time (see section 5.1 and Ref. [182]). In an early publication from Kinder and Goldys [260], the critical thickness of GaSb dot formation is quoted to be less than 2 ML, also obtained by comparing different samples by AFM. For this value, however, a constant growth rate was assumed which was extrapolated from growing thick GaSb layers, which could be a critical premise. Later on Motlan et al. from the same group specify only deposition times and no definite values of a critical thickness [52, 74, 263]. An astonishingly smaller value of the critical thickness between 0.3 and 0.5 ML is given by Pitts et al. [57], also after studying the GaSb growth surface by AFM. On the other hand, when the investigated sample was not cooled down after GaSb deposition for examination by AFM but was immediately overgrown by GaAs, flat GaSb films were maintained up to a deposition of 1 ML. Both values, however, might be somewhat arguable, because the growth rate again was assumed to be constant and, even more, it was extrapolated from certain volumes of observed QDs after certain deposition times as evaluated from AFM measurements under ambient conditions.

The majority of results on GaSb QD growth has been obtained using MBE. Amongst these, most authors specify the critical thickness of dot formation to amount between 2 and 3 ML, as for examples in Ref. [46, 49, 55, 59, 69, 256]. Even larger values of about 4 ML can be found, too [44, 267], but also a critical thickness of only about 1 ML was reported [50]. These data will be discussed in detail in section 9.3.2. Summarizing this variety of literature results, controversial values ranging from 0.4 ML to 4 ML are reported for the critical thickness of dot formation, which at least for the MOCVD-grown samples are obtained under assumptions which are not necessarily fully appropriate.

In XSTM studies, the total GaSb content of capped layers can be analyzed, amounting here to 1 ML for the QW near the onset of QD formation and equally to 1 ML for the WL. This value is not necessarily the critical thickness of dot formation, as a part of the originally deposited GaSb material can have been transferred into QDs or have segregated from the GaSb layer upon capping. Due to the observed GaSb content, however, the critical thickness of dot formation must at least amount to 1 ML. The XSTM images of the GaSb layers shown in section 5.2 are characterized by a nearly perfect cleavage surface of the GaAs matrix several nm below or above the layers, containing no incorporated Sb atoms. Therefore, in

spite of the strong intermixing directly at the GaSb layers, no significant segregation during overgrowth can be detected. It cannot be excluded that a part of the initially deposited GaSb has stayed at the growth surface as surfactant during overgrowth, but the observed lack of significant Sb segregation and reincorporation increases the probability that the observed GaSb content of 1 ML is also the critical thickness of dot formation.

Two publications confirm the observed results: Besides studying growth surfaces, Müller-Kirsch has also evaluated the GaSb content of capped GaSb layers with and without QDs from high-resolution TEM images and by simulating PL data [182]. He derived an intermixed $GaAs_{0.6}Sb_{0.4}$ layer of 2 ML height at the cross-over from 2D to 3D growth, resulting in a total GaSb amount of about 0.8 ML, which agrees well with the value of 1 ML found here by XSTM. Using x-ray diffraction and a rather complex epitaxial growth sequence, Pitts et al. studied the maximum incorporation of Sb into GaSb QWs before QD growth sets in, also resulting in approximately 1 ML [57], again in good agreement with the XSTM data.

7.3 Structures from quantum wells to quantum dots

Knowing that the formation of QDs starts after depositing 1 ML or slightly more GaSb, the question remains how the transition from 2D to 3D growth occurs. The initial GaSb film on GaAs consists of flat islands and small trenches, as it was discussed in section 7.1, revealing a 2D island growth. The QWs of layer 1 and 2, shown in Fig. 7.2(a,b), are results of such a GaSb layer growth, with the difference that the 2 s growth interruption under TESb flux following GaSb deposition at layer 2 has lead to a slightly more homogeneous well structure. Additionally, Sb-rich 2D islands of only a few nm size and a high density of $\sim$ 6 x 10^{11} cm^{-2} have been observed in layer 2 (see section 5.2.2 for details). Two typical examples of these Sb-rich flat structures are shown again in Fig. 7.4(a), clearly recognizable by their strongly increased image contrast. No such Sb-rich islands have been found in layer 1, thus the slightly longer GaSb deposition at layer 2 has supplied the necessary material and the growth interruption enabled the material to agglomerate in these self-assembled Sb-rich islands. The observance that layer 1 and the QW of layer 2 beside the islands contain the same amount of GaSb confirms that the additional material of layer 2 has moved into these areas of increased Sb concentration. Thus, the observed small 2D islands are first self-assembled Sb accumulations and possibly act as QD precursors.

The cross-over from 2D to 3D growth occurs during the additional 3 s GaSb deposition

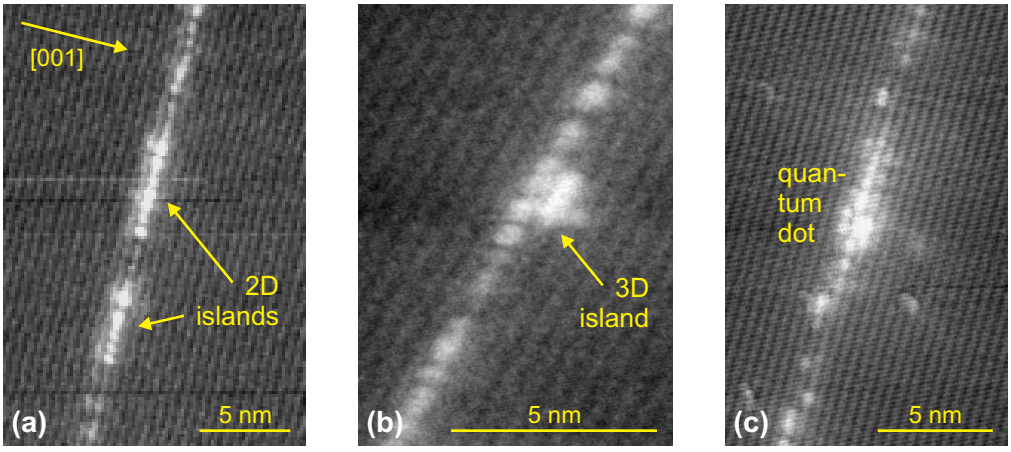

FIGURE 7.4: Comparison of XSTM filled state images of (a) 2D-islands in layer 2, (b) a tiny 3D-island in layer 3, and (c) a quantum dot in layer 3. For details see sections 5.2.2 and 5.2.3.

time making up the difference between layers 2 and 3. The smallest known 3D GaSb structures are the tiny islands observed in layer 3 like that shown again in Fig. 7.4(b). No comparable structures have been mentioned in literature yet, what is not very surprising, because most earlier work on GaSb QDs has used characterization methods like AFM [48, 49, 51, 55–58, 256, 260, 263, 374], SEM [56, 267] or TEM [44, 51, 53, 262, 263, 374], which are not able to resolve structures of only 2 or 3 nm size. The density of these tiny 3D islands is with $\sim 5 \times 10^{10}$ cm^{-2} about one order of magnitude smaller than that of the 2D islands of layer 2, but it is similar to that of the QDs also found in layer 3, amounting to $\sim 3 \times 10^{10}$ cm^{-2}. It cannot securely be said whether the tiny 3D islands have emerged from the 2D GaSb-rich islands, the latter ones not being observed in layer 3 any more. The total GaSb content of a tiny 3D island is approximately the same as that of a 2D GaSb-rich island, as estimated from the volumes of typical examples of the structures. Another possibility is that the longer GaSb deposition lead directly to the formation of 3D GaSb structures during the subsequent growth interruption.

As both the tiny 3D islands and small, but distinctive QDs as the one shown again in Fig. 7.4(c) are observed within layer 3, GaSb QDs most probably develop from such tiny 3D islands which act as precursors. The qualitative difference between both kinds of structures is that the XSTM images reveal significant strain and electronic confinement only for QDs, as has been discussed in section 5.2.3. The coexistence of the islands with only about 2 nm size and the QDs with typically 4 to 8 nm lateral extension and about 2 nm height in the same GaSb layer is comparable to the large size fluctuation found for larger GaSb QDs by top-view TEM (see section 5.3.2 for details).

From XSTM images like Fig. 7.4(c) it can be seen that the WL in the direct neighborhood of the QD contains very few Sb atoms. This indicates a growth and ripening of the QDs not only by direct incorporation of deposited material, but also by mass transfer along the growth surface from the surrounding WL. It should be noted that for the InAs/GaAs system a general mass transfer from the WL to ripening QDs has been reported, together with a coexistence of QDs and small 3D clusters [375].

The electronic confinement within the GaSb QDs has also been confirmed by the PL data shown in section 5.3.1, exhibiting a PL emission energy of the QDs of 1.2 eV. This energy corresponds to the small size of the QDs. The energy separation between confined states within a QD depends critically on its size [3, 37, 211], implying a minimum QD size for the existence of a first confined state. In the InAs/GaAs material system, this minimum size is between 3 nm and 5 nm of lateral extension [2]. For GaSb/GaAs QDs, however, the confinement condition must be fulfilled only for VB hole states. Because the energy separation between confined hole states is generally much smaller than between electron states (see Fig. 2.10 and Refs. [3, 37]) due to the about one order of magnitude larger effective masses of the holes also for GaSb [164], and because of the large VB offset for GaSb/GaAs QWs and small QDs of 0.5 eV [75], the minimum size for electronic confinement is thus significantly smaller in the GaSb/GaAs system. Therefore, the observed small size of typically 4 to 8 nm base diameter does not inhibit the QDs to be optically active.

Comparing the shape and size of the QDs studied here with literature data, it is found that they are not only smaller than typical InAs/GaAs QDs [24, 33, 38, 95, 100, 119, 120, 122], but also smaller than most GaSb/GaAs QDs. Although results obtained by *ex-situ* top-view characterization methods on uncapped, oxidized GaSb QDs [49, 52, 56, 69, 267] cannot be compared with XSTM data, also *in-situ* STM measurements on uncapped QDs during growth [46, 257] and studies on overgrown QDs [51, 59, 263] obtained GaSb QD sizes of more than 10 nm. Smaller QD sizes are not published, but Müller-Kirsch et al. reported stoichiometry fluctuations of a strongly intermixed GaAsSb WL [71, 73, 265], which can be compared with

the structures observed here: Possibly those reported fluctuations, which exhibited a PL peak at an energy about 0.1 to 0.2 eV below the WL peak, actually were structures similar to the QDs studied here, but could not be resolved as 3D structures due to the limited atomic resolution of HRTEM used in that work.

The flat QD shape with a small aspect ratio observed for the QDs studied here agrees well with published results on larger capped QDs grown by MOCVD [51, 263]. From the observed coexistence of precursor structures and QDs in the same layer and from the small size of the QDs in comparison with published data, it can be assumed that the QDs studied here represent an early stage of MOCVD QD growth.

In conclusion, the following pathway of GaSb QD formation can be proposed: The initial GaSb deposition on GaAs(001) produces a thin film consisting of 2D islands of 10 to 20 nm size, separated by small trenches. Continuing GaSb growth up to the critical thickness of dot formation, which amounts to about 1 ML or more, the formation of several nm large flat 2D islands of increased Sb concentration can occur during a short growth interruption. With further continued GaSb deposition, three-dimensional growth sets in by forming tiny 3D islands, which then ripen to optically active QDs which can further increase in size. This process includes a GaSb depletion in the WL close to the growing dot. During overgrowth, the initial trenches of the WL get filled with GaAs. Significant intermixing occurs, probably already during GaSb deposition, during the growth interruption thereafter, and during the capping process, leading to a QD stoichiometry of about 60% - 100% GaSb concentration and strongly intermixed QWs and WLs with less than 50% GaSb content.

Chapter 8

XSTM results on MBE-grown samples

While the data on MOCVD-grown samples concentrated on the onset of QD formation, a broader range of GaSb/GaAs QD structures could be studied on samples grown by MBE. As the MBE method allows a more direct control of the GaSb deposition and the growth process than MOCVD (see chapter 2.2), it was possible to study several GaSb layers with systematically varied amounts of deposited material within one MBE-grown sample. Additionally, samples grown in two different places by different cooperation partners could be compared.

8.1 Sample structures

The results on MBE-grown structures can be devided in data derived from two samples: Sample C has been grown by Ganesh Balakrishnan in the group of D. L. Huffaker at the Center of High Technology Materials in Albuquerque at the University of New Mexico, USA [376], and sample D by Ian Farrer in the group of D. A. Ritchie at the Cavendish Laboratory at the University of Cambridge, UK [377].

Both samples were fabricated in a VG-V80H MBE system, respectively, using conventional solid sources for gallium, antimony, and aluminum as well as a cracker source for arsenic. Sample C was grown with As_2, received from the cracker unit operated at high temperatures, while for sample D the cracker source was operated at 600°C, resulting in an arsenic beam consisting of As_4. Antimony was provided as Sb_4 in both samples. Detailed sample structures can be seen in Fig. 8.1: On GaAs(001) substrates, highly n-doped with silicon, first a thick GaAs layer was grown (300 nm in sample C, 200 nm in sample D), followed by an AlGaAs buffer layer of 100 nm thickness. Thereafter, the heterostructures consisting of several GaSb QD layers and GaAs spacers were deposited, followed by 200 nm AlGaAs, respectively. An additional 5 nm AlGaAs / 5 nm GaAs / 5 nm AlGaAs marker was grown above the second GaSb layer of each sample, helping to rapidly identify the individual layers during the XSTM measurements. The complete structures were finished by a GaAs cap layer, which is about 800 nm thick and undoped in sample C and 1000 nm thick and p-doped with a Be dopant concentration of 5×10^{16} cm^{-3} in sample D.

The actual heterostructure of sample C consists of four GaSb layers with increasing amount of deposited material, separated by 90 to 100 nm thick GaAs spacer layers and the AlGaAs marker mentioned above, and is embedded within two additional 100 nm thick GaAs layers. Sample D contains three GaSb layers, with GaAs spacers of 120 nm thickness between the first and second and 215 nm including the AlGaAs marker between the second and third, also embedded within additional GaAs layers of 150 nm thickness each.

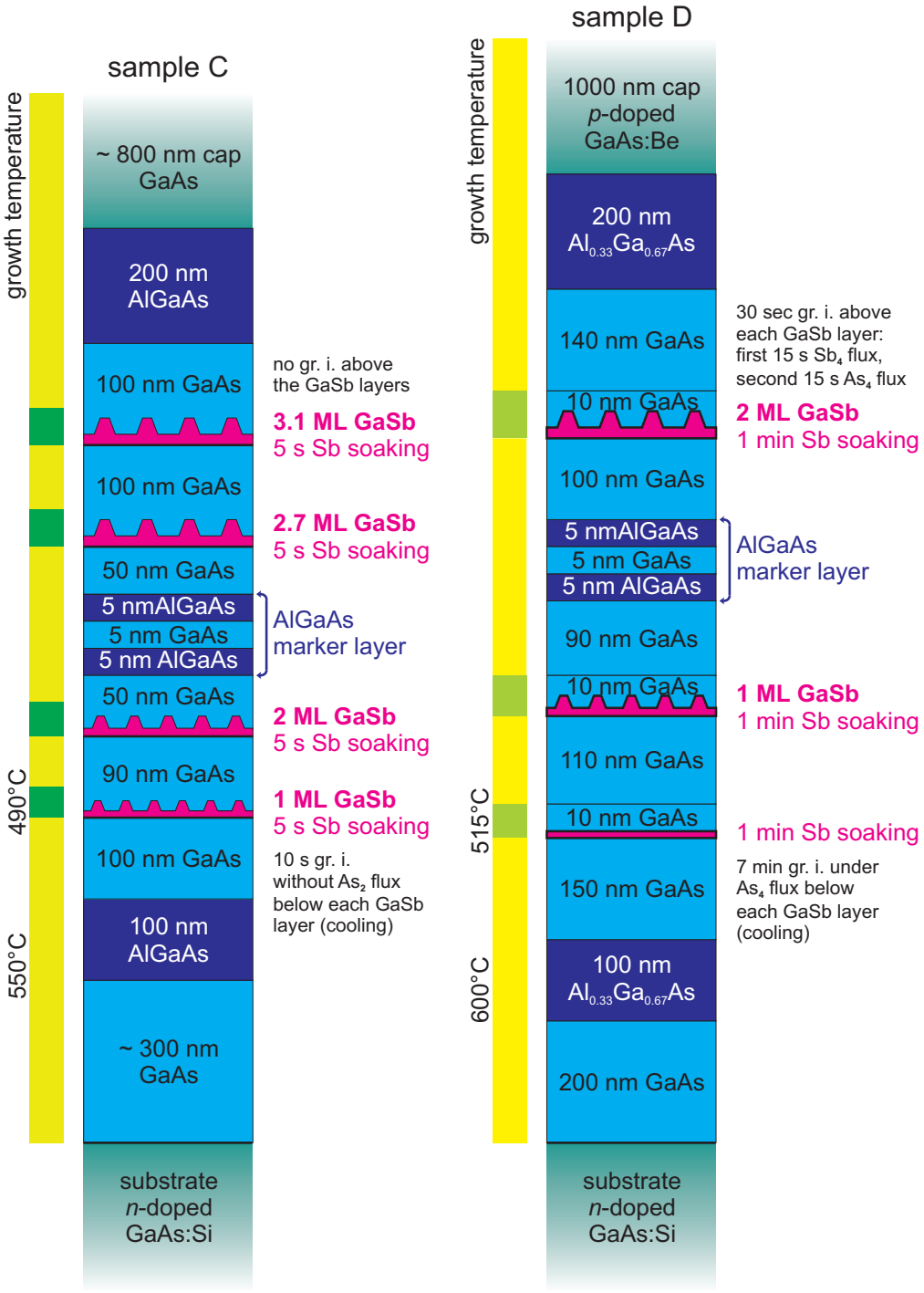

FIGURE 8.1: Comparison of the detailed sample structures of the MBE-grown samples.

While the layer sequence of both samples is very similar, the growth rates, temperatures and the detailed parameters for depositing GaSb layers differ quite strongly for both samples, representing different approaches and special experiences with GaSb growth in the two involved epitaxy groups. For sample C, a growth rate of 0.3 ML/s was chosen for all layers, while the growth temperature was changed between 550°C for all GaAs and AlGaAs layers and 490°C for the GaSb layers and the following 5 to 10 nm of GaAs, respectively. Sample D was grown with a higher growth rate of 0.7 ML/s for all layers. The temperatures here were

600°C for the GaAs and AlGaAs layers and 515°C for the GaSb layers and the subsequent 10 nm of GaAs, respectively, as measured during growth by an infra-red pyrometer.

One main challenge of GaSb/GaAs QD growth by MBE is the precisely controlled change of the group-V atoms during epitaxy and the resulting abruptness of the interfaces (see section 2.2.2 and Refs. [55, 57, 59, 177]). Usually epitaxial growth is controlled by the group-III flux, while the group-V atoms are offered abundantly as a permanent background, also during growth interruptions (see chapter 2.2). When Sb atoms are offered to a GaAs surface during epitaxy, considerable As-Sb exchange reactions occur, leading to an Sb-rich growth surface [50, 55, 57, 59]. Thus it has been found to be helpful for GaSb QD growth to expose the underlying GaAs surface to an antimony flux during a growth interruption (GI) prior to GaSb deposition, a process called "Sb soaking" [55, 59, 69].

Such an Sb soaking was used in both samples, but with special emphasis in sample D: Here, the first GaSb layer was formed only by this Sb-for-As exchange process during a 1 min long Sb soaking, with the gallium source being closed during the whole antimony supply. For the second layer, the same 1 min long Sb soaking was followed by a direct deposition of 1 ML GaSb, and in the third layer 2 ML GaSb were grown subsequently to 1 min of Sb soaking. GaSb growth was followed for all three layers by a GI of 15 s under antimony background for annealing the deposited material and subsequently 15 s during which the valve of the arsenic cracker cell was opened again, before GaAs growth was continued. This exit valve of the As_4 cracker unit, needing several seconds to be operated, is used additionally to the conventional shutters of the effusion cells. The latter can be closed and opened much faster, but can reduce the arsenic flux only by about 80%, while the cracker valve enables the growth of much purer GaSb material [55]. The growth temperature was reduced during a 7 min GI prior to each Sb soaking and held at this value until the GaSb layer was covered with 10 nm GaAs, then during another 7 min GI it was raised again.

At sample C, the four GaSb layers were grown with increasing amounts of deposited material of 1 ML, 2 ML, 2.7 ML, and 3.1 ML. Each layer was preceded by 5 s of Sb soaking, expectedly corresponding to sufficient Sb to replace nearly one ML As at the surface. Even prior to this, growth interruptions of 10 s took place without supply of either antimony or arsenic, so that the reconstruction of the underlying GaAs surface became metal rich. This sequence of GI, Sb soaking, and GaSb growth was chosen to increase the QD uniformity and density. During the 10 s GI also the growth temperature was reduced for GaSb growth for all four layers. It was increased again during GaAs deposition when the GaSb layers had already been overgrown by about 5 to 10 nm.

While the GaSb growth sequence of sample D was ascertained by calibrated growth rates and experience from reference samples, RHEED measurements enabled a direct control of the deposited material at sample C. For the latter sample, in spite of the small amount of only 1 ML of deposited GaSb at the first layer, a clear QD signal was monitored by RHEED for all four GaSb layers during growth.

8.2 Overview images

In XSTM images of the overgrown samples GaSb QDs could be observed in all four layers of sample C and also in those two layers of sample D for which GaSb material was directly deposited. Overview images of the first three GaSb layers of sample C and of the third GaSb layer of sample D can be found in Figs. 8.2 and 8.3, respectively. All STM images of samples C and D were taken with tunneling currents I_T between 50 pA and 100 pA.

Figure 8.2 is dominated by cleavage-induced surface steps running mainly along the $[1\bar{1}1]$ and $[1\bar{1}2]$ directions, but the three GaSb layers are also clearly visible by their bright contrast.

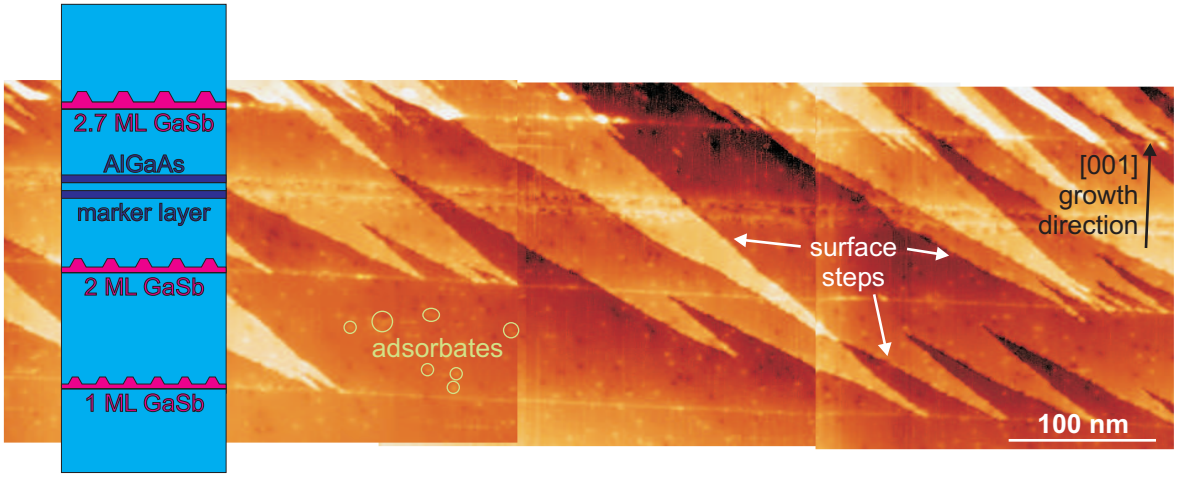

FIGURE 8.2: Overlapping XSTM overview images of sample C, taken at V_T = -2.7 V, together with the sketched sample structure. GaSb layers 1 to 3 and the AlGaAs marker can be identified, together with many cleavage-induced surface steps. Small spots are adsorbates on the cleavage surface.

The helpful role of the thin AlGaAs double layer as marker is obvious. Additionally, many adsorbates, arising from residual gas contamination of the cleavage surface, can be seen as small bright or dark spots. At this low magnification, individual QDs are only weakly observable within the GaSb layers. Especially the presence of the surface steps makes it difficult to identify the QDs and to observe their structure: Firstly, the image contrast of these one or several atomic ML high steps exceeds that of the QDs. Secondly, as the course of the surface steps is partly random but finally governed by strain, these steps often run parallel to the wetting layers (WLs) or end directly within a QD. Therefore, multiple attempts to position the XSTM tip on macroscopically different positions of the cleavage surfaces were necessary to obtain data on all seven GaSb layers at areas with a sufficiently low step density.

In XSTM images of sample D, the GaSb layers generally exhibit a somewhat weaker image contrast, corresponding to less strain or a lower Sb content of the nanostructures, although their nominal GaSb content is comparable to that of the thinner layers of sample C. Figure 8.3 shows overview images of the third GaSb layer of sample D, displayed with an about two times larger magnification compared to Fig. 8.2. At this image size, individual, very flat QDs can be recognized by their increased contrast. Similar QDs, embedded in a distinctive WL, could be obtained in GaSb layers 2 and 3. Layer 1, however, which contains no directly deposited GaSb but has formed only due to Sb soaking, is rather a thin region of individual GaSb atoms than a continuous layer. This first layer will be discussed in more detail in chapter 9.2.

Those results and a comparison of this soaking-induced layer with the other two layers of sample D will reveal new insight into group-V exchange processes, their influence on QDs and the onset of GaSb QD formation; while the data on sample C, containing more and larger

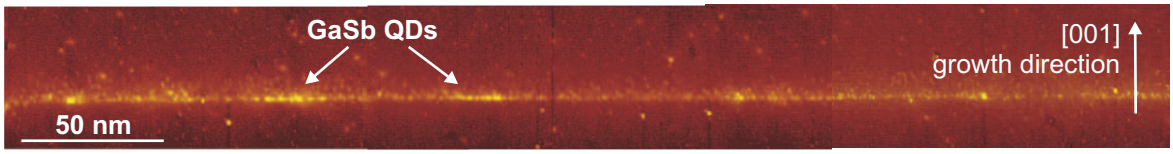

FIGURE 8.3: Overlapping XSTM images of sample D, taken at V_T = -2.7 V, showing the third GaSb layer containing flat QDs.

QDs in GaSb layers with a broader range of deposited material, are more suited to study the atomic structure and further development of GaSb QDs.

The appearance of the QDs in XSTM images of both samples C and D can generally be grouped into two kinds of structures: Besides QDs with trapezoidal cross sections, corresponding to the well-known QD shape of a truncated pyramid, also cross-setions showing small paired features, symmetrically to each other, with a more or less pronounced gap between them are found regularly, which can be attributed to ring-like QD structures. Typical examples of both types of QD cross sections in samples C and D are presented in the next two sections, including a statistical analysis of the apparent QD structure, respectively. By comparing these statistical data with numerical simulations on random cleavage processes the origin of the different appearance of QD cross sections will be revealed. The exact atomic structure of the QDs and the evolution of their shape will be discussed in chapter 10.

8.3 Quantum dots in sample C

A total number of 140 GaSb QDs in sample C has been investigated, distributed over four layers with increasing amount of deposited GaSb material and QD densities increasing correspondingly from 4×10^{10} cm^{-2} in the first layer to 9×10^{10} cm^{-2} in the fourth layer, evaluated from the XSTM data as described in section 5.2.3.

8.3.1 Quantum dot shapes in XSTM images

Nearly half of the QDs, 69 of 140, have a rather compact appearance like those two shown in Fig. 8.4(a,b), imaged in layer 2 (a) and layer 3 (b). Their shape generally resembles that of common capped QD structures, which are well-studied for example in the In(Ga)As/GaAs system [92, 95, 97, 100, 119]. In detail, the cross sections through the QDs reveal a trapezoidal

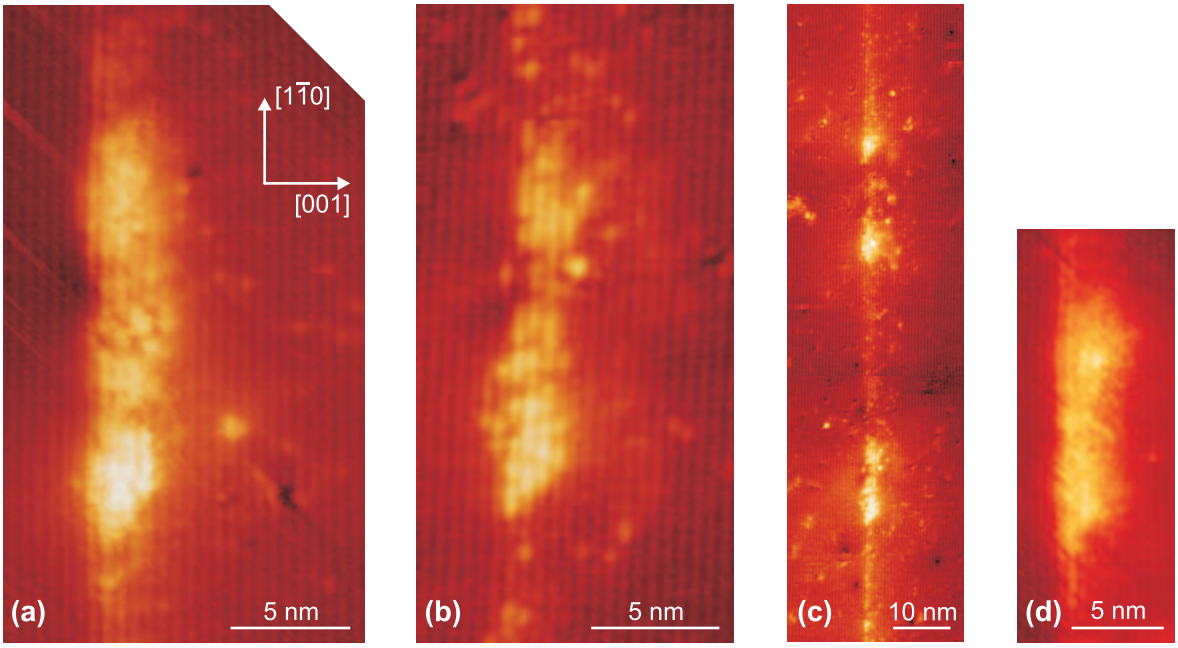

FIGURE 8.4: XSTM filled state images of sample C: Close-view images of (a) a QD in layer 2, taken at V_T = -1.7 V, and (b) a QD in layer 3, taken at V_T = -2.6 V, (c) overlapping images of the QD shown in (b) together with another, ring-shaped, QD structure, acquired at V_T = -2.5 V, and (d) a close-view image of another QD in layer 2 with a depression at the top center, acquired at V_T = -1.9 V.

shape, which can clearly be seen in Fig. 8.4 by the strong contrast, with a rather flat (001) top facet and comparatively steep side facets. Typical base lengths are between 10 and 20 nm with heights roughly about 2 nm. The interfaces between the GaSb QD and the surrounding GaAs are not perfectly abrupt, but in some places smeared over about one atomic chain. In addition, the varying image contrast within the QDs indicates an alloyed $GaAs_xSb_{1-x}$ material with inhomogeneous chemical composition. Within the GaAs matrix grown on top of the GaSb layers, several bright spots are visible both above the QDs and above the WL. These spots can be attributed to single Sb atoms, indicating antimony segregation into the overgrowth layer.

However, in Fig. 8.4(c) together with the nice, compact QD shown in (b) also a different QD structure can be seen in the upper part of the image: This structure appears as a pair of bright, nearly axially symmetric features, each with a lateral extension of about 6 nm and a height of four to five atomic chains or about 2.5 nm, distanced to each other by about 10 nm. Therewith this structure is of the same height and slightly larger in lateral extension than the neighboring compact QD, and it is a typical example for the other half of the QD structures in the sample: Indeed, 71 of 140 QD structures observed in sample C consist of two paired features with a more or less distinct gap in between.

A close-view image of the paired QD structure shown above is presented in Fig. 8.5(a), together with an even more pronounced example of such a structure observed in layer 4 [Fig. 8.5(b)]. These structures represent a cross section through a quantum ring, as the sketch of Fig. 8.5(c) illustrates: The paired features of bright appearance occur when the ring of high GaSb content is cut, while the dark gap in between is a region containing only a few or no Sb atoms at all. Actually, many ring-shaped QD structures are not that well defined as those in Fig. 8.5(a,b), but are asymmetric or with much smaller central gaps containing some residual Sb atoms, as the structure of Fig. 8.5(d) shows.

To confirm the assumption of the observed paired features representing ring-shaped structures and to exclude the possibility that they are only a random distribution of individual small islands, the free distance between neighboring GaSb structures in the XSTM images was evaluated statistically for layers 2 and 3, as shown in Fig. 8.6(a). For this analysis a paired feature was first considered as two independent islands, resulting in a broad, irregular distribution of QD distances along [1$\bar{1}$0]-direction with a strong increase for very small distances

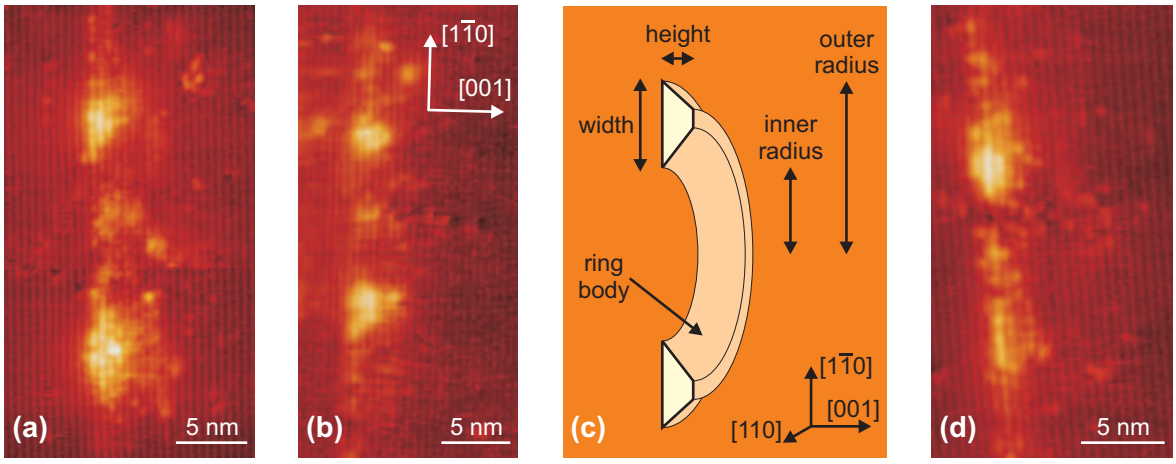

FIGURE 8.5: Ring-shaped QDs in sample C: (a,b) close-view XSTM images of (a) layer 3, taken at V_T = -2.3 V, and (b) layer 4, taken at V_T = -1.8 V; (c) sketch of a cross section through a ring, the notation of the geometric parameters used in the text is indicated; (d) XSTM image of an asymmetric ring structure in layer 3, acquired at V_T = -1.7 V.

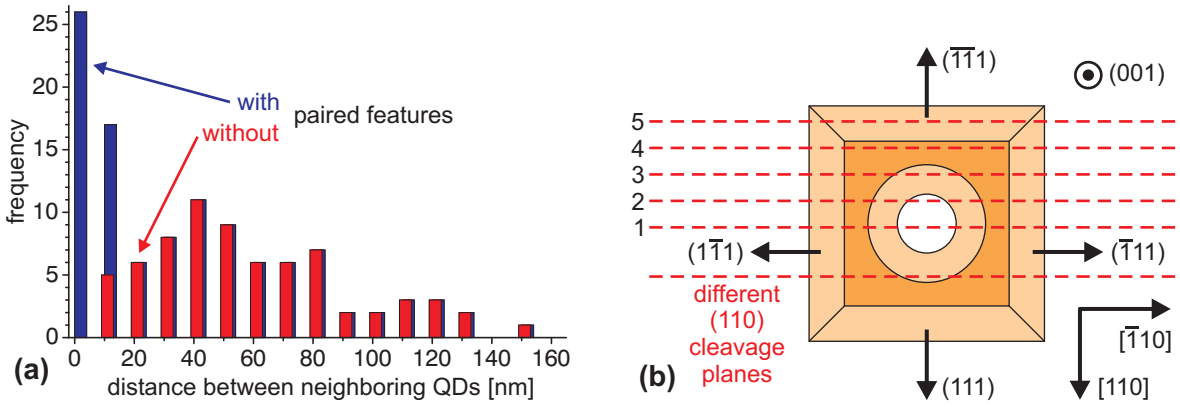

FIGURE 8.6: (a) Histogram of the free distances between neighboring QDs along $[1\bar{1}0]$-direction in layers 2 and 3, interpreting the paired features either as two separate QDs (blue columns) or as one ring-shaped structure (red columns), obtained from XSTM images. (b) Model of different cross sections through a ring-shaped QD.

(blue columns). Alternatively, each paired feature was considered as one ring-shaped QD (red columns). In the latter case, a nice distribution of next-neighbor QD distances results, ranging from 8 nm to 148 nm in the observed area with a maximum peak at about 40 nm and an expected exponential decay for longer distances. The statistic average of 60 ± 33 nm corresponds to a QD density of about 8×10^{10} cm^{-2}. In contrast to this rather broad and smooth distribution, the free distance between the paired features – i.e. the inner ring diameter – only ranges from 1 to 14 nm with an average of 5.4 ± 2.9 nm. This very narrow distribution shows no correlation to that of the QD distances, verifying that it can well be distinguished between the paired features of a cleaved ring structure and two independent, neighbored QDs.

The fact that the extension of the central gap (the inner diameter) varies between the images of different ring-shaped QDs needs not necessarily be due to actual differences of the ring structures: Because the position at which a QD is cleaved in an XSTM experiment is random, different QDs with nearly the same structure will result in very different cross sections in XSTM images, as sketched schematically in Fig. 8.6(b). Central cross sections along line 1 and 2 will exhibit a central gap of decreasing extension, as in the images of Fig. 8.5, but a cut through the edge of a ring structure along line 4 will result in a rather compact, continuous cross-sectional image. Therefore, also the two nice QDs of Fig. 8.4(a,b) could actually have a ring-shaped structure, which is cut at the edge. Indeed, in both images the brightest contrast, standing for high GaSb content and large strain, can be found in the outer parts of the QDs, while the center is a bit darker and more inhomogeneous, indicating less strain and GaSb content. Especially when a ring is cut at its edge in that way that the larger part of the ring is still in the sample underneath the cleavage surface, a strain distribution which is larger at the outer parts and smaller in the center will result. Additionally, some of the compact QDs observed in sample C exhibit a depression in the center of the top face, as it can weakly be seen already in Fig. 8.4(b) and very clearly in Fig. 8.4(d), showing another QD in layer 2. Such a depression agrees well with the expected cross section along line 3 of the sketch in Fig. 8.6(b).

8.3.2 Statistical and simulated data on quantum dot cleavage

Considering that the paired features observed in sample C as well as the QDs with a rather compact appearance can both represent cross sections through ring-shaped QD structures, the

question arises whether all observed structures are actually rings, or whether ring-shaped and conventional, continuous QDs coexist as two different structures. To answer this question, a detailed statistical analysis of all QDs observed in sample C will be compared with simulated data on random cross sections through ring structures.

In all four layers of sample C, QD images with and without central gap (i.e. paired features and compact looking QDs) were obtained to about the same amount in the XSTM data. As the absolute sizes of the structures vary due to the size distribution of the QDs within one layer and due to an increasing average QD size from layer to layer, a parameter is needed which can describe the characteristics of the central gap independent of the total size of the structure. Therefore the ratio of apparent inner to outer ring diameter $\tilde{r} = d_{in,\,cut} \,/\, d_{out,\,cut}$ was studied, which is zero for a QD image with compact appearance and nonzero but smaller than one for a paired feature. This ratio was evaluated for all 140 QDs observed in sample C, as shown by the red columns of the histogram in Fig. 8.7. As expected, the value $\tilde{r} = 0$ was obtained 69 times, corresponding to XSTM images showing a rather compact QD. For those QDs revealing a ring shape in the images, the measured inner and outer diameters result in a ratio varying from nearly zero up to 0.7, with a statistical average of $\tilde{r} = 0.35 \pm 0.14$. The irregular jump in the histogram between ratios of 0.3 and 0.4 is probably only due to statistical noise.

In order to either confirm or disprove the assumption that the statistical XSTM data represent a random distribution of cross sections exclusively through ring-shaped QDs, such a distribution was simulated as follows: Firstly, for a given ring structure with a certain ratio of actual inner and outer diameter $r = d_{in} \,/\, d_{out}$ the apparent ratio $\tilde{r}$ was calculated in dependence of the position were the QD is cleaved [see Fig. 8.6(b)], obtaining a frequency distribution of different ratios (obviously, the diameter $d_{in,\,cut}$ appearing in an XSTM image is nearly always smaller than the actual diameter d_{in} and only equal if the ring is cut centrally). In a second step, the calculation was repeated many times while the actual ratio of diameters was varied in small steps from $r = 0.1$ to 0.9. Probably the inner diameter is not the same for all rings but varies, as the total size of the structures also does. Therefore a

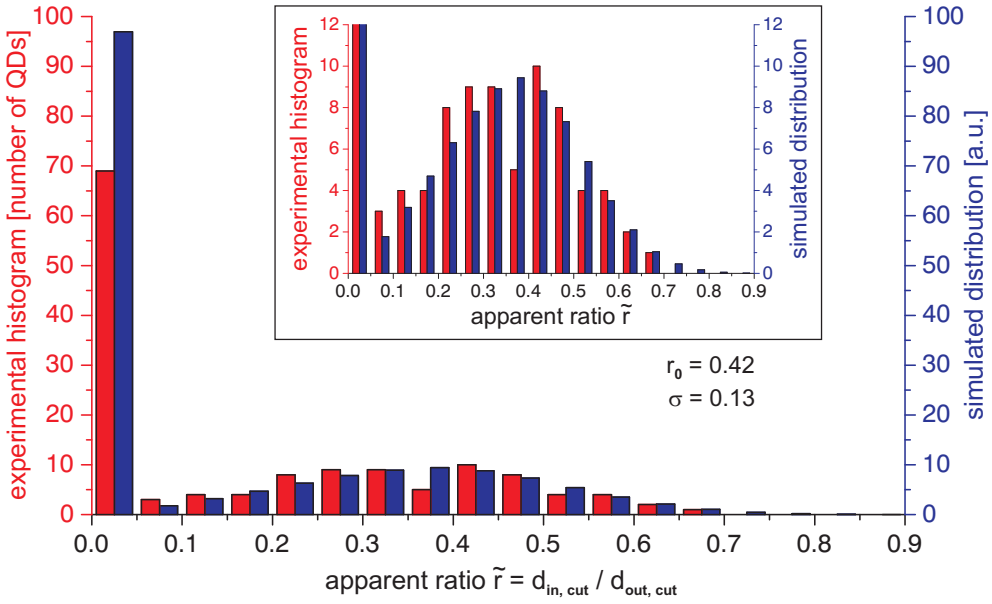

FIGURE 8.7: Distribution of the ratio $\tilde{r}$ of apparent inner to outer ring diameter, obtained from the XSTM images of the QDs in sample C (red column) and by simulation (blue column) using the indicated parameters r_0 and σ. The inset shows a magnification, leaving out the large peak at $\tilde{r} = 0$.

Gaussian distribution of the actual ratio r is assumed with an average value r_0 and a standard deviation σ. Consequently, the calculated distributions of $\tilde{r}$ for various actual ratios r have to be weighted by this Gaussian distribution. Finally, the parameters r_0 and σ are optimized to receive a best fit of the calculated, weighted distribution with the experimental histogram. The details of this procedure, the used algorithms, and the distributions corresponding to the single steps are presented in App. B, while the final result is represented by the blue columns in Fig. 8.7. It should be noted that the ring-shaped QD structures were assumed to have a square outer base with a circular central gap, as shown in Fig. 8.6(b). This assumption is partly based on the observed atomic structure of the QDs, which will be discussed in section 10.1.1. Additionally, it is shown in App. B that the choice of either a square or a circular outer shape of the QDs has only marginal influence on the calculated distribution.

In Fig. 8.7 the experimental histogram and the result of the simulated cleavage distribution are compared. For fitting the simulated distribution of the apparent ratio $\tilde{r} = d_{in,\,cut} \,/\, d_{out,\,cut}$ to the experimental histogram only the values between $\tilde{r} = 0.05$ and $\tilde{r} = 0.9$ were taken into account, corresponding to those structures which show a central gap in the cross section. Indeed, a very good agreement between both distributions can be found here, keeping in mind the small statistical database. But importantly, the peak for $\tilde{r} = 0$, corresponding to the structures with the appearance of a compact QD, has not been considered for fitting but results from the calculated distribution. If the sample contained both compact and ring-shaped QDs, the red peak for $\tilde{r} = 0$ should be significantly higher than the blue one, which is not the case, meaning that all QDs actually have a ring-shaped structure.

The fact that the experimental peak for $\tilde{r} = 0$ misses about 30% of the calculated value may be explained – additionally to the rather large statistical error – by different visibilities of differently cleaved QDs in the XSTM images: In images of lower quality a paired feature, corresponding to a centrally cut QD, is much more distinct and thus much easier to detect than a QD cut at the edge, which results in a more diffuse contrast. Especially when almost the entire QD is cleaved away, the low strain-induced contrast may prevent a detection of this QD. In the other case, when the major part of the QD remains within the sample upon cleavage, its strain distribution increases the XSTM image contrast at both outer parts of the QD image, as shown above, leading to the possible appearance of a paired feature even if the ring-shaped QD is cleaved at the edge.

Beside the fact that all QDs have a ring shape, also the statistical average of the actual inner to outer diameter of this ring can be derived from the simulations, amounting to $r_0 = 0.42$ with a standard deviation of $\sigma = 0.13$.

8.3.3 Dependence on the amount of deposited GaSb material

While the (apparent) ratios of inner to outer diameter of the ring-shaped QDs are nearly the same for all four layers of sample C, the outer shape of the QDs varies between the layers. While the exact atomic structure including the specialities associated with the ring shape will be discussed in more detail in chapter 10, the dependence of the outer QD shape on the amount of deposited material will be investigated in the following.

QD shapes like those displayed in Fig. 8.8(b,c) are typical for layers 2 and 3 and for the majority of the QDs in layer 4, with base lengths varying between about 10 and 20 nm and heights of about 3 to 4 atomic chains or 1.5 to 2.5 nm. For these layers, the QD density increases with the amount of deposited material, but no significant changes of the QD size can be found. The situation is different in the first layer, where smaller and especially very flat QDs were observed, as the one shown in Fig. 8.8(a): The base length of this QD is 15 nm, slightly smaller than for the QDs shown in Fig. 8.8(b,c). But the GaSb material is mainly concentrated in one atomic chain and only in some places extends over a second chain,

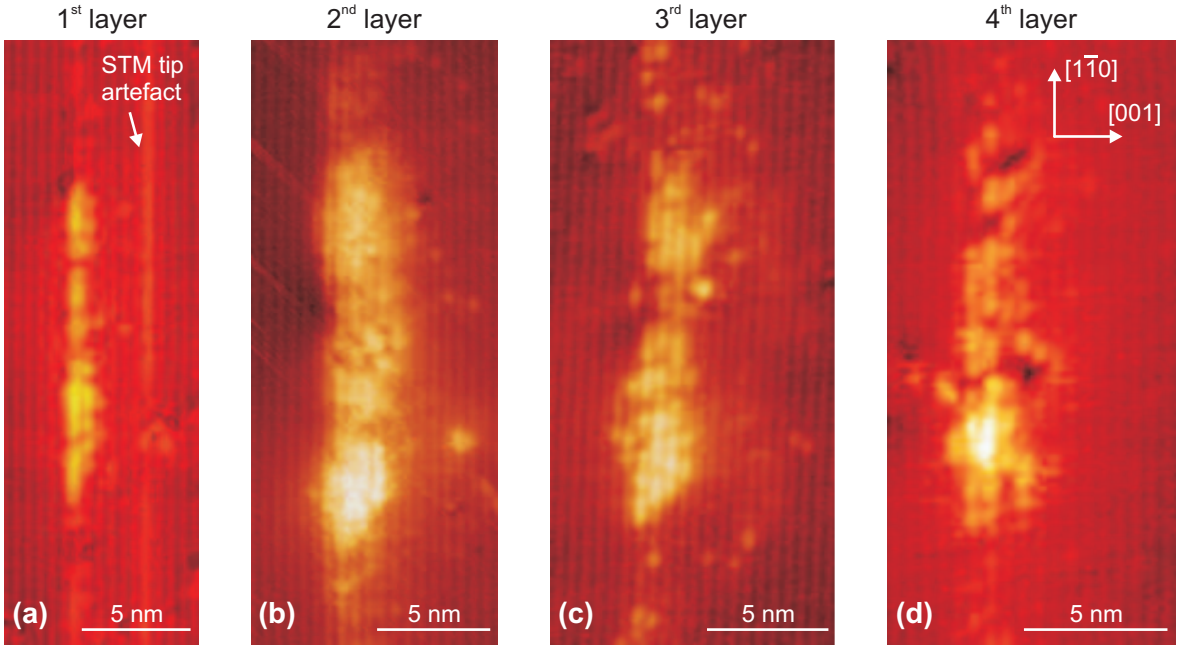

FIGURE 8.8: XSTM filled state images of QDs in layers 1 - 4 of sample C, respectively; acquired at tunneling voltages of (a) V_T = -2.2 V, (b) V_T = -1.7 V, (c) V_T = -2.6 V, and (d) V_T = -2.0 V.

corresponding to a QD height of $\sim$ 1 nm. Again, several segregated Sb atoms can be seen above the QD, while the spotty bright line parallel to one atomic chain is just an artifact, resulting from an adsorbed molecule shifted along one atomic chain by the scanning tip.

In the fourth layer, the observed QDs generally have a similar size to those of layers 2 and 3. However, in some QD structures like the one shown in Fig. 8.8(d), dramatic changes of the image contrast occur over a very small range within the QD. Especially the dark "holes" with a size of two or three atoms cannot be explained by electronic effects but rather represent defects in the crystal lattice. Such defects may have emerged during the cleavage at positions of strongly varying local strain due to a locally strongly varying chemical composition. However, they might also represent actual nanovoids, though being much smaller than those reported recently for the InAs/GaAs material system [127, 132], or they could possibly indicate dislocations within the QD. In the latter case, the large amount of GaSb in the considerably large QD and the corresponding strain would have let to a partial relaxation of the QD. The possibility of dislocations will be further discussed in section 8.7.

For a detailed comparison of the size of the studied QDs in dependence on the layer in which they were observed, and therefore in dependence on the amount of nominally deposited GaSb material, the structural parameters of all observed QDs were statistically analyzed. Although the total number of 140 observed QDs is, as mentioned above, a large value for XSTM experiments, it is still a rather poor statistical database, leading to relatively large errors.

In Table 8.1 the following parameters are given: In layers 1 to 4, corresponding to increasing amounts of nominally deposited GaSb, differently large ranges of the four layers could be investigated, resulting in different numbers of observed QDs. Both for the QD base length and their height, the mean values are given as arithmetic average together with the standard deviation and as median, respectively. While the arithmetic average is the more common statistical parameter, some extraordinary small or large QDs which might be untypical for the corresponding layer have less influence on the median value. Knowing the mean QD size, the QD density was calculated for each layer as described in section 5.2.3. Thereby the range of sight of the XSTM was assumed to be only about the mean QD size, as the possible

layer	GaSb deposited [ML]	scanned range [μm]	QDs found	QD base length average [nm]	QD base length median [nm]	QD height average [nm]	QD height median [nm]	density [10^{10} cm^{-2}]	GaSb in QDs [ML]
1	1.0	5.1	27	12.7 ± 4.1	13.0	1.6 ± 0.3	1.8	4.3 ± 0.8	0.17
2	2.0	4.7	55	16.3 ± 4.9	17.0	2.0 ± 0.3	1.8	7.3 ± 1.0	0.59
3	2.7	3.1	37	15.4 ± 4.3	14.5	2.1 ± 0.4	2.1	8.1 ± 1.3	0.63
4	3.1	1.5	21	15.2 ± 4.0	14.5	2.1 ± 0.3	2.1	9.3 ± 2.0	0.71

TABLE 8.1: Statistical data on structural parameters of QDs observed in layers 1 to 4 of sample C.

detection of completely buried QDs is probably compensated by the number of those QDs cleaved at the edge which were overlooked, as indicated by the results of the simulations discussed above. For each layer, a statistical error of the QD density could be evaluated from the number of observed QDs. Finally, from the QD base length, their height, and their density the total amount of material incorporated within the QDs was calculated, assuming a square QD base, a truncated pyramidal shape with a ratio of top extension to base length of 0.8, and a central circular gap with a diameter of 0.4 times the base length, corresponding to the ring shape analyzed above. Additionally, a chemical composition of the QDs of only 60% GaSb was considered, which will be discussed in chapter 10.1.2. Accordingly not the total QD material but the incorporated GaSb is given in the right column of Table 8.1.

Some key results of the statistical data are visualized in Fig. 8.9, supporting the trends described above: The mean size of the QDs is nearly constant for layers 2 to 4, while significantly smaller QDs are observed in layer 1. Although the QD density increases with the amount of deposited material, only a small fraction of the nominally deposited additional GaSb material gets incorporated into the QDs, especially in layers 3 and 4.

In several XSTM publications it is stated that only the largest values of measured lateral QD extensions may be considered as the actual QD base length, as all smaller values correspond to QDs which are not centrally cut at the cleavage [124, 217]. This is true for QDs with {101}, {102}, or similar side facets, as in this case the rectangular QD bases are cut diagonally. However, if the QDs are characterized by {111} side facets, as it is most probably the case in this sample (see section 10.1.1), the measured lateral extensions could directly be regarded as base length of the corresponding QDs.

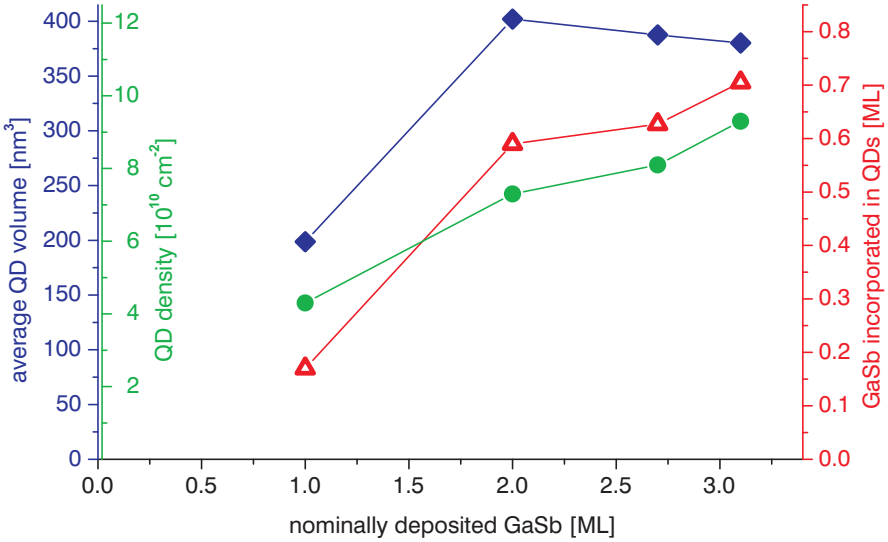

FIGURE 8.9: Dependence of the average QD volume, the QD density, and the amount of GaSb incorporated in the QDs on the nominally deposited material, as obtained from the XSTM images of sample C by statistical analysis.

8.3.4 Shape anisotropy of the QDs

Using XSTM, cross sections through the QDs either along the $[1\bar{1}0]$- or along the [110]-direction can be studied at one time. From literature, the question whether a shape anisotropy of the QD base should be expected or not remains ambigious: There are only a few studies published, characterizing GaSb QDs in top-view geometry, which have sufficient lateral resolution. Among these, the majority of the authors report on an anisotropy, with a ratio of the lengts of side A to side B ranging from 1.2 [44] up to 2.0 [52] and a larger extension in [110]- than in $[\bar{1}10]$-direction [46, 59]. However, also symmetric QD base shapes have been reported for both MOCVD- [51] and MBE-grown [67] GaSb QDs.

To evaluate the symmetry of the base shape, different specimens of sample C have been cleaved in the (110) and in the $(\bar{1}10)$ cleavage surface, respectively. All QD images shown yet stem from the (110) cleavage surface, only because the database on this surface is larger and the STM tips used at this specimen achieved a better lateral resolution, which is a random effect.

Comparing the data obtained from both cleavage surfaces, no systematic differences are evident. The mean values of the measured QD base lengths differ slightly, but these differences are much smaller than the statistical error and have opposite trends for the single layers of the sample. The statistical base of these measurements is too small to observe very small anisotropies, but an asymmetry of more than 20% to 30% between both sides of the QD base can be excluded.

8.4 Quantum dots in sample D

As mentioned above, QDs have also been observed in the second and third layer of sample D; again obtaining images with a rather continuous QD appearance, like those shown in Fig. 8.10(a-c), as well as cross sections of QDs revealing a more or less pronounced central gap, shown in Fig. 8.10(d-g). The database of these QDs is too small to repeat the statistical analysis und simulations performed for sample C. Nevertheless, the amount of QD cross sections with and without central gap is nearly the same also in both layers of sample D, respectively, so it can be concluded that probably all QDs of sample D are ring-shaped, too. The ratio of apparent inner to outer diameter varies rather strongly for the ring structures in sample D, ranging from rings that are nearly filled but have a significantly lower contrast and thus a lower GaSb stoichiometry in the central region [Fig. 8.10(d,e)] up to structures with a very large central gap, like the one shown in Fig. 8.10(g).

Especially the QDs in layer 2 appear to be rather small, with an inhomogeneous and weak image contrast. Two representative QDs of this layer are shown in Fig. 8.10(a,d), extending laterally over only 10 nm and 12 nm, respectively. Only at some regions of the QDs their height exceeds one atomic chain, extending here over a second chain or about 1.2 nm in total. The image contrast varies strongly within these QDs, indicating a low average GaSb composition with only some regions of higher GaSb content.

For QDs in layer 3 lateral extensions of about 20 nm are typical [Fig. 8.10(b,e,f)], but also large structures with up to 30 nm like the one shown in Fig. 8.10(g) have been observed. Nevertheless, also in most of these QDs the GaSb is mainly concentrated at one atomic chain, and only some regions of the QDs reach a height of two or three chains. The image contrast of most QDs in layer 3 is stronger and more homogeneous than in layer 2, standing for a higher average GaSb content, as it can be seen in Fig. 8.10(b,e-g). Additionally to such flat, but rather continuous ring-shaped QDs, also GaSb structures like the one shown in Fig. 8.10(c) were observed, having a different appearance: No well-defined three-dimensional structure

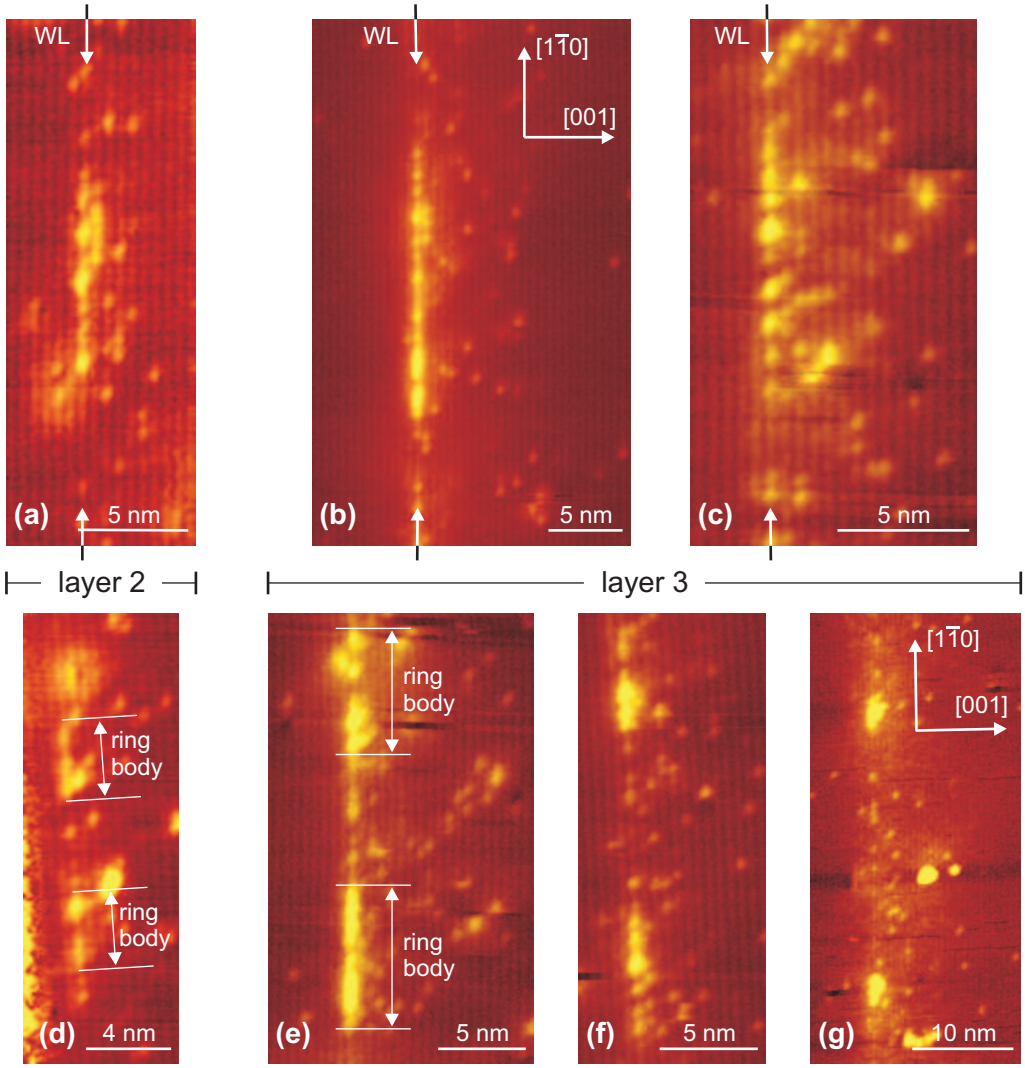

FIGURE 8.10: XSTM images of ring-shaped QDs in sample D, cleaved through (a-c) the ring body and (d-g) through the central gap: (a,d) Small GaSb QDs in layer 2, (b,c,e-g) GaSb QDs in layer 3. The images were acquired at (a,b,d) V_T = -2.4 V, (c,e,f) V_T = -2.1 V, and (g) V_T = -3.0 V.

can be determined here, but an agglomeration of individual Sb atoms is found over about 11 nm within the WL, leading to a locally increased image contrast, which – with decreasing Sb content – also extends to the first and second atomic chain above. It cannot exactly be said whether this structure is a diluted QD or a density fluctuation of the WL strongly segregating in growth direction. Generally, strong Sb segregation is evident for all QDs in sample D, as all images show many individual Sb atoms incorporated in the GaAs matrix above the QDs.

The structural results obtained from the XSTM images of representative QDs are also confirmed by statistical data of all QDs observed in sample D, although it should be kept in mind that the database is relatively small especially for layer 2. The QD density was evaluated to $3.8 \pm 1.9 \times 10^{10}$ cm^{-2} in layer 2 and $5.1 \pm 1.2 \times 10^{10}$ cm^{-2} in layer 3, with average base lengths of 14.6 ± 6.7 nm and 18.8 ± 6.4 nm as well as heights of 1.2 ± 0.2 nm and 1.3 ± 0.4 nm for QDs in layers 2 and 3, respectively.

Comparing the QD structures of sample D with those of layers 1 and 2 in sample C, which have nominally the same amount of deposited GaSb, the QD densities and base lengths

are found to be similar, while the very small heights of the QDs in sample D have to be emphasized. In most QD structures the height does not exceed two atomic chains, with the GaSb content being concentrated to the bottom chain. Additionally, the QDs in layer 2 of sample D are characterized by a varying and in average rather low GaSb content.

8.5 Wetting layers

In both samples the GaSb QDs are embedded within wetting layers. On a nm scale these WLs generally exhibit a rather inhomogeneous and even discontinuous structure, as can be seen in Figs. 8.11 and 8.13. At atomic resolution the WLs have a spotty appearance, representing individual Sb atoms within a more As-dominated intermixed GaSbAs material, and strong Sb segregation is evident above all WLs. Sb-free gaps within the WLs of several nm lateral extension can be recognized, consisting of pure GaAs. Beside this general behavior, also structural differences between the individual layers of both samples are obtained.

Figure 8.11 shows XSTM images of the four WLs of sample C, with nominal amounts of deposited GaSb of 1.0 ML, 2.0 ML, 2.7 ML, and 3.1 ML, respectively. The resolution and image quality of Fig. 8.11(b) falls behind those of the other three images, but this is attributed to the varying tip condition. Regarding the structure of the WLs, however, layer 1, shown in Fig. 8.11(a), is outstanding: Here the total amount of incorporated Sb is significantly smaller than in the other three layers. The WL itself is strictly limited to one atomic chain, containing large gaps. An image contrast hardly exceeding that of single segregated Sb atoms underlines the low Sb stoichiometry of the WL. Although the image contrast is not significantly larger in the other three WLs, too, those layers have a larger vertical extension, as can be seen in Fig. 8.11(b-d). Intermixed WLs of about two, sometimes three atomic chains height show a smooth transition into a region of strong segregation, extending over about 10 nm with a declining amount of incorporated Sb atoms.

In order to study the chemical composition quantitatively, the local lattice constants for all four WLs of sample C were evaluated, as described in detail in chapter 6. The results are

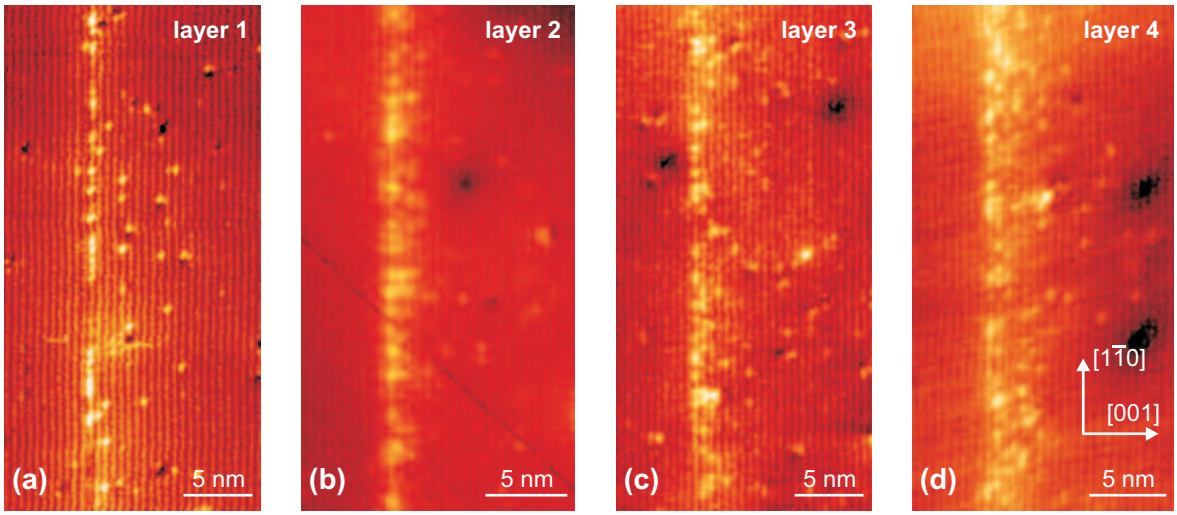

FIGURE 8.11: XSTM filled state images of the GaSb WLs in layers 1 to 4, respectively, of sample C, acquired at (a) V_T = -2.5 V, (b) V_T = -2.0 V, (c) V_T = -1.9 V, and (d) V_T = -2.0 V. The small dark holes visible in (a) are atomic vacancies within the cleavage surface, while the larger dark depressions present in (b-d) represent charged atoms like dopands, contaminants or antisite lattice defects. The diagonal dark line in image (b) is a deficient STM scanline.

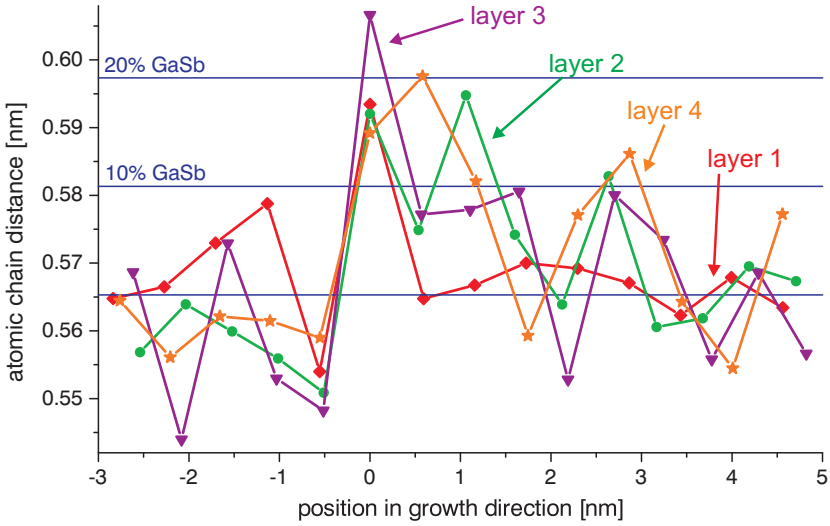

FIGURE 8.12: Analysis of the chemical composition of the WLs in sample C.

plotted in Fig. 8.12: In accordance with the weak image contrast, typical GaSb contents of the WLs of only 10% to 20% are derived for the rather continuous, gap-free regions. The WL of layer 1 is indeed restricted to one atomic chain, while at the other three WLs the lattice constant is increased over several chains. Although the data are averaged over the results of several XSTM images, respectively, a noise in the range of 0.01 to 0.02 nm, corresponding to ±10% GaSb, could not be avoided for layers 2 to 4. Therefore the exact course of the curves and especially a comparison of individual data points for WLs 2, 3, and 4 is not that significant. However, a WL height of about two to four atomic chains or 1 to 2 nm, a WL GaSb composition decaying in growth direction with a maximum of about 20%, and a measurable amount of segregated and incorporated Sb atoms above the actual WLs can be derived from the chain distance analysis as common trends for layers 2, 3, and 4. From this, the total amount of incorporated antimony can be estimated to about 0.3 ML in layer 1 and 0.9 ML in layers 2 to 4, respectively. Thereby differences of less than 0.06 ML are found between layers 2 to 4, which is below the resolution of the chain distance analysis of about 0.1 ML, although Fig. 8.11(b-d) gives the impression of a slight increase.

While the principal appearance of the WLs in sample C is similar to those in sample D, the latter contain even less GaSb. Figure 8.13(a) shows layer 2 of sample D, nominally containing 1 ML GaSb. Again a thin WL and segregated Sb atoms above can be seen, but this WL consists more of totally Sb-free gaps than of the actual GaSbAs layer itself. Thus, this layer does hardly fulfill the definition of a wetting layer any more. In layer 3 of sample D, shown in Fig. 8.13(b), the gaps are much smaller than in layer 2, and more segregated Sb can be found above the WL, too. However, although 2.0 ML GaSb were nominally deposited at this layer, the WL itself is mainly concentrated to only one atomic chain, and the total amount of incorporated Sb is significantly smaller than in the corresponding layer of sample C. The chain distances cannot be evaluated quantitatively for the WLs of sample D due to the low GaSb content, the strong Sb segregation, and the weak image quality, but the total amount of GaSb within the WL of layer 3 can be estimated to be less than 0.5 ML.

Comparing the WLs of both MBE-grown samples with the MOCVD structures, clear trends are evident: The MOCVD-grown WLs and QWs are more sharply defined, with a GaSb content of up to 50% but a vertical extension of only one to two atomic chains, as discussed in chapter 7.2. Hardly any segregated Sb atoms can be found above the MOCVD-grown layers. The broadened and more intermixed WLs and the strong segregation above the layers within the MBE-grown samples indicate a higher mobility of the antimony during the MBE process.

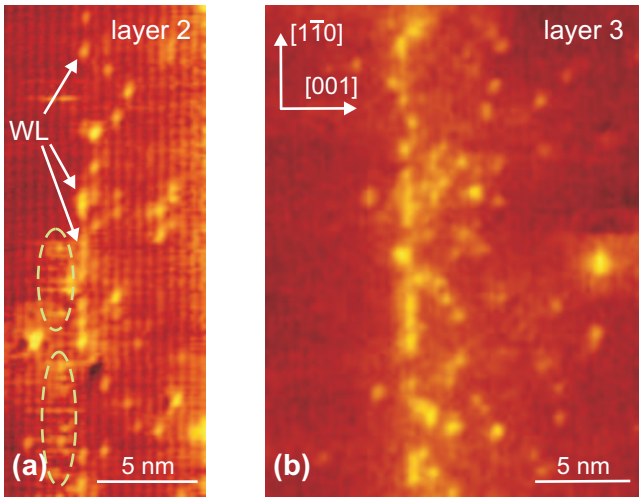

FIGURE 8.13: XSTM filled state images of the GaSb WLs of sample D: (a) Layer 2, acquired at V_T = -2.4 V, (b) layer 3, acquired at V_T = -2.1 V. The streaky spots in the lower left part of image (a), marked by green dashed ellipses, are STM tip artifacts.

Gaps within the WLs, while varying in size and density for the different layers, are observed in all GaSb samples. For MOCVD growth, as explained in section 7.1, these gaps indicate a 2D island growth mode of GaSb. In MBE, the strategy of a soaking layer leads to a more complex situation, as will be discussed in detail in sections 9.2 and 10.3. Nevertheless, the observed gaps, which are unique and typical for the GaSb/GaAs material system, seem to indicate a similar kind of 2D island growth also for MBE.

8.6 Optical results

In order to be able to supplement the structural data with optical results, two reference samples have additionally been grown of layer 2 and 3 in sample D, using identical growth parameters in the same MBE machine but optimizing the sample structure for optical measurements. Thus undoped GaAs substrates have been used, no AlGaAs barriers and a thinner GaAs cap layer without doping have been grown, and each reference sample contains only one GaSb layer, in contrast to the XSTM sample structure shown in Fig. 8.1. Both reference samples were studied using optical spectroscopy by Till Warming in the group of D. Bimberg.

8.6.1 Optically active QDs in sample D

Figure 8.14(a,b) shows photoluminescence (PL) and photoluminescence excitation (PLE) spectra, taken at a temperature of 7 K with moderate excitation densities, for the sample corresponding to layer 3 of sample D: In the PL spectrum, three peaks are evident and can be related to luminescence from the GaAs bulk, the GaSb WL, and from GaSb QDs. The GaAs peak is located at 1.49 eV, close to the literature value of the GaAs band gap of 1.52 eV (the small discrepancy can be explained by the GaAs electron-hole recombination energy being slightly reduced by the exciton binding energy or by defects located slightly within the bandgap). Nearly the double PL intensity is arising from the GaSb WL, exhibiting a rather narrow peak with a full width of half maximum (FWHM) of about 35 meV and a maximum at 1.38 eV. This WL peak shape indicates a relatively high electron-hole recombination probability and agrees well with the rather compact structure of the corresponding WL observed by XSTM in sample D, appearing as a thin layer with only small gaps, as shown in Fig. 8.13(b). The QD peak is significantly lower and broader, showing a FWHM of about 130 meV and a maximum at 1.11 eV (or 1119 nm). The broadness confirms the large size distribution of the QDs in layer 3 of sample D discussed above, which is characterized by an

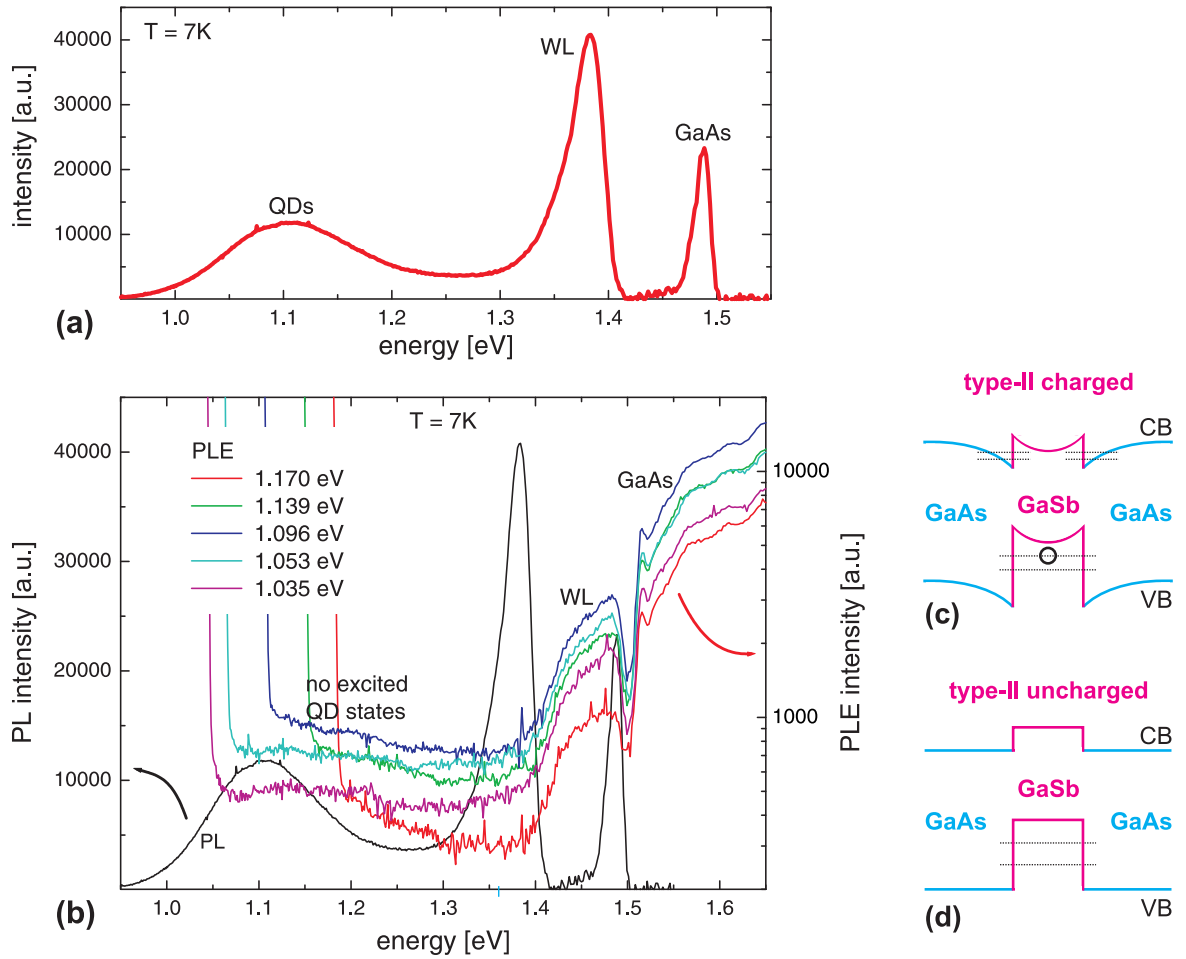

FIGURE 8.14: Low-temperature optical characterization of the 2 ML reference sample, corresponding to layer 3 of sample D: (a) PL spectrum, (b) PL spectrum (black, left axis) together with different PLE spectra (colors, right axis) with the respective detection energies indicated. The corresponding band alignment of the GaSb/GaAs QDs is sketched schematically for (c) PL and for (d) PLE spectroscopy.

average base length of 18.8 ± 6.4 nm. Additionally, the rather small intensity of the QD peak compared with other material systems is also expected because of the type-II band alignment of the QDs.

While the WL PL peak position of 1.38 eV at this MBE-grown sample is similar to that of the MOCVD-grown sample amounting to 1.37 eV, as discussed in section 5.3.1, the QD peaks of 1.20 eV for the MOCVD QDs and 1.11 eV at the MBE sample differ considerably, resulting in an increased energetical distance of 0.27 eV between the WL and the QD peak at the MBE structures. Thus, the MBE QDs studied here have a clearly larger electronic confinement than the MOCVD QDs shown above, in agreement with their larger base lengths, independent of the ring-shaped structure. Comparing these PL data with published values on other MBE-grown GaSb QDs [44, 45, 47, 48, 55, 56, 58–60, 69, 256], the WL peak energy observed here is relatively large, as the literature values vary between 1.23 eV and 1.41 eV. This indicates a comparatively small electronic confinement in the WL studied here, agreeing well with the small amount of incorporated GaSb. However, the QD PL peak measured at 1.11 eV lies well within the very small range of 1.09 to 1.14 eV which includes most published values [44, 45, 47, 48, 58, 59, 69, 256]. This result is astonishing, as the reported QD structures corresponding to those PL energies are much larger than the QDs observed

here. A possible explanation might be that most of the authors have measured the sizes of their QDs *ex-situ* in top-view geometry on free-standing QDs [48, 58, 69, 256], so that any shape transitions upon overgrowth are not considered, though all PL results are taken at capped QDs, as also the XSTM data.

Following the PL measurements, also PLE spectra were taken from the reference sample of 2 ML, shown in Fig. 8.14(b). Using PLE, electron-hole pairs are excited resonantly with a varying excitation energy, while the detection energy is held fixed. Here, five different detection energies were chosen which all lie within the PL peak of the GaSb QDs, obtaining a strong GaAs bulk signal and a weaker signal corresponding to excited WL states (please note the logarithmic scale of the PLE intensity axis). The energy difference of 0.05 to 0.1 eV between the PL peak and the PLE shoulder of the WL is partly due to the excited states contributing to the PLE signal and additionally given by the Stokes-shift between emission and absorption states [378].

Astonishingly, no excited QD states could be observed, only a very small and broad increase of the PLE signal for energies smaller than 1.3 eV can be seen. This means that electron-hole pairs can relax from the GaAs matrix or from excited WL states to the GaSb QD ground state and recombine there, but that it seems to be hardly possible to directly create excited QD electron-hole pairs. In other QD material systems like InAs/GaAs clear peaks of excited QD states would be expected, and the actual existence of QDs in this reference sample was proven before by PL, therefore the lack of excited QD states in the PLE spectra is not completely understood yet. In literature, many PL data on GaSb/GaAs QDs can be found [44, 45, 49, 51, 54–56, 59, 64–66, 69, 71, 73–76, 263–265], but only two PLE studies are known to me [47, 255], also revealing only a very weak QD PLE signal.

One idea to partly explain the lack of a clear QD signal in PLE spectroscopy is sketched in Fig. 8.14(c,d): As mentioned in section 2.4.1, the staggered type-II band alignment provides a strong confinement of holes in the GaSb nanostructures, but the weak electron confinement in the surrounding GaAs matrix is only created by the Coulomb attraction of previously captured holes. The situation of PL spectroscopy with excitation energies larger than the matrix bandgap comprises partly filled QDs and thus the existence of confined states for both electrons and holes, as displayed in Fig. 8.14(c). Using PLE spectroscopy at low temperature, however, excited electron-hole pairs are generated resonantly, so in the initial state the GaSb QD is uncharged, as sketched in Fig. 8.14(d), and confined electron states do not exist. As a consequence, the resulting PLE response at energies slightly above the QD PL peak is broad and unstructured due to the lack of electron confinement, and the small overlap of electron and hole wavefunction results in the weak signal. Both observations then could be regarded as an indication of a type-II band alignment.

In order to conclude the optical measurements on the 2 ML reference sample, corresponding to layer 3 of sample D, two main results need to be emphasized: Firstly, in spite of their small size and especially small height, the QDs exhibit a relatively large hole confinement. Secondly, although these QDs are strongly intermixed, the PLE signal differs significantly from that of type-I QDs and gives evidence of a type-II band alignment.

8.6.2 Optically inactive small islands in sample D

The other reference sample, corresponding to the second layer of sample D with nominally 1 ML deposited GaSb, was likewise studied by PL spectroscopy. However, although the GaAs peak and a WL signal were observed, no photoluminescence could be obtained from QDs at all, even at increased laser excitation densities. From this lack of QD signal, it has to be concluded that the small 3D structures obtained in layer 2 of sample D, which have also been called QDs above in a structural point of view, do actually not exhibit any zero-dimensionally

confined QD states.

Comparatively little statistical data exist for these structures, but they have base lengths of about 15 nm and a height of about 1.2 nm, accompanied by a very Sb-poor stoichiometry. Considering that the QDs in layer 3 of the same sample show a rather strong electronic confinement in spite of their very flat shape, and that the optically active MOCVD-grown QDs in sample A (see chapter 5) are also very small with base lengths of less than 10 nm and heights of up to 2 nm, the low GaSb content of the small islands in layer 2 of sample D seems to be the reason for the lack of electronic QD confinement rather than their size.

8.6.3 Optical results on QDs in sample C

For the MBE-grown QD layers in sample C no reference samples exist. Nevertheless, optical measurements were performed using the XSTM sample with its complex structure (see Fig. 8.1). Thus, a rather weak PL intensity was expected due to the thick cap layer, several AlGaAs layers and the use of a doped wafer, as well as a possibly blurred superposition of the different WL and QD signals. However, hardly any PL signal related to GaSb was obtained: Even with very high laser excitation densities, beside a strong GaAs bulk luminescence only a very small GaSb WL signal (about 1000 times smaller than in the reference samples of sample D) and no GaSb QD signal at all could be measured.

The reason for this behavior is not yet clear. Of course a large fraction of the exciting laser power gets absorbed within the more than 1 μm thick GaAs and AlGaAs layers above the GaSb nanostructures, nevertheless a sufficient amount of light should still reach the embedded GaSb layers. Another explanation would be the dominance of non-radiative recombination. Dislocations within QDs are such centers of non-radiative recombination, so a significantly high percentage of spatially relaxed QDs or a strong occurence of other kinds of dislocations within the GaSb layers would explain why nearly no luminescence from these layers can be obtained.

8.7 Dislocations

Dislocations are line defects within the crystal. They can reduce strain, influence the charge carrier transport, and act as centers of non-radiative electron-hole recombination [2, 3, 9, 26]. Usually, the growth of coherently strained QDs is limited by plastic relaxation building dislocations (see also section 2.2.1), which inhibits any optical activity of the QD.

Figure 8.15(a) shows a dislocation line which emerges at the edge of a QD of the third layer of sample C, having a relatively large base length of about 30 nm. The dislocation proceeds most probably along the [112]-direction (with a measured angle towards the WL of about 50°), disrupting the GaAs atomic chains, and ends after about 17 nm. However, this dislocation line is the only one found within the whole investigated scan range of more than 14 μm. Therefore, this kind of crystal defect is quite rare within the sample and seems to be related to the exceptionally large size of the QD beside which it is located. No similar structure has been observed in sample D.

While a considerable number of dislocations running through the GaAs matrix around the GaSb nanostructures can thus be excluded, the existence or absence of dislocations restricted within the QDs is more difficult to verify. Cross-sectional transmission electron microscopy images of free-standing GaSb/GaAs QDs grown under similar conditions and in the same MBE chamber as sample C show a large number of misfit dislocations within the QDs, arising at their bottom interface to the GaAs matrix. An example of these images, acquired by Ganesh Balakrishnan in Albuquerque, New Mexico, USA, is shown in Fig. 8.15(b): From

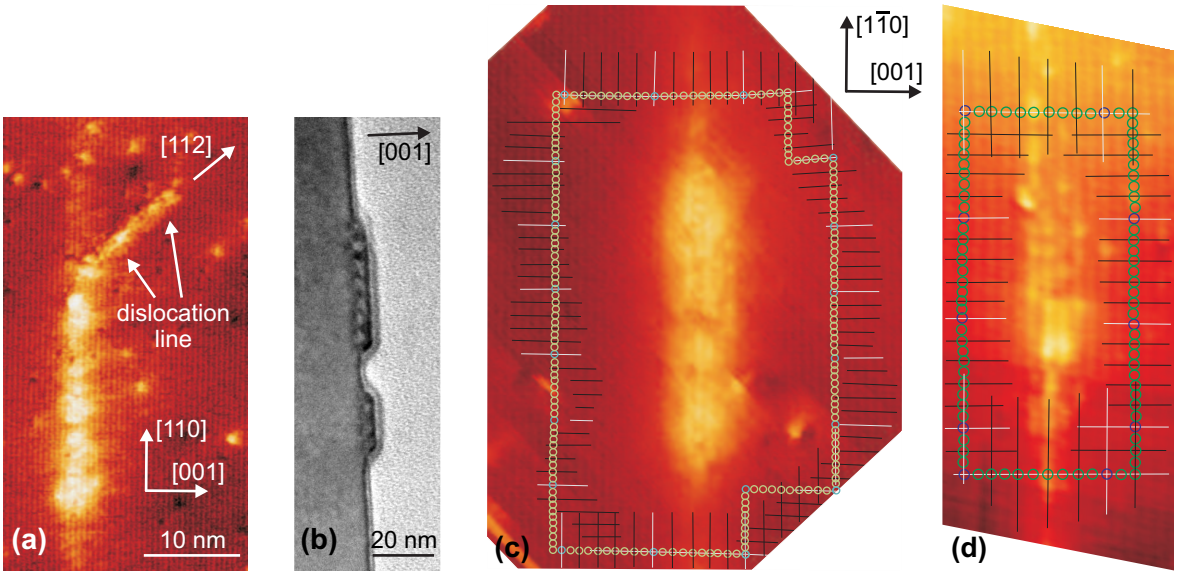

FIGURE 8.15: (a) XSTM image of a dislocation line near a QD in the layer 3 of sample C, acquired at V_T = -2.1 V. (b) TEM image of free-standing GaSb QDs on GaAs, showing misfit dislocations. (c,d) Evaluation of Burgers vectors in XSTM images of QDs in the layer 2 of sample C, acquired at (c) V_T = +1.8 V and (d) V_T = -2.6 V: No dislocations are contained within these QDs.

left to right, the GaAs matrix, the GaSb WL and two QDs, a thin oxide layer, and a bright image background can be seen. However, the two QDs are rather large with base lengths of 45 and 25 nm, respectively, and cannot directly be compared with the capped QDs studied in this work: Although they have been initially grown under similar conditions, the QDs for the TEM sample had to be cooled down without being capped, and during this cooling the monitoring RHEED signal changed dramatically, indicating drastic changes of the QD morphology. This behavior is a nice example that care has to be taken when comparing results from different characterization methods.

So the question remains, whether the existence of dislocations within the QDs can be decided using the XSTM images. If a misfit dislocation arised within the QD due to the lattice mismatch between GaAs and GaSb, it would modify the atomic positions in such a way that two paths of the same nominal length along atomic chains underneath and above the QD would contain different numbers of atoms. This is a simplified description of characterizing the dislocation by its Burgers vector [26, 379]. The Burgers vector can be analyzed from an XSTM image with atomic resolution in x and y by considering a loop around the QD consisting of lines along the [1$\bar{1}$0]- and the [001]-direction and counting the atoms of this loop at each side of the QD. This procedure has been exercised for five QDs of sample C which could have been imaged with sufficient atomic resolution, and in all cases the number of atoms underneath and above the QD is the same, meaning that no Burgers vector exists and no dislocation is contained within the QD. Two examples of this procedure are displayed in Fig. 8.15, for a QD with a rather homogeneous (c) and even with a rather inhomogeneous image contrast (d).

Due to the limited resolution of the XSTM images this procedure could not be repeated for other QDs, especially not for any one in layer 4 of sample C, in which some larger QDs with a locally strongly varying image contrast were observed (see section 8.3.3). Therefore, the existence of dislocations cannot completely be excluded, especially not for this layer 4. However, at least the large majority of QDs is definitely free of dislocations and is coherently strained.

Chapter 9

Sb segregation and atomic exchange processes

Having studied the GaSb nanostructures in the MBE-grown samples C and D and knowing many structural results about WLs and ring-shaped QDs, the self-assembled formation of these structures remains as key question. Before the details of the atomic QD shapes and possible growth mechanisms of the ring structures can be discussed (see chapter 10), some underlying physical effects taking place upon growth and especially overgrowth of GaSb/GaAs nanostructures will be focused on in this chapter. It will be shown that segregation, diffusion, and atomic exchange processes, which occur in nearly all III-V heterostructures, are of strongly increased importance for the GaSb/GaAs material system, especially at the atomic interfaces. In order to analyse such exchange and segregation processes from the XSTM data, first the involved XSTM imaging mechanisms, taking place on the atomic scale, need to be understood.

9.1 XSTM imaging of Sb atoms in GaAs

A good example of the relevance of the tunneling polarity on the information available in XSTM images is given in Fig. 9.1: All six images show the same GaSb QD or a part of it, but the three images on the left hand side were taken with negative sample voltages, while the images on the right hand side were acquired at positive polarity. At negative sample bias the image is sensitive for group-V atoms, thus Sb and As can be distinguished at the atomic level, whereas at positive sample bias the Ga atoms are imaged. As a consequence, individual Sb atoms can be seen within the chains of As atoms and in the intermixed QD in Fig. 9.1(a), while in Fig. 9.1(b) the QD appears rather homogeneous: Here, with a positive bias, the structural contrast dominates which is mainly given by outward relaxation of the QD and therewidth by its strain. The different appearance is even more pronounced at the WL, which appears as a broadened, diffuse stripe at positive sample voltage, whereas at negative voltage the inhomogeneous atomic structure of the intermixed layer can be seen. It should be noted that both images show atomic resolution in [001]- and $[1\bar{1}0]$-direction [which gets more apparent in Fig. 9.1(c-f)], so the less pronounced appearance of the nanostructures in Fig. 9.1(b) is not due to image quality.

As a final consequence of polarity dependence, the segregated Sb atoms which can clearly be seen above the WL and the QD in Fig. 9.1(a) cannot be found at all in (b). To further study this effect, a small part of the images is shown with larger magnification in (c) and (e). Here, the image contrast has been adjusted to the individual Sb atoms within the GaAs matrix, thus the strained QD containing much GaSb material is outshined and appears

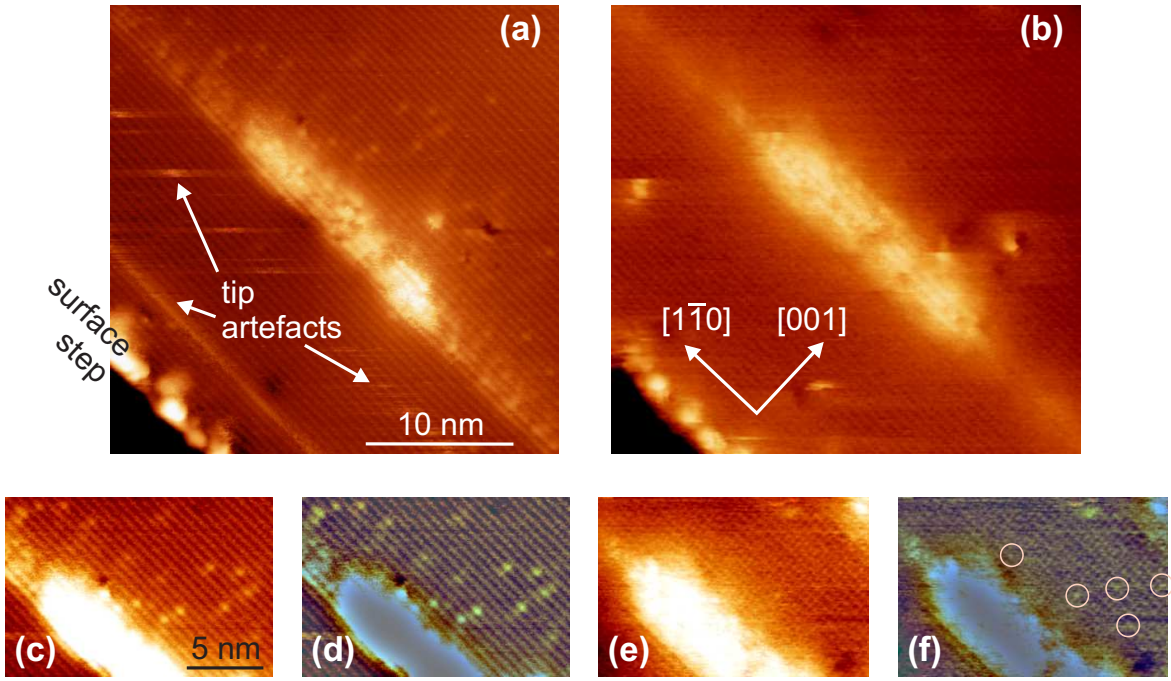

FIGURE 9.1: XSTM images of the same GaSb QD, observed in layer 2 of sample C: (a,c,d) filled state images, acquired at V_T = -1.7 V, (b,e,f) empty state images, acquired at (b) V_T = +1.8 V and (e,f) V_T = +1.7 V. In (d) and (f) the image background is subtracted to highlight individual Sb atoms. Some Sb atoms are marked in (f) by circles.

completely white. Additionally, the slowly varying image background has been subtracted in Fig. 9.1(d,f) to further pronounce short-range differences in the image contrast, highlighting individual atoms. As a result, several single Sb atoms within the GaAs matrix can clearly be seen in (c) and (d), corresponding to negative sample voltage. However, in (e) and (f) with positive bias, only a few Sb atoms can be found above the QD, marked by small circles in (f), giving a very small image contrast. The bright spots in the upper right corner are too large to represent single atoms and are probably adsorbates on the cleavage surface. Additionally, the positions of the Sb atoms in (e) and (f) are not correlated to those in (c) and (d), so that different atoms have been imaged.

In order to understand this appearance, the atomic structure of the zinkblende crystal at the (110) cleavage surface, consisting of GaAs and single Sb atoms, has to be considered, as sketched in Fig. 9.2. The relaxed and buckled (110) surface is characterized by GaAs atomic zigzag chains of alternating height. Using STM at common tunneling conditions, either the Ga or the As atoms of the upper rows are imaged, depending on the polarity, so only each second ML in [001]-direction is visible [106]. For an Sb atom (1) directly within the topmost (110) plane, the buckling is slightly larger than for an As atom, because its atomic radius and the bond lengths to the neighboring Ga atoms are larger. The Sb atom protrudes geometrically about 6 pm further out of the cleavage surface than the As atoms, according to Kim et al. [380]. Thus, its filled dangling bond is closer to the STM tip, leading to an increased tunneling current at negative sample voltage. The tunneling probability is additionally locally enhanced for this polarity at low absolute voltages due to the electronic properties of antimony compared with arsenic. However, the Ga atoms and especially their empty dangling bonds are hardly influenced by the adjacent Sb atoms in the topmost plane. Furthermore, the small CB offset leads to negligible electronic differences. Thus, at positive tunneling voltage, no sign of these Sb atoms can be found in the STM images.

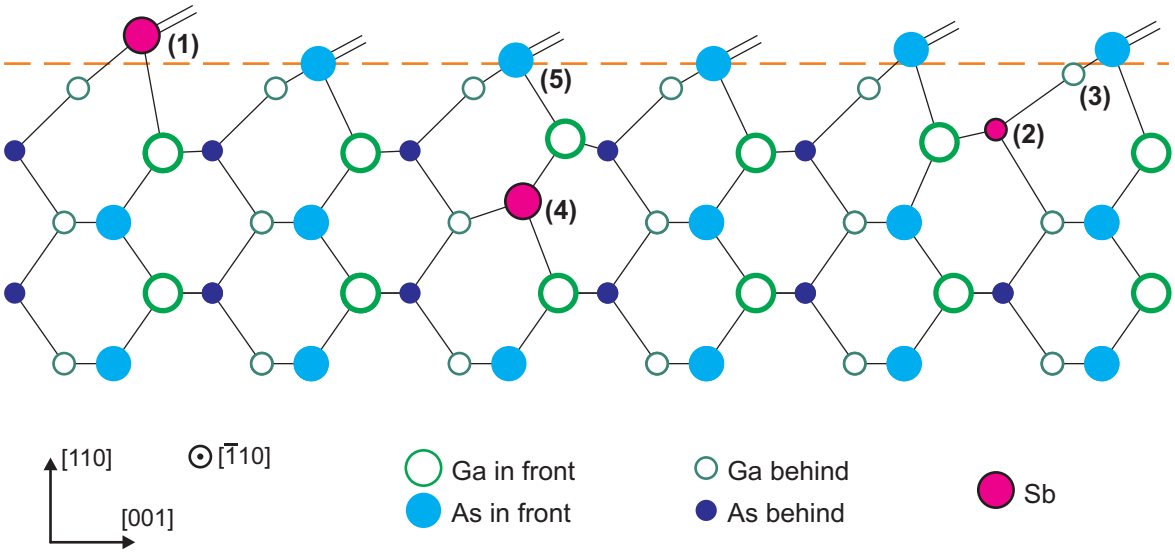

FIGURE 9.2: Side-view of the buckled GaAs(110) surface, containing single Sb atoms in the first, second, and third atomic layer. The position in [110]-direction of the undisturbed As surface atoms is indicated. The shifts of the atomic positions due to the Sb atoms are not drawn to scale.

A different situation occurs for an Sb atom (2) in the subsurface (110) plane. This atom cannot directly be imaged, but its larger size and bond length shifts the neighboring Ga atoms, which in turn slightly shift the As atoms beside. As a result, at the position of the subsurface Sb atom, one surface Ga atom (3) and also four surface As atoms are protruding slightly further out of the cleavage surface than without Sb. Consequently, in filled state images the tunneling current should be slightly increased over a region of four As atoms (which can hardly be seen in the images due to the dominant contrast of the individual surface Sb atoms), while in empty-state images the current is increased at one Ga atom (3) bonded to the subsurface Sb atom. Thus, the existence of this second layer Sb atom can also be observed in STM images taken with positive voltage, originally sensitive to group-III atoms. This effect is responsible for the appearance of Fig. 9.1(e,f) described above: The structural contrast due to some second layer Sb atoms can weakly be seen in the images, but this contrast is significantly lower than the combination of structural and electronic contrast associated with the top layer Sb atoms in Fig. 9.1(c,d). As atoms of different planes are imaged, the absence of any correlation between the Sb positions in (c,d) and (e,f) can now well be understood.

According to the crystal structure, even Sb atoms within the third (110) plane can weakly influence the geometry of the cleavage surface: As can be seen in Fig. 9.2, the size and bond length of such an Sb atom (4) slightly raises the surface As atom (5) directly above. Thus, third layer Sb atoms could principally be seen in STM images with negative sample voltage. The inverse case of a third layer As atom within a GaSb matrix has been observed as a slight depression by Steinshnider et al. [381], but in that case an extremely good image quality and surface flatness supported the observability of this weak contrast difference. Nitrogen atoms, another group-V element, in a GaAs matrix generate a clearly larger dark image contrast, so that even third layer N atoms can clearly be seen in XSTM images [298, 382]. This is due to stronger variations within the atomic structure: While the As and Sb atomic radii amount to 124.5 pm and 145 pm, respectively, N atoms have a radius of only 71 pm [371].

For analysing the amount of segregated Sb atoms, it is important to know whether all Sb atoms observed in a filled state XSTM image are located within the first (110) plane, or

whether also the second and third layer have to be considered. The Sb atoms in Fig. 9.1(c,d) exhibit strong variations of their image contrast, which could indicate an origin from different layers. However, the images have been acquired at negative sample voltages and the increased contrast is concentrated to single atoms instead of groups of four, so that Sb atoms from the second layer can be excluded. Additionally, the geometric contrast due to second layer Sb atoms is already very small, as can be seen at the empty state images (e,f), and therefore the contrast of third layer Sb atoms should be expected to be even smaller and not resolvable in the images shown here. Several XSTM studies are reported which clearly observed first layer Sb atoms in GaAs [380, 381, 383, 384], partly with excellent image quality over large areas [385–387], but to my knowledge no clear evidence of third layer Sb is given.

The situation is similar for the InAs/GaAs system: With 260 pm the InAs bond length comes very close to the GaSb bond length of 262 pm, with the GaAs bond length amounting to 242 pm [380]. The appearance of first and second layer In in GaAs was studied in detail [372], but it is assumed by several authors that all In atoms observed in group-III sensitive XSTM images belong to the cleavage surface, and the third layer is not considered [97, 217, 373, 388].

In conclusion, from comparison with literature data and especially from considering the very small geometrical effects of subsurface antimony, in the following all Sb atoms observed in a GaAs matrix in filled state XSTM images will be assumed to belong directly to the (110) cleavage surface.

9.2 Soaking and group-V-exchange

9.2.1 Soaking of growth surfaces

Self-assembled III-V semiconductor heterostructures are usually grown using group-V surplus, meaning that during epitaxy more group-V atoms are offered than can be incorporated, so that growth is controlled by the parameters regarding the group-III elements. Thus, an abrupt change between group-III atoms like In and Ga is much more easy to realize than between group-V atoms like As and Sb (see section 2.2.2). Additionally to the interface quality, also the stoichiometry of nanostructures formed upon deposition of nominally pure GaSb can strongly be influenced by an arsenic background during GaSb epitaxy, which to some extend was already observed for the MOCVD-grown structures (see section 7.2).

Besides these more technical aspects related to the growth of III-V heterostructures, interfaces between GaSb and GaAs are also different from those between InAs and GaAs for more fundamental physical reasons: Interfaces with a common group-V atom, like InAs and GaAs, are influenced by group-III surface segregation, while interfaces with a common group-III atom, as it is the case for GaSb and GaAs, are dominated by group-V exchange reactions [50, 84, 389], leading to strong As-Sb intermixing [69].

These different effects have intensively been studied on InAs-GaSb superlattices, also by using XSTM [308, 384, 385, 390]. In this system, also the effect of Sb soaking was investigated, meaning the exposure of an InAs layer to an Sb flux: Already in 1993, Wang et al. observed an Sb-for-As exchange at the InAs growth surface upon soaking, saturating at an amount of about 1 ML, as measured with x-ray photoelectron spectroscopy [391, 392].

This concept of Sb soaking has been adopted to the growth of GaSb nanostructures on GaAs, too, in order to produce a sharp GaSb/GaAs interface and to decrease the arsenic background in the MBE reactor prior to GaSb deposition, leading to stoichiometrically purer nanostructures [44, 55, 59, 69, 267, 393]. Already Hatami et al. used an Sb soaking step prior to GaSb deposition when growing the first GaSb/GaAs QDs. They reported on 1 ML or 2 ML thick GaSb layers formed by anion exchange upon Sb soaking, depending on soaking

time [44, 393]. Suzuki et al. [69] and later on Nakai et al. [59] observed using RHEED a change of the growth surface from a $c(4 \times 4)$ reconstruction of GaAs(001) to a (1×3) reconstruction typical for GaSb during soaking with Sb_4, indicating that at least 1 ML of GaAs was exchanged by GaSb. A smaller amount of only 0.2 ML GaSb was estimated by Silveira et al. to form upon very short Sb soaking times [50]. On the other hand, Ledentsov et al. [393] and Farrer et al. [55] reported that up to 2 ML of GaSb can be formed via exchange of As by Sb atoms, obtaining a first ML GaSb after 10 s soaking, and a second ML GaSb after additional 20 s, with a saturation thereafter. It should be noted that the concept of Sb soaking is typical for, but not restricted to MBE growth, as it has successfully been used for MOCVD growth of GaSb/GaAs heterostructures, too, by Pitts et al. [394].

9.2.2 Soaking-induced GaSb quantum well

Also for both MBE-grown samples studied here, the GaAs growth surface was soaked with Sb for all GaSb layers, following a growth interruption under As flux prior to GaSb deposition. In sample C, this Sb soaking endured only 5 s, while in sample D a soaking time of 75 s was chosen. The result of such a soaking step can particularly be studied for sample D, as here layer 1 was caused only by soaking, without any direct deposition of GaSb.

A typical XSTM image of this first layer, capped with GaAs, is shown in Fig. 9.3. Many individual Sb atoms within the GaAs matrix are evident as small, bright spots. For clarification, the incorporated Sb atoms are marked in Fig. 9.3(b) by small blue circles. In addition, some bright vertical stripes parallel to the GaAs atomic chains, which are XSTM tip artifacts, and three large, bright spots, given by adsorbates from the residual gas on the cleavage surface, are observed.

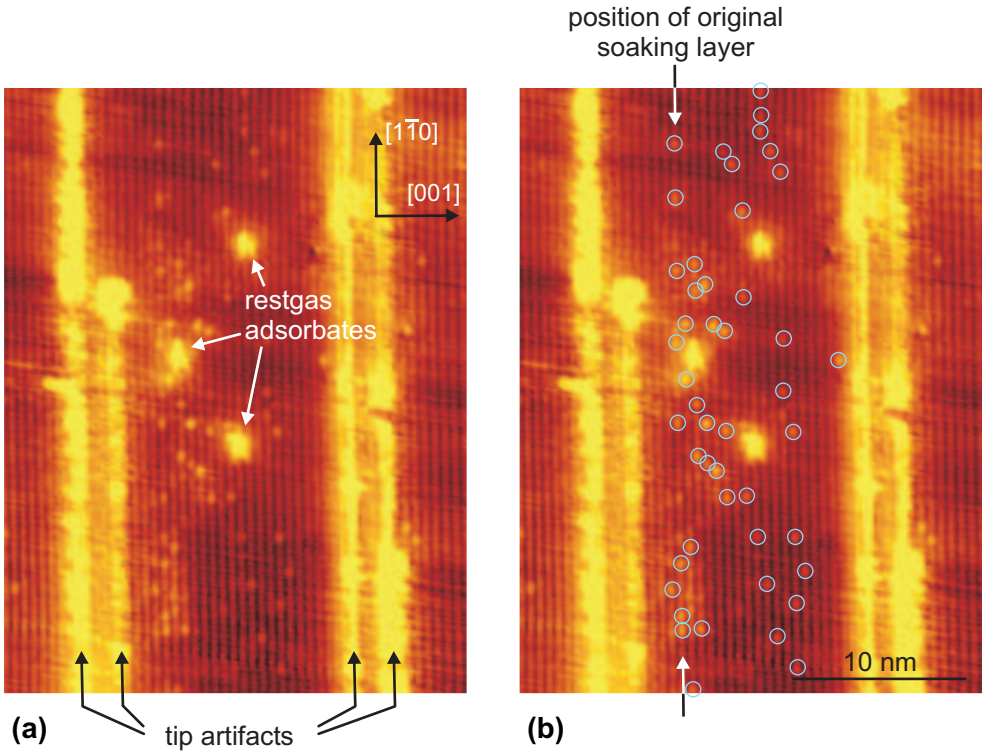

FIGURE 9.3: XSTM filled state image of layer 1 of sample D, taken at V_T = -2.7 V. The vertical bright stripes are due to tip artifacts. Both figures show the same image, but the positions of incorporated Sb atoms are marked in (b) by small blue circles.

It is evident in Fig. 9.3 that the material induced by Sb-for-As exchange during Sb soaking has not remained within an atomically flat layer, but became intermixed and segregated during GaAs capping. The area of increased Sb content extends in growth direction over about 15 atomic chains or 8 nm, with a sharp beginning, where the amount of Sb atoms per atomic chain jumps from zero to its maximum value from one chain to the other, and an Sb content continually decreasing in [001] growth direction. The total Sb content within this broadened layer can be evaluated by counting the Sb atoms within a distinct area and comparing this number with the corresponding number of group-V atomic positions in $[1\bar{1}0]$-direction. The area imaged in Fig. 9.3 has an extension in $[1\bar{1}0]$-direction of 35 nm, including 87 lattice sites for group-V atoms. In comparison, the number of Sb atoms marked in Fig. 9.3(b) amounts to 47. Considering that only every second (001) ML can be imaged and assuming that all marked Sb atoms are located within the cleavage surface, as discussed above, the total amount of incorporated Sb results to 1.1 ML.

Considering earlier results of GaSb growth obtained by I. Farrer [55], about 1 ML of antimony or slightly more was expected from the chosen growth conditions to be incorporated at the growth surface [395], agreeing very well with the experimentally obtained value. Thus, the model of an Sb-for-As exchange upon soaking is nicely confirmed. Additionally, the distribution of incorporated Sb atoms over several nm in [001]-direction, as shown in Fig. 9.3, gives information about the overgrowth process: It is generally assumed that the Sb-for-As exchange results in a GaSb composition mainly concentrated at the growth surface, no or only very short-range Sb diffusion into the underlying GaAs matrix is expected [55, 59, 84, 387, 392, 396]. Thus, the spreaded distribution imaged here develops upon overgrowth of the GaSb layer, as antimony segregates into the deposited GaAs material. The observed concentration profile of a maximum GaSb content at a first, distinct atomic chain, followed by a decrease in growth direction over several nm, fits well to the idea of Sb segregation during capping. As the total amount of GaSb found in this layer agrees with the expected value, it can be supposed that almost all Sb atoms get re-incorporated into the overgrowth layer, although a larger amount of initially incorporated Sb atoms that was only partly re-incorporated upon overgrowth cannot be excluded. It should be noted that according to Wang et al. [391], the effect of Sb soaking could have even been enhanced if an Sb_2 cracker source was used for epitaxy instead of Sb_4 as it was the case here. The exact profiles and possible consequences of Sb segregation will be further analyzed and discussed in the next sections.

9.3 From 2D to 3D growth

9.3.1 Smallest MBE-grown quantum dots

While the soaking-induced GaSb layer does not contain any three-dimensional structures, GaSb quantum dots have been observed for both MBE-grown samples C and D in the layers grown by directly depositing GaSb following the soaking step. Regarding sample D, the smallest 3D structures, observed in layer 2 corresponding to 1 ML GaSb deposition, are not optically active, while the QDs of layer 3, which have been formed by depositing 2 ML GaSb, show a clear PL signal (see section 8.6). For sample C, no luminescence data are available, but the statistical analysis of layer 1, also consisting of nominally 1 ML deposited GaSb, revealed a mean QD base length of about 13 nm with an average height of 1.6 nm (section 8.3.3). Compared with sample D, this size and the rather high GaSb stoichiometry come closer to the optically active QDs in layer 3 than to the small 3D structures in layer 2 (see section 8.4). For illustration, typical structures of the discussed three layers are shown in Fig. 9.4. A very flat shape is obvious for all structures. However, while at sample D the shape remains

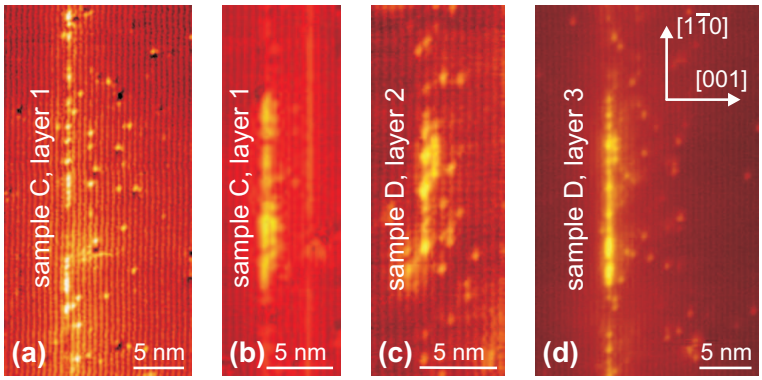

FIGURE 9.4: XSTM filled state images of GaSb layers of both MBE-grown samples: (a,b) Layer 1 of sample C, corresponding to 1 ML GaSb deposition, acquired at (a) V_T = -2.2 V and (b) V_T = -2.5 V. (c) Layer 2 and (d) layer 3 of sample D, corresponding to 1 ML and 2 ML deposited GaSb, respectively, taken at V_T = -2.4 V.

flat even for the QDs formed after deposition of 2 ML GaSb, the corresponding layer 2 of sample C contains much larger and higher QDs.

Remembering that in sample C GaSb deposition was preceded by only 5 s Sb soaking, but in sample D the soaking time was 75 s, one would have expected a more enhanced Sb-for-As exchange and therewith a higher amount of GaSb at sample D, which should still remain after directly depositing equal amounts of GaSb at both samples. However, the opposite behavior has been observed by the fact that the QDs in sample C contain more GaSb material. Thus, the idea of the Sb soaking time directly influencing the QD size is too simplified, especially as other growth parameters seem to have stronger influence on the final QD structure.

Among these, three parameters have to be taken into account: The first is the growth temperature, which has generally been higher at sample D with 600°C for GaAs and 515°C for GaSb, compared to 550°C and 490°C at sample C, respectively. A higher growth temperature increases the mobility of the atoms and would be of special significance if the relevant processes were kinetically limited. On the other hand, the growth rate was chosen to 0.3 ML/s for sample C but 0.7 ML/s for sample D, so the higher mobility given by the increased temperature is compensated by a faster growth.

The third and probably most important difference when comparing the growth of both samples lies within the overgrowth sequence of the GaSb layers: At sample C, after GaSb deposition the formed layers were immediately overgrown by GaAs, while at sample D a 30 s long growth interruption took place, the first 15 s under Sb flux, and the second 15 s under increasing As flux. Therewith, the material was given time to redistribute after deposition. The observed QD structures indicate that this redistribution did not lead to higher QDs with an increased GaSb content, on the contrary, a partial leveling and dilution of initially existing QD structures is likely. From the InAs/GaAs material system it is known generally that fast overgrowth leads to stoichiometrically pure QDs and WLs [92], while segregation and dilution effects have been observed during growth interruptions [118, 125, 221]. For GaSb/GaAs QDs, probably group-V exchange processes not only lead to Sb-for-As exchange at the GaAs growth surface upon Sb soaking, but also induce an As-for-Sb exchange at the GaSb layer during the GI. As the strain within the GaSb layer is highest at the QDs, the tendency for an Sb atom to move laterally on the growth surface or to be replaced by an As atom is highest here.

9.3.2 Critical thickness of dot formation

Before the processes involved during overgrowth of the GaSb layers will be further discussed in the next section, now the focus is switched to the astonishing fact that QDs have been formed even upon deposition of only 1 ML GaSb, which is contradictory to most published

values of the critical thickness of dot formation in the GaSb/GaAs system [44, 46, 49, 51, 55, 59, 69, 256, 260, 264, 267]. For MOCVD growth, the difficulties to exactly specify the amount of deposited GaSb material upon which QD growth sets in have already been discussed in section 7.2. But also for MBE growth, typical published values of the critical thickness lie between 2 and 3 ML [46, 49, 55, 59, 69, 256] or even above [44, 267].

However, a detailed look on the exact growth conditions and the meaning of the given values is necessary: While Bennett, Thibado et al. reported on a 2D to 3D growth transition to occur between 2 ML and 3 ML GaSb growth without using an Sb soaking step [46, 256] and Wang et al. observed an onset of islanding after depositing 1.1 nm GaSb corresponding to nearly 4 ML [267], most other authors include both the directly deposited GaSb and additionally the amount of GaSb formed upon Sb soaking when defining a critical thickness of dot formation [49, 50, 55, 59, 69]. Hatami et al. estimated the thickness of the GaSb layer formed upon soaking to 2 ML and needed additional 2 ML deposited GaSb until they observed QD formation by TEM and x-ray diffractometry [44]. Suzuki et al. used RHEED to observe a change from 2D to 3D growth after the deposition of 1.5 ML GaSb following an Sb soaking associated with further 1 ML GaSb, resulting in a total GaSb amount of 2.5 ML [49, 69]. The same values are also given by Nakai et al. [59]. Silveira et al. measured the inherent stress in very thin GaSb/GaAs samples upon GaSb growth by evaluating the bending of the flexible samples and stated the onset of QD formation to occur already after 0.8 ML direct GaSb deposition plus another 0.2 ML GaSb formed by Sb-for-As exchange, although accompanying RHEED measurements indicated an amount of 1.6 ML deposited GaSb to be necessary for QD formation [50]. Farrer et al. again estimated the thickness of the GaSb layer formed upon soaking to 2 ML and observed QD formation, using AFM, after additional deposition of 0.75 ML GaSb [55].

Care has to be taken regarding the accuracy of all these values as the thickness of the soaking-induced GaSb layer can only roughly be estimated from RHEED [59, 69] or other diffraction measurements [44]. Additionally, although these layers have to be antimony-rich, they need not necessarily consist of pure GaSb but can be slightly intermixed, which would reduce the total amount of incorporated Sb. The amount of directly deposited material can more precisely be verified by intensity oscillations of the RHEED signal or by a carefully calibrated flux, although these values, too, are difficult to obtain for GaSb growth.

For the samples of this work, the amount of antimony that originally was exchanged for arsenic during Sb soaking, prior to GaSb deposition and prior to capping, could not be determined. But the direct deposition of GaSb was gauged by RHEED for sample C, confirming the rather exact deposition of 1.0 ML in layer 1. The existence of small QDs in this layer shows that the critical thickness of dot formation, regarding only the directly deposited GaSb independent of the material gained by anion exchange, has to be slightly below 1 ML here. This value is at the lower edge of the range of literature data. Remembering that the QDs of layer 1 have a very flat structure, the question arises whether these QDs could be seen at all when using TEM or AFM, or whether some of the published values describe rather the formation of larger GaSb QDs than the actual onset of QD formation.

Regarding the results of sample D, another uncertainty about the critical thickness of dot formation becomes apparent: Similar to sample C, the deposition of 1 ML GaSb, in addition to the material induced by soaking, has lead to the formation of 3D islands. Though, in layer 2 of sample D these islands are too flat and too intermixed to be optically active, and only for the QDs in layer 3 formed by depositing 2 ML GaSb an electronic confinement was obtained. Thus, the change from 2D to 3D growth can be different from the onset of QD formation, at least if the term quantum dot is used in a strict, electronic meaning. Additionally, the comparison of samples C and D shows that the onset coverage for QD formation is not a

constant value but depends, within some extent, on the exact growth conditions.

Nevertheless, it can be concluded that the change from 2D to 3D growth can occur already slightly before the direct deposition of a full ML GaSb, following an Sb soaking step.

9.3.3 Amount of incorporated GaSb

Using XSTM, the epitaxial processes taking place at the growth surface cannot directly be studied, but the structure of the capped samples can be analyzed. Thus, the structure of the soaking-induced QW of sample D, already presented in section 9.2.2, yields a total amount of incorporated antimony of 1.1 ML. Unfortunately, the image quality and the rather poor statistics limit the quantitative evaluation of layers 2 and 3 of sample D, but the four GaSb layers of sample C could nicely be analyzed.

The WL and a typical QD of layer 1 are shown in Fig. 9.4(a,b), the ring-shaped QD being cleaved through the ring body. From the average size and density of the QDs, the assumed ring shape, and the average chemical composition, the total GaSb content within all QDs of layer 1 could be calculated to 0.17 ML, as it was discussed in section 8.3.3 (see Table 8.1). According to the analysis of the local lattice constant, the WL contains about 0.3 ML GaSb (see section 8.5). Finally, the Sb atoms have to be considered which segregated from the GaSb WL and got re-incorporated in the GaAs overlayer. These atoms can be counted within the XSTM images in the same way as it was done in Fig. 9.3 for the soaking-induced QW, resulting in a total Sb content of about 0.5 ML. Thus, layer 1 contains a total of about 1.0 ML GaSb.

In the same way as for the first layer, also the GaSb content of the other three layers of sample C was analyzed. The results for all four layers are summarized in Table 9.1 and visualized in Fig. 9.5. A large difference between the first and the other three layers is evident: As the size and density of the QDs is especially small in layer 1, the material contained within all QDs is consequently much less for this layer compared to the others, which show quite similar values. Also the WL is very thin for layer 1 and nearly equally antimony-rich for layers 2 to 4. As a consequence, the total GaSb material incorporated within the layers amounts to about 1.0 ML in layer 1 and varies only slightly around 2.0 ML in the other layers.

For the four layers of sample C GaSb has been deposited following a 5 s Sb soaking step. Thus, a small amount of antimony being incorporated by anion exchange during the soaking should be expected. This explains the total GaSb content in layer 1 and especially layer 2, which is slightly larger than the nominal amount of deposited material. On the other hand, layer 1 of sample C still contains slightly less GaSb material than layer 1 of sample D, which was formed only by Sb soaking, thus the extent of Sb-for-As exchange in sample C has to be significantly smaller. In the XSTM images of capped GaSb layers it is not possible

layer	nominally deposited GaSb [ML]	total GaSb material within QDs [ML]	total GaSb material within WL [ML]	segregated Sb atoms in GaAs overlayer [ML]	total GaSb content [ML]
1	1.0	0.2	0.3	0.5	1.0
2	2.0	0.6	0.9	0.6	2.1
3	2.7	0.6	0.9	0.4	1.9
4	3.1	0.7	0.9	0.5	2.1

TABLE 9.1: GaSb material incorporated within the different layers of sample C (approximate values).

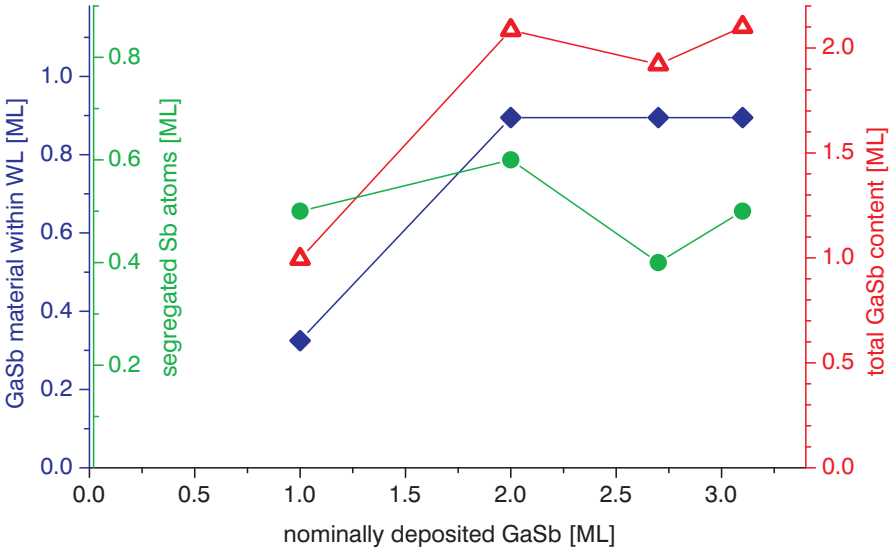

FIGURE 9.5: Comparison of the four layers in sample C regarding the GaSb content within the WL, the amount of segregated Sb atoms incorporated within the GaAs overlayer, and the total GaSb content including QDs, WL, and segregated Sb.

to distinguish between directly deposited GaSb and antimony that was incorporated during soaking, but apparently the material within the GaSb layers is not simply the sum of a constant amount of GaSb given by anion exchange plus the directly deposited material.

Even more, for layers 2 to 4 the increase of material deposition seems to have no explicit influence on the amount of actually incorporated GaSb. Instead, the amount of material seems to saturate after about 2 ML GaSb deposition. As the epitaxy was observed by RHEED, indicating that the additionally deposited GaSb was actually incorporated in the GaSb layer during growth, the excess material has to be taken away again during overgrowth. Accordingly, there seems to be a maximum strain energy which can be permanently accumulated in the GaSb layers, corresponding to about 2.1 ML GaSb. When this level is exceeded during growth, the additional antimony may get incorporated at the GaSb growth surface, where the strain is partly relaxed, but upon overgrowth this excess antimony does not remain within the GaSb layer but gets removed, either as surfactant, i.e. as floating layer at the growth surface (see next section), or by re-evaporation.

Another interesting detail of GaSb QD growth is revealed by the GaSb content of the WLs: While the WL of layer 1 contains only 0.3 ML GaSb, about 0.9 ML were obtained in the WLs of the other layers, respectively. Nevertheless, all four layers exhibit QDs. Thus, the beginning of 3D growth seems not to instantly replace the 2D growth, as the WL increases in thickness parallel to QD growth. This would not only be a different behavior to e.g. the InAs/GaAs material system, where QD growth consumes all additionally deposited material or even a part of the WL [2, 20, 22, 375], but would also be different from classical Stranski-Krastanow growth. However, this idea cannot be verified, as the observation of less GaSb material within the first WL could possibly also be explained by the layer sequence itself: Assuming that a part of the initially deposited antimony remains at the growth surface as surfactant, this material will additionally contribute to the GaSb content of layers 2 to 4, while such a contribution does not exist for layer 1.

The amount of about 1 ML GaSb incorporated within the WLs of layers 2 to 4 is equal to the GaSb material observed in the MOCVD-grown WL and the QW near the onset of QD formation (see chapter 7.2). Therefore, this value can be assumed universal for capped GaSb WLs – indicating that layer 1 of sample C represents some kind of incomplete WL – independent of the growth method.

9.4 Sb segregation during overgrowth

9.4.1 Analysis of Sb segregation

GaSb material which got dissolved and completely removed from the heterostructures can of course not directly be detected by XSTM. Those Sb atoms, however, that segregated from the GaSb layers but got incorporated within the GaAs overlayer, are visible in the XSTM images. They can, for example, be seen as small bright spots above the WLs and QDs of both samples C (Figs. 8.4 and 8.11) and D (Figs. 8.10 and 8.13), respectively. From such images, segregation profiles can be generated by counting the Sb atoms seperately for each atomic chain above the GaSb layer. While the density and lateral extension of the QDs and the number of sufficiently resolved XSTM images are too small to quantitatively analyze segregation above the QDs, it was possible to successfully evaluate the segregation above the WLs. Corresponding profiles are shown in Fig. 9.6(a-d) for all four layers of sample C: Directly at the WL the GaSb stoichiometry is so high that individual Sb atoms cannot be resolved, but within the next 50 atomic monolayers directly above the WL in growth direction the Sb atoms can be counted. By dividing the number of Sb atoms per ML through the corresponding number of atomic lattice sites, a GaSb stoichiometry can be specified for each chain separately, plotted as an individual bar in the histogram. Thereby only each second ML can be analyzed due to the structure of the cleavage surface (see section 3.4).

Comparing the four histograms, different starting values of the GaSb content are apparent, ranging from about 16% in layer 2 down to less than 8% in layer 3. However, this discrepancy does not necessarily indicate a different total amount of incorporated Sb atoms in the four GaAs overlayers, as the first columns plotted in the histograms may correspond to different GaAs MLs in respect to the WL position: Firstly, an uncertainty of $\pm$ 1 ML is generally inherent to the data obtained from the XSTM images. Additionally, in the images of layers 1 and 2 already the first atomic chain above the WL base could be analyzed, while in the images of layers 3 and 4 evaluating the segregated Sb atoms could only be started at the second chain above due to the image contrast of the WL.

Nevertheless, all four segregation profiles show a very similar decay with a decreasing slope, therefore exponential decay curves are fitted to the data. While principally the exponential decay fits the data quite well, a rather large noise is obvious due to the small database of only a few Sb atoms per atomic chain. The fitted decay lengths l_0 of the exponential curves amount to 6.5 ± 0.7 ML, 6.8 ± 0.9 ML, 7.2 ± 1.1 ML, and 7.5 ± 0.5 ML for layers 1, 2, 3, and 4, respectively. This means that the ratio of decreasing GaSb stoichiometry between successive atomic MLs is similar in all four layers, showing that the segregation processes during overgrowth of the four different layers are rather uniform.

Because the slope is comparable for all layers, the data can be averaged in order to increase the database and reduce statistical noise. The resulting segregation profile of sample C is shown in Fig. 9.6(f) by blue columns. A closer view at a section of the histogram is also given in (e), here additionally showing the statistical errors of the data. Besides the segregated Sb atoms located within several nm above the GaSb layers, a small nearly constant concentration of Sb atoms can be observed as a background in XSTM images of the complete heterostructure of sample C. Such Sb atoms are already observed several nm underneath the first GaSb layer, therefore they cannot stem from intentionally grown GaSb, but are most probably due to a permanent small antimony flux in the MBE reactor. As the Sb source of the MBE is closed only by a conventional shutter and no additionally valved cracker unit is used, such an antimony background is easily explainable. From the XSTM images, the Sb background incorporated in the sample was evaluated to 0.25%, resulting in the asymptotic level in Fig. 9.6.

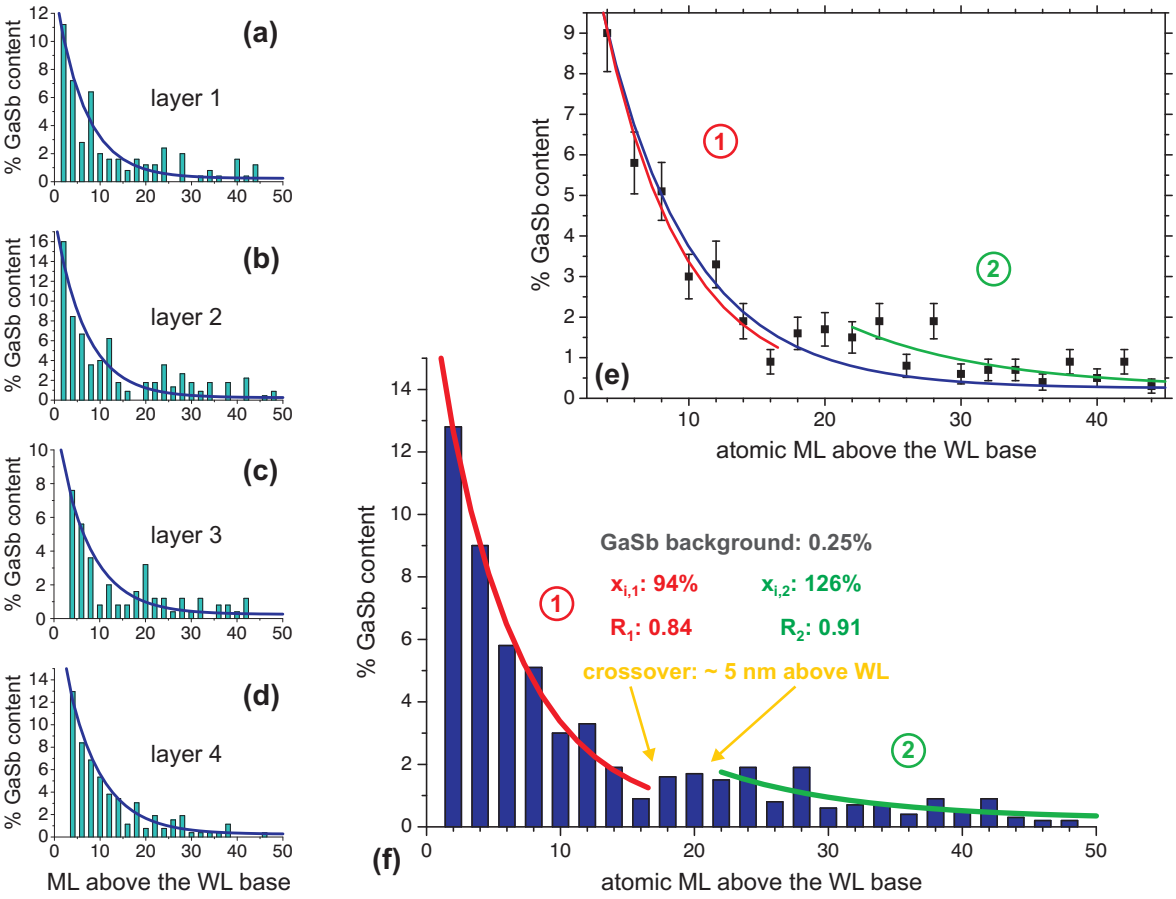

FIGURE 9.6: Segregation profiles for layers 1 to 4 of sample C, showing (a-d) individual histograms of the GaSb stoichiometry in each second atomic ML above the respective WL and (e,f) histograms which are averaged over all four layers. The blue curves are exponential decay fits to the data. At a closer view at a cutout of the histogram including the statistical errors of the data (e), fitting the complete data by one exponential curve (blue) proves to be not ideal. Instead, two regions have to be distinguished, characterized by a fast decay (red curve, region 1) and a somewhat slower decay (green curve, region 2), with a crossover at about 20 ML. The corresponding segregation seeds and coefficients (see text) are indicated for both regions in (f).

At a careful analysis of the segregation profile, an anomaly of the exponential decay gets evident at around 20 ML above the WL base [indicated by orange arrows in (f)]. At this position, the GaSb concentration increases slightly over about 8 ML, before it decreases again exponentially, but at a somewhat slower decay. Consequently, it is not wise to fit the complete data by only one exponential decay curve, but the region directly above the WL up to about 20 ML and the region further above should be distinguished and fitted separately, resulting in a much better fit, as shown in (e). Before the physical meaning and the origin of these separate regions can be discussed, first an improved understanding of the segregation profiles is necessary.

To describe the effect of segregation upon overgrowth quantitatively, Steinshnider et al. [385] have developed a model, based on a notation given by Muraki et al. [397], which is used here, too, in a slightly modified form: When capping of the GaSb layer begins, obviously a certain amount of more or less mobile Sb is available, forming a segregation seed x_i. Upon capping, a fraction R of this seed is expelled and floats at the growth surface, while the reminding part $1 - R$ gets incorporated into the next monolayer. Thereby R defines a

phenomenological segregation coefficient. Thus, for a given monolayer indexed n, there is a certain Sb stoichiometry $x(n)$ that gets incorporated, and another fraction $x_{floating}(n)$ that remains floating at the growth surface. As the amount of Sb in the monolayer $n+1$ depends on that in layer n and on the segregation coefficient, the segregation can be described by the two recursive relations

$$x_{floating}(n+1) = R\, x_{floating}(n) \tag{9.1}$$

$$x(n) = (1-R)\, x_{floating}(n-1)\,, \tag{9.2}$$

with the segregation seed $x_i = x_{floating}(0)$. Also the constant Sb background can be considered, giving the term x_0:

$$x_{floating}(n+1) = R\,[x_{floating}(n) + x_0] \tag{9.3}$$

$$x(n) = (1-R)\,[x_{floating}(n-1) + x_0]\,. \tag{9.4}$$

These independent recursion relations can be solved and combined to the following one-dimensional segregation profile:

$$x(n) = x_i\, R^{n-1}\,(1-R) + x_0\,(1-R^n)\,. \tag{9.5}$$

In a continuous model, this discrete formula would actually transform into an exponential decay function characterized by a decay length l_0 plus a constant offset. Thus, from the fitted parameters obtained from the experimental segregation profiles the coefficients of Eq. 9.5 can be calculated for both regions 1 and 2 indicated in Fig. 9.6(f), respectively. The fitted exponential curves have the form $y = A\exp(-x/l_0) + x_0$, and the discrete segregation parameters result to

$$x_0 = 0.0025\,;$$

$$x_i = \frac{A + x_0}{\exp\frac{1\,\mathrm{ML}}{l_0} - 1} \quad \Longrightarrow \quad x_{i,1} = 0.94\,, \qquad x_{i,2} = 1.26\,;$$

$$R = \exp\frac{-1\,\mathrm{ML}}{l_0} \quad \Longrightarrow \quad R_1 = 0.84\,, \qquad R_2 = 0.91\,.$$

Concentrating firstly on region 1, the obtained parameter $x_{i,1} = 0.94$ stands for an initial segregation seed of nearly 1 ML, which gets incorporated during overgrowth. This value seems to disagree with the data of Table 9.1, indicating the amount of Sb observed in the QDs, in the WL, and in the overgrowth layer of the GaSb layers 1 to 4, respectively. However, for that table all Sb atoms observed within about three atomic chains above the base of the WL were attributed to the WL itself, and only all Sb atoms further above were counted for the overlayer, while here the segregation analysis was extrapolated from the overlayer to the WL. Correspondingly, a substantial part of the obtained segregation seed, forming at the WL base, is incorporated again within the first one to three MLs above. The more significant value is the obtained segregation coefficient of $R_1 = 0.84$, implying that during overgrowth of the GaSb layers the probability of a floating Sb atom to get incorporated in the next GaAs ML is only about 16%, while the probability to remain at the growth front amounts to about 84%.

In region 2, the segregation coefficient is even increased to $R_2 = 0.91$, meaning that only about 9% of the floating Sb atoms get incorporated per ML, in good agreement with the decreased slope of the corresponding exponential decay curve in Fig. 9.6(f). The obtained segregation seed – extrapolated to the base of the WL – amounts here to $x_{i,2} = 1.26$, exceeding by far the value of $x_{i,1}$, again in good agreement with the slight increase of the measured

GaSb content between MLs 18 and 24 in the histogram of Fig. 9.6(f). At the first view, this increase of the GaSb content per ML combined with an increased segregation coefficient at about 20 ML above the WL base is unexpected and even seems to be impossible, as this would imply that the remaining amount of Sb atoms in the floating layer gets somehow increased at this position. However, remembering the growth structure of sample C (see section 8.1), the crossover between both segregation regimes, which can be located at about 18 to 24 ML or 5 to 7 nm above the WL base, occurs just at that area of the overgrowth layer where the growth temperature was increased from 490°C (GaSb growth) to 550°C (GaAs growth). Consequently, a change of the segregation behavior can well be expected here: The increase of the segregation coefficient R between regions 1 and 2 thus stands for a decreased incorporation probability of the remaining Sb at higher temperatures.

Considering the raised growth temperature, also two explanations for the increased amount of Sb atoms available for incorporation into the overgrowth layer further above are possible: Firstly, an increase of the growth temperature is combined with an also increased temperature at various mechanical parts of the MBE chamber around the sample itself, including the sample holder, leading to a re-evaporation of antimony which was formerly deposited at the surfaces and is now available for incorporation into the sample.

Secondly, it has been assumed above and will be explained in the next section that during overgrowth some antimony remains at the growth surface as surfactant layer, meaning that the Sb atoms influence the growth kinetics and surface energy, but do not get incorporated at all [103], in contrast to the Sb floating layer. Accordingly, the originally deposited Sb atoms are divided into three parts upon GaAs overgrowth, namely a first part which directly remains within the QDs or WL, a second part which forms the floating layer and gets incorporated within several MLs above the GaSb layer, and finally the surfactant atoms. The ratio between these three parts is probably determined by the initial amount of Sb atoms, the strain within the GaSb layer including the QDs, the surface energy, and the growth kinetics. Therefore it can well be imagined that an increase of the overgrowth temperature varies the distribution of Sb atoms in the floating and the surfactant layer, supplying additional antimony for incorporation, explaining the observed changes between the two segregation profiles.

9.4.2 Origin of Sb segregation and intermixing

After the strong Sb segregation present in both investigated MBE-grown samples could empirically be described by a one-dimensional model, and having in mind the strong intermixing of antimony and arsenic in the observed GaSb nanostructures, the basic questions remain: Which are the reasons for the strong segregation and intermixing, and why are these effects so extraordinarily pronounced in the GaSb/GaAs system?

For a possible answer, first the macroscopic level with the crystal parameters is considered. The main driving force of QD formation and changes during overgrowth is the strain inherent to the heterostructure, given by the lattice mismatch and the stiffness of the materials. The latter can be described by the elastic moduli c_{11}, c_{12}, and c_{44} of the crystals, which are listed for GaSb, InAs, and, in comparison, for GaAs in Table 9.2. Accordingly, the elasticity of

material	c_{11}	c_{12}	c_{44}	lattice constant [nm]
	elastic moduli [$\times 10^{10}$ N m^{-2}]			
GaSb	8.8	4.0	4.3	0.6096
InAs	8.3	4.5	4.0	0.6058
GaAs	11.9	5.4	6.0	0.5653

TABLE 9.2: Room-temperature lattice properties of GaSb, InAs, and GaAs, from [164].

GaSb is very similar to that of InAs, while the stiffness of GaAs is slightly larger. Thus, for comparing the strain only the lattice mismatch has to be considered, which amounts to 7.84% for GaSb/GaAs and 7.16% for InAs/GaAs. Therewith, the strain in GaSb/GaAs layers is about 9% larger than in InAs/GaAs layers with the same amount of material, resulting in 18% more strain energy, so that a partial removal of antimony from the GaSb layer releases slightly more energy than a corresponding process at InAs layers.

However, this difference is too small to fully explain the strong Sb segregation and intermixing, and processes taking place at the atomic level have to be regarded as the main contribution. Three features will be discussed in the following, namely anion exchange processes, the surfactant nature of antimony, and the surface reconstructions of GaSb(001) layers.

While the Sb-for-As exchange process is intentionelly used during Sb soaking of the GaAs growth surface prior to GaSb deposition, the unwanted opposite exchange reaction also occurs during overgrowth of the GaSb layers with GaAs: Strong As-for-Sb exchange has been clearly verified by mass spectrometry [389, 392, 398], RHEED [392], x-ray photoelectron spectroscopy [391, 392], x-ray diffraction [386], and XSTM experiments [386, 392]. Thereby, As-for-Sb exchange at the GaSb surface has been found to occur more efficiently and with more material redistribution than the opposite Sb-for-As exchange, because GaAs has a much larger bond strength than GaSb [392]. The values for the amount of exchangable GaSb material vary in literature between 0.85 ML observed by Xie et al. [398] and up to 3 ML reported by Nosho et al. [386]. Anyway, the exact literature values, in most cases obtained for the surfaces of strain-free thick GaAs or GaSb layers, respectively, are not directly transferable to the case of a strained GaSb WL on GaAs. Nevertheless, the principle mechanism of strong Sb-for-As exchange occurs here as well. Additionally, Wang et al. [392] observed that As-for-Sb exchange is not limited to the growth surface, but can extend into the bulk: As mentioned above, upon Sb soaking of a GaAs surface the amount of exchanged material saturates when 1 or 2 ML GaSb are formed [44, 55, 69]. However, the increase of Sb exchanged by As during As soaking of a GaSb surface gets slower after a certain time, indicating the termination of surface exchange, but remains to continue linearily for several minutes [392]. Thus, not only the chemical composition at the material interface changes, but strong intermixing also of the GaSb layer underneath results.

The extent of As-for-Sb exchange depends on the molecular species used as arsenic source: In the case of As_4, the necessary dissolution of the molecular bonds prior to incorporation is more complex than for As_2, thus the latter is more reactive to a GaSb surface when used as soaking material. According to Nosho et al. [386], no anion exchange at all occurs upon soaking with As_4, whereas Wang et al. [391] as well as Brown et al. [84, 396] report that also under the use of As_4 an As-for-Sb exchange occurs, but to a smaller extent as in case of As_2.

With this premise, on the first sight it seems astonishing that sample C, grown with As_2, contains larger QDs with purer GaSb material than sample D, grown with As_4. However, also the other growth parameters have to be taken into account: Firstly, in sample C the GaSb layers were immediately overgrown with GaAs, leaving less time to surface exchange reactions as in sample D, where a growth interruption under increasing arsenic pressure took place prior to GaAs overgrowth. This GI was necessary, as for the growth of sample D a valved As cracker source was used, which can effectively reduce the As background during GaSb growth, but needs several seconds to be opened again [55]. Secondly, the growth temperature chosen for the GaSb layers was 490°C in sample C but 515°C in sample D. In this temperature regime, the As-for-Sb exchange increases with increasing substrate temperature [389, 398], as does the amount of Sb atoms in the floating layer [see Fig. 9.6(f) and the change of the segregation profiles discussed above]. Thus, the smaller reactivity of the arsenic species used for sample D was probably more than compensated by a longer As soaking time and an

increased temperature, as compared with sample C, resulting in a stronger intermixing of the GaSb layers. Additionally, for the use of As_4 instead of As_2, a reduced As-for-Sb exchange efficieny, but an enhanced incorporation of segregated Sb material into the overgrowth layer was reported [391].

Once some antimony of the GaSb layers has been exchanged by arsenic, this Sb material has to remain somewhere. Besides the possibility of direct re-evaporation, the excess Sb can remain at the growth front, from which it can also be re-evaporated later on, or get incorporated into the overgrowth layers. The latter case of antimony floating on the growth surface for some time and getting reincorporated has been extensively described for InAs layers grown on GaSb [385, 387, 389, 392] and to some extend also for the GaSb/GaAs system [57, 84, 394]. Indeed, this process has lead here to the segregation profiles described above. Although the re-incorporation of floating Sb atoms is energetically unfavorable because of the larger bond length and weaker bond strength of GaSb compared with GaAs, it nevertheless happens due to the large Sb supply from the floating layer and for entropy reasons [392].

As the material observed by XSTM in the capped GaSb layers – including the respective GaAs overlayers – is, at least for the upper layers, less than the amount of originally deposited material (see section 9.3.3), some antimony must have been removed from the sample during overgrowth, in addition to the floating Sb atoms. The role of antimony as surfactant, riding up on the growth surface, decreasing the surface energy [399, 400], and limiting the surface diffusion rates of other atoms [103], but not getting incorporated, is a well-known effect in several material systems: An Sb supply during the deposition of Ge on Si, for example, drastically changes the formation of the corresponding Ge/Si nanostructures, although no Sb gets integrated in the heterostructure (see, for example, [401] or [402] and the references therein). During the last years, the Sb surfactant effect has also been used in the InAs/GaAs system for increasing the InAs content of the nanostructures and thereby redshifting their photoluminescence to the technologically important lasing wavelength of 1.3 μm, both for QW [403, 404] and for QD structures [103, 400, 405]. Therefore it is assumed that also in the case of the GaSb/GaAs nanostructures studied here a considerable amount of the originally deposited Sb atoms acts as surfactant upon GaAs overgrowth, explaining the apparent loss of GaSb material in the capped structures.

The effects of As-for-Sb exchange, Sb as surfactant, and a floating Sb layer have in common that Sb atoms comparatively easily can get exchanged or removed from the GaSb layer, leading to intermixing and segregation processes upon overgrowth that are much stronger than in the case of InAs/GaAs QDs or other material systems. To understand this special behavior of Sb at the growth surface in the GaSb/GaAs system, the (001) surface reconstructions of GaSb and especially GaSb films on GaAs have to be regarded and compared with typical surface reconstructions of other materials.

At typical growth conditions, the (001) growth surfaces of III-V semiconductors are terminated by group-V atoms like As or Sb [171, 294]. Thus, the group-III atoms like In or Ga are completely bonded by group-V atoms, while the surface Sb atoms exhibit dangling bonds, or form some dimer structures for energy reduction. Correspondingly, Sb atoms should easier be repelled from the GaSb surface than In atoms from InAs, and the group-V exchange processes at interfaces with a common cation are expected to be stronger than group-III exchange processes at common anion interfaces. This effect can partly explain the observed strong As-for-Sb exchange, but it is strongly enhanced by a uniqueness of the GaSb(001) surface reconstructions.

For homoepitaxial GaSb(001) [258, 406, 407] and also for unstrained thin films [389, 392] often a (1×3) or a $c(2 \times 6)$ reconstruction was suggested. According to calculations from Righi et al. [408], a (4×3) reconstruction would be energetically favourable to (1×3) or

(2×3) structures for GaSb(001), but would lead to similar patterns in RHEED experiments, so probably in some earlier works an actual (4×3) may have been misinterpreted as (1×3) reconstruction. Indeed, GaSb(001) surfaces in three stoichiometrically different (4×3) reconstructions were observed by Barvosa-Carter using STM [409].

For substrate temperatures below about 380°C - 420°C, the $(n \times 3)$ can change to a (1×5) reconstruction, which contains more excess Sb at the topmost layers [389, 392]. This excess Sb has been found to be an additional source of strong Sb segregation [389, 392], although significant Sb segregation has been observed for different (4×3)-reconstructed surfaces, too [385]. At low temperatures and Sb-rich growth conditions, also (2×8), (2×10), or $c(2 \times 10)$ reconcstructions have been observed, exhibiting an even more Sb-enriched surface [258, 407, 410].

Even more unique than the observance of these Sb-rich surfaces is the fact that GaSb(001) never reconstructs in a $c(4 \times 4)$ geometry, although stable $c(4 \times 4)$ reconstructions exist for most other III-V semiconductor surfaces, including GaAs and InAs [258]. Instead, GaSb favours surface reconstructions containing many Sb dimers, because the Sb-Sb bond is stronger than the Ga-Sb bond, in contrast to As-As bonds, which are weaker than Ga-As or In-As bonds [408].

In order to fully understand the influence of surface reconstructions on the segregation observed above the GaSb layers of samples C and D, also the strain within these layers has to be considered, as strain can generally influence the energetics of surfaces. InAs thin films on GaAs, for example, exhibit surface reconstructions which are different to those of homoepitaxial InAs or GaAs at the same growth conditions. The sub-ML deposition of InAs on a (2×4)- or $c(4 \times 4)$-reconstructed GaAs(001) surface typically leads to a (1×3) or (2×3) reconstruction [179, 411, 412], which, by the way, indicates InGaAs alloying. With further InAs deposition, at about 1 ML, the reconstruction of the growth surface changes into a (2×4) [411–413]. For the WLs of InAs/GaAs QD layers, it is more difficult to resolve the surface reconstructions than for flat films, but in recent years some results have been obtained using STM: Krzyzewski et al. found a (4×2) reconstruction for low As_2 fluxes and a (1×3) one for more conservative growth conditions [309], while Costantini et al. [198] report a coexistence of both structures. Jacobi and Márquez, finally, only observed a (2×4) reconstruction [31, 176].

To my knowledge, no surface reconstructions for the WL of a GaSb/GaAs QD layer has been published yet. However, the change of GaAs(001) reconstructions upon Sb soaking have been studied: Laukkanen et al. [414] have grown GaAs at 580°C and As-rich conditions, leading to the formation of the (2×4) reconstruction. This surface was soaked by Sb_4 while the substrate temperature was reduced to 450°C. With decreasing temperature, the RHEED pattern corresponding to the (2×4) reconstruction first became broader and then, below 500°C, disappeared while a (2×8) diffraction pattern arose. The suggested structural model for the (2×8) reconstruction has an Sb coverage of 1.25 ML. A (2×8) reconstruction had already earlier been reported by Whitman et al. [415], consistently observed with RHEED, x-ray photoemission spectroscopy, and STM, after soaking a GaAs(001) surface with Sb_4 at 490°C. Possible structures of the (2×8) and the (2×4) reconstructions are shown in Fig. 9.7. While Laukkanen et al. proposed a $\delta 2$ configuration for the (2×4) reconstrucion, Esser et al. [416] have reported on $\alpha(2 \times 4)$ and $\beta 2(2 \times 4)$ surface reconstructions of thin GaSb films on GaAs(001).

The exact surface reconstructions of the GaSb WLs in sample C and D prior to overgrowth are not clear. A measurement during epitaxy was not possible, as the RHEED signal was dominated by the QD geometry. Also a direct comparison with the cited publications cannot be performed as those include only Sb soaking, but no direct GaSb deposition. However,

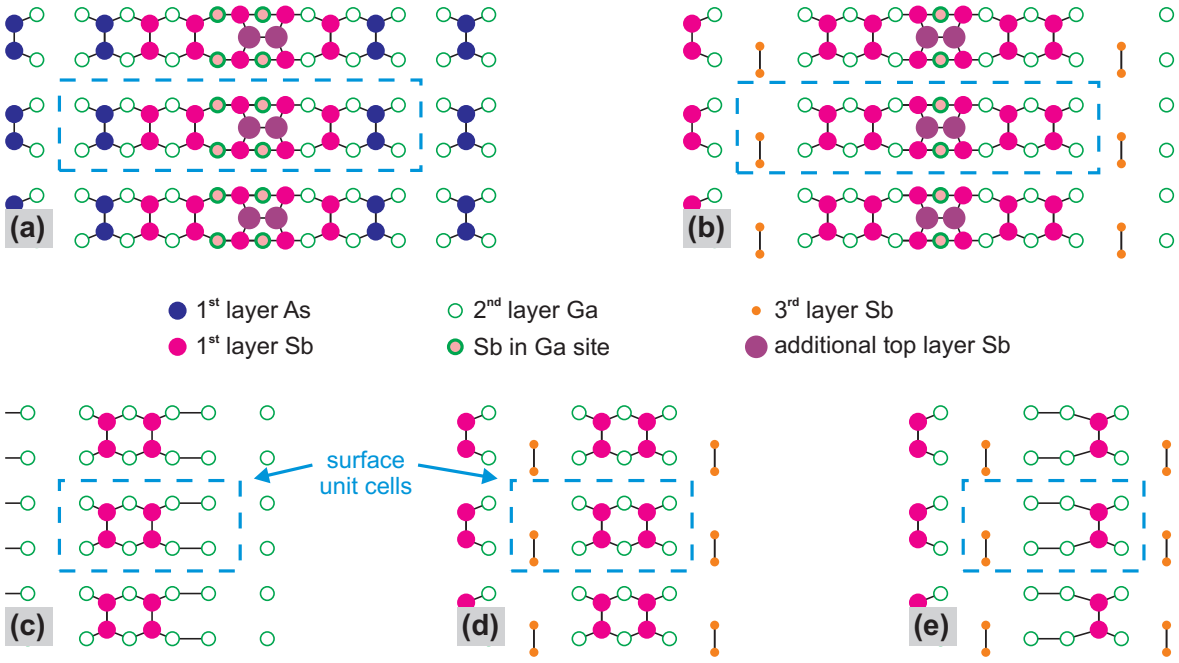

FIGURE 9.7: Atomic models of Sb-on-GaAs(001) surfaces, displaying a (a,b) (2×8), (c) $\alpha(2 \times 4)$, (d) $\beta_2(2 \times 4)$, and (e) $\delta_2(2 \times 4)$ reconstruction, according to (a) [415], (b,e) [414], and (c,d) [416].

because in sample D the soaking-induced layer exhibited similar segregation as the other two GaSb layers, and because also the results for sample C are comparable, it can be assumed that the GaSb layers of both samples had either a (2×4) or a (2×8) reconstruction, too. Thereby, at least for the GaSb layers of sample C, grown at 490°C, a (2×8) structure is more probable than a (2×4) one. In both cases, a large amount of excess Sb has been available at the growth surface, becoming a floating or surfactant Sb layer upon overgrowth.

These unique GaSb/GaAs surface reconstructions thus can explain the observed strong Sb segregation which is not known in that amount from other QD systems. For the well-studied InAs/GaAs system, the situation is very different, as not only the (2×8) reconstruction is not common, but even more because both the As-rich (1×3) and (2×4) reconstructions observed in WLs restrict In segregation. Also for other QD systems with a common group-III atom, the surface reconstructions do not contain that much excess group-V material as do the GaSb surfaces on GaAs(001).

It should be noted that additionally to segregation in growth direction, also the lateral atomic diffusion on the growth surface is strongly influenced by its surface reconstruction [179]. This can explain why a strong anisotropy, which has been observed for some InAs/GaAs QDs [31, 35], does not exist for the GaSb/GaAs QDs studied here.

In conclusion, the strong Sb segregation upon GaAs overgrowth, which could be modeled by a temperature-dependent exponential decay corresponding to an Sb floating layer and additional Sb surfactants, is induced by a very Sb-rich reconstruction of the GaSb(001) growth surface, providing many excess Sb atoms, in combination with a comparably weak Ga-Sb bond.

Chapter 10

Formation and atomic structure of ring-shaped quantum dots

Having understood some of the antimony-related effects taking place during growth, now the formation of ring-shaped quantum dots can be studied in more detail. Therefore, firstly the atomic structures of the QDs will be analyzed from the XSTM data. Then, by comparing these results with published ring structures in other material systems, a model of the growth of GaSb/GaAs nanostructures observed here will be discussed.

10.1 Atomic structure of quantum dots

All QD layers of both MBE-grown samples C and D contain ring-shaped QD structures, also called quantum rings (QRs), as have been analyzed in sections 8.3 and 8.4. For sample C, a distribution of the ratio of inner to outer ring diameter was obtained with a maximum at $r_0 = 0.42$ and a standard deviation of 0.13. Both from this statistical result and from an optical inspection of the XSTM images it is obvious that the extension of the central gap of the ring varies from QD to QD, partially also leading to asymmetric or irregular ring shapes.

Keeping these results on this sort of inner QD shape in mind, now the typical outer contour as well as the chemical composition of the QDs shall be analyzed. Figure 10.1, showing XSTM images of typical QD structures of sample C, underlines the ability of XSTM to study the atomic structure and to elaborate local variations of the stoichiometry and Sb distribution. Considering the strong segregation effects taking place during overgrowth, as shown above, the possibility to study capped nanostructures, which is inherent to the XSTM method, is additionally important.

Structures like those shown in Fig. 10.1 are common for the QDs in layers 2 and 3 and for most QDs in layer 4 of sample C. Layer 1 is characterized by rather flat nanostructures, which have a smaller height and also a slightly smaller base length than those in the other layers (for details see section 8.3.3). Nevertheless, the shape of a truncated pyramid with flat bottom and top facets and rather steep side facets is found in all layers. A strongly varying stoichiometry within the QDs has been observed for all layers, too.

10.1.1 Outer shape of the quantum dots

Due to the varying contrast and the slightly diffuse and intermixed interfaces, it is difficult to specify the exact shape of the QDs. For the QD shown in Fig. 10.1(a), the contour can approximately be determined, as visualized in Fig. 10.2(a) by a thin dashed line. Accordingly, this QD has a lateral extension of 15.5 nm at the base and 11.5 nm at the top with a height of

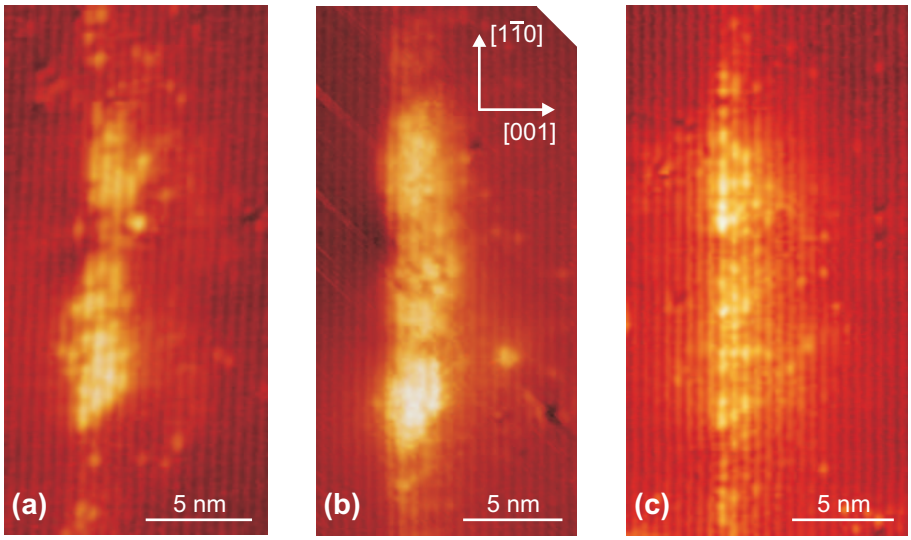

FIGURE 10.1: XSTM filled state images of typical GaSb QDs of (a) layer 3 and (b,c) layer 2 of sample C, acquired at (a) V_T = -2.6 V, (b) V_T = -1.7 V, and (c) V_T = -2.4 V.

four atomic chains, corresponding to 2.4 nm. At the sides, the QD seems to be characterized by plain facets. The angle between contour lines from these side facets and the QD base can be measured in the XSTM images, amounting to 51° and 46° for the upper and lower side of the QD shown here, respectively. For the QD shown in Fig. 10.1(b), angles of 52° and 41° can be evaluated, while the side facets of the QD of Fig. 10.1(c) have an angle of 49° and 57°, respectively. The large variance of these measured angles displays the large error inherent to these data, consisting of three parts: The first is the imperfect abruptness of the interfaces mentioned above, in combination with often missing atomic resolution in [1$\bar{1}$0]-direction in the XSTM images, making it difficult to determine exactly where the border between the QD and the surrounding matrix is. This difficulty is further increased by the small height of the QDs, extending only about four atomic chains. Finally, the calibration of the XSTM has an error of about 10% due to piezo effects and thermal drift. This error can be eliminated in images with atomic resolution, as it is nearly always done for the [001]-direction, but only a few images like the one shown in Fig. 10.1(b) offer atomic resolution in both directions and are corrected correspondingly; the QDs in most other images may appear slightly compressed or sheared in [1$\bar{1}$0]-direction (for details see section 3.4).

Assuming a simple QD shape of a four-sided truncated pyramid with low-indexed side facets, there are two possible structures, as sketched in Fig. 10.2: For QD models with {101} and {111} side facets, the top view from [001]-direction (b,e), the (110) cross section (c,f) and the corresponding planes in the cube of the Zincblende unit cell (d,g) are plotted, respectively. For the top view, a square QD base is sketched – a rectangular base with differently long sides, which is not generally excluded, would lead to a somewhat more complex structure. The angle between the side facet and the base in a (110) cross section for a QD with {101} side facets is $\alpha = \arcsin \frac{1}{\sqrt{3}} = 35.3°$, and for {111} side facets $\beta = \arctan \sqrt{2} = 54.7°$. Thus, the measured angles varying between 41° and 57° mostly lie between these calculated values, with a tendency towards the {111} oriented side facets.

From Figs. 10.2(b) and (e) another difference between the {111} and {101} bounded QD shape regarding XSTM data is evident: For the {111} shape, the sample cleavage cuts the QDs parallel to a side of their base, while QDs with {101} facets are cut parallel to a diagonal of their base. In the latter case, the observed lateral extension of a QD measured by XSTM actually is the length of a diagonal cut of its base, which depends on the position of the cross section within the QD. In the case of {111} side facets, however, the measured extension equals the length of one side of the rectangular base, independent of the cleavage position.

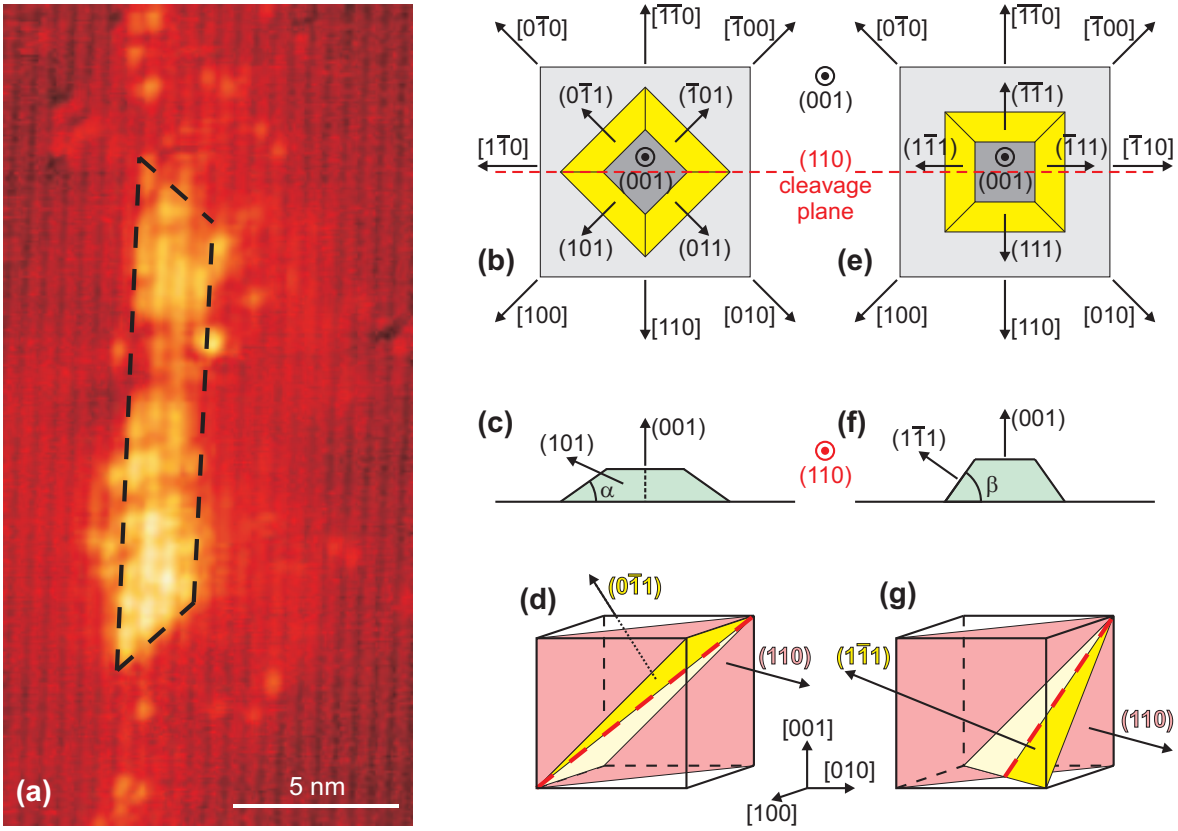

FIGURE 10.2: (a) XSTM image of the QD shown in Fig. 10.1(a). The contour of the QD is highlighted by a dashed line. Possible QD structures assuming (b-d) {101} and (e-g) {111} side facets are displayed in (b,e) top view, in (c,f) (110) cross section and (d,g) regarding the intersection of the relevant planes in the Zincblende cube.

It should be noted that the higher-indexed $(1\bar{1}2)$ side facet shows the same angle in the cross section as the (101) facet, accordingly a (201) facet would lead to the same angle as a $(1\bar{1}1)$ facet. However, at least the (201) facet has not been observed for QDs yet. Additionally, calculations of the strain relaxation in cleaved QDs, performed by H. Eisele [124], have shown that a cut through a QD bounded by {101} or {201} facets produces a laterally strongly varying strain profile of the QD because of the strongly varying amount of QD material lying underneath the cleavage plane. This would lead to a strongly increased image contrast at the QD center and a significantly weaker contrast at the outher parts of the QD in XSTM images, which is not the case for the data shown here. Considering these arguments and the tendency of the measured angles, the QDs studied here most probably seem to be characterized by {111} side facets.

Remembering the ring structure of the QDs, the question still needs to be answered why the QD base is assumed to be square and not circular. Firstly, any cut through a circular QD would result in a cross section showing a rather small angle between the base and the side of the structure, comparable to a cross section through a square QD characterized by {101} facets, while the XSTM images reveal considerably larger angles. Secondly, assuming a circular base, from the XSTM images with a compact QD appearance (like those shown in Fig. 10.1), resembling cross sections through the edge of the ring, a considerably smaller lateral extension of the QD should be obtained in average than from images with paired features (see Fig. 10.3), representing ring structures cut in the center. A ratio of about 0.7 between the average QD extensions in both types of XSTM images would be expected.

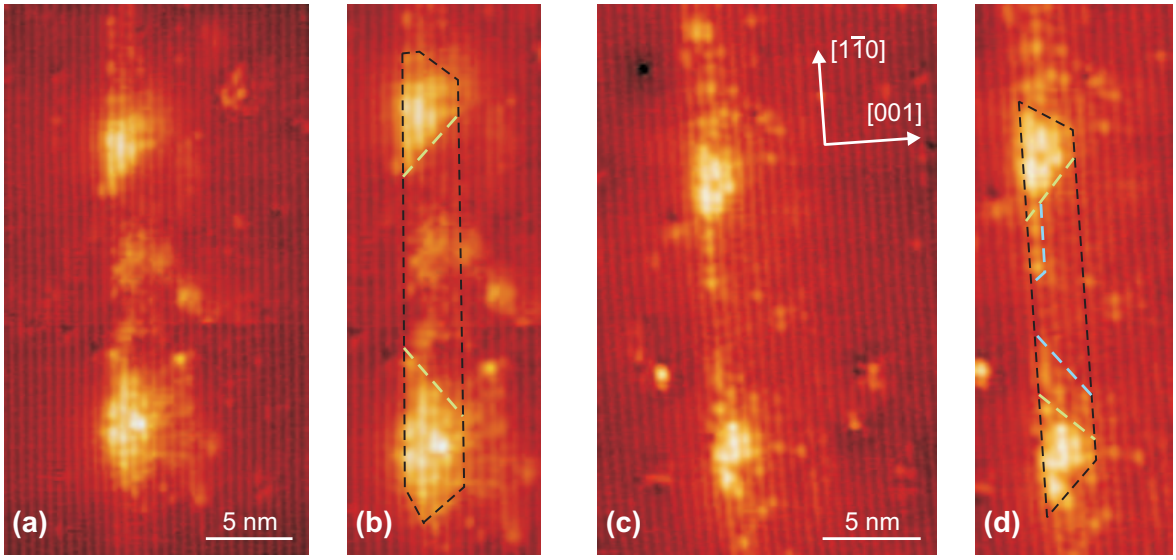

FIGURE 10.3: XSTM images of centrally cleaved ring-shaped QDs in layer 3 of sample C, acquired at (a,b) V_T = -2.3 V and (c,d) V_T = -1.8 V. The outer contours of the QDs shown in (a,c) are marked in (b,d) by black lines, while the inner face of the ring body is marked green. In (d) the area of additional diluted GaSb material within the gap of the ring is indicated by blue lines.

Analyzing the experimental XSTM data, however, the average QD extensions of centrally and marginally cleaved ring structures differ only about 6% to 7%, excluding a circular QD base. The small discrepancy observable in the data, with the larger average length for the centrally cut structures, may indicate that the QD base is also not exactly square but sometimes slightly extended in the center. But it could as well be due to an increased GaSb stoichiometry in the center of the square base compared with its edges, leading to a sharper interface between the QD and the surrounding matrix for the centrally cut structures and a slight underestimation of the actual length for structures cleaved at the edge.

The inner face of the ring body, i.e. the interface between the GaSb QD and the central gap filled with GaAs, is much less regular than the outer QD shape, as it can be seen in Fig. 10.3. It seems to be approximately circular, and generally the diameter of the gap increases from the bottom to the top of the QD. Thus, a cross section through the ring body ideally has a double-trapezoidal shape, with the outer sides slightly steeper than the inner ones, although this shape is often asymmetric or imperfect. Additionally, instead of an abrupt interface between GaSb at the ring body and GaAs in the central gap, often a cross-over characterized by strongly diluted GaSb material can be found, as it is indicated in Fig. 10.3(d).

10.1.2 Local stoichiometry

Knowing the shape of the QDs, the missing information to completely resolve the atomic structure is the local stoichiometry. Therefore, the distance between neighboring atomic chains in growth direction has been analyzed as a measure for the local lattice constant and thus for the chemical composition, as described in detail in chapter 6. The results for two typical QDs of sample C are shown in Fig. 10.4, obtained as averaged data from several XSTM images. The chemical composition has been evaluated separately for the central region and for the outer parts of the QD images, underlining the varying local stoichiometry within one structure.

Focusing at first on the QD shown in Fig. 10.4(a), several details need to be discussed. The GaSb composition is inhomogeneous, varying between the edges and the center of the

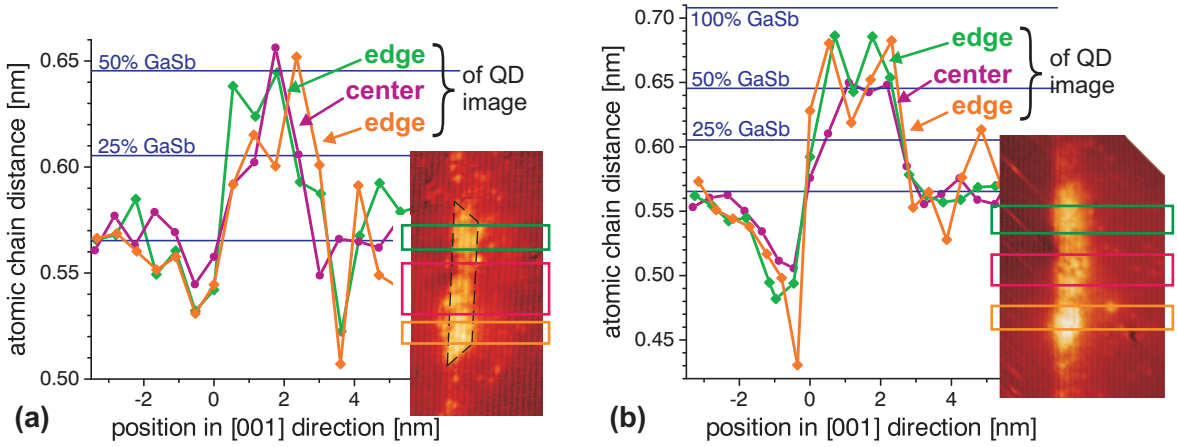

FIGURE 10.4: Analysis of the chemical composition of QDs in sample C: The variation of the local lattice constant for different regions of the QDs shown in the insets is plotted together with calculated values for a $GaSb_xAs_{1-x}$ QW.

structure as well as from bottom to top, with a maximum of about 60% being reached just at some parts of the QD top, while its bottom consists of only 20% to 40% GaSb. The increased lattice constant extends over five atomic chains at the outer parts of the structure, marked in green and orange, but only over four chains at the center of the QD image, marked in purple, which can well be understood remembering the ring shape of the QD: Obviously, this ring structure has been cleaved just at the edge of its central gap, which is widest at the top of the QD, so that the topmost atomic chain of the cross section in Fig. 10.4(a) is already affected by the gap, while the other four chains still resemble the ring body. This idea is further supported by a comparison of an optical inspection of the XSTM image with the chain distance analysis: Although the image contrast is weakest in the QD image center, which usually indicates a lower stoichiometry, the analysis of the local lattice constant yields about the same GaSb composition within the QD also in this area. Thus, the idea mentioned above (section 8.3.1) that the image contrast is significantly affected by the ring structure is nicely confirmed: When a GaSb ring is cleaved slightly in front of the central gap, resulting in a cross section as the one shown in Fig. 10.4(a), the strain related to the GaSb content is lower at the center of the cross section, where the gap consisting of GaAs is behind, than at the edges of the QD image having the GaSb-rich ring body in the back.

The QD shown in Fig. 10.4(b) has a similar shape and size as the one discussed above, but a significantly higher GaSb content, reaching up to a GaSb composition of about 90%, at least at the outer parts of the QD image. For the center of the QD cross section, a slightly weaker GaSb content is obtained, which could indicate that the material near the central gap of the ring is partly diluted. The strain corresponding to the large amount of GaSb incorporated within the ring body is underlined by a very strong undershoot-like reduction of the measured chain distances underneath the QD, extending over about four atomic chains into the GaAs matrix. To a minor part this undershoot stems from a systematic error of the evaluation method due to the local bending of the cleavage surface (see section 6.3), but the major part is actually due to the GaSb-related strain which significantly compresses the underlying GaAs. If the GaSb-GaAs interfaces were equally abrupt at the QD bottom and top, a similar reduction of the chain distances would also be expected at the GaAs above the QD. The fact that no such reduction is present is a strong indication for Sb segregation in growth direction out of the QD. Indeed, in the XSTM image many individual Sb atoms can be seen as small bright spots above the QD. Nevertheless, the GaSb composition is not decreased at the top

of the QD, thus the idea of these indiviual Sb atoms just having segregated from the top layer of a readily formed QD structure is much too simplified, also because a large amount of segregated Sb atoms can be found above the WL, too.

A different approach to further study the chemical composition and the strain distribution in and around the QD analyzed in Fig. 10.4(b) is chosen in Fig. 10.5, showing a regular XSTM image (b), a contour plot (a), and a highpass-filtered image (c) of the same QD. In the contour plot, the complete z range of 1.0 nm is divided into eight intervals separated by black lines, representing lines of the same apparent height. For better contrast, a full color map is used here. Interestingly, the height is not only strongly increased at the QD itself, but also weakly at the regions underneath and above. Underneath the QD, where no Sb atoms are incorporated, the increased height is due to a strain-relaxing outward bending of the cleavage surface. Accordingly, the apparent height is largest at that region underneath the QD edge which corresponds to the strong undershoot of the chain distance analysis shown in Fig. 10.4(b) by the orange curve. Above the QD and the WL, both a structural image contrast induced by strain relaxation and an electronic image contrast from the segregated Sb atoms contribute. The corresponding area of increased apparent height has an extension in growth direction two or three times larger than the QD itself.

In order to differentiate between the long-range structural contrast and the short-range electronic or chemical contrast and therewith between strain effects and the distribution of Sb atoms, firstly the regular STM image of Fig. 10.5(b) was smoothened by averaging every image pixel with its neighbors weighted by a Gaussian distribution. Then 90% of this image background were subtracted from the original image, resulting in the high-pass filtered image shown in Fig. 10.5(c). The WL and especially the QD now appear as an accumulation of many individual bright Sb atoms. In addition, Sb segregation directly above the WL and even more above the QD is evident. The blurred bright stripes visible underneath the QD always in the same distance to the GaSb layer are scan artifacts from the XSTM measurements. Only two or three spots which could be attributed to Sb atoms are present underneath the layer.

Strong Sb segregation can have even more drastic consequences on the QD structure,

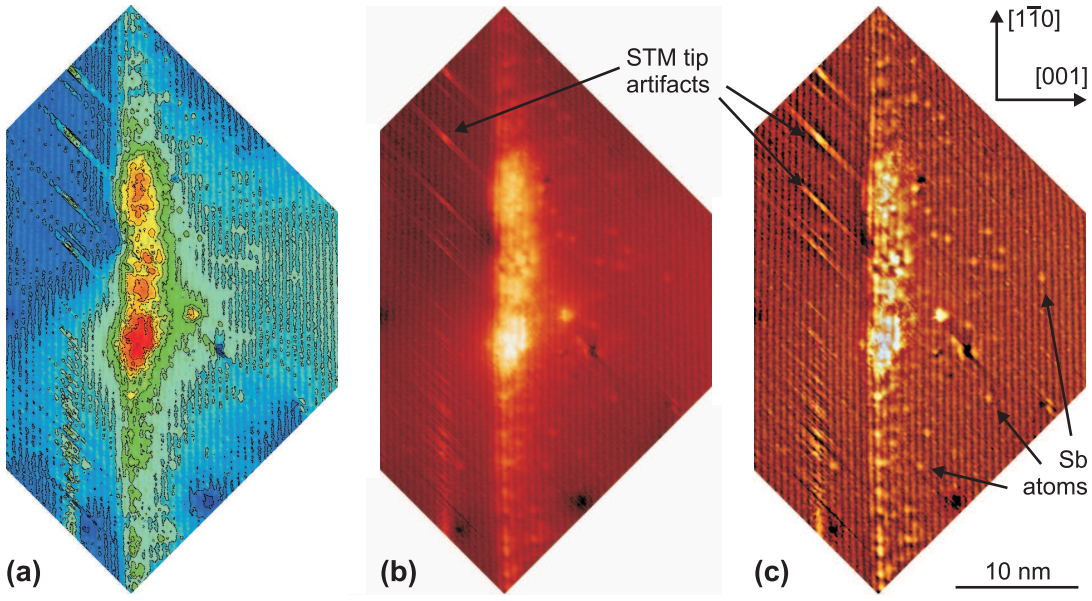

FIGURE 10.5: Filtered XSTM images of the same GaSb QD in sample C, displaying (a) an equal-height contour plot, (b) the regular image, acquired at V_T = -1.7 V, and (c) a high-pass filtered image.

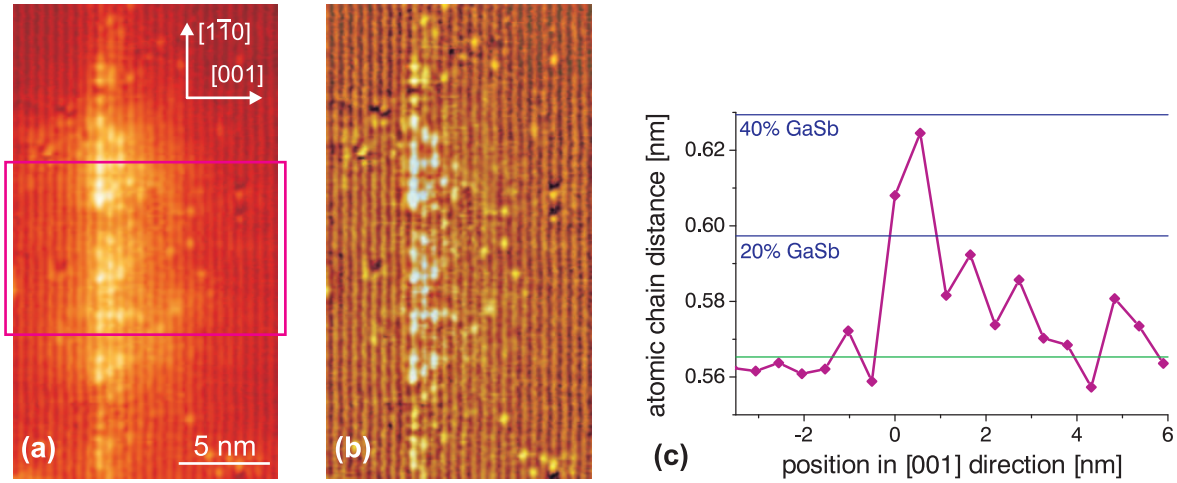

FIGURE 10.6: A diluted GaSb QD in layer 2 of sample C: (a) Filled state and (b) high-pass filtered XSTM image, taken at V_T = -2.4 V, and (c) analysis of the chemical composition.

as demonstrated by the strongly diluted QD shown in Fig. 10.6(a): While the shape of a truncated pyramid with a base length of 15 nm and three atomic chains or 1.8 nm height can still be recognized, within the QD areas of comparatively low image contrast on the one hand and individual bright Sb atoms on the other hand are noticeable. By evaluating the local lattice constant within a broad stripe across nearly the complete QD, a maximum GaSb content of this QD of only about 40% was analyzed [see Fig. 10.6(c)]. While the bottom interface of the QD is relatively sharp, the GaSb composition decreases smoothly from about 20% to zero over five to six atomic chains or 3 nm at the top of the QD and above it. Thus, for this structure the interface between the QD itself and the GaAs overlayer containing segregated Sb atoms is not well-defined any more, in contrast to the QDs shown in Fig. 10.4. Many individual Sb atoms can well be seen in Fig. 10.6(b), showing an XSTM image filtered by background subtraction analogously to the method described above.

Due to the good image quality and the comparatively low GaSb content it is possible to count the individual Sb atoms in the XSTM image of this QD, resulting in a GaSb composition between 30% and 40% in the bottom two atomic chains, about 25% in the third chain, and between 10% and 20% in the fourth and fifth chain. For the next ten atomic chains the GaSb content changes only between 10% and zero. It should be kept in mind that only each second atomic ML can be seen in the XSTM images, and that the strain analysis evaluates the distance between neighboring chains, thus always obtaining the average stoichiometry of two neighboring chains. The good agreement with the counted Sb atoms once more indicates the validity of the stoichiometry determination from chain distance data.

In contrast to this diluted structure, a QD with a chemical distribution considerably different to those discussed yet is shown in Fig. 10.7: Here, a GaSb composition of about 80% in one part and rather pure GaSb in the other part of the ring structure is observed. However, this high GaSb content is concentrated to only two atomic chains, neighbored by one to three chains with a low GaSb concentration of 10% to 20%. This rather compact GaSb distribution within the ring body is accompanied by a QD structure characterized by a large central gap with a ratio of apparent inner to outer ring diameter of $\tilde{r} = 0.5$. As a consequence of this nearly perfect ring structure with its high GaSb content a strongly varying local strain at this structure leads to a considerable bending of the atomic chains directly at the bottom and below the ring body, as shown in Fig. 10.7(b,c).

From a comparison of the chemical compositions of the different QD structures in sample C

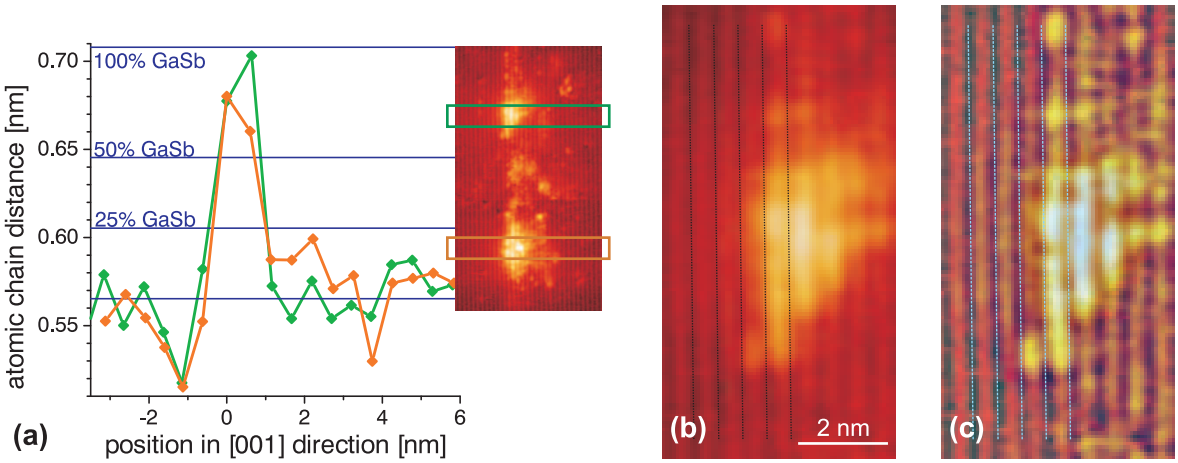

FIGURE 10.7: A GaSb QD in layer 3 of sample C with a compact ring structure: (a) Analysis of the chemical composition, (b) magnification and (c) high-pass filtering of the upper part of the XSTM image shown in the inset of (a), acquired at V_T = -2.3 V. A part of the atomic lattice is indicated by black and blue lines: The atomic chains are bended by the large strain inherent in the ring body.

it seems that the broad distribution of the inner ring radius characterized by a distribution of ring ratios of $r = 0.42 \pm 0.13$ comes along with a distribution of the GaSb content within the ring-shaped QDs, too, ranging from strongly diluted QDs over those with a varying GaSb composition of about 30% to 60% up to structures consisiting of nearly pure GaSb.

For the QDs of sample D, an analysis of the local lattice constant results in an even stronger variation of the GaSb composition both between different QDs and within single QD structures. Considerably high GaSb concentrations are only reached within the bottom two chains of the generally very flat structures, but nevertheless GaSb contents locally reaching about 50% in QDs of layer 2 and up to 80% in QDs of layer 3 are evaluated. In addition, also diluted QD structures with a GaSb composition of only 30% and less were observed.

10.2 Literature data on quantum rings

10.2.1 Quantum ring structures in other material systems

Self-assembled ring-shaped semiconductor QDs, mostly being called QRs, have first been observed in the InAs/GaAs system in 1997 by J. M. García et al. in the group of P. M. Petroff at the University of California in Santa Barbara, USA [202, 223, 224]. Intending to study the initial overgrowth process, they capped InAs QDs with differently thick GaAs layers and studied the growth surface with AFM at ambient conditions. Thereby, after growing InAs QDs at 530°C, capping them with 2 nm GaAs at the same temperature, annealing them also under the same temperature for 30 s to 60 s, and finally cooling them down to room temperature under arsenic flux, islands with crater-like depressions in the center were observed [202]. Later on, the growth conditions were optimized [225, 226] and the QRs were studied systematically using photoluminescence and capacitance-voltage spectroscopy [223, 226] as well as resonant tunneling I-V-spectroscopy [417] and optical spectroscopy for varying external magnetic fields [224, 225]. These electronic results could theoretically be modeled by Barker et al., showing strong dependence on the ring geometry and stoichiometry profile [240].

Usually, the structure of InAs/GaAs QRs was determined using AFM in top-view arrangement [202, 224–227, 418]. An example of such AFM images is given in Fig. 10.8(a), taken from Ref. [227]. These ring-shaped islands, capped with 2 nm GaAs, have a density of

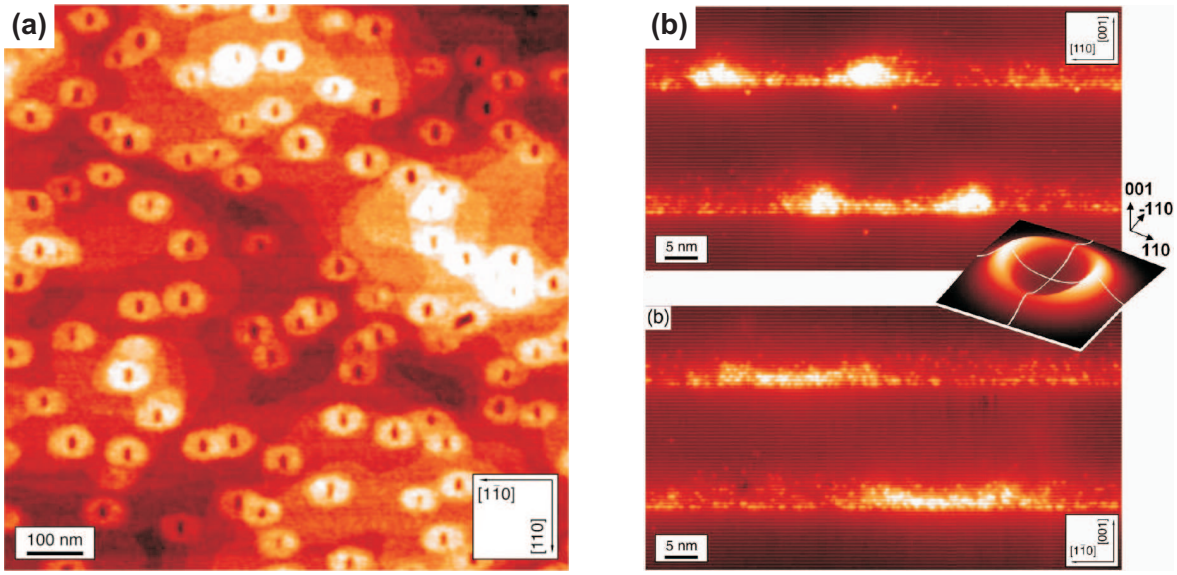

FIGURE 10.8: InAs/GaAs QR structures, from [227]: (a) AFM top-view image of InAs QDs capped with 2 nm GaAs, (b) XSTM images of 2 InAs/GaAs layers containing QRs, cleaved in the (1$\bar{1}$0) (upper image) and (110) plane (lower image), acquired at V_T = -3.0 V. The inset shows a model of the QR structure.

$\sim 1\times10^{10}$ cm^{-2} and are slightly anisotropic, with a larger elongation along the [1$\bar{1}$0]-direction. The outer sizes are about 100 by 70 nm^2 with an average height of about 1 nm. The holes are also asymmetric with a size of 30 by 20 nm^2 and a depth of about 0.5 to 1.5 nm. It should be noted, though, that all these values were acquired from structures capped with 2 nm GaAs using AFM under ambient conditions. From spectroscopic measurements and a modeling of the experimental data, an electronic diameter of the QRs of 28 nm was evaluated [224]. This value is far below the QR sizes obtained by AFM.

This discrepancy could be explained when the structure of completely overgrown InAs/GaAs QRs was studied with XSTM by P. Offermans et al. in the group of P. M. Koenraad at Eindhoven University of Technology, the Netherlands [227, 418]. The samples studied in that work consisted of InAs QDs which were grown by MBE at 540°C, partially capped with 2 nm GaAs, annealed at 500°C for 1 min under As_2 flux, and further overgrown with GaAs. This sequence was repeated several times to form an InAs/GaAs QR superlattice. Two XSTM images of that work are shown in Fig. 10.8(b), comparing cross sections through InAs QR structures in the (1$\bar{1}$0) (upper image) and in the (110) (lower image) cleavage plane.

According to the XSTM results, the corresponding InAs structures are no real rings, as Offerman et al. have stated [227, 418]: "The nanostructures have a crater-like shape which can be attributed to the remainder of the quantum dots after the QR formation process. It can be clearly seen that these quantum craters do not have an opening at the center." The diameters of the InAs structures along [110] and [1$\bar{1}$0] are evaluated to 23 nm and 20 nm, respectively, with a total height of 3.6 nm and an InAs thickness of 1.6 nm at the center of the structure. From comparing the different ring shapes obtained by AFM and XSTM, the authors conclude that only the XSTM images reveal the actual shape of the InAs nanostructures, while the AFM data are dominated by the material additionally deposited during capping. Thus, the apparent rings of the AFM images, having a comparatively large diameter, consist of GaAs rather than InAs.

Meanwhile, the growth of ring-like structures by partially capping and annealing InAs/GaAs QDs has been realized by several other groups, too, using MBE [213, 230, 231]

or MOVPE [228]. Thereby, the ring-like shapes within the growth surface, which had been resolved by AFM, were confirmed with synchrotron x-ray scattering in small angle grazing incidence geometry by M. Sztucki et al. [230]: They used comparatively low temperatures of 490°C during InAs QD growth and 450°C during partial capping of the QDs with 3 nm GaAs and obtained rings with an average outer diameter of 51 nm. These rings had comparatively large craters with 1.7 nm depth and a diameter of 0.8 times the outer ring diameter. Although the shape of the rings has circular symmetry, the InAs concentration, as evaluated by simulating the x-ray intensity maps, varies strongly and amounts to more than 80% along $[1\bar{1}0]$-, but less than 20% along [110]-direction.

Costantini et al. have studied the initial overgrowth of InAs QDs with GaAs for a broader range of growth conditions using STM [35]. They found that the question whether ring-like structures evolve upon partial capping of QDs or not does not only depend on the growth temperature and the thickness of the capping layer, but also on the capping rate: When the InAs QDs were overgrown very slowly (0.08 ML/s), strongly elongated structures without any craters or depressions resulted, but for a faster overgrowth (0.6 ML/s), ring-like structures were observed. The importance of the exact position and duration of the growth interruption taking place after partial capping has been studied in detail in the group of this work, using XSTM [125, 127, 132, 221]: After Eisele et al. verified a total dissolution of formerly existing QDs during an extended GI [221], Lenz et al. even observed the coexistence of conventional InGaAs QDs together with ring-like structures and QDs containing nanovoids within the same WL, all three structures resulting from an interplay of different QD sizes and segregation effects during the GI [127].

InAs/GaAs is not the only material system, apart from the GaSb/GaAs QRs studied here, in which ring-like structures were observed instead of more compact QDs; and a careful comparison of the structural and growth details of different systems will help to understand the formation of QRs. It should be noted, however, that all studies mentioned below have been performed in top-view geometry on free-standing QRs, lacking the information that can possibly be obtained by comparing top-view and cross-sectional investigation, and missing all effects that take place during capping of the QRs. InAs/InP was the second material system for which the formation of ring-like structures was succeeded, obtained by Raz et al. at the Technion–Israel Institute of Technology in Haifa, Israel [232]: Similar to the structures shown above, InAs QDs were grown on InP(001) and partially capped with 1 nm InP prior to a GI of varying duration, all steps were done at 495°C using MOCVD. In AFM studies performed after cooling the sample, large asymmetric rings with outer diameters of about 220 nm along [110] and 110 nm along $[1\bar{1}0]$ were found. However, for PL studies identical samples were further overgrown with InP after the initial GI, and for GI times up to 1 min these samples showed the same PL spectrum as a reference QD sample. Only for GIs lasting 4 min or longer, the PL signal changed significantly, which can be attributed to the formation of QRs. Thus, the transformation of partially capped QDs into these much larger QRs upon annealing takes several minutes here and is therewith drastically slower as in the InAs/GaAs system, where growth interruptions of several seconds are sufficient for QR formation.

Additional insight in the QR formation was obtained by Sormunen et al. at the Helsinki University of Technology, Finland, who also formed InAs/InP QRs using MOCVD [233, 419]: They grew very large InAs QDs on InP at 560°C and annealed them for 10 s or more under either tertiarbutylphosphine (tBP) or tertiarbutylarsine (tBAs), without an additional partial capping. The resulting structures kept a compact QD shape for tBAs flux, but became clearly ring-like upon annealing under tBP at growth temperature. This shows that instead of a directly deposited partial capping layer, also the soaking of the QD layer with resulting group-V P-for-As exchange may trigger QR formation.

Similar results as for the mentioned III-V nanostructures were also obtained in the Ge/Si material system, using both MBE growth [235] and UHV chemical vapor deposition (CVD) [236]: Ge QDs were grown on Si(001) and partially capped with Si. In the case of CVD growth, a 3 min GI followed the partial capping, while at MBE growth, the overgrowth was very slow so that no additional GI had to be performed. With increasing thickness of the cap layer, a QD shape was restored or only slightly changed, ring-like structures evolved, or a smooth growth surface was obtained. In contrast, Mashanov et al. observed a co-existence of QD and ring-like structures after partial capping, using MBE growth [237]. Thereby, the QRs had a larger diameter and height than the partially capped QDs.

In contrast to all ring-like structures mentioned above, GaSb/GaAs is the only material system in which QRs can evolve without any partial capping or soaking step, even without intentional annealing. Kobayashi et al. at the University of Tokyo, Japan, first observed such GaSb/GaAs ring structures [60]: Using MBE, they grew GaSb QDs on GaAs at 490°C and a growth rate of 0.1 ML/s. Omitting the common Sb soaking step, they directly deposited 3.5 ML GaSb on GaAs(001), yielding a spotty RHEED pattern indicating 3D growth. After this, and without any intentional annealing step they cooled down the sample (which probably may have been accompanied by As-for-Sb exchange reactions due to some As background in the chamber) and analyzed the growth surface with AFM. As a result, clear ring-like structures at a density of about 5×10^9 cm^{-2} were observed, with typical outer diameters of 50 – 70 nm, heights of about 1 nm, inner diameters of 15 – 20 nm and depths of the central hole of about 2 nm. When slightly more GaSb material was deposited, GaSb QDs were observed additionally to the QRs, until for 5 ML or more deposited GaSb large, elongated, and relaxed GaSb islands dominated the growth surface. It should be noted, though, that the structural data stem from AFM measurements at ambient conditions, which can partly mislead the size analysis, as discussed above.

10.2.2 Proposed formation of quantum rings

It is generally assumed that InAs/GaAs and similar ring-like structures evolve by a substantial material redistribution during the GI or annealing step following the partial cap. At this growth step, the InAs WL is completely covered by GaAs, while the summits of the QDs probably protrude out of the partial cap layer. This is especially confirmed by the XSTM data on corresponding InAs/GaAs structures: A few nm above the initial InAs WL, at the position where the partial cap layer was finished and an extended GI took place, a second thin InAs layer was observed, which shows that during the GI at this stage In atoms from the partially capped QDs have been spread out over the whole growth surface [127, 227, 418].

In order to explain this material redistribution, basically two different models have been proposed, based either on kinetic or on thermodynamic considerations. The kinetic model describes a diffusion-driven transformation from QDs to QRs [225, 420]: Regarding the lateral diffusion on the growth surface, under typical growth conditions the mobility is much higher for In atoms than for Ga [420], resulting in a strong out-diffusion of In out of the QD center. No compensating in-diffusion can take place as in the direct neighborhood of the QD the growth surface consists of GaAs. Thus, the observed rim around the crater-like depression mainly consists of material that was formerly within the QD center.

Such a diffusion-driven material transport could also explain the often observed anisotropy of the QRs, as In diffusion is preferred along the $[1\bar{1}0]$-direction as compared with the [110]-direction [35, 225, 227, 230], which can be explained by surface reconstructions of the [001] growth surface [179]. However, also the opposite behavior of QRs elongated along [110] was reported for MOVPE-grown structures, being explained in this case by an anisotropy in the migration length of Ga precursors in MOVPE growth [228].

The thermodynamic model focuses on the changes in surface free energy induced by the partial capping of QDs. An equilibrium balance of surface forces, which is given for free-standing QDs, is no longer valid in the changed geometry of partially capped QDs, assuming a pyramidal QD shape. Thus, a net force remains which points radially outward from the QD, inducing a material redistribution from the former QD center into a new-built rim [225, 421]. However, this model implies that the InAs material is considered as liquid, in spite of the InAs bulk melting point at 942°C [164], including a de-wetting process at the QD and a floating In or InAs layer at the growth surface, regarding InAs QDs as wetting droplets [226, 421].

Both models have intensely been discussed in literature regarding different QR systems [60, 225, 226, 230–233, 235]. For InAs/GaAs QRs, some authors favor the diffusion model, as it can explain a significant material transport as well as an inhomogeneous stoichiometry [230]. Others prefer the wetting droplet model and consider the elastic energy as the driving force of QR formation, in combination with a simultaneous Ga-In alloying process, which again is more kinetically driven [226]. Costantini et al. finally proposed that the overgrowth of InAs QDs generally consists of two regimes, the initial one being governed by fast dynamics, which result in island shapes close to thermodynamic equilibrium, while the second regime is controlled by kinetically limited surface diffusion [35].

Considering the formation of QRs in the InAs/InP system, the kinetic model based on different diffusion rates of different group-III atoms can be excluded [232, 233]. Instead, group-V exchange reactions and especially elastic strain relaxation were proposed to be the driving force for QR formation here [233]: At the top summit of free-standing QDs, the local lattice constant is closest to the bulk value of the QD material, therefore this place is very unfavorable for the incorporation of cap material. When InAs QDs are annealed in a P-rich atmosphere, P-for-As exchange occurs at the growth surface and can release some As atoms at the QD summits. These released As atoms will, as a consequence of strain, migrate outward and get incorporated at the side of the QDs, forming a ring around the initial QD.

Also for the Ge/Si material system, strain relaxation is proposed to be the driving force for QR formation [235, 236], while both the diffusion and the wetting droplet model are assumed to be of low significance [235]. Therefore, again the summit of free-standing Ge QDs is the most unfavorable place for Si incorporation, which will drive Si adatoms from the QD center to its side. The more Si gets accumulated at the side of the QD, the more Ge which was previously located at the QD center will also migrate to the side by short-range surface diffusion to alloy with Si. This process leads to a height decrease at the QD center and the formation of a ring structure around.

In conclusion, different processes have been proposed to cause the evolution of QDs into QRs. While In diffusion and the wetting droplet model are most discussed for the InAs/GaAs QRs, from other material systems the relaxation of strain has been favored as main driving force. All models have in common that the ring-like structures that can be seen in top-view geometry on the growth surface have just formed upon partial capping during a subsequent GI or annealing step around the initial QD. These rings thus consist of the cap material, possibly alloyed with the former QD material.

10.2.3 Persistent currents and Aharonov-Bohm effect

Ring-like semiconductor nanostructures can be grown in stacked layers in a similar way as QDs [422], and first attempts have successfully been undergone to use stacked QR layers in classical QD applications like laser devices, yielding shorter lasing wavelengths [423]. However, beside such applications, another aspect of nano-scale QRs regarding fundamental quantum physics is much more exciting, namely the existence of persistent currents and so-called Aharonov-Bohm–type oscillations.

Y. Aharonov and D. Bohm predicted theoretically, already in 1959, that in the quantum regime, charged particles can be influenced by electromagnetic potentials even if they are not affected by any fields and do not feel any forces [424]. An exemplary setup for this effect, proposed by Aharonov and Bohm, is sketched in Fig. 10.9(a): An electron beam is split in two paths and combined again. In the middle of both paths, there is a cylindrical solenoid, meaning a long coil which is formed to a ring, of (nearly) infinite height, so that an magnetic field is only present within the closely packed loops of the solenoid and not outside. Nevertheless, it can be shown theoretically that the passing electrons are influenced by the vector potential in that way that the solutions to their wavefunctions obtain an additional phase term depending on the magnetic flux in the solenoid. So, when the split electron beams are brought together again, interference effects will take place, being solely a quantum mechanical phenomenon. A continuous increase of the magnetic flux will then lead to periodic oscillations of the interference pattern.

Later on, quantum mechanical interference effects based on magnetic fluxes were generally called Aharonov-Bohm effects (AB effects) or Aharonov-Bohm oscillations (AB oscillations), being realized in several different areas of physics [425, 426]. A basic requirement for the AB effect is a strict phase coherence, therefore any phase loss from scattering of the electrons destroys the AB effect. Thus, the electron confinement within a true QR structure is an ideal prerequisite to observe AB oscillations.

An additional, but related quantum mechanical effect in nano-scale rings is the appearance of persistent currents: In a strictly one-dimensional conducting ring, with no electron scattering, a magnetic flux through the ring is expected to produce a persisting equilibrium current, similar as a superconducting ring with a Josephson junction. This was first predicted by Buettiker et al. in 1983 [427], showing that the potential of the ring under the influence of the external vector potential leads to the formation of a (one-dimensional) band structure, in which the k wavenumber of the electron within the band is determined by the magnetic flux through the ring. Evidence for weak persistent currents was, for example, found in copper rings of 0.55 μm size, as the magnetization of these rings oscillated in dependence on an oscillating magnetic flux through the rings [428]. However, temperatures far below 1 K were necessary to avoid substantial electron scattering within these rings of mesoscopic scale.

Considering a charge carrier being confined within a QR (an electron or a hole in an InAs/GaAs QR, a hole in a GaSb/GaAs QR, or a charged exciton), its state probability is mainly restricted to the ring body, but within this the particle can move freely. Thus, the orbiting particle gets influenced by the magnetic flux through the interior of the ring, and the phase of its wavefunction becomes changed. As the wavefunction itself and the exact position and movement of the particle is principally indeterminable according to fundamental

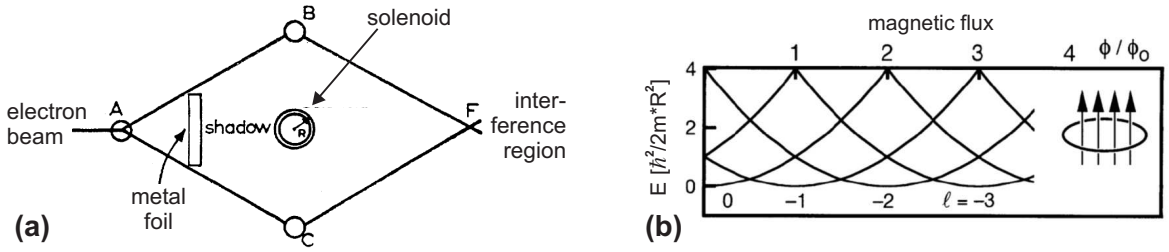

FIGURE 10.9: (a) Experimental setup suggested by Aharonov and Bohm: A coherent electron beam is split into two paths, surrounding a solenoid with a certain magnetic flux, and interferes again; from [424]. (b) Calculated energy levels of an ideal one-dimensional ring for increasing magnetic flux; from [224].

quantum physics, the probability density of a single particle state can be considered as an overlay of contributions from both circular directions, including interference effects. Thus, the corresponding eigenenergies of a single charge carrier within the QR will oscillate with the magnetic flux through the ring. For the occurence of such a AB–type oscillation, it does not matter whether the ring body itself is also exposed to the magnetic field or not, as any direct interaction of confined charge carriers with this field would lead to forces which change continuously with increasing magnetic field, but not to oscillations.

For an idealized one-dimensional QR of radius R in a magnetic field, the energy levels are determined by the periodic boundary conditions to

$$E_m = \frac{\hbar^2}{2m_{eff}} k_m^2 \,, \quad \text{with } k_m = m\frac{1}{R} \,,$$

whereby m is the magnetic quantum number and m_{eff} the effective mass of the charge carrier. When the QR is penetrated by the magnetic flux $\phi = \pi R^2 B$ resulting from a magnetic field B perpendicular to the ring plane, the AB effect leads to an additional phase contribution, and the resulting energies are

$$E_m = \frac{\hbar^2}{2m_{eff}R^2} \left(m + \frac{\phi}{\phi_0} \right)^2 , \quad m = 0, \pm 1, \pm 2, \ldots ,$$

according to [224], with the magnetic flux quantum ϕ_0. Thus, with increasing magnetic field, the minimum of the ground state energy changes from $m = 0$ over $m = -1$ to $m = -2$, and so on, whenever the magnetic flux through the QR is a multiple of the flux quantum. These oscillating energy levels are displayed in Fig. 10.9(b).

The main challenge now is to observe experimental evidence on such AB oscillations in actual ring-like nanostructures. This was first realized indirectly by Lorke et al. for InAs QR-like structures grown by García and Petroff in 1999, using capacitance and far-infrared transmission spectroscopy in dependence on the magnetic field [224]. For this purpose, the QRs were situated within a field-effect transistor, so that the gate voltage could be tuned and thus the number of electrons per ring could be controlled. From the transmission spectra, electronic excitations could be observed at characteristic energies, which shift slightly with varying magnetic field, showing a weak AB–type oscillation. This energy shift with increasing B field, together with corresponding calculated energy levels, is shown in Fig. 10.10(a). These experimental data were an incentive for further theoretical work, which could explain and reproduce the observed capacitance and state-filling results [241] and could model the exact ring geometries and stoichiometry profiles [240]. Just recently, also an astonishingly strong single electron persistent current could be demonstrated for the same nanostructures using a very sensitive torque magnetometer [429].

A more direct detection of the AB effect in QR-like structures was succeeded by Bayer et al., using artificial InGaAs/GaAs QRs of 90 nm and 30 nm outer and inner diameter, respectively, fabricated by lithography techniques: They studied the emission energy of such single QRs and observed clear oscillations of the energy of charged excitons with increasing magnetic field [430].

While the original AB effect is found only for charged particles, also for the electrically neutral exciton AB oscillations in the energy of optically active states have been proposed theoretically [77, 238] and were also observed in experiment [239]. This can be explained by a small spatial displacement between the electron and the hole, leading to a polarization of the exiton, being induced by locally different electron and hole state densities [77, 238, 240] or by a type-II band alignment [77, 239]. The calculated electron density for a GaSb/GaAs QR is shown in Fig. 10.10(b).

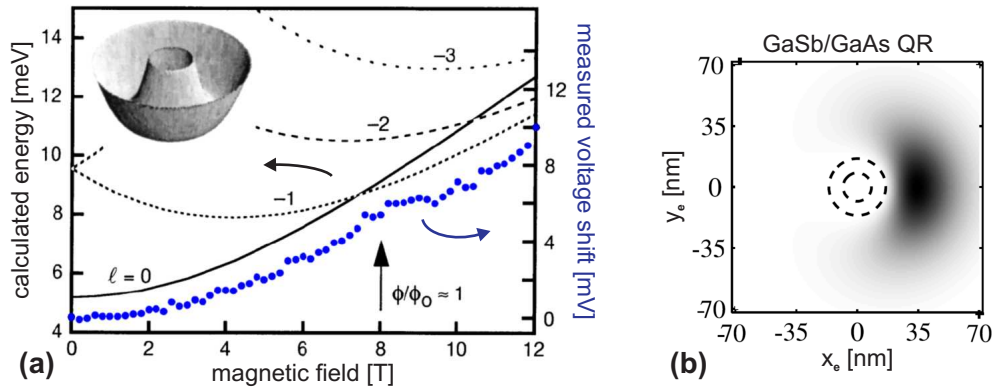

FIGURE 10.10: (a) Calculated energy levels of a wire with a parabolic cross section bent into a ring (see inset) for an increasing external magnetic field. The dotted blue curve represents experimental data (right-hand scale), showing the gate voltage shift of the lowest capacitance maximum of an InAs/GaAs QR embedded in a FET; adapted from [224]. (b) Calculated electron density (without magnetic field) of a GaSb/GaAs QR with an outer and inner diameter of 16 nm and 8 nm, respectively; from [77]. The angular position of the center of the electron density within the ring is arbitrary.

Up to now, AB oscillations have been observed experimentally for type-I QRs [224, 430] and for type-II QDs [239], but not for type-II QRs. However, according to extensive calculations the latter structures are best suited to observe large persistent currents and pronounced AB oscillations [77]. Combining this prediction and the fact that the commonly used InAs/GaAs QRs are no real rings but still contain some intact InAs layers at the bottom center (see above and [217]), the GaSb/GaAs QRs observed in this work are very promising structures to show a strong AB effect.

10.3 Ring formation

Concluding the structural results of this work on MBE-grown GaSb/GaAs QDs, comparing them with literature, and keeping in mind the strong Sb segregation and Sb-As–exchange reactions analyzed in chapter 9, a pathway for the formation of ring-shaped QD structures can be deduced.

10.3.1 Origin of ring formation in the GaSb/GaAs material system

For the comparatively well-known InAs/GaAs QRs, typically the diffusion model and the wetting droplet model (see section 10.2.2) are discussed. Obviously, different diffusion lengths of group-III elements cannot be responsible in the GaSb/GaAs system with a common group-III atom. As the shape anisotropy observed for InAs/GaAs QRs is explained by In diffusion on the growth surface being differently preferred in different directions [35, 225, 227, 230], the lack of a corresponding anisotropy in the GaSb QRs can well be understood.

The wetting droplet model, on the other hand, is based on thermodynamic considerations valid for a sufficiently long growth interruption, taking place after a partial capping of former QDs with a compact shape. No partial capping step was used here, on the contrary, as the GaSb layers were overgrown with at least 10 nm GaAs at fast growth rates of 0.3 ML/s or even 0.7 ML/s. For sample C, this overgrowth took place immediately after GaSb deposition, without any intentional growth interruption. Additionally, an assumption for the wetting droplet model is a perfectly flat base interface of the QDs and QRs, as the liquid droplet does not modify the underlying atomic chains [421]. However, the XSTM data of this work

show unambigiously that the GaAs matrix underneath a GaSb QR is compressed and the atomic positions are shifted (see section 10.1.2), at least for an overgrown sample at room temperature.

Instead, strain relaxation has to be the driving force of QR formation here, as it has already been proposed for the InAs/InP [233] and the Ge/Si system [235, 236]. Also for the InAs/GaAs system, strain has been considered to result – at respective growth conditions – in a dissolution of formerly existing QDs [125, 221] or in the formation of crater-like structures or even nanovoids within QDs [118, 127, 132]. Indeed, between these material systems, the lattice mismatch and strain is highest for GaSb on GaAs, even larger than for InAs/GaAs nanostructures. Strain relaxation is assumed to be the main reason for the truncation of QDs [35, 36, 118] and for the formation of composition profiles within QDs [95, 100] upon overgrowth — here, in the case of QRs, the effects of strain relaxation go even beyond.

The reason why strain relaxation has such drastic consequences in the GaSb/GaAs system lies within the weak Ga-Sb bond and the amount of excess Sb on the GaSb growth surface reconstructions, which by strong group-V exchange reactions lead to the formation of an Sb floating layer and therewith to strong segregation and even to Sb acting as surfactant (see section 9.4.2). These processes cause a partial dissolution of former compact GaSb QD structures upon overgrowth with GaAs.

10.3.2 Growth model for ring-shaped GaSb quantum dots

Considering the effects discussed above and the observed structural results, the following growth mechanism for ring-shaped GaSb QDs is proposed, being sketched in Fig. 10.11:

The growth starts on a GaAs(001) buffer layer (a). During Sb soaking, Sb-for-As exchange occurs at the growth surface, so that about 1 ML GaAs gets exchanged by GaSb (b). At the following direct GaSb deposition, the thickness of the GaSb layer increases until the critical thickness of dot formation is reached and QD growth sets in (c). With further GaSb deposition, the QD density and size increase, including a certain size fluctuation. Until now, the QDs have a pyramidal shape with a more or less sharp summit, which is typical for free-standing QDs, e.g. with rather flat site facets like {137}. The GaSb WL is terminated by a very antimony-rich surface reconstruction of (2x4) or, more probably, (2x8) geometry, and it is probably not completely continuous but interrupted by thin trenches.

When GaSb deposition is finished and the Sb flux is switched back to As flux, the crucial step for the shape evolution of the nanostructures is reached. Within a few seconds of growth interruption or initial GaAs overgrowth, the excess antimony gets released from the GaSb surface and forms a floating layer, and substantial As-for-Sb exchange takes place (d). The shoulders of the QDs possibly undergo less As-for-Sb exchange than the WL as they have another surface reconstruction. Even more important, the strain distribution in the QDs differs from that of the WL, including that upon overgrowth the strain within the sharp summits of the QDs increases drastically as they are forced to fit into the GaAs atomic lattice. As a consequence, the Sb atoms with their rather weak Ga-Sb bonds are repelled from the QD centers and become part of the floating layer. This effect does not only lead to a truncation of the pyramidal shape, as it is also the case in other material systems, but goes further by repelling even more antimony down to the bottom of the QD centers, where it is replaced by arsenic, stabilizing the structure and lowering the strain. When the structures are completely capped, the repulsion and exchange of Sb have lead to an evolution of the formerly compact QDs into QRs (e). Additional to the truncation and the formation of a central gap, the outer contour of the QDs became steeper, as the ring-shaped QDs are now bordered by {111} site facets.

As a consequence of the As-for-Sb exchange, the WL has become strongly intermixed.

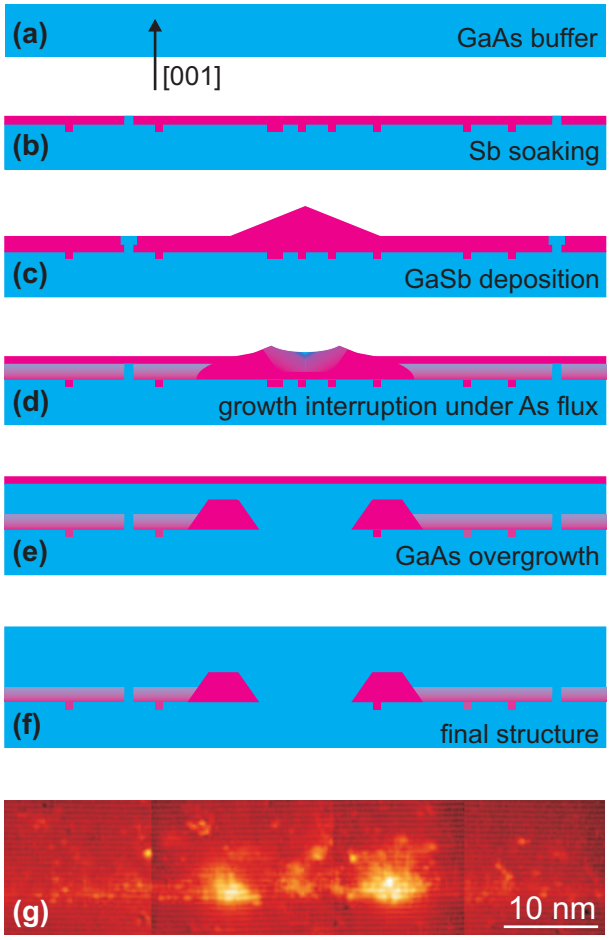

FIGURE 10.11: (a-f) Proposed mechanism of MBE GaSb growth and subsequent GaAs overgrowth, leading to the formation of ring-shaped GaSb QDs: A GaAs buffer layer (a) is initially soaked by Sb (b), resulting in a GaSb layer due to Sb-for-As exchange. Upon direct GaSb deposition (c) the growth of QDs with a sharp summit sets in, which increase in size and density with further deposition, together with an increase of the WL thickness. During a growth interruption under As pressure or when GaAs overgrowth starts strong As-for-Sb exchange occurs (d), leading to a truncation or partial dilution of the QDs and to the formation of an Sb floating layer. The strain-driven shape transition of the QDs into ring-shaped structures is completed upon further GaAs overgrowth (e), together with strong Sb segregation, until finally a diluted WL containing QRs can be observed (f), which is exemplary shown in the XSTM data of (g).

From a floating Sb layer at the growth surface, a lot of antimony gets incorporated upon further overgrowth, forming an Sb segregation profile above the initial GaSb layer (not shown in the model). Finally, when the overgrowth of the sample is completed, the residual antimony which has not become incorporated but acted as surfactant gets completely removed from the nanostructure region (f). The result of this process is a capped GaSb layer containing ring-shaped QDs, as observed in this work (g).

Some details of the proposed growth mechanism deserve to get further discussed:

The exact amount of GaSb which gets incorporated by Sb-for-As exchange during Sb soaking prior to GaSb deposition is unknown for sample C, while it could be determined to about 1.1 ML for sample D. It might well be that random fluctuations of the thickness of this soaking-induced GaSb layer act as some kind of precursors for QD growth: This idea is supported by the observation that the bottom interface of the WL is typically very flat, while for several QDs small protrusions of GaSb material underneath the bottom atomic chain of the WL are observed, as for example in Fig. 10.1(a,b).

A significant difference exists for the growth processes of samples C and D, as in sample D the GaSb deposition was followed by 15 s GI under Sb flux and additional 15 s under increasing As flux, while in sample C no intentional GI took place. Additionally, the growth temperature of 515°C in sample D was 25°C higher than in sample C, further enhancing the surface exchange reactions. As a consequence, the QDs in sample D have a smaller height than in sample C, showing that an increased As-for-Sb exchange process leads to a further flattening of the nanostructures. Probably this flattening is additionally supported by the increased lateral mobility of the surface atoms due to the increased temperature. The importance of

atomic group-V exchange processes was confirmed recently for another material system, also by an XSTM study: Çelebi et al. found that the height of InAs QDs capped with InP was about 2 ML smaller than the height of equally grown QDs capped with InGaAs, which they attributed to a P-for-As exchange process upon overgrowth [130].

Beside the flattening of the QDs, the As-for-Sb exchange also leads to a dilution of the WL, combined with strong Sb segregation into the GaAs overlayer. The QDs are also more or less affected by this dilution process, varying in their chemical composition from less than 20% GaSb content up to nearly pure GaSb. From the XSTM measurements it cannot be concluded if the observed stoichiometry of the nanostructures is completely due to group-V-exchange and segregation processes during the capping or if the initial GaSb growth layer was already intermixed. At least for sample D a rather pure GaSb layer should have been expected, as in the corresponding growth setup the arsenic restgas pressure was specially decreased by using a valved cracker cell. Nevertheless, also this technique could not prevent the resulting QDs from exhibiting an even stronger variation of chemical composition than the structures of sample C, probably due to the longer GI after GaSb deposition and the increased temperature.

Despite the differences in the growth process, all QDs in both samples C and D were found to have a ring-shaped structure instead of a compact one. Even the duration of the GI prior to GaAs overgrowth only influences the exact shape but not the general occurence of the QRs. Thus, the strain-induced formation of QRs probably starts during the more or less extended As-for-Sb exchange process but can also occur within seconds upon a comparatively fast overgrowth. This striking result shows that the self-assembled and spontaneous evolution of compact QDs into QRs upon capping is a general aspect of GaSb/GaAs QD growth using MBE and not only restricted to a small growth window.

It should be reminded that most structural data on GaSb/GaAs QDs in literature have been obtained for free-standing QDs by using AFM [45, 48, 49, 55, 56, 58, 59, 62, 69, 70, 255–257], SEM [267], TEM [62], or STM without atomic resolution [46]. All these studies, confirming a more or less sharp summit of the free-standing QDs, have been performed prior to a possible transition of the compact QDs into ring-shaped structures. Only a few structural results on capped QDs have been published: A part of these were obtained by cross-sectional TEM [45, 59], averaging the strain information over the complete thickness of the sample specimen and thus being unable to detect ring-structures. In other studies the GaSb QDs were capped using exceptionally low temperatures [45], after a special Ga irradiation step [56], or using an additional Au layer [67]. Also strain-sensitive TEM images of GaSb QDs capped by a 50 nm thick GaAs/AlGaAs heterostructure can only show the existence of the QDs but not their exact structure [44, 47]. To my knowledge, there are no structural studies with sufficient resolution to confirm that any GaSb QDs capped under typical growth conditions do actually have a compact structure. Instead, the results of this work strongly suggest that – also for most literature data – the ring-shape is the typcial structure of MBE-grown capped GaSb QDs. This assumption gets further confirmed by the photoluminescence results of sample D shown in section 8.6: Although generally the QD shape determines the energy levels of the confined states and therewith the PL energy [13, 37, 246], the PL peak at 1.11 eV of the ring-shaped QDs in layer 3 of sample D agrees perfectly well with typical GaSb QD PL energies in literature [44, 45, 47, 58, 59, 65, 69].

Besides the formation of the central gap resulting in a ring structure, the shape transition of the GaSb QDs upon capping also includes a steepening of the side facets. Such a steepening is a general aspect of QD overgrowth, which is already known from the InAs/GaAs system, where typically {101} side facets are found [35, 97, 100, 118, 122]. Here, even steeper {111} side facets are obtained for the QDs in sample C. From simple geometric considerations it can

be concluded that the compressive strain at the top of a GaSb ring structure is significantly lower than it would be for a respective compact QD with a truncated pyramidal shape. Therefore it is energetically favorable to increase the material content in the upper part of the ring body and thus to form steeper side facets.

The comparison of the structural results of layers 1 to 4 of sample C still keeps some challenging questions. All four layers contain ring-shaped QDs at a density increasing from layer to layer, while the average QD size is significantly smaller for layer 1 but similar for layers 2 to 4. Astonishingly, the WL of layer 1 contains less than half the amount of GaSb than those of the other three layers, although QD formation had set in and therefore this WL should have reached the same critical thickness of dot formation as the other three. This effect may partly be explained by different Sb extraction from the WLs upon overgrowth due to the formation of an Sb floating layer: Prior to layer 1, no such floating layer exists, but once some GaSb has been overgrown, the surfactant nature of antimony probably leads to a permanent Sb floating layer at the growth front until the whole sample is completed. Thereby the initial floating layer has to be built of Sb atoms originating from layer 1 by strong As-for-Sb exchange, while at layers 2 to 4 the surfactant Sb layer already exists. However, it is hardly imaginable that this effect alone can lead to the observed GaSb content in the WL, being three times larger in layers 2 to 4 than in layer 1.

Instead, it seems as if the formation of GaSb QDs cannot sufficiently be described by Stranski-Krastanow (SK) growth, but is a combination of the SK and Volmer-Weber island growth mode, meaning that after the initial formation of three-dimensional structures further GaSb deposition leads to an increase of the size and density of these QDs as well as to an increase of the WL thickness. The gaps which are observed in the XSTM images of all GaSb WLs further support this idea of an combined SK and island growth mode: Although the formation of trenches between interconnected 2D GaSb islands upon GaSb layer growth has directly been observed only for growth conditions without an Sb soaking step yet [45, 46, 257], the gaps in the WLs of samples C and D indicate a similar GaSb island growth process even upon a combination of Sb soaking and direct GaSb deposition using MBE.

While from layer 1 to layer 2 of sample C an increase of both the average QD size and the thickness of the WL is observed, surprisingly layers 2 to 4 contain about the same total amount of GaSb, namely 2 ML, in spite of the additional GaSb deposition. Therefore, the strain within the GaSb layers may play a double role: While the strain is the driving force for the formation of QDs and also for the transition of such compact QDs into ring-shaped structures upon overgrowth, there also seems to exist an upper limit of total strain in the complete layer: When this limit is reached, any additional antimony seems to get repelled from the GaSb layer upon overgrowth.

Obviously some of the ideas and specific growth aspects discussed in this section cannot be taken as secure conclusions but need further investigation in forthcoming experiments. However, the main mechanism of spontaneous QR formation, which is observed uniquely at the GaSb/GaAs system, could unambigiously be resolved, being the combination of large strain and the possibility to easily repell or exchange Sb atoms from the strained structures upon overgrowth.

Chapter 11

Electronic properties and type-II band alignment

Most existing or intended applications of GaSb/GaAs QDs rely on the large hole confinement energy and the type-II band alignment (see sections 2.4.1 and 2.5). Also the QRs are very promising structures for a superior realization of phenomena like the Aharonov-Bohm effect due to the assumed type-II alignment (see section 10.2.3).

On the other hand, the structural and compositional analysis of the observed nanostructures by XSTM has shown that many of the structures are strongly intermixed with GaAs, raising the question whether these structures still show a type-II alignment or are instead of type-I.

In literature the exact band structure of intermixed $GaAs_{1-x}Sb_x$/GaAs QDs in dependence on the Sb content can, to my knowledge, not be found yet. However, several studies have investigated the electronic properties of $GaAs_{1-x}Sb_x$/GaAs QWs for different x values: A type-II band alignment has unambigiously been evaluated for a stoichiometriy of $x = 0.3$ [76], and also for Sb contents down to $x = 0.17$ [275] or $x = 0.16$ [431] type-II behavior was observed, while QWs with $x = 0.12$ were found to be of type-I [432]. Liu et al. finally evaluated the transition from type-I to type-II to occur at $x = 0.14$ [169, 276].

Accordingly, the band alignment of the intermixed GaSb layers studied here can strongly be expected to be a type-II one. Nevertheless, an experimental confirmation of this assumption especially for the intermixed QDs and QRs, which have not been dwelled on in literature, is essential. Besides the knowledge about the existence of a type-II or type-I alignment, also the determination of the exact band structure would be desirable, including the often discussed amount of the VB offset [44, 67, 68, 75–77]. It should be reminded here that in most cases the published band alignment has not been measured directly, but the type-II alignment is derived from an observed blueshift of the luminescence with increasing excitation energy [47, 65, 66].

A more direct way to locally study the electronic properties including the band alignment is to analyze their influence on STM images or to directly measure the LDOS using STS imaging or STS point spectra, which is the focus of this chapter: GaSb/GaAs nanostructures exhibit a unique image contrast mechanism which is related to the strong CB offset, the type-II band alignment, and effects due to tip-induced band bending. Understanding this contrast mechanism, STS or CITS images of GaSb QDs can be interpreted; and finally from STS point spectra, acquired at different positions at and around GaSb QDs and QRs, the local band alignment can be derived.

11.1 Specific image contrast

In STM images on cleaved semiconductor nanostructures, the image contrast is generally given by a structural contribution, displaying the outward protrusion of the partly relaxed nanostructure, and by an electronic contribution (for details see section 3.3). Therefore, from the appearance of GaSb/GaAs nanostructures in XSTM images, conclusions on their electronic properties can be drawn.

11.1.1 Bias-dependent appearance of GaSb/GaAs quantum wells

It has been explained in section 3.2.3 and shown in section 9.1 that the polarity of the tunneling bias determines which sort of atoms is imaged. As a consequence, the local chemical composition and atom distribution of the GaSb/GaAs nanostructures is better resolved at a negative polarity, imaging the different group-V atoms; while at a positive polarity, showing the common Ga atoms, the strain-driven structural protrusion of the cleaved material dominates. A corresponding behavior is also well known from other material systems like InAs/GaAs nanostructures, in the latter case with different group-III elements being distinguished at positive sample bias [100, 127].

Unique for these measurements on GaSb/GaAs nanostructures, however, is the image contrast behavior shown in Fig. 11.1: At positive sample voltages all nanostructures appear smoothly broadened with an image contrast changing from GaSb to GaAs over several nm (a,d,f), while at negative sample voltages the QDs (b,c) and especially the QWs (e)

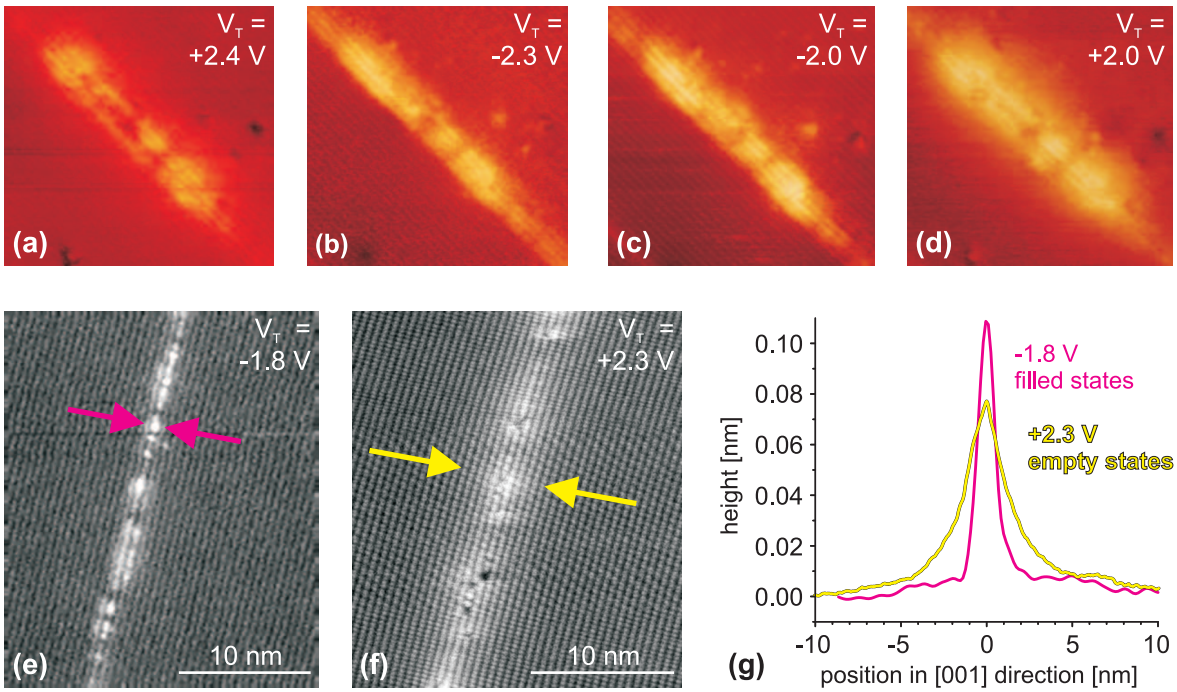

FIGURE 11.1: Specific STM image contrast of GaSb/GaAs nanostructures, shown at (a-d) an MBE-grown QD of layer 2 in sample C and (e-g) the MOCVD-grown QW of layer 2 in sample B. In empty state images the neighborhood of the QDs appears brighter than the GaAs matrix far away (a,d), while in filled state images the apparent change from QD to GaAs contrast is very abrupt (b,c), independent of the amount of the voltage. Especially a QW appears very thin and sharply defined in filled state images like (e), while the same QW looks smoothly broadened in empty state images like (f), as indicated by arrows. Apparent height profiles across the QW, smoothened in growth direction to exclude the atomic corrugation, are shown in (g).

are sharply defined. It should be noted that the interfaces of the MBE-grown QDs actually are somewhat blurred, in contrast to the MOCVD-grown QWs. Although the filled states images, showing the As and Sb atoms, are expected to look rougher due to the short-range chemical fluctuations of the intermixed nanostructures, this effect is by far not sufficient to explain the strong discrepancy observed in the images.

The different tunneling behavior at both polarities can more quantitatively be seen in height profiles, which were taken across the QW shown in Fig. 11.1(e,f). After smoothening the profiles to exclude the atomic corrugation, these height profiles underline the different appearance of the same QW at different polarity (g). A nearly step-like increase of the tip height at the interface of the QW imaged with negative sample bias is evident, while the apparent height increases smoothly over an area of about 10 nm when imaged with positive sample bias. If the broaded appearance of the nanostructures in empty state images was due to strain, the same strain should occur also in filled state imaging, which is unambigiously not the case.

In order to explain this specific GaSb/GaAs image contrast, the staggered type-II band alignment has to be considered, in combination with the effect of tip-induced band bending (TIBB, see section 3.2.2). The proposed contrast mechanism is schematically shown in Fig. 11.2: TIBB occurs in the sample at the position of the tip, locally bending the bands near the sample surface. At positive sample voltages the bands are bend upwards, so that the VB

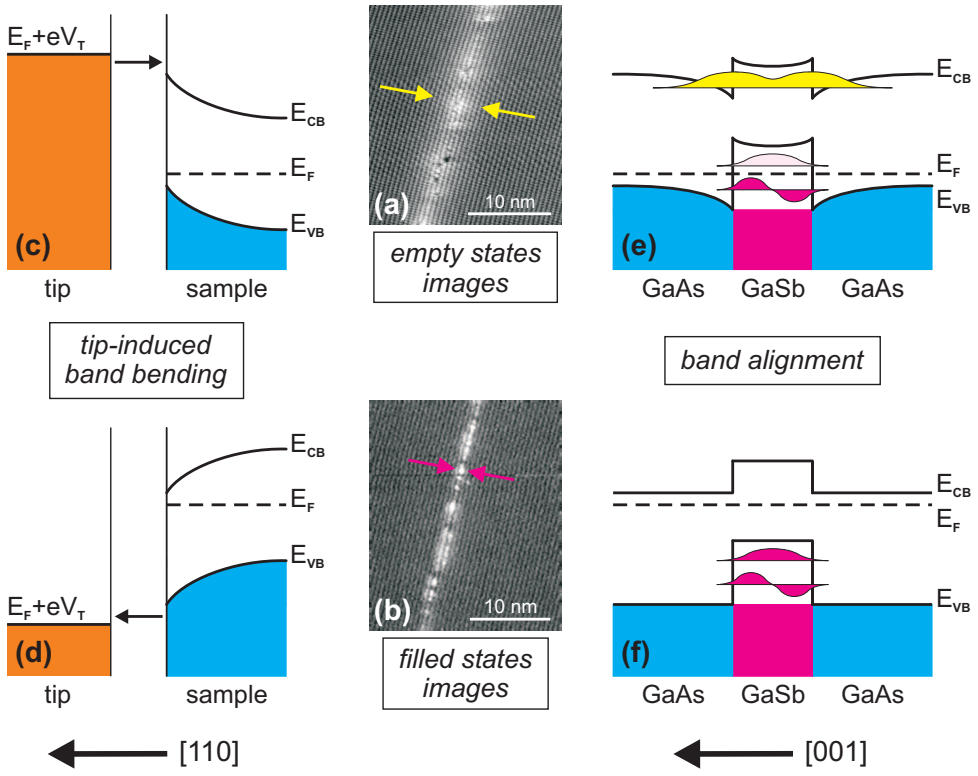

FIGURE 11.2: XSTM image contrast mechanism of GaSb/GaAs nanostructures, leading to (a,b) the strongly different appearance at different bias polarity: The effect of tip-induced band bending is shown for (c) empty state and (d) filled state imaging. As a consequence, the band structure is locally shifted at the nanostructures with respect to the Fermi energy (e,f), which in the case of positive sample voltages can lead to a charging of the nanostructure and an additional band bending. The direction of the band bending is indicated at the bottom. Band offsets and the amounts of band bending are not drawn to scale, and the depicted wavefunctions (e,f) are only for illustration, corresponding to filled VB states (magenta), empty VB states (pink), and empty CB states (yellow).

shifts close to the Fermi energy, which remains fixed, as shown in Fig. 11.2(c). Analogically at negative sample voltages the bended CB gets near the Fermi energy (d). In the latter case, all electronic states in the GaAs and GaSb CB are empty and the VB states are filled, so when the filled states are imaged a clear increase of the tunneling current results directly at the position of the GaSb due to the VB offset and the high LDOS of localized states, as sketched in (f). At positive sample voltages, in contrast, the GaAs bulk VB maximum comes so close to the Fermi energy that the energetically highest localized GaSb VB states shift above the Fermi level. As a consequence these states get depleted of electrons or – in other words – filled by holes, resulting in a net charge of the structure. Such a charge will in turn lead to a band bending parallel to the sample surface, inducing weakly localized CB states in the GaAs surrounding the GaSb (e). These empty GaAs CB states, which are localized within a few nm around the GaSb nanostructure, lead to an increased current in empty state imaging, strongest close to the nanostructures but smoothly declining over a few nm.

Accordingly the sharply defined, thin QW appearance upon filled state imaging actually corresponds to the electronic VB states of the GaSb QW [magenta states in Fig. 11.2(f)]. At empty state imaging, in contrast, the increased tunneling probability from CB states of the GaAs directly surrounding the QW [yellow states in Fig. 11.2(e)] causes the broadened appearance. At both polarities, also the different tunneling probabilities into the GaAs and GaSb states contribute to the XSTM signal, which is further influenced by the strain-induced structural contrast of the nanostructures.

11.1.2 Calculation of tip-induced band bending and tunneling current

In order to verify the model described above, calculations on the amount of TIBB and simulations of the resulting tunneling current were performed by R. M. Feenstra at the Carnegie Mellon University in Pittsburgh, Pennsylvania, USA. For these simulations, he assumed an STM tip with 10 nm radius of curvature and an opening angle of the apex of 90°, a GaSb layer width of 2 nm, and a band alignment for an undoped GaAs/GaSb/GaAs QW heterostructure with a VB offset of 0.6 eV and a type-II CB offset of 0.1 eV. With these values, Poisson's equation was numerically solved using a finite element method as described in Ref. [433]. Thereby the tip-vacuum-semiconductor configuration including the specific shape of an STM tip was parameterized by a specific coordinate system using so-called "prolate spheroidal coordinates" [433], generalized here for three dimensions.

The resulting calculated band bending is given in Fig. 11.3(a): The electrostatic potential energy variations at the cleavage surface directly opposite the tip apex are plotted as a function of the tip position relative to the center of the GaSb QW. Thus, the variation of the TIBB across the QW in [001] direction can be tracked in that curve. Surface potential energies are shown for four different sample voltages of V_T = +2.5 V, +2.0 V, -2.0 V, and -2.5 V, corresponding to different moderate bias voltages at both polarities.

For positive sample voltages, the band bending at the sample surface opposite the tip strongly varies as the tip moves from the GaAs matrix to the GaSb QW and further on. The effect is qualitatively the same for both exemplary values of V_T = +2.5 V and +2.0 V, but increases in size with increasing voltage. In order to understand the potential variation, again the model of the contrast mechanism shown in Fig. 11.2 needs to be considered: At sufficiently large positve sample voltages, the GaSb is partly depleted of electrons [Fig. 11.2(e)], so that the resulting charge density pins the Fermi energy and prevents a stronger band bending. As the tip moves away from the QW and the GaSb states increasingly get out of the influence of its electric field, a stronger band bending is necessary to compensate the charge of the tip.

In contrast, for negative sample voltages the potential energy profiles shown in Fig. 11.3(a) are relatively flat, with the amount of TIBB being comparatively large over the complete

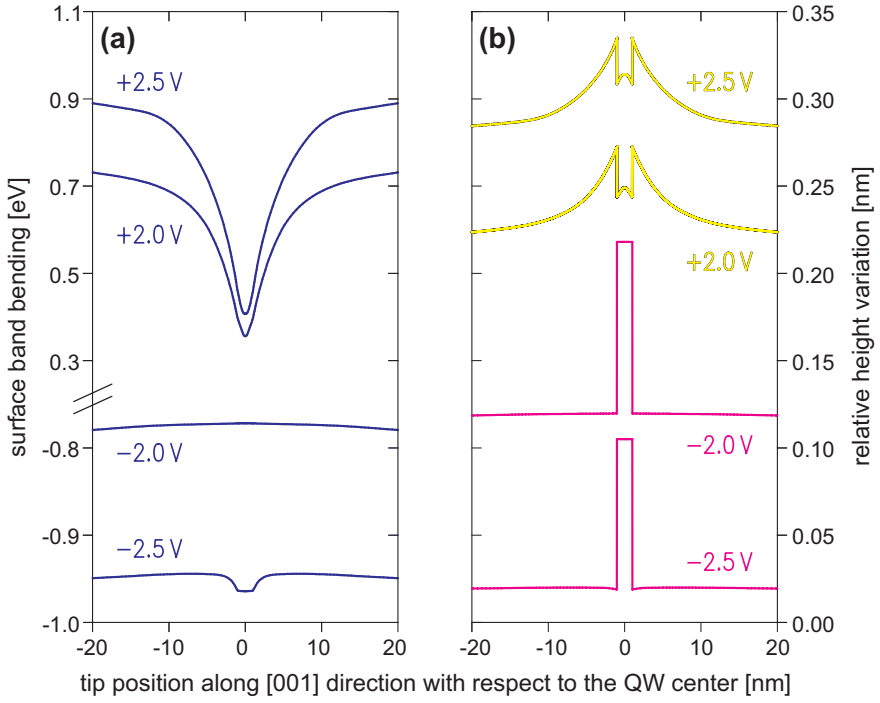

FIGURE 11.3: (a) Calculated electrostatic potential variation at positions on the sample surface directly opposite the STM tip apex, plotted in [001] direction relative to the center of a GaSb QW for different sample voltages. (b) Simulated tip height variations obtained from (a), with arbitrary zero levels.

heterostructure. Significant differences between the GaSb and GaAs area only occur for larger amounts of sample voltage, where also the amount of band bending is increased, but these differences still have a much weaker extension than for positive voltages. This strong band bending both at the GaAs and GaSb corresponds to a Fermi energy being close to the CB minimum, which for GaSb lies even slightly above the GaAs value [Fig. 11.2(f)]. At larger negative voltages like V_T = -2.5 V the TIBB seems to be large enough to pull the CB close to or under the Fermi energy, as in that case the small GaAs/GaSb CB offset leads to the observed specific behavior at the GaAs/GaSb interface [Fig. 11.3(a)].

Accordingly, the assumed band alignment shown schematically in Fig. 11.2(e,f) is well confirmed by the calculations, especially for smaller bias voltages of both polarities.

Taking the band bending results, tunneling currents were simulated in a semi-classical approximation using effective-mass bands, following a method described in Refs. [107] and [302] for a one-dimensional potential and extending it for the three-dimensional case. Effective masses for the CB and VB of 0.063 and 0.53 for GaAs, respectively, and 0.041 and 0.82 for GaSb were used, taken from Ref. [164]. With the GaAs electron affinity $\chi = 4.07$ eV and an assumed tip work function of $\phi = 4.74$ eV, which is well in the range of possible tungsten work functions for different crystal geometries [434], flat-band conditions occur for zero sample voltage. The tip-sample distance at the GaAs matrix was assumed to be 0.8 nm.

The resulting tip height variations are shown in Fig. 11.3(b), plotted in yellow for positive sample voltages of V_T = +2.5 V and +2.0 V and in magenta for negative voltages of V_T = -2.5 V and -2.0 V. The curves are shifted in height for better visibility, so the given values are only relative and do not indicate absolute heights.

For negative voltages, the simulated current profiles display a narrow maximum at the QW, sharply defined at the GaSb/GaAs interfaces, which resembles well the contrast observed in STM images like the one shown in Fig. 11.2(b). It should be noted that the calculations are based on electronic properties like band offsets and TIBB and do not take into account the strain-induced structural protrusion of cleaved nanostructures. Additionally, the calculations assume that the material interfaces are abrupt and that the tunneling current is confined to the position at the cleavage surface directly opposite the tip apex. Due to these restrictions

the rectangular profiles of the simulated tip height do not exactly match the slightly broadened actual profiles at negative bias, like the measured one displayed in Fig. 11.1(e,g). The apparent heights of the GaSb QW of 0.1 nm at the calculated profile for V_T = -2.0 V and slightly more than 0.1 nm at the measured profile for V_T = -1.8 V agree nicely.

The tip height profiles calculated for positive voltages exhibit a strongly different shape: They are quite broad, independent of the amount of voltage, with the tunneling probability increasing over a range of 20 nm as the tip is approaching the GaSb QW. This broad increase resembles well the smoothly broadened appearance of the GaSb QWs in actual STM images, like the one shown in Fig. 11.1(f,g).

A discrepancy between simulated [Fig. 11.3(b)] and measured [Fig. 11.1(g)] profiles exists directly at the position of the QW for positive sample voltages: Here a slight depression of the tip height is calculated, as the number of states available for tunneling is decreased at the GaSb due to the type-II CB offset. However, as this depression is not present in the measured GaSb QW profile, it can be expected that quantum effects reduce or completely eliminate this decrease of tunneling probability, which is not considered in the present semi-classical calculation. Regarding the situation at the CB near the GaSb QW for positive voltages, the states concentrated at the GaAs near the QW will show a considerable tailing into the GaSb band gap, as already depicted by the yellow area in Fig. 11.2(e).

The amount by which the empty GaAs CB states penetrate into the GaSb band gap region can roughly be estimated using the model of a one-dimensional finite potential barrier [141]: Regarding a barrier of width Δx and height V_0, the quantum mechanical tunneling probability $T(E)$ for states with energy E is given by

$$T(E) = \frac{4\epsilon}{4\epsilon + (1+\epsilon)^2 \sinh^2\left(\frac{1}{\hbar}\sqrt{2m_{eff}(V_0 - E)}\Delta x\right)} \quad \text{, with } \epsilon = \frac{V_0 - E}{E}\,.$$

Using the GaAs CB effective mass m_{eff} of 0.063, a CB offset $V_0 = 0.1$ eV, a barrier width of half the WL height $\Delta x = 1$ nm, and a room temperature energy $E = k_B T = 0.025$ eV, the tunneling probability for a GaAs state results to $T(E) = 0.85$. Therefore the GaAs CB states extend throughout the complete GaSb QW without significant decrease of their amplitude. Correspondingly also no measurable decrease of the tunneling probability directly at the QW should be expected, which is exactly the case in the STM images [Fig. 11.1(f,g)].

While this consideration is valid for thin QWs, the situation may change when QDs with a larger height and much more initial strain are imaged, the latter resulting in an increased CB offset (see section 2.4.1). As a consequence, a decrease of the tunneling current in the center of QDs imaged at positive sample bias can be expected. Indeed, a thin region of darker appearance can be seen in the QD images of Figs. 11.1(a,d), acquired at $V_T = +2.4$ V and +2.0 V, respectively. This dark region is not present in the images of the same QD taken at negative sample bias, shown in Figs. 11.1(b,c).

Although all these observations and simulation results support the model of a type-II related XSTM image contrast as introduced above, one assumption of the model needs to be further discussed: For positive sample voltages, the model implies that the GaSb QD states within the VB are partly depleted of electrons, which induces a charging of the system. Though the GaSb layers and the surrounding GaAs are undoped, the wafer and the cap layer of both MOCVD-grown samples are n-doped, so that the whole sample can be regarded as slightly n-type. In this case, an electron depletion in the GaSb corresponds to the situation of inversion (see section 3.2.2), as the electrons being the majority charge carriers are replaced by holes.

The question whether inversion occurs at all upon STM imaging of semiconductors is currently discussed by several authors like R. M. Feenstra, N. D. Jäger, and Ph. Ebert

[138, 330, 435]. Based on experimental findings and theoretical considerations inversion was excluded for bulk GaAs with a band gap of 1.4 eV [330, 436], while it was observed for Ge samples, for which a surface band gap (considering a reduction of the bulk band gap by surface states) of 0.5 eV was obtained [138, 435]. The reason is that for the occurence of inversion charge carriers necessarily have to tunnel across the band gap of the sample, which in principle is possible if the bands are sufficiently bent at the space charge region by strong TIBB, and this tunneling current decreases exponentially with increasing band gap energy [138, 330]. At the GaSb/GaAs nanostructures, the band gap between the GaSb VB maximum and the GaAs CB minimum accounts approximately to about 0.8 eV – or slightly more due to the localized nature of the GaSb states. Nevertheless, for this value an occurence of inversion can be expected [138, 436]. Even more, the observed image contrast gives strong experimental evidence for the existence of inversion at GaSb/GaAs QWs.

For the MBE-grown samples the situation is less critical, as the cap layers are undoped (sample C) or even p-doped (sample D) and thus the structures are not n-type. Accordingly, the occurence of electron depletion at the GaSb layers can more easily be realized for the MBE-grown samples, especially for sample D.

In conclusion, a specific contrast mechanism is observed in XSTM imaging of GaSb/GaAs nanostructures, consisting of an interplay between the type-II band alignment and tip-induced band bending. At negative sample voltages, the effect of TIBB is nearly the same both at the GaAs and the GaSb, and the nanostructures appear sharply defined as the filled VB states and the additional confined states of the GaSb are imaged. For positive voltages, the amount of TIBB is stronger at the GaAs as the GaSb is partly depleted of electrons, which in the case of n-type doping corresponds to inversion. As a consequence weakly localized electronic states exist in the GaAs neighboring the nanostructure. These states contribute to the tunneling current upon empty state imaging, together with the VB states and, to a small extent, with the depleted GaSb states, resulting in a smoothly broadened appearance of the GaSb structures.

11.2 Probing the confined states: CITS imaging of GaSb nanostructures

Conventional STM imaging of GaSb/GaAs nanostructures is limited regarding the analysis of electronic properties by two restrictions: Firstly, STM in the constant current mode does not probe electronic states at discrete energies, but a weighted average of states between the Fermi energy E_F and the energy corresponding to the tunneling bias $E_F + eV_T$. Secondly, it is obviously not possible to acquire STM images at bias voltages corresponding to band gap energies of the host material, therefore the imaged localized states of the nanostructures are always superposed by resonances and bulk states.

Both restrictions can generally be overcome by use of lock-in technology to image the differential conductance dI/dV and by performing current imaging tunneling spectroscopy (CITS), as described in section 3.2.4. Using these techniques to study III-V semiconductor nanostructures is challenging due to the relatively large bandgap of the materials, the required mechanical and electronic stability of the STM system, and especially regarding the stability and electronic uniformity of the probe tip. Only a few, though impressive studies on localized QD states using CITS technique have been published, based on current images [108, 109] and dI/dV data [110].

A first series of CITS images at GaSb samples is shown in Fig. 11.4(a-e), taken at the WL of layer 1 in the MBE-grown sample C: While a regular STM image (a) was taken in constant current mode at a stabilization voltage of V_T = -2.3 V, at a grid of 64 times 64

points the image aquisition was stopped, the feedback loop was opened, and the bias voltage was stepwise varied up to -1.0 V. After such a voltage ramp, during which the corresponding current was measured at specific voltages, the feedback was enabled again, the tunneling current was stabilized, and image aquisition was continued until the next point of the grid was reached. From the currents at every grid point a current image can be computed for each of the specific voltages (c-e), in addition to the STM image. Regarding the voltages applied here for CITS, the images are expected to correspond to energies within the GaAs VB and even slightly above.

The GaSb WL is clearly visible in the constant current topography image of Fig. 11.4(a) by its inhomogeneously increased contrast, consisting of Sb-richer and Sb-poorer areas. The oscillation of the contrast appearing in the image under an angle of about 50° towards the WL is due to the time delay produced by the voltage ramp which causes thermal drift at each grid point. In the current image (b), acquired simultaneously with the filled state image (a) at the stabilization voltage, no structures at all can be seen, just as it is expected for constant current imaging. However, at smaller absolute values of the voltage, realized by the CITS technique, the WL is apparent in the current images, too, as shown in (c-e). The position of the tip was controlled by the feedback loop in such a way that constant current conditions were fulfilled at V_T = -2.3 V, meaning that the tip-sample distance was already increased at the GaSb WL. The fact that nevertheless the WL has a brighter image contrast in the CITS images shows that for decreasing absolute values of the voltage the current decreases faster at the GaAs than at the GaSb. This effect gets even more pronounced when the contrast range

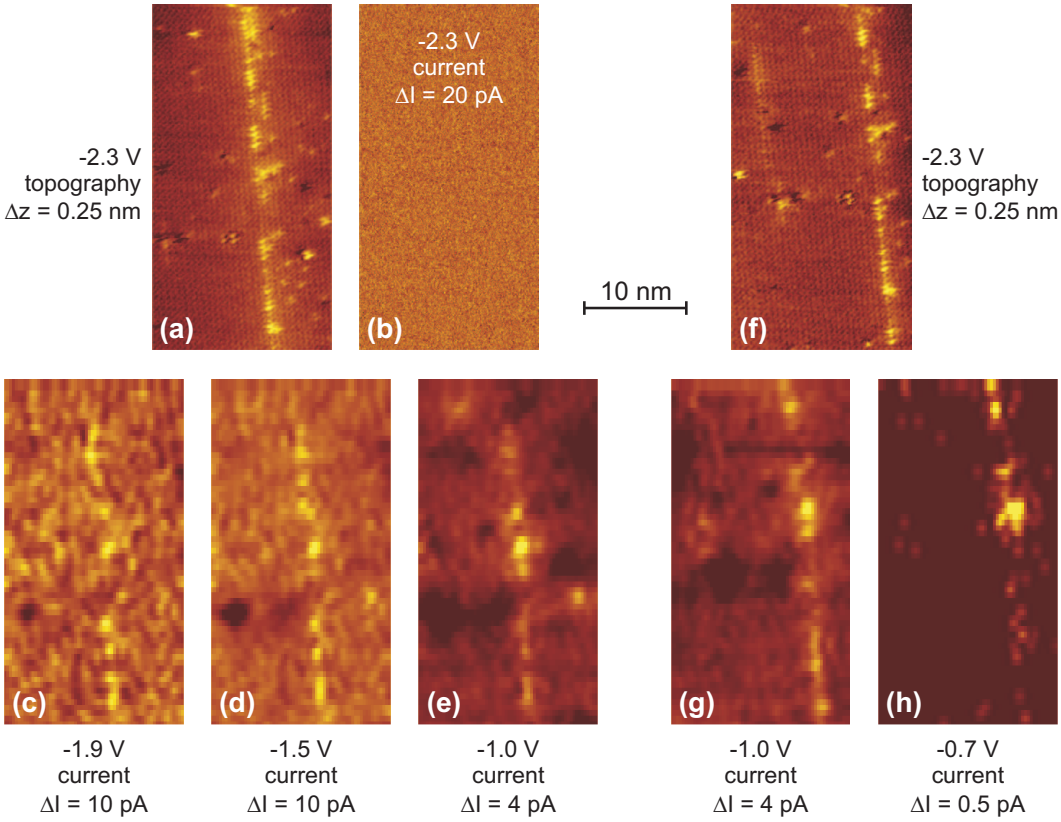

FIGURE 11.4: CITS imaging of the WL of layer 1 in sample C: (a,f) constant current filled state images, acquired at the stabilization voltage of V_T = -2.3 V, (b) the current image corresponding to (a), (c-e) CITS images taken upon the aquisition of image (a) at a grid of 64 × 64 points, and (g,h) CITS images corresponding to (f). The contrast range (color) of each image is indicated.

of the CITS images is considered: At -1.9 V and -1.5 V still considerable tunneling occurs from the GaAs into the tip, while the tunneling probability is increased at the GaSb (c,d). At a voltage of -1.0 V, corresponding to (e), hardly any tunneling probability is left at the GaAs, while at the GaSb WL the current is decreased, too, but is still significantly larger than at the surrounding material.

In another CITS series taken at the same position of the WL, shown in Fig. 11.4(f-h), the CITS voltage was even further reduced to -0.7 V (h). At this condition no tunneling at all takes place at the GaAs matrix, while a weak but still significant current is imaged at the GaSb WL. Accordingly, at this image the tip Fermi energy lies within the GaAs bandgap, and only the confined GaSb WL states are imaged. With decreasing absolute voltage of the CITS images the appearance of the WL gets more and more inhomogeneous (c-e,g-h), exhibiting regions of increased and others of decreased tunneling probability, correlating with structural details of the layer (a,f). This behavior shows impressively that local variations of the GaSb content within the WL strongly influence the energy of the localized states.

Also at the GaAs surrounding the GaSb some fluctuations of the current, although weaker than within the WL, are present especially at smaller absolute values of the voltage (d,e,g). Thereby most areas of decreased current are localized around defects of the sample surface, which can be seen in the topography images (a,f). This is probably due to small potential variations induced by Fermi-level pinning at the defects and shows how such defects can inhibit the diffusion of charge carriers. It should be noted that the voltages of the CITS images showing localized states or an absence of bulk GaAs tunneling cannot directly be associated with absolute band energies due to the occurence of tip-induced band bending.

A more detailed CITS series, obtained for positive sample voltages at a QD within layer 2 of the MBE-grown sample C, is shown in Fig. 11.5, containing CITS current and dI/dV images. The QD which has been studied is displayed in detail in (a), taken from a reference image acquired without any spectroscopy modes. The weaker image quality and the contrast oscillations of the constant current topography image of the CITS series (b) are due to the reduced point resolution and to drift during the time delay related to the spectroscopy.

Regarding the current images, several regimes can be recognized: The image acquired simultaneously with the topography shows only noise, as expected (c). For CITS voltages higher than the stabilization voltage of $V_T = 1.8$ V the GaSb structures appear darker in the current images (e,f), while for smaller voltages they look rather bright (g-n). Both features have the same reason already observed for the QW discussed above: With decreasing voltage the electronic image contrast increases, as the relative difference between the tunneling currents at the GaAs and at the GaSb increases, too. Due to the constant current mode applied for $V_T = 1.8$ V, the tip-sample distance is enlarged at the QD to compensate the increased tunneling probability given by an increased integrated LDOS. At larger voltages less additional states are added to the integrated LDOS of the GaSb QD than it is the case for the GaAs, so that the QD appears darker. At smaller voltages, however, the integrated LDOS decreases faster at the GaAs than at the GaSb, giving the QD a brighter appearance.

For voltages of 1.7 V and 1.6 V, besides the bright GaSb contrast considerable tunneling also occurs from the GaAs, both near the QD and also some nm away (g,h). This changes as the voltage decreases to 1.3 - 1.5 V (i-k): Now the current from the GaAs is significantly lower and increases only when the tip comes closer to the GaSb nanostructures. Therefore this situation exactly resembles the observed image contrast analyzed above, implying a smoothly broadened appearance of the GaSb structures at positive voltages (compare also Fig. 11.1). At this moderately low voltage regime tunneling into the empty states of the GaAs CB locally bent near the charged GaSb nanostructures is very effective. As the voltage is further decreased to 1.2 V (l), this tunneling channel gets closed, and finally at 1.1 V or

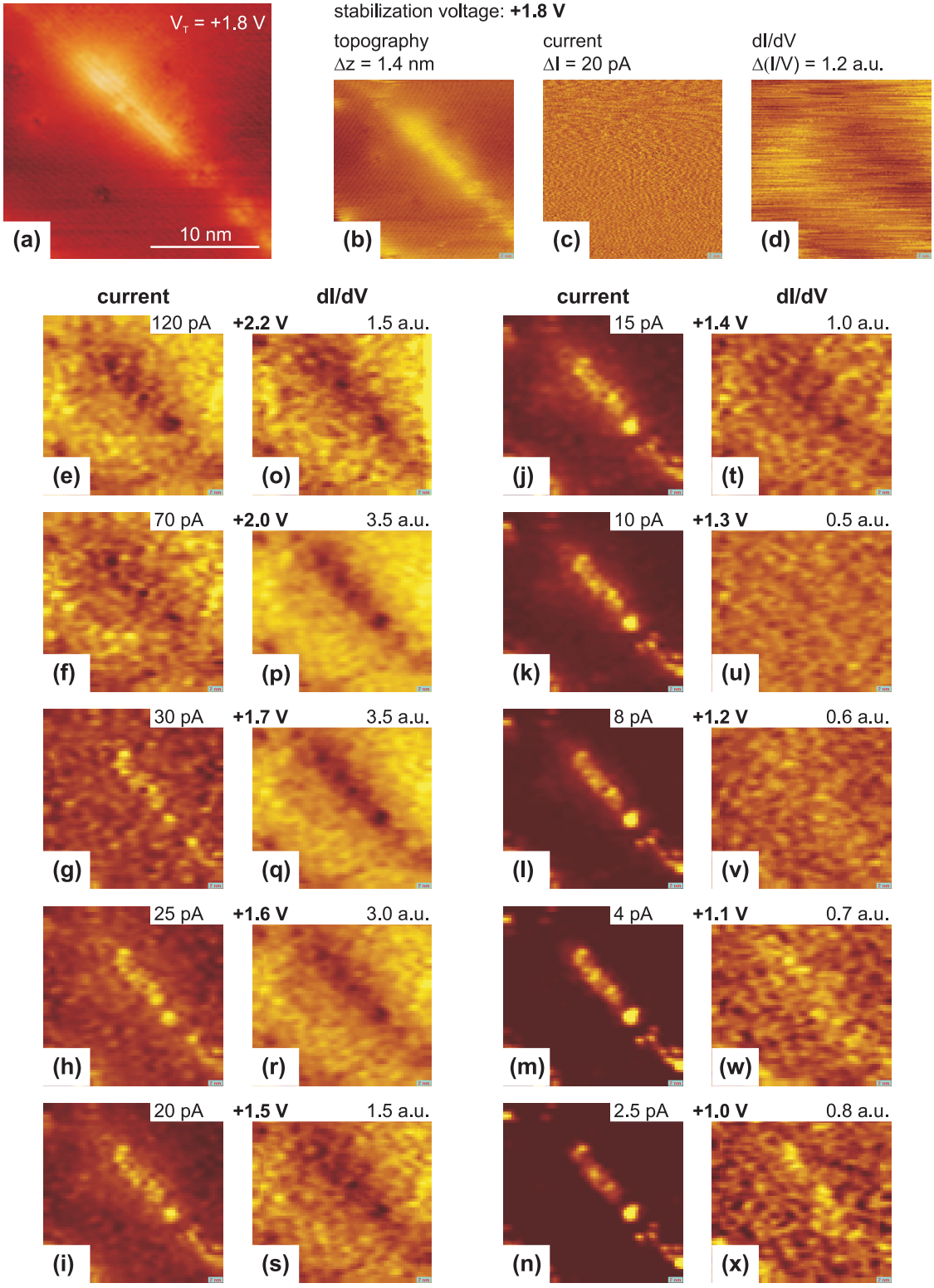

FIGURE 11.5: CITS imaging of a QD of layer 2 in sample C: (a) reference image without CITS, (b) empty state image with simultaneously acquired (c) current and (d) dI/dV images. (e-n) CITS current images taken upon the aquisition of (b) at a grid of 64 × 64 points, and (o-x) corresponding CITS dI/dV images. The sample voltage and contrast range (color) of each image are indicated, extending in the dI/dV images over several pA/V.

1.0 V no tunneling at all occurs at the GaAs but only at the GaSb (m,n). At these conditions all CB states are out of reach and the electrons coming from the tip can only tunnel into the depleted GaSb states.

Thereby three local maxima of the current can be discovered within the QD, while the complete area of increased current resembles well the shape of the QD as exhibited in the topography images (a,b). At closer inspection of these images, some structural defects of the WL surface directly below the QD and a little further in the lower right corner of the images can be recognized. The very bright spot in the CITS current images and also the inhomogeneous spots of irregular shape in the lower right corner of Figs. (j-n) probably can be correlated to these surface defects of the WL. The remaining spots of the current observable at low voltages are those of the QD, while the WL states at the upper left corner of the images only appear at slightly higher voltages. This behavior is in good agreement with the expected electronic properties of the nanostructures, where the QD states also should have larger confinement energies than those of the WL.

While up to here only CITS current images were regarded, additional information can be received from the CITS dI/dV images obtained using lock-in technique (o-x). In most of these images and also in the STS image (d) acquired simultaneously with the topography the GaSb layer appears dark, while it gets bright for the lowest voltages. Astonishingly, the cross-over of the contrast does not occur at the stabilization voltage, as for the current images, but at the much lower voltage of 1.3 V (u). Again one has to consider that due to constant current imaging at the stabilization voltage the tip is closer to the sample at the GaAs than at the GaSb. dI/dV images show the sample LDOS for the energy corresponding to the tunneling voltage at the position of the tip. The local variation of the tip-sample distance inhibits a direct comparison of the LDOS for GaSb and GaAs, but for voltages larger than 1.3 V the GaSb LDOS does at least not exceed the GaAs LDOS far enough to compensate the increased distance. Especially for voltages between 2.0 V and 1.6 V [please note the increased contrast range in (p-r)] the dI/dV signal is much weaker at the GaSb than at the GaAs. The contrast turns around for small voltages below 1.3 V: At these energies the GaAs LDOS falls to zero as the band gap is reached, but the confined GaSb states holding a large LDOS can be seen with a bright contrast in the dI/dV images.

Although the noise level is too high and the spatial and energetical resolution of the CITS images too low to map probability densities of individual GaSb QD wavefunctions, the local observance of QD states in XSTM images is an experimental success. The nature of these confined GaSb states and especially of the type-II induced localized GaAs states near the nanostructures will be further analyzed in the next section by evaluating STS point spectra.

11.3 Type-II induced electronic states in XSTS spectra

While STS and CITS imaging can – with experimental challenges and limitations of the resolution – probe the spatial distribution of the LDOS at some discrete energies, the continuous variation of the LDOS over the energy at distinctive points can be investigated by STS I–V- and dI/dV–V-spectra, as generally described in section 3.2.5.

STS spectra have been taken at both MBE-grown samples C and D. By comparing spectra acquired at different positions directly at, near, and far away from the GaSb nanostructures, their electronic properties can be studied. Before such spectra will be shown and discussed, it is necessary to understand the physical meaning of the measured data, and how they have to be processed.

11.3.1 Physical significance and normalization of point spectra

In order to increase the dynamic range of the measurements and thus being able to resolve electronic effects near the band gap, all spectra have been acquired using the variable gap mode: During the voltage ramp of a single spectrum the tip-sample distance was automatically varied in such a way that it decreased for decreasing absolute values of the voltage. Accordingly any spectral features occuring at small absolute voltages appear enlarged in the measured curves. For knowing the actual dependence of the tunneling current on the voltage the spectra have to be normalized.

The dependence of the tunneling current I on the tip-sample distance s is approximately exponential, given by

$$I \sim I_0 \exp(-2\kappa s) \quad . \tag{11.1}$$

Thereby κ is the half inverse decay length of the tunneling current [278], and only weakly dependent on the tip-sample distance s and on the tunneling voltage V_T at typical STS conditions. Thus a constant value can be approximated, amounting to $\kappa \approx \sqrt{2m\bar{\phi}}/\hbar$ with the electron mass m and an average barrier height $\bar{\phi}$ [106]. Using the variable gap mode, the tip-sample distance is usually varied linearly with the absolute voltage: $\Delta s = -c_{vg}\,(|V_0|-|V|)$, with the stabilization voltage V_0. The constant of gap variation c_{vg} is typically within the range of 1 Å/V.

In order to exclude the influence of the distance variation from the spectra, each value of the measured current I_{ex} has to be normalized by

$$I_{norm} = I_{ex} \cdot \exp\left[-2\,\kappa\, c_{vg}\,(|V_0| - |V|)\right] \quad . \tag{11.2}$$

While the variable gap constant c_{vg} is freely chosen at the experiment, the correct value of the inverse decay length κ is not trivial. In a first and rough approximation it can be assumed to be $\kappa \approx 1\text{Å}^{-1}$ [106]. A more accurate way is to evaluate the best fit of κ experimentally: The decay length of the current can directly be evaluated by measuring the tunneling current as a function of the tip-sample distance in an I–s-spectrum. Unfortunately, such a measurement was technically not possible in this work, so another approach is chosen here.

The measured current of an I–V-spectrum with variable gap mode is compared to a reference spectrum taken with the same tip and comparable tunneling conditions, but without varying the tip-sample distance. With decreasing absolute voltage, the current I_{ref} of the reference spectrum decreases much faster than the current I_{vg} of the spectrum with variable gap mode, and the ratio I_{vg}/I_{ref} increases exponentially with decreasing voltage. When this ratio is plotted logarithmically over the voltage, a linear curve is obtained. The relevant decay length κ can then directly be derived from the slope of this line, amounting to $m = 2\,\kappa\, c_{vg}$.

An example for the normalization of I–V-spectra is given in Fig. 11.6: Two spectra acquired at different sample positions are shown (a). While the blue curve comes close to the shape of typical bulk GaAs spectra, the green one appears strongly different. With decreasing amount of negative voltage the absolute current first decreases, before at smaller negative voltages it seems to be shifted in voltage with respect to the blue curve, and finally a small additional current is found at small positive voltages. When the current is plotted at a logarithmic scale [dashed curves in (b)], the latter feature gets even more pronounced.

However, the appearance of the green curve is strongly influenced by the use of the variable gap mode: For both spectra, also the normalized currents are plotted in (b), with the red curve corresponding to the blue one and the orange curve to the green one, respectively. The increased range of the normalized current is apparent by the different axis scales. Several aspects are noticeable after normalization of the green curve into the orange one: Firstly, the

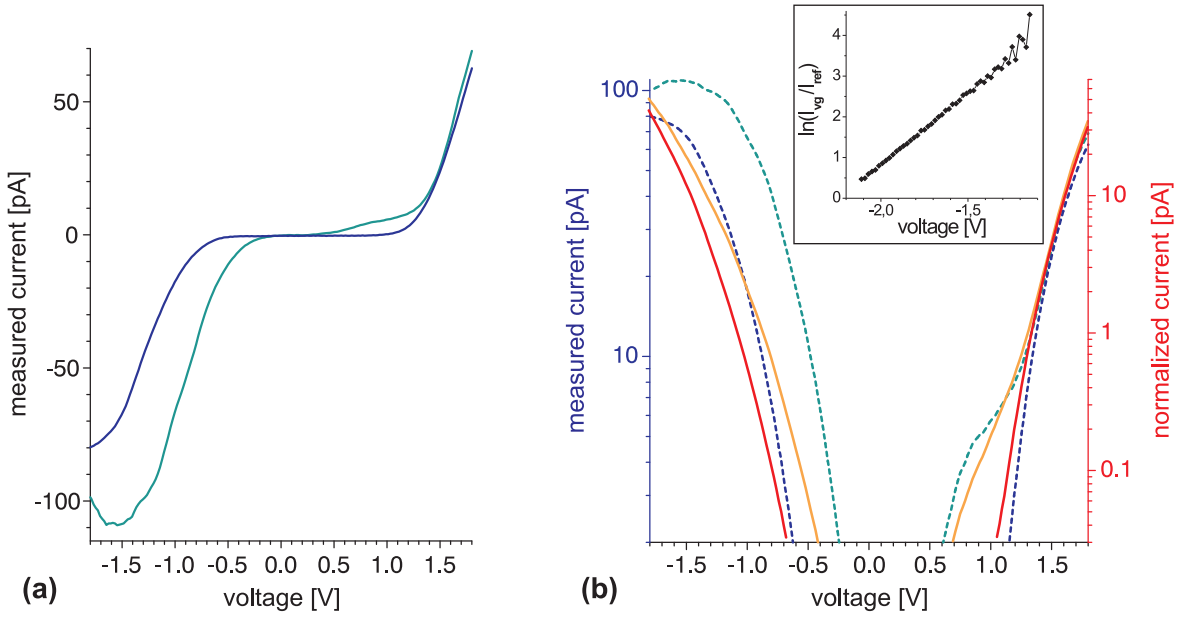

FIGURE 11.6: Normalization of I–V-spectra: (a) I–V-spectra acquired using the variable gap mode at two different sample positions, plotted on a linear scale. (b) Logarithmic plot of the spectra shown in (a) (dashed curves), and of the same spectra after normalizing the current (straight curves). The red curve corresponds to the blue one and the orange curve to the green one, respectively. In the inset, the ratio of measured current through the current of a reference sample taken at fix tip-sample distance is plotted at a logarithmic scale. The slope of this curve gives the exponential normalization factor for the measured current.

hump of the current at large negative voltages was only given by the variation of the tip-sample distance and is not related to an actual physical property. Instead, both normalized spectra exhibit a quite similar current and shape at higher negative voltages. With decreasing negative voltage the distance between both curves slightly increases, but not to such a large amount that could be expected from the shift of the blue and green curves. Finally, the additional current contribution at small positive voltages is pronounced in the orange curve, too, but the actual slope of this distribution is significantly different from the one of the green curve.

The experimental evaluation of the correct normalization factor is shown in the inset of Fig. 11.6(b): The ratio of measured current of the blue spectrum and the current of a reference spectrum, acquired at a fix tip-sample distance, is plotted at a logarithmic scale over the corresponding voltage for a suited range, which is limited by the noise of the current ratio increasing dramatically when the current of the reference sample approaches zero. For the lowest absolute voltages shown in the plot the beginning of that noise can be seen. The slope of the plotted data was used to normalize both spectra of Fig. 11.6, resulting in an experimental value of the decay length of $\kappa = 0.5$ Å^{-1}.

In analogy to the I–V-spectra, also the dI/dV–V-spectra obtained by simultaneously using the lock-in technique are influenced by the variable gap mode. A very elegant way to normalize the differential conductance dI/dV is to divide it by the absolute conductance I/V, which eliminates the dependence on the varied distance. Even more, the value $(dI/dV)/(I/V)$ represents a normalized sample LDOS, independent of the distance of the tip [105, 305, 306]. However, because GaAs and also GaSb have a large band gap with zero conductivity due to the absence of surface states, $(dI/dV)/(I/V)$ diverges with decreasing voltage when the

band gap is reached, as the current I approaches zero faster than the voltage V or the differential conductance dI/dV. This is demonstrated in Fig. 11.7(a) for the I–V-spectrum shown above (blue curve), the corresponding dI/dV–V-spectrum (green curve), and their calculated quotient $(dI/dV)/(I/V)$ (grey curve).

Several solutions to overcome this problem are suggested in literature [278, 302, 303, 307, 308], having in common that the diverging signal is broadened in different ways. Three approaches have been tried to normalize the conductance spectra of this work, which will be introduced and compared in the following.

A first and rather straightforward method to overcome the zero conductivity for small voltages is to add a constant offset, as suggested by Prietsch et al. [307]. Thereby the conductivity I/V is replaced by the term

$$\overline{I/V} = \sqrt{(I/V)^2 + c^2} \quad , \tag{11.3}$$

with c being a suitable constant, which should be chosen very small in order not do dominate

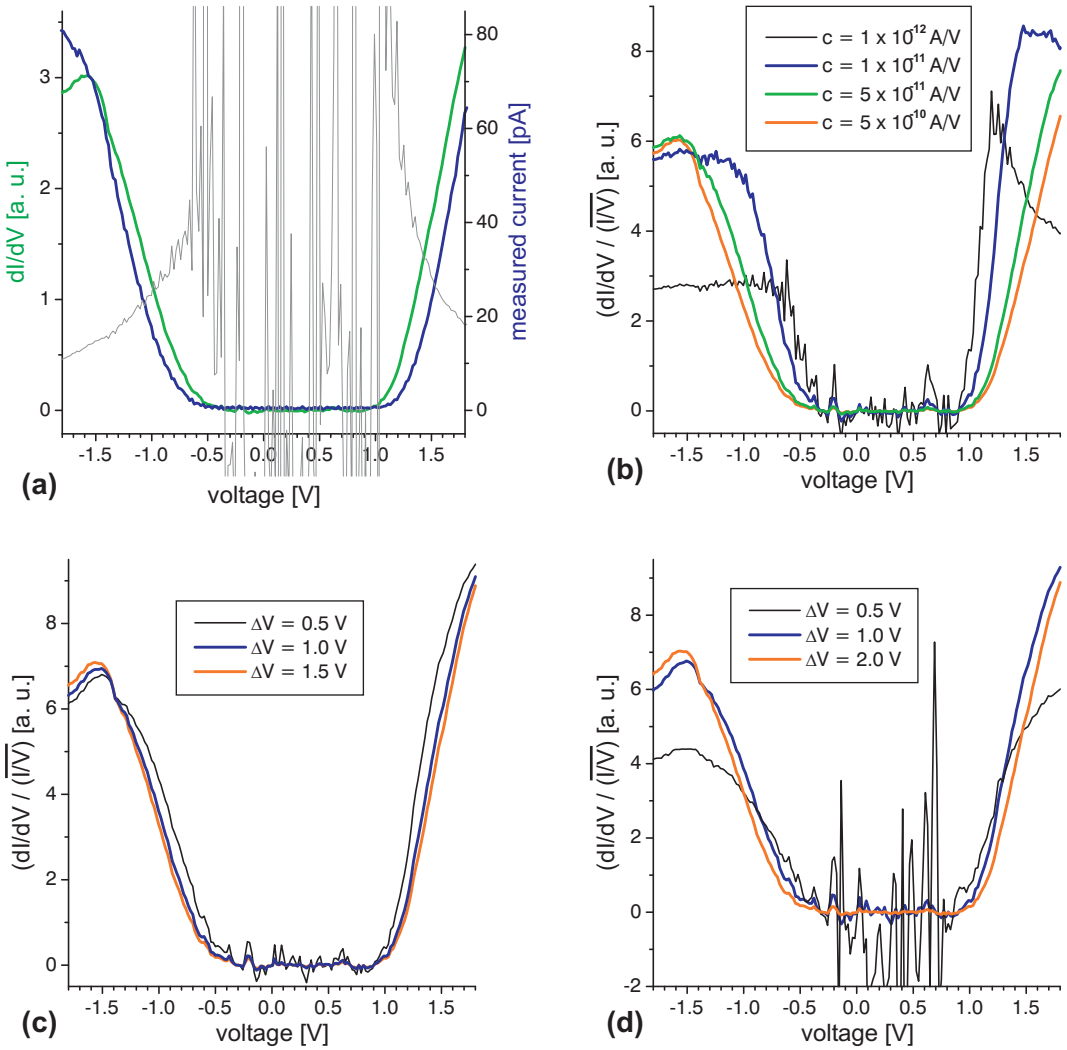

FIGURE 11.7: Normalization of dI/dV–V-spectra: (a) dI/dV–V- (green curve) and I–V-spectrum (blue curve), together with the calculated value $(dI/dV)/(I/V)$ (grey curve), which strongly diverges. (b-d) $(dI/dV)/(\overline{I/V})$–V-spectra, obtained by normalizing the spectra shown in (a) by (b) broadening with different offsets c or by convolution with (c) an exponential function or (d) a Gaussian function of different voltage widths ΔV. The values of the used constants and voltage widths are indicated.

the conductivity, but large enough to inhibit the divergence and reduce the noise in the band gap region. The best choice of c depends on the local electronic properties of the sample and the quality of the spectra, so for each set of spectra the offset has to be adapted empirically. Several tries of certain offsets and their influence on the normalized spectra can be seen in Fig. 11.7(b): Using an offset of only $c = 1 \times 10^{-12}$ A/V already stops the divergence, but leads to strong noise and to deficiently large values at the CB onset (small positive voltages). With $c = 1 \times 10^{-11}$ A/V the shape of the curve is better reproduced, but still relatively high noise is left. The value $c = 5 \times 10^{-11}$ A/V seems to be the best choice here, resulting in a smooth curve, while at larger values like $c = 5 \times 10^{-10}$ A/V the complete spectrum gets unnecessarily flattened. Although this method using an unweighted, constant offset is insensitive especially to weak features and small differences within the spectrum, it though produces an effective normalization of the differential conductance. Additionally, it is by far the fastest and easiest one of the used methods.

Instead of adding an offset and thereby artificially shifting the conductance, a more sophisticated way to broaden the conductance for avoiding zero values is to convolute it with a suitable function. Feenstra and Stroscio have suggested the convolution with an exponential function [278, 302, 303], according to:

$$\overline{I/V} = \frac{1}{2\Delta V} \int_{-\infty}^{\infty} \frac{I(V')}{V'} \exp\left(\frac{-|V'-V|}{\Delta V}\right) dV' \quad . \tag{11.4}$$

Thus for any certain voltage, the broadened conductance is convoluted by an infinite voltage integral, weighted around the respective voltage by an exponential function of given width ΔV. To evaluate real spectra, the integral can be transferred into the sum over all voltage points of the spectrum. As the integral is infinite, the sum over measured voltages has to be artificially continued beyond the largest values of positive and negative applied voltage. Therefore the current corresponding to these lowest and highest voltage can be estimated to occur for all other voltages below and above, respectively. Due to the exponential weighting these artificially extended values can maximally contribute over about an energy width ΔV outside the experimentally obtained values.

Similarly to the first method, also here a parameter has to be chosen by hand, which is the voltage width ΔV. This parameter again should be kept as small as possible, but on the other hand it should at least cover the half width of the semiconductor energy gap to prevent divergence of the normalized conductance. For spectra on doped GaAs, typically widths of $\Delta V = 0.5$ V can be used [302]. However, as no dopant-induced components reduce the GaAs band gap at the samples investigated here, this value is too small to avoid significant noise, as Fig. 11.7(c) shows. At a larger value of $\Delta V = 1.5$ V the resulting curve is very smooth, but for both polarities the curves of the normalized conductance are slightly shifted towards higher absolute voltages. The parameter $\Delta V = 1.0$ V has been proven to be the best choice for the spectra studied here.

Although the latter method of normalization has become widely known and accepted, the question remains why the measured conductance at a specific voltage should be convoluted by an exponential function containing the absolute value of this voltage. Instead, the use of a Gaussian distribution containing the square of the voltage seems to be at least more intuitive for weighting a specific value. In this case, the broadened conductance would amount to:

$$\overline{I/V} = \frac{1}{2\Delta V} \int_{-\infty}^{\infty} \frac{I(V')}{V'} \exp\left(\frac{-(V'-V)^2}{\Delta V^2}\right) dV' \quad . \tag{11.5}$$

Curves obtained by normalizing the dI/dV–V-spectrum with this method are shown in Fig. 11.7(d). As the weighting of the Gaussian function is more narrow than that of the

exponential function used above, the voltage width ΔV has to be chosen slightly larger here: While at a value of $\Delta V = 0.5$ V dramatic noise of the normalized conductance results, best results were obtained for values ΔV between 1 and 2 V. Due to this narrower weighting of the Gaussian function, this method of normalization should be best suited to resolve small features within the dI/dV–V-spectra. Accordingly, the dI/dV–V-spectra shown below have been normalized by this method, being convoluted with a Gaussian function of the width $\Delta V = 1.4$ V or 1.5 V.

11.3.2 STS point spectra of GaSb nanostructures

Several GaSb nanostructures of both MBE-grown samples could be investigated by means of STS point spectra. While for sample C only I–V-spectra were obtained, for sample D also dI/dV–V-spectra could successfully be acquired.

A typical set of I–V-spectra acquired at and around a QD of the third GaSb layer in sample C is presented in Fig. 11.8, with individual spectra being colored according to their local position. The area at which the spectra, presented in (a), were taken is shown in (b): During aquisition of a constant current STM image taken at a stabilization voltage of V_T = -2.3 V (not shown here), the scanning process was interrupted at ten distinct points. At each of these points, the feedback loop was disabled and the voltage was varied from -2.0 V to +2.0 V in small steps of 30 mV. For each voltage point the corresponding current was measured during a time of 40 ms after an initial delay time of 20 ms, which is necessary to avoid capacitance effects. As the absolute voltage was decreased, the tip-sample distance was simultaneously reduced by 1.2 Å/V.

At every position, ten spectra were taken with alternating direction of the voltage ramp, with the feedback being shortly enabled after every second spectrum to stabilize the tip-sample distance. As the current signal of a single spectrum is strongly affected by electronic noise, these ten spectra are averaged for each position. After yielding the experimental data, the measured currents were normalized with regard to the used variable gap mode as described above. No reference spectrum with fixed tip-sample distance was available here, so the spectra could only be normalized assuming a common value of the decay constant of $\kappa = 1$ Å^{-1}.

Comparing the ten spectra corresponding to the positions indicated in (b), a clear correlation between the spatial position and the shape of the spectrum gets apparent: Five spectra have been taken directly at the QD, showing a very similar shape (red curves). Significantly different from these, but similar to each other, are the three blue curves corresponding to positions at the GaAs several nm away from the GaSb layer. The remaining two curves belong to the positions indicated in green in (b), being located at a diluted region of the WL and at the GaAs near the WL, respectively. For positive voltages, both corresponding spectra look similar and lie between the blue curves (GaAs matrix) and the red ones (GaSb QD). For negative voltages, however, the green curve corresponding to the diluted WL behaves like the GaSb QD curves, while the spectrum taken underneath the WL comes closer to the GaAs spectra, although slightly shifted for small negative bias.

As the spectra corresponding to comparable spatial positions exhibit a nearly identical shape, they were averaged for further noise reduction and for clearer illustration, the resulting curves being shown in (c). From a comparison of the three curves several conclusions can be drawn: Firstly, the voltage interval of zero current, displaying the semiconductor band gap, is much larger for the GaAs matrix than for the GaSb QD. At negative sample voltages, corresponding to filled state tunneling from the VB, the blue and red curves of GaAs and GaSb have a similar and homogeneous shape, but are shifted to each other by $\sim$ 0.4 V. Such a behavior is expected due to the large VB offset between GaAs and GaSb, slightly

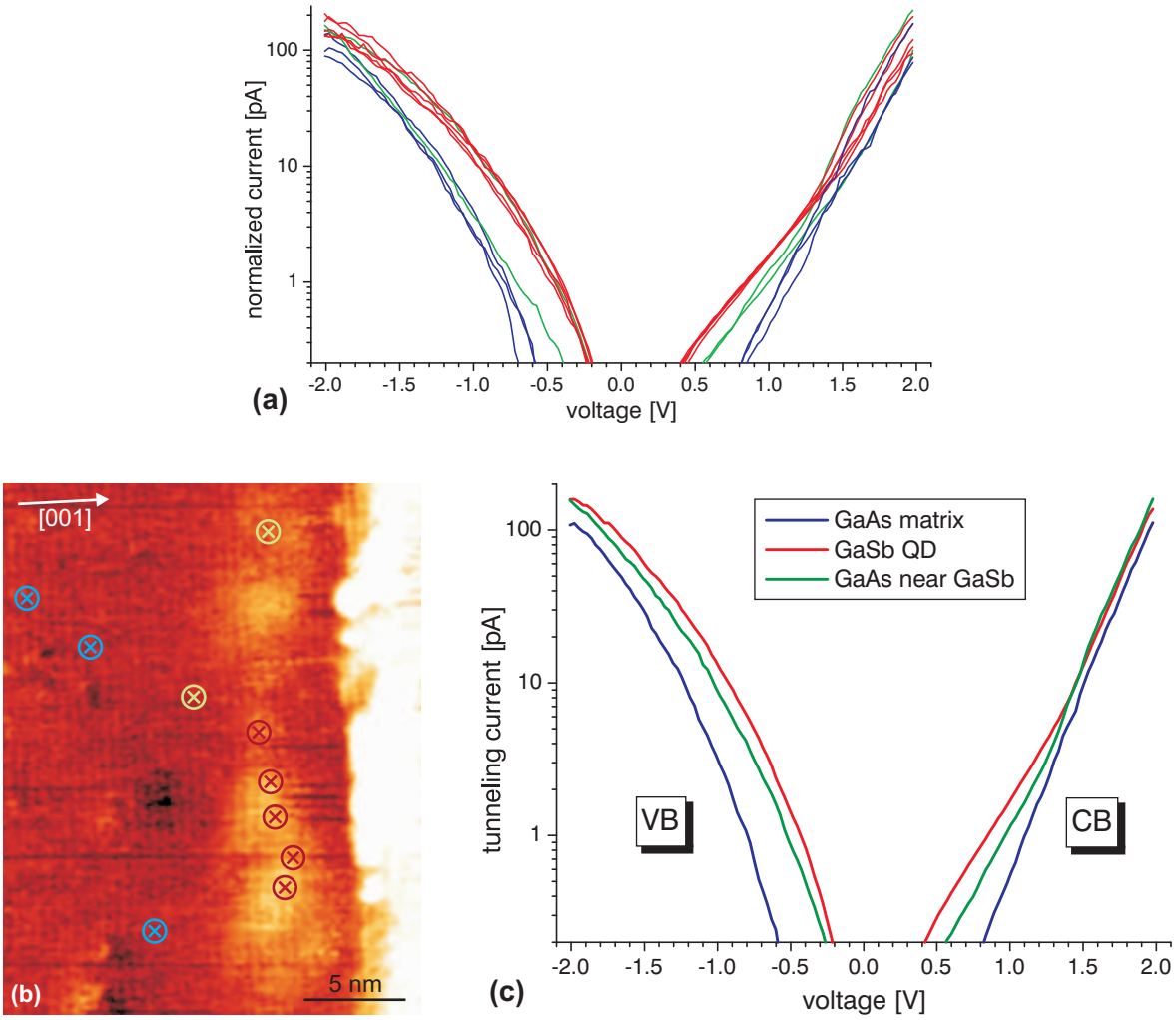

FIGURE 11.8: I–V-spectra taken at layer 3 of sample C: (a) Ten spectra of normalized current over voltage are plotted, taken at the positions indicated in the STM filled state image (b), acquired at V_T = -2.3 V. A few nm beside the GaSb layer a large surface step dominates the image contrast. (c) According to their spatial position, spectra taken at the GaSb QD (red curve), at the GaAs several nm away (blue curve) and at the GaAs near the GaSb layer (green curve) are averaged.

reduced by quantum effects. For positive bias, imaging the empty states of the CB, all three curves lie closely together at larger voltages. With decreasing voltage, however, the blue curve of the GaAs spectra continues homogeneously, while the GaSb-related spectra exhibit an increased current at voltages below about +1.4 V as compared to GaAs, which on a first hand is unexpected regarding the type-II CB offset. On the other hand, the observed feature looks very similar to spectra containing a dopant-induced component of the current [107, 301]. However, as all epitaxially grown layers are undoped, another mechanism has to be responsible for this contribution of additional small currents at small positive voltages. Obviously, this mechanism should be due to the type-II band alignment, and to the specific tunneling conditions resulting from this band structure in combination with tip-induced band bending, described in section 11.1.

Before such effects are discussed and the spectra are analyzed in more detail, additional data derived by dI/dV–V spectroscopy should be taken into account. Such spectra, preventing the energy integration of the tunneling current, have the advantage of directly representing the sample LDOS at the corresponding energy.

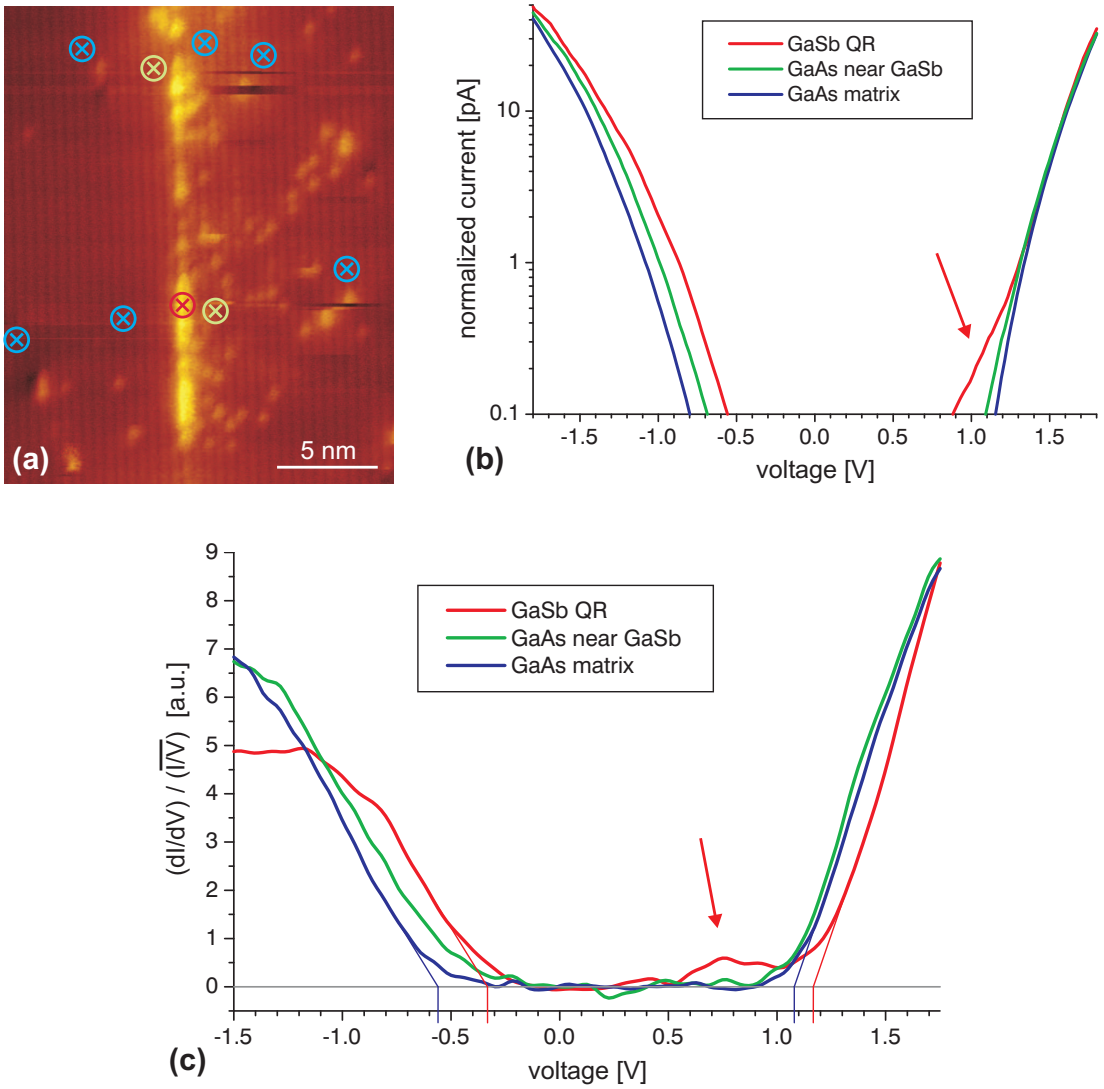

FIGURE 11.9: STS point spectra taken at layer 3 of sample D: (a) Filled state STM image, acquired at V_T = -2.1 V, showing a ring-shaped GaSb QD and the positions of nine spectra. The corresponding (b) I–V-spectra and (c) dI/dV–V-spectra are averaged for the different positions as shown in (a). In (c), the voltage values of the GaAs and GaSb VB maxima and CB minima, respectively, are extrapolated from the spectra and indicated. The red arrows depict the region of GaSb hole occupation.

Figure 11.9 shows a QR in layer 3 of sample D together with I–V- and dI/dV–V-spectra taken at different positions at and around this GaSb nanostructure. At each position indicated in the STM image (a), ten spectra were acquired and averaged, similarly as described above, applying a variation of the tip-sample distance of c_{vg} = 3.5 Å/V. By comparing the I–V-spectra with reference spectra taken at a fixed distance, the inverse decay length could be evaluated to κ = 0.50 Å^{-1}, which was then used to normalize the spectra. The measured differential conductivity dI/dV was normalized by the absolute conductivity $\overline{I/V}$, broadened by a convolution with a Gaussian function of width ΔV = 1.5 V. Simultaneously to the data of Fig. 11.8, the spectra shown in Fig. 11.9 were averaged according to their position: The spectra taken at the positions marked in blue in (a) are combined in the blue curves of (b) and (c), representing GaAs several nm away from the nanostructures, green curves correspond to positions at the GaAs, but only 1 to 2 nm away from the GaSb QR, and the red curves show the spectra taken directly at the QR.

The I–V-spectra are qualitatively very similar to those taken at the QD of sample C, shown in Fig. 11.8(c): At the VB side, the GaSb curve is shifted by $\sim$ 0.3 eV to smaller negative voltages with respect to the GaAs curve, with the green curve (GaAs near the GaSb) in between. For larger positive voltages all three curves are close together, while for small positive values an additional current contribution can be seen in the red curve corresponding to the GaSb QD. By comparing these spectra with those taken at sample C, qualitatively the same behavior can be found for both ring-shaped GaSb QDs, while the smaller height of the very flat QD structures in sample D results in slightly smaller confinement energies.

More information on the properties of GaSb nanostructures can be derived from the dI/dV–V-spectra [Fig. 11.9(c)]. From the slope of the curves corresponding to the GaSb QD (red), the GaAs matrix (blue), and the GaAs near the GaSb layer (green), three different regimes can be distinguished: For sufficiently large absolute voltages of both polarities, the conductivity increases monotonously with increasing absolute voltage at all positions, as expected for the increasing LDOS of the VB and CB, respectively. Between these VB and CB states the conductivity is zero, clearly indicating the bandgap. Only in the GaSb spectra, however, a small but definite additional contribution is observed between +0.5 and +1.0 V (marked by a red arrow).

The VB maxima and CB minima should easily be determinable from the curves by the values at which the LDOS falls to zero. In the actual spectra, however, these expected distinct onsets of the dI/dV-values are smeared out over about 0.2 V, due to the necessary averaging of individual spectra and to a broadening given by the oscillator amplitude of the lock-in technique and the thermal broadening. In order to nevertheless evaluate the respective values from the spectra, the fast decay of the GaAs and GaSb spectra was extrapolated linearly until zero, as shown in Fig. 11.9(c). For GaAs a VB maximum of -0.6 eV and a CB minimum of +1.1 eV were obtained, corresponding to the Fermi energy being slightly above midgap. The fact that the apparent band gap of 1.7 eV is about 0.3 eV above the literature value was already expected, as tip-induced band bending would enlarge this value. For the GaSb QD, a CB minimum of +1.2 eV could be evaluated, while the energy of -0.3 eV corresponds to the confined hole ground state. Although the absolute values of these energies and the obtained band gap underlie the effect of TIBB, the relative values are much more significant: Accordingly, a hole localization energy of 0.2 to 0.3 eV was found, in agreement with the value derived from the I–V-spectra. Even more, a type-II alignment with a CB offset of 0.1 eV could directly be obtained for the investigated GaSb QD.

While the blue GaAs spectra and most parts of the GaSb spectra of Fig. 11.9 could be understood, the additional GaSb LDOS at small positive voltages and the green curve of the spectra acquired at GaAs near the nanostructures still need to be explained. Therefore the exact tunneling conditions for the positions at the QD, just beside the QD and far away at the GaAs matrix have to be taken into account. These conditions are sketched schematically in Fig. 11.10, both for negative (a-c) and for small positive sample voltages (d-f).

At negative bias, the TIBB causes the Fermi energy to be close to the CB, so that all VB states and also the confined GaSb hole states are filled [for additional visualization see also Fig. 11.2(f)]. At the GaAs tunneling can occur from the VB states into the tip, as depicted in Fig. 11.10(a). At the GaSb QD, confined states contribute to the LDOS, together with a continuous spectrum from GaSb resonances (c). Consequently, the GaSb LDOS is larger than the GaAs one at lower voltages, as seen in the spectra.

Although the confined GaSb states are strongly localized, they penetrate into the GaAs band gap, characterized by an exponential decay over a few nm. A similar behavior is valid for the GaSb resonances, too. So when the STM tip is at GaAs regions directly neighboring a GaSb nanostructure, additional to the GaAs states also tunneling from the decaying GaSb

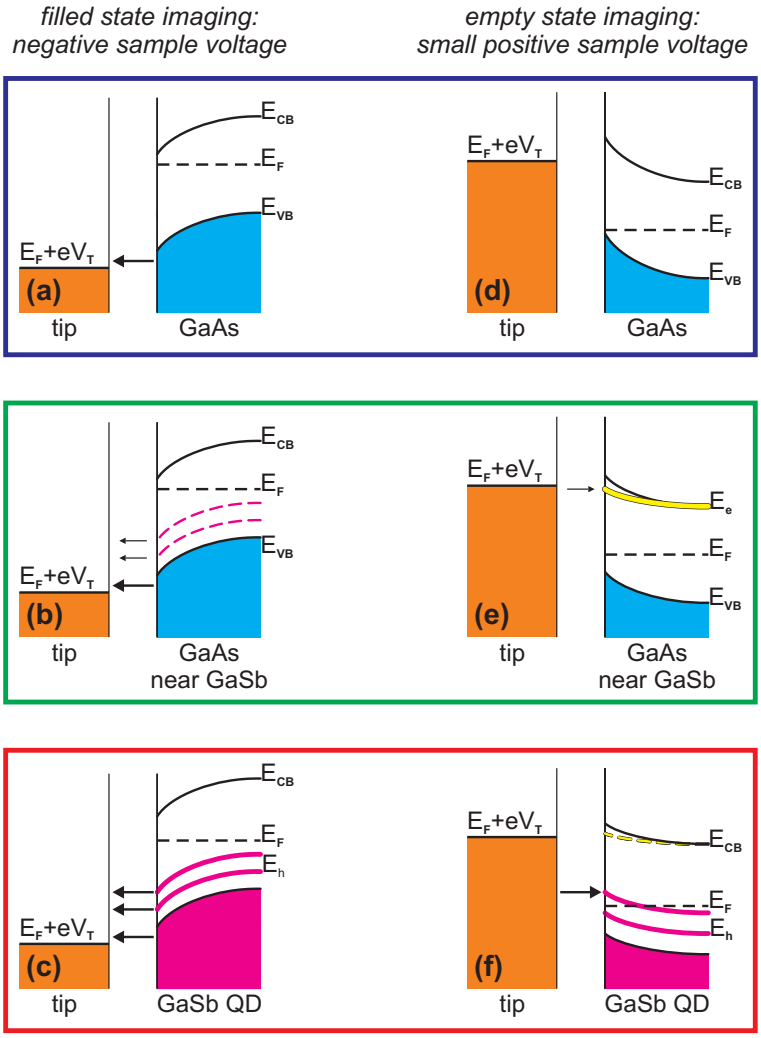

FIGURE 11.10: Different tunneling conditions at GaSb/GaAs nanostructures due to TIBB, sketched for (a-c) negative and (d-f) small positive sample voltages. The displayed configurations correspond to GaAs several nm away from GaSb (blue curves in Figs. 11.8, 11.9, and 11.11), to GaAs near the GaSb structures (green curves), and to a GaSb nanostructure (red curves). TIBB and confinement energies are not drawn to scale.

states can occur to a small amount, as depicted in (b). This effect causes the slightly increased LDOS at GaAs positions directly below or above the GaSb layer as compared to the GaAs matrix, observed in the spectra for negative voltages (green curves). The amount of this additional contribution depends strongly on the distance to the GaSb structures and on the decay length of the confined states.

Different mechanisms occur for positive sample voltages, leading to an upward band bending. This band bending shifts the onset of tunneling into empty GaAs CB states to higher voltages, as shown in (d). Accordingly, at small positive voltages no tunneling occurs at GaAs positions, and the apparent GaAs band gap is larger than the literature value.

At the GaSb, the TIBB causes a partial electron depletion or hole occupation, as explained above (see section 11.1), due to the large offset between GaAs VB and hole quantum-state energy. These depleted GaSb states are the reason for the additional contribution in GaSb I–V- and dI/dV–V-spectra at small positive voltages, as electrons can easily tunnel from the tip into such depleted states, as shown in (f). The requirement is a sufficient TIBB, which obviously is given already at +0.5 V. With increasing bias voltage, also tunneling from the tip into GaSb CB states occurs and dominates over the small contributions from the localized states. However, due to the type-II GaSb/GaAs CB offset, larger voltages are necessary for GaSb CB tunneling as for GaAs, leading to the small shift of the GaSb spectra in relation to GaAs at larger positive voltages.

Because of the hole occupation of the GaSb and the resulting charge, the TIBB is weaker at the GaSb than at the GaAs matrix. At the GaAs close to the nanostructures it increases with increasing distance over a range of several nm, as shown in section 11.1. As a result, weakly confined electron states arise at the GaAs neighboring the GaSb at energies below the GaAs CB, contibuting to the LDOS, as depicted in (e). Electrons can thus tunnel from the tip into these additional empty GaAs states (shown in yellow) at tunneling voltages which are not sufficient to enable tunneling at the GaAs matrix (black).

These weakly confined electron states can also slightly penetrate into the GaSb, as indicated by the dashed yellow line in (f) and already discussed in section 11.1, additionally contributing to the small conductivity at GaSb for energies slightly below the CB.

The influence of the different effects contributing to these complex tunneling conditions depends on the properties of the investigated GaSb nanostructures and on the specific tip conditions. As a consequence, some effects may occur stronger in one set of spectra and other effects in a second set, although the tunneling mechanism as such is always the same. This gets underlined by a comparison of the spectra of Fig. 11.9 discussed above and those of Fig. 11.11, also taken at a GaSb QD in layer 3 of sample D.

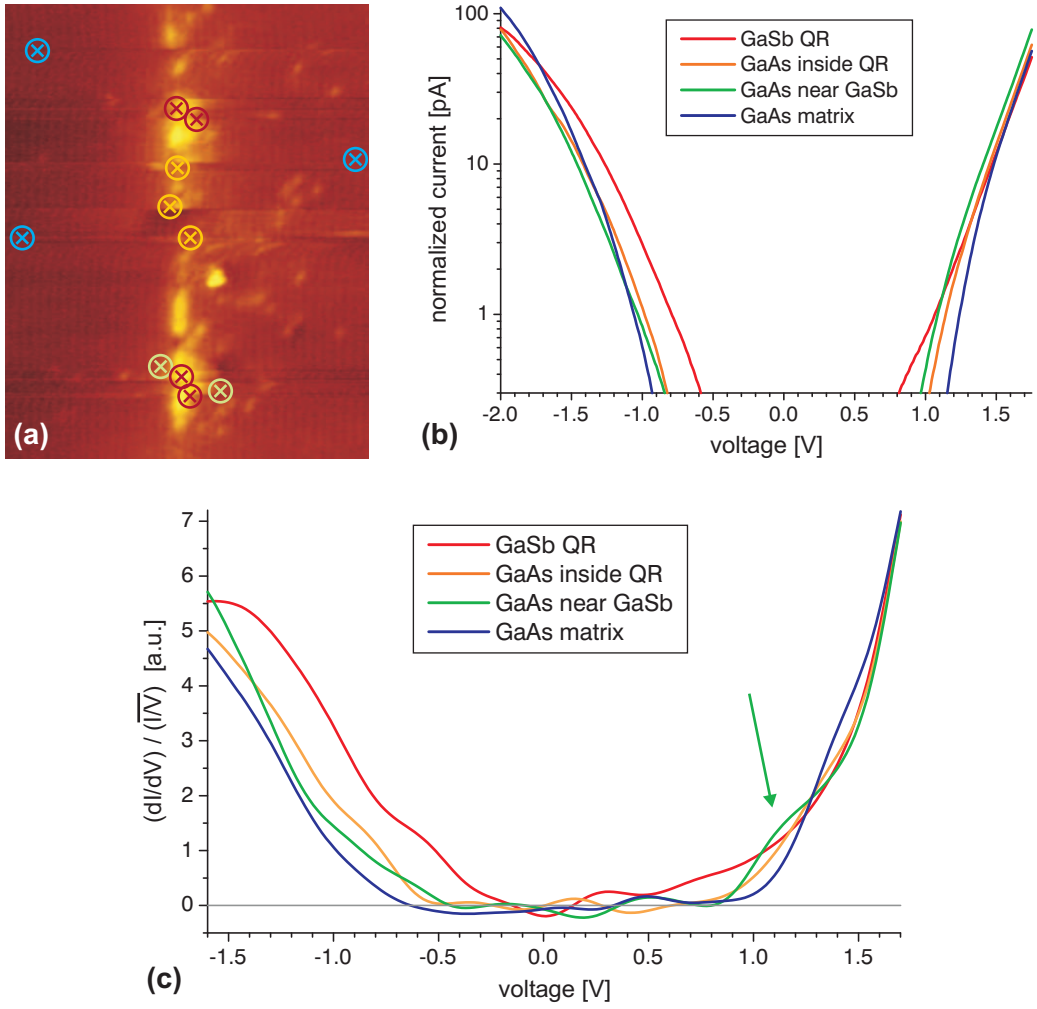

FIGURE 11.11: STS point spectra taken at a different QD in layer 3 of sample D: During the aquisition of the filled state STM image shown in (a), taken at V_T = -2.1 V, twelve I–V- (b) and dI/dV–V-spectra (c) were taken at the positions indicated in (a) and averaged accordingly. The arrow in (c) depicts the region of weakly localized empty states.

Both I–V- and dI/dV–V-spectra of Fig. 11.11 were acquired similarly as described above, using the variable gap mode with a distance variation of $c_{vg} = 2$ Å/V. I–V-spectra were normalized using a reference spectrum, yielding an inverse decay length of $\kappa = 0.5$ Å^{-1}.

The general appearance of the spectra is very close to that of the spectra shown above, nevertheless some differences can be obtained. Firstly, the voltage shift between the GaSb and GaAs dI/dV–V-spectra is slightly larger here for negative voltages, corresponding to a hole localization energy of about 0.35 eV. Secondly, at the GaSb spectrum for positive voltages the contribution due to hole occupation smoothly passes over into the LDOS increase at the GaSb CB, making it impossible to distinguish between both effects. On the other hand, the effect of additional tunneling into localized GaAs electronic states near the GaSb structures is very pronounced in this set of spectra, shown by the green curve and indicated by the arrow. Thus by comparing different sets of spectra, the contributions of both kinds of charge carriers in GaSb/GaAs quantum structures to the LDOS could well be observed.

Finally, an important conclusion about the electronic nature of the ring-shaped GaSb QDs can be drawn from the data: In Fig. 11.11 it is distinguished between spectra acquired at GaAs positions slightly above or below the GaSb layer, displayed by green curves, and spectra taken at the GaSb-free interior of the ring, shown in orange. No substantial difference between both positions can be derived, neither from the I–V- nor from the dI/dV–V-spectra. Correspondingly, the observed QDs also electronically behave as an actual ring, with the GaAs interior of the ring behaving just the same as the GaAs around the ring.

In conclusion, different sets of point spectra taken at QDs and QRs of both MBE-grown samples confirm the GaSb/GaAs specific tunneling mechansim derived earlier from observed STM image contrasts. Thereby the type-II character of the nanostructures could quantitatively be studied, giving clear evidence on GaSb hole occupation and a resulting weak electron confinement in the surrounding GaAs. Additionally, the hole localization energy could be obtained to about 0.3 eV for the flat QDs in sample D and to about 0.4 eV for the slightly higher QD structures in sample C.

Chapter 12

Conclusion

After presenting a rich variety of GaSb nanostructures in GaAs within the main part of this work, and having discussed many details on the formation and evolution of GaSb quantum dots (QDs) as well as their electronic properties, this chapter has the task to summarize these results and draw conclusions for future growth, characterization, and application of GaSb/GaAs QDs. For this purpose, both the MOCVD- and MBE-grown structures will be highlighted and compared to distinguish between general aspects of GaSb/GaAs QD formation and the complex interplay of specific growth conditions, thereby evaluating the different physical effects determining the resulting atomic structure of the QDs.

Within the MOCVD-grown samples studied here only small QDs of up to 8 nm base length and 2 nm height could be observed, revealing a rather broad size distribution with a QD density of $\sim 3 \times 10^{10}$ cm^{-2}. The local stoichiometry of the QDs varies, too, from about 60% maximum GaSb content up to nearly pure material. Due to the small size and the varying chemical composition the QD shape is not well pronounced, but comes close to that of a truncated pyramid. The small size together with the obtained size and stoichiometry distribution coincide with a rather broad QD photoluminescence (PL) signal, showing a maximum at 1.2 eV, measured at low temperature.

The QDs are surrounded by an intermixed wetting layer (WL) with a GaSb content of up to 40% and a vertical extension of about 3 monolayers (ML) or 1 nm. In spite of the significant intermixing of GaSb and GaAs material in the QDs and the diluted WL, hardly any Sb atoms were observed within the GaAs matrix underneath and above the nanostructures, demonstrating the absence of long-range segregation or diffusion processes in growth direction.

By comparing this QD layer with two QWs grown under similar conditions, several steps during the initial formation and further ripening of QDs could be revealed. As the exact amounts of deposited GaSb material remained unknown due to strong uncertainties in the MOCVD growth rate of monolayer thin GaSb films on GaAs, the different layers can only be characterized by the GaSb deposition time. After 21 s GaSb deposition, directly followed by GaAs overgrowth, a QW of about 2 ML vertical extension and a composition of about 50% GaSb was observed, resulting in a total GaSb content of 1 ML. The average chemical composition varies significantly on a scale of a few nm, and even gaps consisting of pure GaAs were found, distributed inhomogeneously over the QW, with lateral extensions of typically 1 to 3 nm, in some cases up to 7 nm. These gaps remain also under further GaSb deposition, though slightly decreasing in size, as similar structures were observed in all GaSb QWs and WLs. They stand for a kind of 2D island growth of the GaSb layer, consisting of broad GaSb islands interrupted by thin trenches, which get filled with GaAs upon overgrowth [46]. Strictly speaking, this corresponds to a slight deviation from classical Stranski-Krastanow growth. A

significant inhomogeneity of all GaSb layers is further confirmed by the fact that the GaAs material directly below the Sb-rich parts of the GaSb layer is compressively strained, which is not the case for a homogeneous QW.

When the GaSb deposition time is increased, the critical thickness of QD formation is reached: A GaSb layer formed upon 22 s GaSb deposition, followed by a 2 s growth interruption (GI) and GaAs overgrowth, was observed to contain the same total GaSb amount of 1 ML, again distributed in an inhomogeneously intermixed layer containing small gaps. Within this generally intermixed QW, flat Sb-rich islands were found at a high density of $\sim 6 \times 10^{11}$ cm^{-2}, showing lateral extensions of typically about 4 nm, which can reach up to 20 nm. These 2D islands do not exceed the vertical extension of the QW, but are characterized by a significantly increased GaSb composition, representing first self-assembled local GaSb accumulations. The necessary GaSb material has been provided by the 1 s longer GaSb deposition, while the following 2 s long GI enabled the GaSb accumulation in the 2D islands by lateral Sb segregation prior to overgrowth. Accordingly, the GaSb layer is intermixed already in this growth stage, meaning that the intermixing cannot just occur upon the overgrowth of a formerly pure GaSb layer, but that already the initial layer has to consist of GaAsSb material. This can be due either to a direct intermixing of the deposited GaSb with the underlying GaAs growth surface, or possibly to an unintended, but hardly preventable As background in the MOCVD reactor during GaSb growth. In any case, the amount of GaSb material and the corresponding strain energy of this layer is still not sufficient to allow the formation of 3D structures.

This changes when the GaSb deposition time is further increased to 25 s, as in this case a WL with again 1 ML total GaSb content and small, but optically active QDs were formed. Besides those QDs, which have already been described above, also tiny 3D GaSb islands were observed in the same layer, exhibiting no electronic confinement and only little strain. These smallest self-assembled 3D GaSb structures ever observed, with lateral extensions of about 2.5 nm and heights of 1.5 nm at a density of $\sim 5 \times 10^{10}$ cm^{-2}, are assumed to act as QD precursors. While these precursor structures appear as small protrusions within a locally continuous WL, the direct neighborhood of the somewhat larger QDs is partly depleted of GaSb, indicating a ripening of the QDs on cost of the surrounding WL by lateral mass transfer. The co-existence of tiny 3D islands and optically active QDs in the same layer is in good agreement with the broad QD peak and the rather smooth transition from the QD to the WL signal in the PL spectra.

Comparing these results with literature PL data on MOCVD-grown QDs [51, 71, 74], an about 0.1 eV larger QD energy and also about 0.1 eV smaller energy separation between QD and WL peak, corresponding to a smaller hole localization, are apparent for the QDs of this work, which can be explained by the small QD size leading to rather small localization energies. Indeed, for all published results on (optically active) QDs grown by MOCVD [51, 52, 61, 71, 263, 264] sizes between 10 nm and 44 nm are reported, by far exceeding the QD sizes obtained here. It should be noted that the applied characterization methods would even not have been able to detect 3D GaSb structures as small as the tiny 3D islands. Anyway, also the coexistence of precursor structures and small QDs in the same layer observed here indicates that these QDs represent a very early stage of GaSb QD growth.

As it was not possible to obtain MOCVD-grown GaSb samples containing larger QDs for structural characterization within this work, which was mainly due to the generally considerable challenges connected with MOCVD growth of GaSb nanostructures, this task has to remain for future studies. The step by step pathway up to the formation of GaSb QDs using MOCVD, however, could be revealed here in detail.

This pathway is considerably different when MBE is used as growth method. Again,

the occurence of more or less pronounced gaps is common for all MBE-grown GaSb layers studied here, indicating a similar 2D island growth mode of thin GaSb films on GaAs. The general appearance of the QWs and WLs, on the other hand, differs significantly from the MOCVD-grown structures, and neither 2D Sb-rich islands nor tiny, compact 3D GaSb islands could be observed. Instead, flat and significantly intermixed QDs of already more than 10 nm baselength are observed even for small amounts of deposited material, which increase in size and GaSb composition with increasing GaSb supply. Additionally and most astonishingly, all GaSb QDs observed in MBE-grown samples exhibit a ring shape, in contrast to the small, compact MOCVD-grown QDs described above.

The outer contour of these ring-shaped QDs depends on the exact growth conditions, ranging from very flat structures to truncated pyramidal shapes with rather steep {111} side facets. However, all these QD structures are not massive, but exhibit a central gap, with an average diameter of about 40% of the outer baselength. The inner contour of the rings is not regularly defined, and in several cases a rather smooth transition from the GaSb ring body over strongly diluted material to the ring center consisting of pure GaAs was observed. In contrast to reported ring-like structures in the InAs/GaAs [224, 226, 230, 231] or other material systems [213, 232, 235, 236], these ring-shaped GaSb QDs have been formed upon considerably fast, nonstop overgrowth, without any partial capping or annealing step. Even more, these GaSb QDs are actual rings, whereas the reported In(Ga)As structures were shown to have a central depression, filled with GaAs and surrounded by an InAs rim only at the top, while the bottom part is still continuous In(Ga)As [227].

Ring-shaped GaSb QDs are obtained already when 1 ML GaSb is deposited, subsequent to Sb soaking and followed by GaAs overgrowth. With increasing GaSb supply, first the observed outer extensions of the QDs increase, too, until a final size is reached with baselengths of about 15 nm to 20 nm and heights varying between 1.3 nm and 2.1 nm for different growth conditions. Further GaSb deposition then only leads to a slight increase of the QD density up to $\sim 9 \times 10^{10}$ cm^{-2}. Parallel to the QD size, also the height of the intermixed WL is found to increase until a final GaSb content is reached, indicating a significant deviation from classical SK growth.

All MBE-grown GaSb layers are characterized by significant intermixing, reaching a maximum GaSb content of the WLs of less than 30%, and strong Sb segregation in growth direction, as many individual Sb atoms can be seen above the QDs and WLs, being incorporated in the GaAs overlayer. Both effects are correlated, as a lower GaSb content of the WL comes along with even stronger Sb segregation. Correspondingly, the total amount of GaSb, consisting of the material within the QDs and the WL as well as the Sb atoms incorporated in the overlayer, was found to have an upper limit of 2 ML. The material distribution between QDs, WL, and antimony within the overlayer has to fulfill this condition, which is given by the maximum strain that can be included in the GaSb layer.

This large strain inherent to GaSb/GaAs QDs in combination with the strong segregation upon overgrowth is assumed to be the driving force for ring formation. Thus, initially compact, free-standing GaSb QDs are supposed to be transformed into rings upon GaAs overgrowth by strain-driven material redistribution, occuring predominantly at the highly strained center of the QD. Correspondingly, the shape of free-standing GaSb QDs is still characterized by a more or less sharp summit, which agrees well with literature data obtained on such structures [44, 55, 69, 256, 267], while the ring shape is observed here for all capped QDs. Also the PL peak energy of about 1.1 eV obtained here for the flat, ring-shaped QDs agrees perfectly well with published PL data on capped GaSb QDs [47, 58, 59, 65, 69]. Since the electronic properties of ring-shaped QDs should be expected to differ strongly from compact ones, it can be assumed that capped GaSb QDs grown under typical MBE growth

conditions generally exhibit a ring structure.

The reason for the strong Sb segregation as well as for the significant intermixing is given by extraordinary strong group-V atomic exchange processes at the GaSb-GaAs interfaces. The process of Sb-for-As exchange at a GaAs growth surface exposed to an Sb_4 flux is well-known and intentionally used as Sb soaking. Indeed, more than 1 ML GaSb is evaluated here to have been incorporated only by such an Sb soaking step. The contrary case of As-for-Sb exchange at a GaSb growth surface under As_2 or As_4 flux, however, is usually unwanted as it causes the Sb segregation observed here: When Sb soaking is succeeded by direct GaSb deposition and subsequent GaAs overgrowth, a strongly inhomogeneous and intermixed, but distinguishable GaSb layer of typically about 2 to 5 ML thickness is obtained in addition to individual, broadly distributed Sb atoms. From the fact that these individual Sb atoms are only found above the GaSb QW, it can be confirmed that the exchange processes related to Sb soaking occur over a very short range of only a few ML, while the extended range of distributed Sb atoms is due to exchange and segregation effects during GaAs overgrowth. This different growth behavior at GaSb-on-GaAs and GaAs-on-GaSb interfaces can be explained by differences of the respective growth surfaces: Especially Sb-rich surface reconstructions of GaSb thin films on GaAs(001) [414–416] were analyzed to be a prerequisite for strong Sb segregation, as the resulting excess Sb in combination with a rather weak Ga-Sb bond enables massive As-for-Sb exchange.

Considering the material supplied by Sb soaking and GaSb deposition as well as the amount of GaSb observed in the capped QDs, WLs, and GaAs overlayers, three different destinations of the deposited antimony that got initially incorporated into free-standing QDs and WLs can be distinguished: A first fraction just remains where it is deposited or moves only over a short distance contributing to intermixing of the WL or shape transitions of the QDs. A second fraction of the Sb atoms is removed from the GaSb layer upon As exposure by As-for-Sb exchange and forms a floating layer at the growth surface, from which it gets re-incorporated during GaAs overgrowth, resulting in individual Sb atoms being distributed within the GaAs overlayer. As-for-Sb exchange additionally results in a third fraction of the Sb atoms, being removed from the GaSb surface but not re-incorporated again, remaining at the growth front as surfactant or being re-evaporated. The ratios between these three fractions depend on the amount of initially supplied GaSb, corresponding to the total amount of strain, on the growth sequence including GIs and fluxes, and on thermodynamic conditions as growth rate and temperature.

This model is confirmed by the analysis of exponential segregation profiles obtained from the XSTM data, corresponding to the re-incorporation of Sb atoms from the Sb floating layer during GaAs overgrowth. Indeed, the amount of material being available for re-incorporation was found to increase with increasing growth temperature, while the evaluated segregation coefficient, meaning the ratio of Sb atoms in the floating layer that are re-incorporated per ML upon GaAs overgrowth, changes simultaneously from 16% to only 9%.

In addition to the growth temperature, the growth sequence itself even more determines the extent of group-V exchange processes and thus the atomic structure of the QDs and WLs. The strongest Sb segregation is observed in samples which are grown including a 15 s long GI under As_4 flux, resulting in very flat QDs and rather low GaSb compositions of both the QDs and the WLs. For example, GaSb islands formed upon deposition of 1 ML GaSb prior to such a GI and subsequent capping exhibit lateral extensions of about 15 nm, which is twice as large as the baselength of the MOCVD-grown QDs, but are found still not to be optically active due to the low GaSb content. However, when the GaSb layers are immediately overgrown with GaAs (although always some time is needed for switching the fluxes), still significant Sb segregation occurs, but the resulting QDs have a larger height and especially a higher GaSb

content of the ring body, with chemical compositions ranging from 40% up to pure GaSb.

Comparing the MBE- and MOCVD-grown QDs of this work, apart from the small size of those formed using MOCVD, the ring shape only occuring in MBE-grown structures is the most striking difference. It cannot completely be excluded that some kind of ring structure might also occur upon further GaSb deposition in MOCVD growth. However, the fact that the GaSb ring structures observed yet have all been grown by MBE can well be explained by the lack of significant intermixing or Sb segregation during GaAs overgrowth using MOCVD, as these processes are essential for ring formation. Accordingly, the role of group-V exchange processes is much less dominant in MOCVD growth. The surface reconstructions could be a possible reason for this, as the mentioned extraordinary Sb-rich reconstructions have only been reported from MBE studies yet and do not necessarily have to occur in MOCVD growth, too. Additionally, the growth methods themselves, including the generally faster growth rates of MOCVD and the different source substances, are probably the main reason for the completely different influence of Sb segregation effects in MOCVD- and MBE-grown GaSb/GaAs nanostructures [74, 263].

For the MOCVD-grown QDs and QWs as well as for the MBE-grown ring-shaped QDs a type-II band alignment could be confirmed. Confined hole states of the GaSb nanostructures and Coulomb-bound electron states in the surrounding GaAs were analyzed to induce a specific contrast in XSTM images. This contrast mechanism could be explained in detail, considering tip-induced band bending interacting with the confined states. In XSTS spectra a type-II CB offset could directly be measured, amounting to about 0.1 eV. Despite of the ring structure of the MBE-grown QDs and the underlying strong intermixing and segregation, a hole localization of $\sim$ 0.3 eV already in rather flat QDs and $\sim$ 0.4 eV in somewhat larger ones was obtained.

Combining these type-II related electronic properties with the actual ring geometry, the MBE-grown QDs are exciting structures for fundamental physical effects like Aharonov-Bohm oscillations, according to theoretical predictions [77]. First respective experiments using magneto-PL and other methods studying the behavior of the ring-shaped GaSb QDs under external magnetic fields are planned for the near future [437].

Considering the electronic properties derived from PL and especially XSTS data in comparison with the structural details obtained by XSTM, an impressively large and yet hardly utilized potential of GaSb QDs for device applications gets apparent: Strong confinement and particularly large hole localization energies were observed at structures which – in respect of device suitability – are still far from perfect, exhibiting rather small sizes and being characterized by strong intermixing and segregation. The growth of large QDs consisting of rather pure GaSb with abrupt GaSb/GaAs interfaces, which is still a challenging task for epitaxy, would result in unique QD properties which were highly promising for optoelectronic and especially charge storage devices.

Regarding the MBE-grown QDs observed in this work, a considerable baselength could be achieved together with a rather pure GaSb stoichiometry at least in a part of the QDs. A GI subsequent to GaSb deposition was shown to result in strong intermixing and a flattening of already existing QDs and thus should be kept as short as possible. In order to further increase the GaSb content of the QDs and to achieve more abrupt interfaces, the strong Sb segregation upon GaAs overgrowth has to be strongly decreased, and therefore the massive As-for-Sb exchange needs to be avoided.

Hardly any Sb segregation was found at the MOCVD-grown nanostructures, which also exhibit a chemical composition with a considerably high GaSb percentage. The observed very small QDs were shown to represent an early stage of QD formation, thus from an extended GaSb deposition during MOCVD growth the formation of significantly larger QDs with rather

abrupt interfaces and a high GaSb content can be expected.

The realization of such QDs and the use of their potential in device applications will require extensive future research in many places. Hopefully the results of this work will contribute to that task, as this first XSTM investigation enhances the detailed and comprehensive understanding of the formation, atomic structure, and electronic properties of GaSb quantum dots in GaAs.

Appendix

Appendix A

Outlook: Tip sputtering and characterization by field ion microscopy

To further improve the structural and electronic quality of the STM tips, a special tip preparation and characterization chamber was designed as an extension of the XSTM chamber, as mentioned in chapter 4.2.2. This setup, which is currently under construction, combines an ion sputtering stage for tip preparation with possibilities for fast and easy field emission current measurements or field ion microscopy as a more sophisticated characterization method.

In this appendix a brief introduction into the techniques of ion sputtering, field emission measurements, and field ion microscopy will be given, followed by the main aspects of the new tip preparation and characterization chamber.

Tip sharpening by Ar^+ sputtering

Amongst the different proposed strategies to remove the oxide layer of etched W tips, sputtering of the tips by ions or electrons is a comparatively extensive method, but it can clean the tip very thoroughly and additionally lead to a further sharpening of the tips [438, 439].

Ion sputtering of STM tips has already been successfully established in this group several years ago [440]: Etched W tips [Fig. A.1(a)] were rotated in an external UHV chamber and sputtered with 4 kV Ar^+ ions at a pressure of about 10^{-5} mbar from the rear under an angle of about 45°. After one hour of sputtering, the acceleration voltage was decreased for a more gentle sputtering, until finally an ultra-sharp tip was produced. During this process, the sharpness of the tip was controlled from time to time by measuring the field emission current (see below). The final shape of the tip was determined by transmission electron microscopy, as shown in Fig. A.1(b), obtaining a radius of curvature of less than 3 nm.

While in that setup single tips were sputtered *ex-situ* and had later to be transferred into the STM chamber through air, a corresponding sputtering stage is now being built within the tip preparation chamber directly attached to the XSTM chamber. It offers three different flanges for the sputtering gun, enabling sputtering under angles of either 35°, 45°, or 55°, and the tips can easily be placed at a rotatable and adjustable sputtering position using the same tip holder system as in the XSTM.

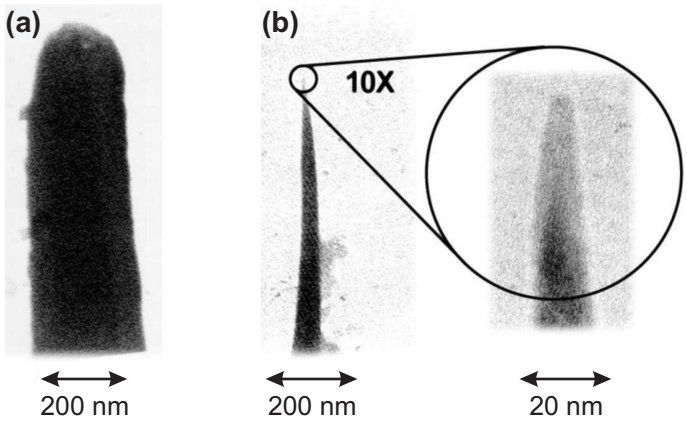

FIGURE A.1: Transmission electron microscopy images of representative STM tips (a) directly after electrochemical etching and (b) after sputtering the tip with Ar^+ ions; taken from [440].

Field emission current

During sputtering of the tip, an indicator is needed which can easily be measured to decide when the acceleration energy has to be reduced and when the sputtering has to be finished in order not to damage an already obtained good tip. Such an indicator is given by the field emission current between the tip and a steel plate acting as counter electrode.

Between the metal tip and any conductive electrode an electric field will form under an applied voltage. If the tip is negatively biased and the field is sufficiently large, electrons will emit from the tip and be accelerated along the lines of electric field towards the anode. This field emission was extensively studied by R. H. Fowler and L. Nordheim already in 1928 [441]. Considering the number of electrons being emitted from a metal surface of unit area per unit time under the applied electric field F, they derived the following expression for the field emission current density j (transformed to the SI system):

$$j = \frac{e^3}{2\pi h} \, \frac{\sqrt{\frac{E_F}{\phi}}}{E_F + \phi} \, F^2 \, \exp\left(-\frac{8\pi\sqrt{2m_e}}{3\,e\,h} \, \frac{\phi^{\frac{3}{2}}}{F} \right) \quad , \tag{A.1}$$

with the electronic charge e and mass m_e and the metal work function ϕ. If ϕ is measured in eV and the electric field in V/m, the current density expressed in A/m^2 amounts to

$$j = \frac{6.2 \cdot 10^{-6} \sqrt{\frac{E_F}{\phi}}}{E_F + \phi} \, F^2 \, \exp\left(-\frac{6.8 \cdot 10^9 \, \phi^{\frac{3}{2}}}{F} \right) \quad . \tag{A.2}$$

Equation A.2, known as the Fowler-Nordheim-equation for field emission, demonstrates a strong increase of the emission current with increasing field F.

For a sharp tip with an approximatedly spherical summit, the electric field is strongest directly at the tip apex and amounts to

$$F = \frac{V}{\kappa R} \tag{A.3}$$

for an applied voltage V and a tip radius of curvature R with $\kappa \approx 4 \ldots 8$ being a geometric factor [442, 443], which can best be approximated by $\kappa \approx 5$ [443, 444]. Replacing the current density j by the total field emission current I (in A) through the emitting region A_t of the tip (with R in m), this current finally results to

$$I = \frac{2.5 \cdot 10^{-7} \sqrt{\frac{E_F}{\phi}} \, A_t \, V^2}{E_F + \phi} \, \frac{1}{R^2} \, \exp\left(-\frac{3.4 \cdot 10^{10} \, \phi^{\frac{3}{2}}}{V} \, R \right) \quad . \tag{A.4}$$

Accordingly, the easily measurable emission current increases strongly with decreasing tip radius and can therefore be used as an indicator for the tip sharpness. For a rough estimation of the tip sharpness it can be sufficient to measure the order of magnitude of the current at a given voltage, or to measure the applied voltage V which is necessary to induce a specific current [440].

For a more exact measurement of the tip radius, I/V^2 can be plotted logarithmically versus $1/V$, resulting in a straight line of slope $-3.4 \cdot 10^{10}\, \phi^{3/2}\, R$ [359, 442].

Field ion microscopy

Exceeding the approximations of the Fowler-Nordheim current, the exact radius and also the complete geometry of the tip apex can be obtained when the current pattern is imaged by field ion microscopy (FIM), which was invented in 1952 by E. W. Müller in Berlin [442, 445].

For FIM imaging, the tip is positioned within a few cm distance opposite a conductive screen, or better, a multichannel plate within a vacuum chamber containing an imaging gas. A typical imaging gas is He, while Ne or H can also be used, at pressures of about 10^{-6} mbar. When a high voltage of several kV is applied between the positively charged tip and the screen, the atoms near the sharp tip get polarized within the very strong electric field and are attracted towards the tip [see Fig. A.2(a)]. In sufficiently large fields directly at the tip surface the atoms get ionized, which is occuring at a critical distance x_c determined by

$$x_c \approx \frac{I - \phi}{eF} \quad , \tag{A.5}$$

with the ionization energy I of the imaging gas atoms, the tip work function ϕ and the electric field F. Taking as example a W tip with a radius of curvature of 20 nm and an applied voltage of 5 kV, an electric field of $F = 5 \times 10^{10} \frac{V}{m}$ results, which – using He as imaging gas with $I = 25$ eV – leads to a critical distance of $x_c \approx 4$ Å for ionization of the He atoms.

Once the imaging gas atoms are ionized, they get accelerated to the screen along the lines of electrical field. These lines originate perpendicularly at the flat screen and also at the surface of the tip, thus a projected image of the tip geometry is present at the screen, as depicted in Fig. A.2(b). As the bending of the tip surface and therewith the electrical field is largest at atomic protrusions and edges of atomical terraces, such features appear as bright spots in the FIM images of the tip.

An impressive example of an FIM image is displayed in Fig. A.2(c), showing a crystalline W tip with a rather large radius of curvature, resulting in many surface terraces with slightly different orientation. From characteristic symmetric spots the tip apex can be identified as a (110) plane, with four additional {110} side facets. Also higher indexed geometries can be recognized, as shown in Fig. A.2(d).

The magnification and the lateral resolution of the FIM are mainly determined by the applied voltage and the radius of the tip. However, there are several effects limiting the resolution, including the initial tangential velocity of the imaging ions due to the finite temperature, the radius of the gas molecule itself, and the quantum mechanical uncertainty of the ion position according to Heisenberg [442]. Additionally, the applied voltage and the resulting electric field are restricted to avoid manipulation of the tip shape by field evaporation [359, 442]. In conclusion, best resolution is obtained with very small tip radii, by imaging at low temperatures, and by using imaging gases with high ionization fields and small atomic radii, thus favoring He as imaging gas for most tip materials. Under appropriate conditions atomic resolution down to less than 2 Å can be achieved [442].

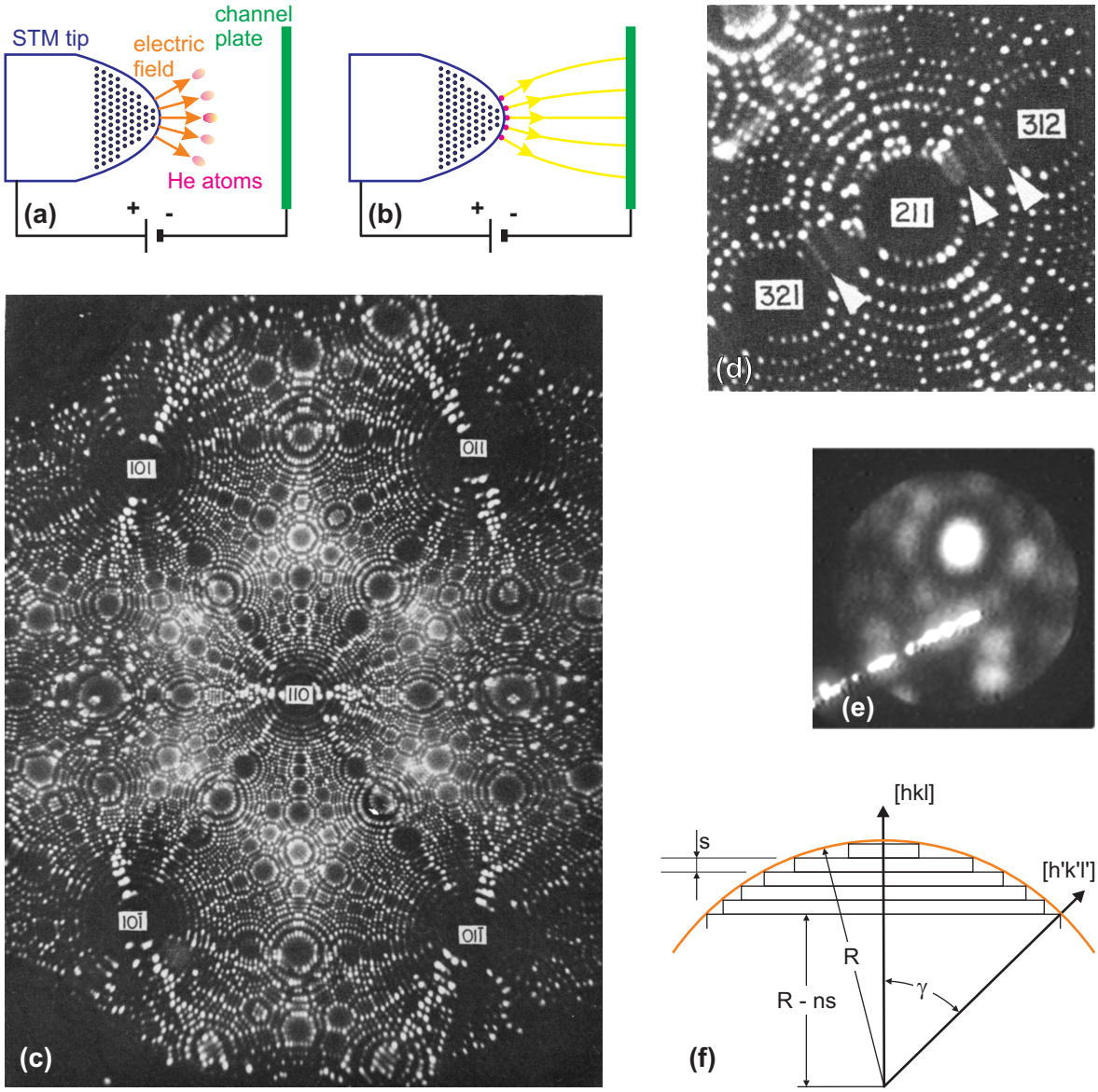

FIGURE A.2: (a,b) Sketches of the FIM principle: Imaging gas atoms get polarized and attracted towards the tip within the strong electric field (a), until they get ionized and are accelarated to the channel plate, imaging the tip (b). (c-e) FIM images of W tips, showing (c) a rather blunt tip in an wide-angle image, (d) a tip with a (211) apex, and (e) a very sharp tip with a (110) apex. The images are taken from (c,d) [442] and (e) [359]. (f) Sketch how to evaluate the local tip radius from a FIM image, adopted from [442].

Coming along with the increased resolution and magnification for decreased tip radii, the distances between neighboring atomic spots on the screen increase, too. Figure A.2(e) shows a very sharp polycrystalline W tip prepared for STM imaging, with one single atom directly at the apex [359]: The rings around the central spot contain only a few atoms and are considerably separated from each other. On the other hand, the angle between distinct surface planes of the tip is constant. Therefore the number of atomic rings which can be counted in the FIM image between characteristic neighboring spots is a measure for the radius of curvature, as it is depicted in Fig. A.2(f) [442]: The angle γ between the planes (hkl) and (h'k'l') and the step height s between neighboring atomic rings are determined by the crystal structure and the lattice constant of the material. Knowing the number n of rings

observed between the corresponding two planes, the local tip radius R amounts to

$$R = \frac{n\,s}{1-\cos\gamma} \quad . \tag{A.6}$$

Therewith the tip radius and the geometry of tips prepared for STM imaging can nicely be determined using FIM [356, 359].

Enhanced tip preparation setup for the XSTM chamber

The three discussed tip preparation and characterization methods – ion sputtering, measuring the field emission current, and imaging the tip geometry by FIM – are combined within the new tip preparation chamber, which is attached to the XSTM chamber and separated by UHV valves.

The complete chamber is specially designed to enable a fast and easy switching between the preparation and characterization stages and to directly transfer the readily prepared tips to the STM. A possible procedure of tip preparation is sketched in Figs. A.3(a-c): At the beginning, a freshly etched tip is taken from the tip storage, which can accommodate up to 28 tips, and is positioned at the tip holder by a wobble stick. The tip holder consists of a rotatable copper cylinder which is insulated against the UHV chamber and connected to a high voltage supply, holding the tip by a magnet. The radial position of the tip can be adjusted over a range of 10 cm by a linear drive at which the copper cylinder is mounted, enabling the tip to be positioned at the center of the ion beam [Fig. A.3(a)]. For sputtering, Ar can be supplied to the chamber via a gas dosing valve.

After the first desired duration of sputtering, the ion beam is switched off and the tip is moved a few cm forward close to a steel plate, which simultaneously acts as a shutter protecting the multichannel plate during sputtering and as an anode for field emission measuring [Fig. A.3(b)]. Large windows in the chamber give an easy optical access for positioning the tip at the different stages. For field emission, the tip is negatively biased by a high voltage and the resulting emission current is measured. According to the current, the sputtering process can be continued as before, the sputtering energy can be changed, or when the current is satisfyingly high the sputtering is not repeated any more and the tip is imaged by FIM.

In this case the shutter is removed, releasing the small entrance to the FIM which is nearly completely shielded by a copper frame. After the Ar has been replaced by He as imaging gas, the sputtered tip gets positioned a few cm in front of the channel plate which is negatively biased against the tip [Fig. A.3(c)]. At the rear side of the channel plate a phosphorus screen is mounted at which the FIM image of the tip can be viewed (or recorded by a camera) through a large window of the chamber.

This window and the flange containing the FIM setup including several high voltage feedthroughs can well be seen in the photograph of Fig. A.3(d), which also shows the flange of the shutter, a gas inlet valve, some windows for optical access, and instruments for UHV generation and measurement. In Fig. A.3(e), opposite to the FIM flange a linear drive can be seen. This linear drive holds a rotary drive (at the right hand of the image), to which the tip is mounted by the long copper cylinder (in the image hidden from view within the linear drive), thus the tip position is adjusted by the linear drive.

The exact setup of the sputtering and characterization stages can be seen in the scaled drawing in Fig. A.4(a). Additionally, a sketch of the complete new chamber and its connection to the XSTM system is shown in Fig. A.4(b). The tip preparation chamber is connected to the loadlock and to the old small preparation chamber by a long magnetic transfer, which enables an easy transfer of sputtered tips to the XSTM and also a fast supply of new tips and samples to the tip preparation chamber or to the XSTM chamber.

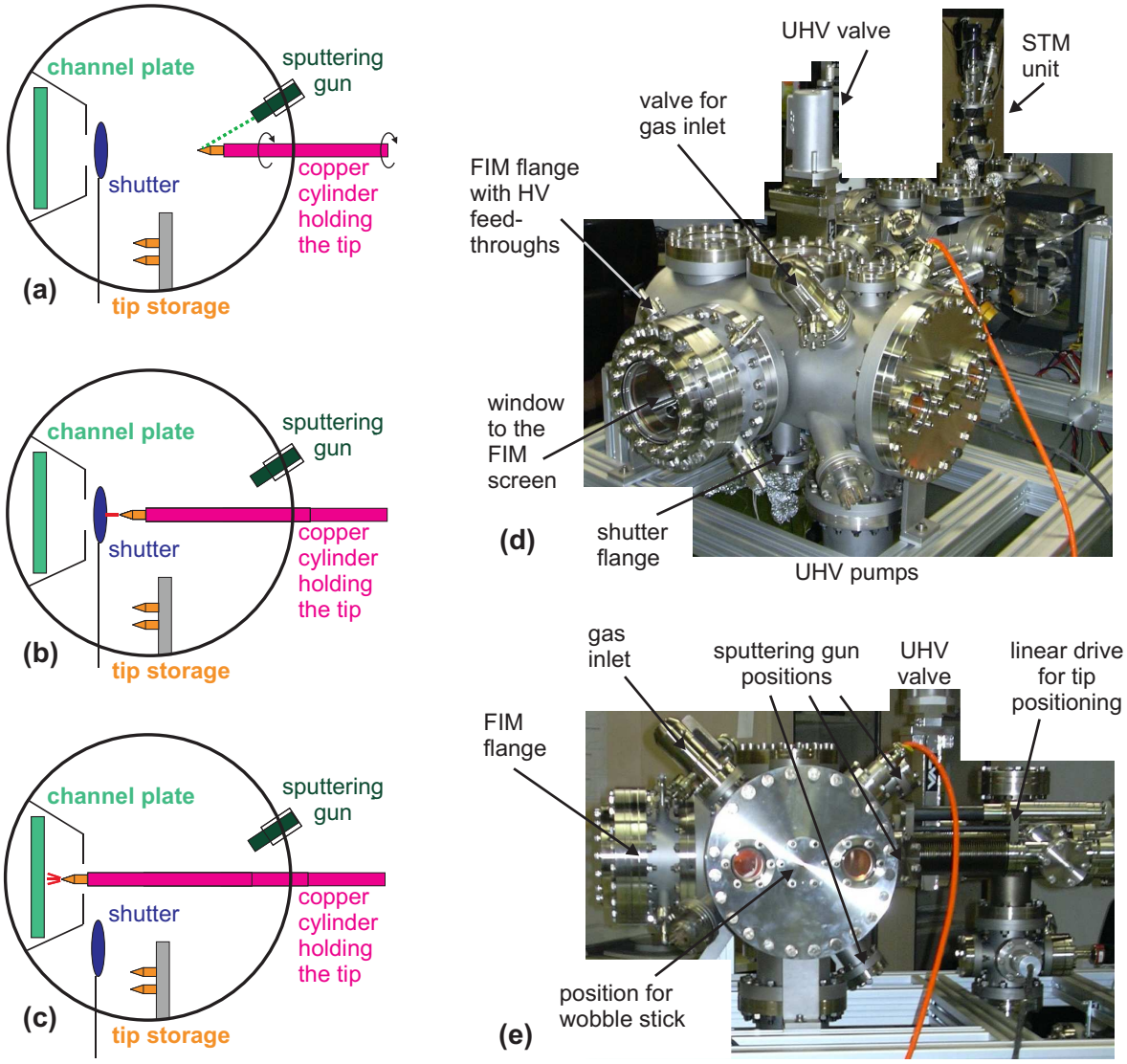

FIGURE A.3: (a-c) Tip preparation and characterization steps, consisting of (a) ion sputtering, (b) measuring the field emission current, and (c) FIM imaging. (d,e) Photographs of the new chamber.

Additionally to the controlled preparation of stable and sharp tips, it is possible and important to image a sputtered tip by FIM prior to its employment in the XSTM experiment and to characterize it again after it has aquired the STM images. In this way the changes to the STM tip structure upon imaging get apparent. Even more, if no such changes can be observed, one can be sure that the used tip has remained its structure analyzed by FIM throughout the whole XSTM experiment.

In conclusion, from the tip preparation expansion at the XSTM chamber setup a better resolution of the STM images and especially a by far increased structural and electronic stability of the tips for aquiring STS spectra can be expected. Moreover, the possibility to atomically characterize a tip before and after imaging in comparison with the aquired STM data will give new insight into the imaging process itself.

The UHV chamber is readily mounted and also the main mechanical parts of the tip preparation setup have already been finished, as can be seen in Fig. A.3(d,e). Currently the rather complex tip positioning stage including the electrical connections is under construction, together with some remaining mechanical feedthroughs. Once this stage is working, the

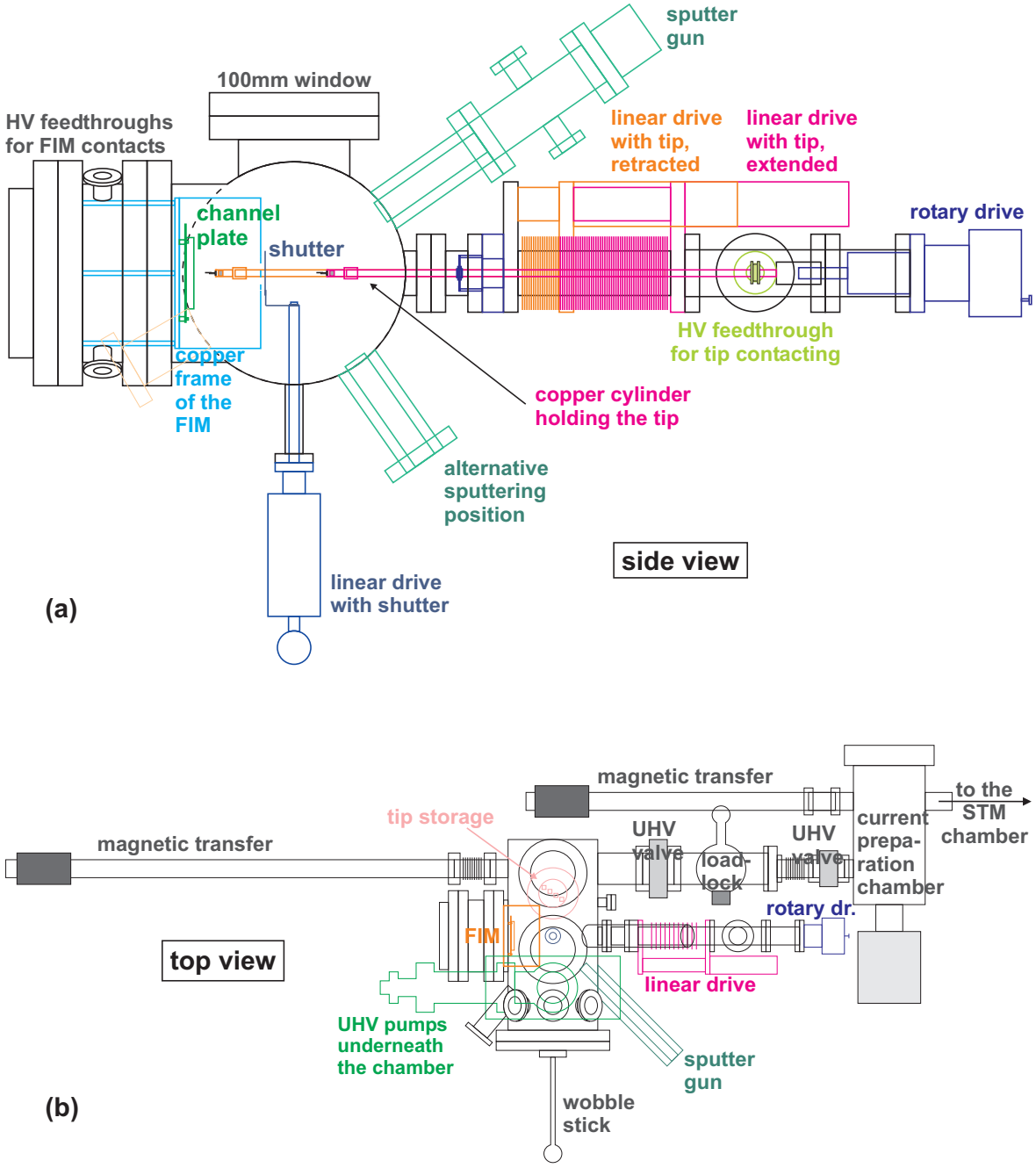

FIGURE A.4: Sketches drawn to scale of (a) the stage for tip sputtering and FIM imaging and (b) the complete tip preparation chamber.

chamber can already be used for tip sputtering and measuring the field emission current, while the FIM itself will be assembled as a last step.

Appendix B

Simulated distribution of cross-sections through ring structures

In the MBE-grown samples C and D quantum dots with a ring-like structure were obtained (see chapter 8). Although in XSTM images QDs with a rather compact appearance, like that shown in Fig. B.1(a), and paired features with a clear central gap, like that shown in Fig. B.1(b), were observed, it was concluded in section 8.3.1 that both types of images can represent a ring-shaped QD and differ only in the position where such a ring was cleaved [for illustration see Fig. B.1(d)].

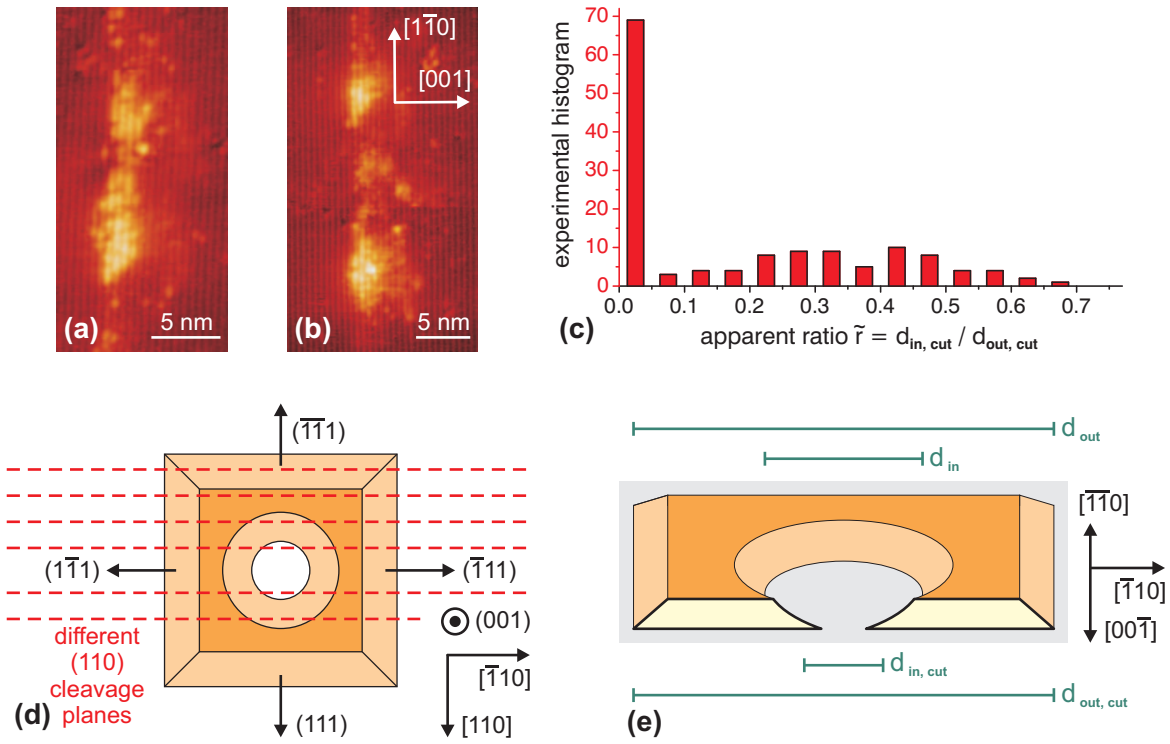

FIGURE B.1: Different cross-sections of cleaved ring-shaped QDs: (a,b) XSTM close-view images of QDs in layer 3 of sample C, taken at (a) V_T = -2.6 V and (b) V_T = -2.3 V; (c) histogram of the ratio of apparent inner to outer ring diameter, obtained from XSTM images of 140 QDs in sample C; sketches of (d) different cleavage positions of a QD and (e) a resulting cross-section.

From the XSTM images of sample C data on 140 QDs could be obtained, which is still a rather small database for statistical analysis, but is a large number of nanostructures for an atomically resolved XSTM investigation. In order to investigate the characteristics of the ring structure, especially the extension of the central gap, the ratio of inner to outer diameter in the XSTM images of ring-shaped QDs was chosen as a parameter which is independent of the total size of the QDs (see also section 8.3.2). The histogram of this parameter, obtained from the experimental data, is shown in Fig. B.1(c). It is important to notice that the actual inner diameter of the ring is in most cases larger than the diameter apparent in XSTM images, as the sketches in Fig. B.1(d,e) illustrate. Therefore it has to be distinguished between the actual ratio of inner and outer ring diameter $r = d_{in} \,/\, d_{out}$ and the ratio of the apparent diameters $\tilde{r} = d_{in,\,cut} \,/\, d_{out,\,cut}$. The latter one is the parameter that can directly be measured in XSTM images [and is shown in Fig. B.1(c)], while the former one determines the actual shape of the QD. Please note that for the assumption of a square-based outer shape of the ring with {111} side facets [Fig. B.1(d)] the apparent and actual outer diameters are identical, $d_{out,\,cut} = d_{out}$.

By calculating a distribution of the apparent ring ratio $\tilde{r}$ and comparing this simulation with the experimental histogram, the question should be answered if all QDs in sample C have a ring shape, or if ring-shaped and conventional, continuous QDs coexist. The concept of this simulation and the different steps will be introduced in the following.

In a first step the apparent ring ratios $\tilde{r}$ resulting from different cross sections through one QD with a constant actual inner diameter d_{in} are simulated. Therefor a parameterization of such a ring structure has to be chosen. For simplifiaction and using the symmetry of the ring, the outer diameter was set to $d_{out} = 2$, so the ring ratio is $r = \frac{1}{2}\, d_{in} = r_{in}$ with an inner ring radius $r_{in} = (0, \ldots, 1)$, and only one irreducible quadrant of the ring structure has to be regarded, as sketched in Fig. B.2(a). The QD is cleaved within this quadrant at the position $x = (0, \ldots, 1)$, with $x = 0$ meaning the QD being cleaved directly in the center and $x = 1$ meaning exactly at the edge. Then the apparent ring ratio as a function of the cleavage position results to

$$\tilde{r} = \sqrt{r_{in}^2 - x^2} \quad \text{for } x < r_{in} \quad , \quad \tilde{r} = 0 \quad \text{else.} \tag{B.1}$$

Due to the symmetry of the circle, Eq. B.1 can be inverted for all cleavage positions inside the ring, i.e. for $x < r_{in}$:

$$x(\tilde{r}) = \sqrt{r_{in}^2 - \tilde{r}^2} \quad . \tag{B.2}$$

In order to simulate the distribution, however, not the exact value of $\tilde{r}$ or $x(\tilde{r})$ is important, but the frequency h how often a value within the interval $[\tilde{r},\ \tilde{r} + \Delta\tilde{r})$ is obtained, i.e. how many different cleavage positions lie within the corresponding interval $[x(\tilde{r}),\ x(\tilde{r} + \Delta\tilde{r})) = [x,\ x + \Delta x)$, as it is sketched in Fig. B.2(b). For the frequencies of $\tilde{r}$ and x one can postulate

$$|\, h(\tilde{r})\, \Delta\tilde{r}\,| = |\, h(x)\, \Delta x\,| \quad . \tag{B.3}$$

Assuming that the frequency $h(x)$ is constant, meaning that all possible cleavage positions have equal probability, and considering the range of the cleavage positions $x \in (0, 1]$, one yields $h(x) = 1$, and the frequency of the apparent ring ratio results to

$$h(\tilde{r}) = \left|\, \frac{\Delta x}{\Delta\tilde{r}} \,\right| \quad . \tag{B.4}$$

Coming back to Eq. B.2, for sufficiently small intervals $\Delta\tilde{r}$ and for cleavage positions $x < r_{in}$ the frequency of the apparent ring ratio can now be given by

$$h(\tilde{r}) = \left|\, \frac{dx(\tilde{r})}{d\tilde{r}} \,\right| = \frac{\tilde{r}}{\sqrt{r_{in}^2 - \tilde{r}^2}} \quad . \tag{B.5}$$

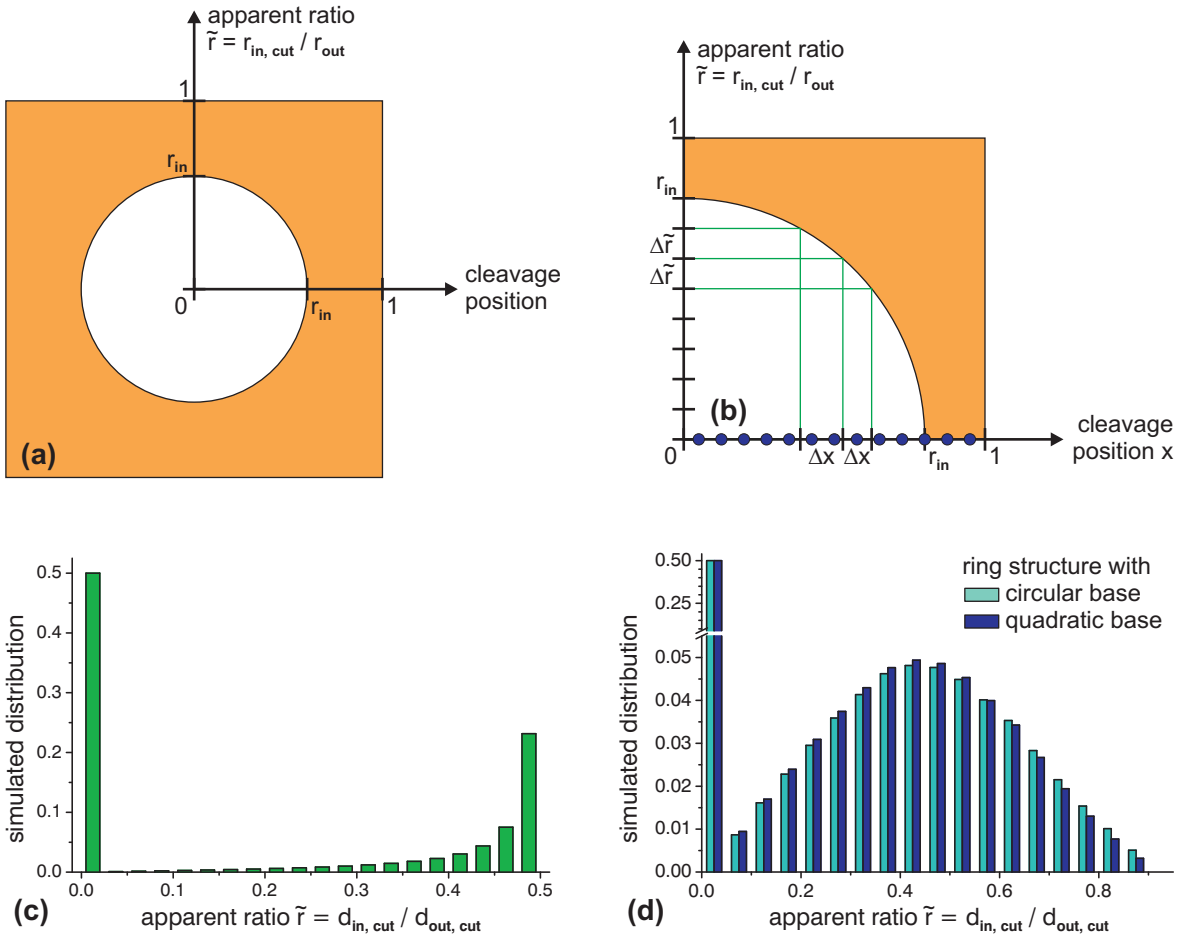

FIGURE B.2: Pathway of simulating the distribution of ring cleavage: (a) Parameterization of a model ring structure, (b) sketch how to obtain the frequency of a certain interval $[\tilde{r},\ \tilde{r}+\Delta\tilde{r})$. (c,d) Calculated distributions of the apparent ring ratio for (c) a structure with constant $r_{in} = 0.5$ and (d) ring structures with varying actual inner radii $r_{in} = (0.1, \ldots, 0.9)$, weighted by a Gaussian distribution with a maximum at 0.5 and a standard deviation of 0.2. In (d) a calculated distribution using a model ring structure with a quadratic base, as shown in (a), is compared with a distribution using a circular-based model.

For all cleavage positions $x > r_{in}$, the apparent ring ratio is $\tilde{r} = 0$, thus the frequency $h(0)$ is proportional to the ratio of the numbers of cleavage positions outside $(r_{in} < x < 1)$ and inside $(0 < x < r_{in})$ the central gap and has to be normalized by the sum over all frequencies with $\tilde{r} > 0$ as follows:

$$h(\tilde{r}=0) \;=\; \frac{1-r_{in}}{r_{in}} \cdot \sum h\,(\tilde{r}>0) \;=\; \frac{1-r_{in}}{r_{in}} \cdot \sum_{x=0}^{r_{in}} \frac{dx(\tilde{r})}{d\tilde{r}} \;=\; 1-r_{in} \quad . \tag{B.6}$$

A calculated distribution of the apparent ring ratio for a ring structure with $r_{in} = 0.5$ is shown in Fig. B.2(c), which obviously still has no agreement with the experimental histogram [Fig. B.1(c)]. In a next step, it is therefore necessary to regard an ensemble of ring structures with a distribution of inner radii r_{in}, which is simulated by a Gaussian distribution G with a maximum at r_0 and a standard deviation σ. Thus for a set of different radii $r_{in} = [r_{min}, \ldots, r_{max}]$ the calculated cleavage distribution for each radius has to be weighted

by the Gaussian distribution as follows:

$$\bar{h}(\tilde{r}) = \sum_{r_{in}} h(\tilde{r}, r_{in}) \cdot G(r_{in}) = \sum_{r_{in}=r_{min}}^{r_{max}} \frac{\tilde{r}}{\sqrt{r_{in}^2 - \tilde{r}^2}} \cdot \exp\left(-\frac{1}{2}\left(\frac{r_0 - r_{in}}{\sigma}\right)^2\right) \quad . \tag{B.7}$$

An example of such a weighted distribution is shown in Fig. B.2(d), using the parameters $r_0 = 0.5$ and $\sigma = 0.2$ and inner ring radii from $r_{in} = 0.1$ to $r_{in} = 0.9$. A high peak for $\tilde{r} = 0$, corresponding to cross-sections showing no central gap, and a broad distribution for larger values of $\tilde{r}$ with a maximum between 0.4 and 0.5 can be seen. The frequency $h(0)$ corresponding to $\tilde{r} = 0$ is calculated analogously to Eq. B.6 and regarding the Gaussian distribution of the radii by

$$\bar{h}(\tilde{r} = 0) = \sum_{r_{in}} h(\tilde{r} = 0,\, r_{in}) \cdot G(r_{in}) \quad . \tag{B.8}$$

Depending on the number of different radii r_{in} employed in the sums of Eqs. B.7 and B.8, the weighted cleavage distribution has to be renormalized to fulfill the condition

$$\sum_{\tilde{r}=0}^{1} \bar{h}(\tilde{r}) \; = 1 \quad . \tag{B.9}$$

It should be noted that only the blue columns in Fig. B.2(d) represent a distribution calculated as described above, while for the distribution shown by green columns the ring structure was modelled differently: Instead of an outer shape with a quadratic base [as sketched in Figs. B.1(d) and B.2(a)] a circular base was assumed here, leading to a slightly different frequency of apparent ring ratio

$$h(\tilde{r}) = \frac{\tilde{r}}{\sqrt{r_{in}^2 - \tilde{r}^2}\,\sqrt{1 - \tilde{r}^2}} - \frac{\tilde{r}\,\sqrt{r_{in}^2 - \tilde{r}^2}}{\sqrt{(1 - \tilde{r}^2)^3}} \tag{B.10}$$

instead of Eq. B.5. Comparing both calculated results in Fig. B.2(d) it can be seen that the choice of the model ring structure has very little influence on the distribution of the apparent ring ratio.

For the calculated results shown in Fig. B.2(d) the variables r_0 and σ of the Gaussian distribution have been chosen arbitrarily. In a final step, these variables now have to be optimized to obtain the best fit between the calculated distribution and the experimental histogram. Thereby all values for $\tilde{r} > 0$ are included in the fitting procedure, while the peak at $\tilde{r} = 0$ is not considered. In order to evaluate the agreement between simulation and experiment, two parameters are regarded, namely the mean deviation of the experimental data from the model and the statistical average of the apparent ring ratios $\tilde{r}$. The latter one can easily be calculated for the complete experimental data set of all QDs observed by XSTM, and it can also straightforwardly be obtained from the calculated results by averaging the apparent ring ratios for all used actual radii r_{in} and cleavage positions x, weighted by the Gaussian distribution. Obviously, the difference between both average values should be as small as possible for a good simulation of the experimental findings.

The mean deviation χ^2 is calculated for the individual columns i of the experimental and calculated distributions for $\tilde{r} > 0$, regarding the number n_{QD} of experimentally observed QDs, by summarizing over all N columns as follows:

$$\chi^2 = \frac{1}{N-1} \cdot \sum_{i=1}^{N} \left(\frac{h_{exp}(\tilde{r}_i) - n_{QD} \cdot h_{calc}(\tilde{r}_i)}{\sqrt{n_{QD} \cdot h_{calc}(\tilde{r}_i)}} \right)^2 \quad . \tag{B.11}$$

A color map of the value of χ^2 for a broad parameter range of the Gaussian variables r_0 and σ is shown in Fig. B.3(a). Good agreement between experiment and calculation, meaning a small mean deviation χ^2, is obtained for an average ring radius r_0 between 0.3 and 0.5 with a Gaussian standard deviation σ between 0.1 and 0.2.

Additionally to the mean deviation, the difference between the average apparent ring ratio in experiment and calculation $\Delta <\tilde{r}>$ is displayed as a color map for the same ranges of r_0 and σ in Fig. B.3(b): Here, for all actual ring radii smaller than $r_0 = 0.5$ a corresponding value of the statistical deviation with $\sigma < 0.35$ exists which leads to good agreement between experiment and simulation.

By comparing the results for both parameters χ^2 and $\Delta <\tilde{r}>$ [Fig. B.3(c)], the pair of Gaussian variables r_0 and σ which leads to the best fit can be obtained to $r_0 = 0.42$ and $\sigma = 0.13$. The value of r_0 can therefore be estimated to be the average ratio of actual inner to outer ring diameter for the ring-shaped QDs in sample C. The corresponding distribution calculated using these parameters and considering all possible actual ring radii between 0.1 and 0.9 is shown by the blue columns in Fig. B.3(c), together with the experimental histogram displayed in red.

While a detailed comparison of both distributions and a discussion of the resulting con-

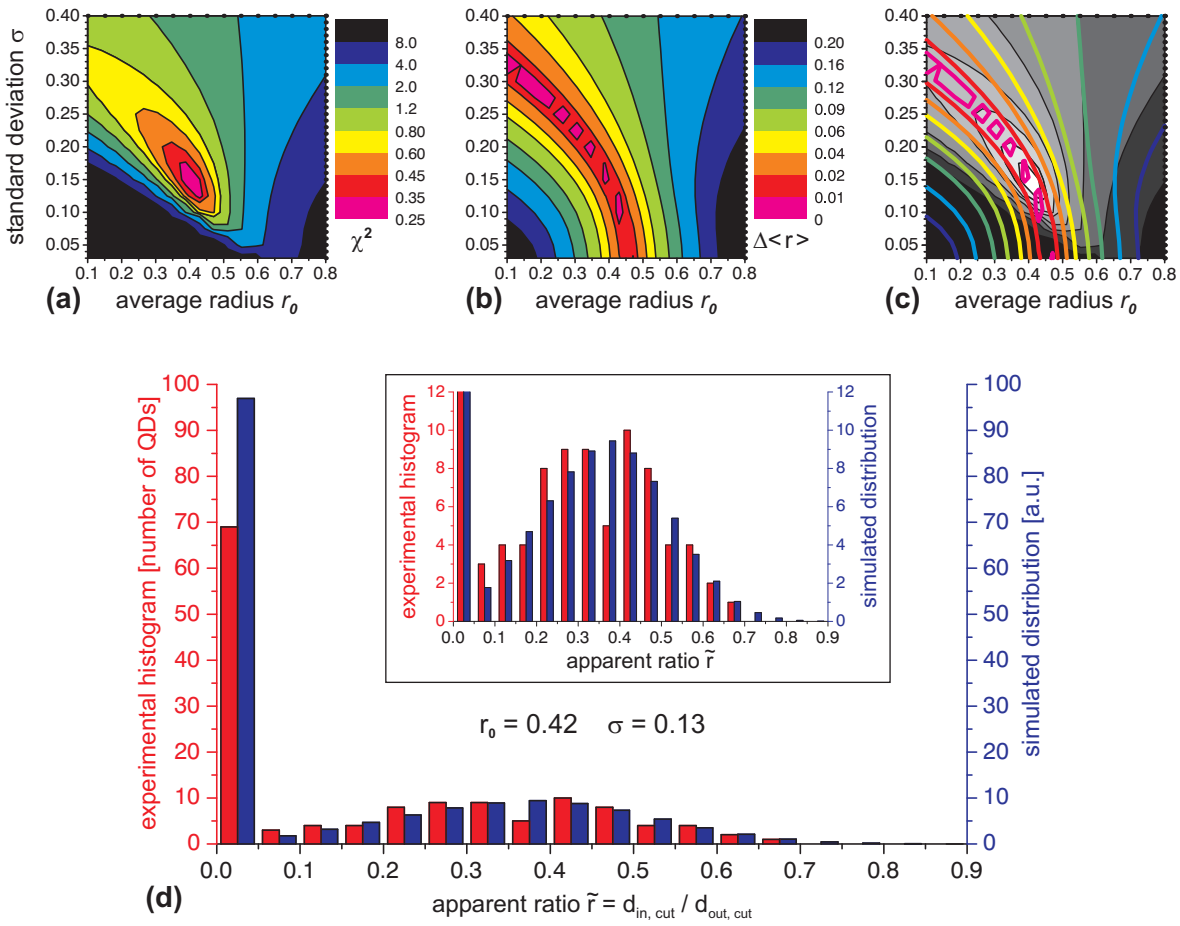

FIGURE B.3: Optimizing the parameters r_0 and σ of the Gaussian distribution to fit the experimental histogram for $\tilde{r} > 0$: Calculated values of (a) the mean deviation between experimental and simulated data χ^2, (b) the difference between the average apparent ring ratios of experiment and simulation $\Delta <\tilde{r}>$, and (c) an overlay of (a), shown as greyscale plot, and (b), indicated by colored lines. (d) A comparison between experimental and simulated distribution for the best fit of $r_0 = 0.42$ and $\sigma = 0.13$.

clusions is performed in section 8.3.2, here only the very good agreement between experiment and simulation is emphasized, especially in regard to the rather poor statistical database and the idealized assumptions used for modeling the ring structure.

List of abbreviations

2D	two-dimensional
3D	three-dimensional
AB effect	Aharonov-Bohm effect
AB oscillation	Aharonov-Bohm oscillation
AFM	atomic force microscopy
CB	conduction band
CITS	current imaging tunneling spectroscopy
CV	capacitance voltage
DLTS	deep level transient spectroscopy
DOS	density of states
DRAM	dynamic random access memory
FIM	field ion microscopy / microscope
FWHM	full width of half maximum
GI	growth interruption
HRTEM	high-resolution transmission electron microscopy
LDOS	local density of states
MBE	molecular beam epitaxy
ML	monolayer
MOCVD	metalorganic chemical vapor deposition
PL	photoluminescence
PLE	photoluminescence excitation
QD	quantum dot
QR	quantum ring
QW	quantum well

RHEED	reflection high energy electron diffraction
SEM	scanning electron microscopy / microscope
SK growth	Stranski-Krastanow growth
STEM	scanning transmission electron microscopy
STM	scanning tunneling microscopy / microscope
STS	scanning tunneling spectroscopy
tBAs	tertiarbutylarsine
tBP	tertiarbutylphosphine
TEGa	triethylgallium
TEM	transmission electron microscopy / microscope
TESb	triethylantimony
TIBB	tip-induced band bending
TMAl	trimethylaluminium
TMGa	trimethylgallium
UHV	ultrahigh vacuum
VB	valence band
WL	wetting layer
XSTM	cross-sectional scanning tunneling microscopy / microscope
XSTS	cross-sectional scanning tunneling spectroscopy

Bibliography

[1] M. Grundmann, *The Physics of Semiconductors*, Springer, Berlin, 2006.

[2] D. Bimberg, M. Grundmann, and N. N. Ledentsov, *Quantum dot heterostructures*, John Wiley & Sons, Chichester, 1999.

[3] M. Grundmann, editor, *Nano-Optoelectronics*, Springer, Berlin, 2002.

[4] H. Kroemer, Proc. IEEE **51**, 1782 (1963).

[5] Zh. I. Alferov, V. M. Andreev, V. I. Korol'kov, E. L. Portnoi, and D. N. Tret'yakov, Sov. Phys. Semicond. **2**, 1289 (1969).

[6] N. Kirstaedter, N. N. Ledentsov, M. Grundmann, D. Bimberg, V. M. Ustinov, S. S. Ruvimov, M. V. Maximov, P. S. Kop'ev, Zh. I. Alferov, U. Richter, P. Werner, U. Gösele, and J. Heydenreich, Electron. Lett. **30**, 1416 (1994).

[7] D. Bimberg, J. Phys. D: Appl. Phys **38**, 2055 (2005).

[8] G. E. Moore, Electronics **38**, 114 (1965).

[9] V. Shchukin, N. N. Ledentsov, and D. Bimberg, *Epitaxy of Nanostructures*, Springer, Berlin, 2003.

[10] P. Michler, A. Kiraz, C. Becher, W. V. Schoenfeld, P. M. Petroff, L. Zhang, E. Hu, and A. Imamoğlu, Science **290**, 2282 (2000).

[11] F. Findeis, M. Baier, E. Beham, A. Zrenner, and G. Abstreiter, Appl. Phys. Lett. **78**, 2958 (2001).

[12] X. Li, Y. Wu, D. Steel, D. Gammon, T. H. Stievater, D. S. Katzer, D. Park, C. Piermarocchi, and L. J. Sham, Science **301**, 809 (2003).

[13] R. Seguin, A. Schliwa, S. Rodt, K. Pötschke, U. W. Pohl, and D. Bimberg, Phys. Rev. Lett. **95**, 257402 (2005).

[14] J. H. Davies, *The physics of low-dimensional semiconductors*, Cambridge University Press, Cambridge, 1998.

[15] R. Leon, P. M. Petroff, D. Leonard, and S. Fafard, Science **267**, 1966 (1995).

[16] M. Grundmann, O. Stier, and D. Bimberg, Phys. Rev. B **52**, 11969 (1995).

[17] M. S. Skolnick and D. J. Mowbray, Physica E **21**, 155 (2004).

[18] L. Goldstein, F. Glas, J. Y. Marzin, M. N. Charasse, and G. LeRoux, Appl. Phys. Lett. **47**, 1099 (1985).

[19] Y.-W. Mo, D. E. Savage, B. S. Swartzentruber, and M. G. Lagally, Phys. Rev. Lett. **65**, 1020 (1990).

[20] D. Leonard, K. Pond, and P. M. Petroff, Phys. Rev. B **50**, 11687 (1994).

[21] D. Bimberg, M. Grundmann, N. N. Ledentsov, S. S. Ruvimov, P. Werner, U. Richter, J. Heydenreich, V. M. Ustinov, P. S. Kop'ev, and Zh. I. Alferov, Thin Solid Films **267**, 32 (1995).

[22] R. Heitz, T. R. Ramachandran, A. Kalburge, Q. Xie, I. Mukhametzhanov, P. Chen, and A. Madhukar, Phys. Rev. Lett. **78**, 4071 (1997).

[23] N. N. Ledentsov, V. M. Ustinov, V. A. Shchukin, P. S. Kop'ev, and Zh. I. Alferov, Semiconductors **32**, 343 (1998).

[24] J. Márquez, L. Geelhaar, and K. Jacobi, Appl. Phys. Lett. **78**, 2309 (2001).

[25] H. Eisele and K. Jacobi, Appl. Phys. Lett. **90**, 129902 (2007).

[26] M. A. Herman, W. Richter, and H. Sitter, *Epitaxy: physical principles and technical implementation*, Springer, Berlin, 2004.

[27] N. P. Kobayashi, T. R. Ramachandran, P. Chen, and A. Madhukar, Appl. Phys. Lett. **68**, 3299 (1996).

[28] T. Walther, A. G. Cullis, D. J. Norris, and M. Hopkinson, Phys. Rev. Lett. **86**, 2381 (2001).

[29] P. B. Joyce, T. J. Krzyzewski, P. H. Steans, G. R. Bell, J. H. Neave, and T. S. Jones, Surf. Sci. **492**, 345 (2001).

[30] P. Kratzer and M. Scheffler, Phys. Rev. Lett. **88**, 036102 (2002).

[31] K. Jacobi, Prog. Surf. Sci. **71**, 185 (2003).

[32] G. Costantini, A. Rastelli, C. Manzano, R. Songmuang, O. G. Schmidt, K. Kern, and H. von Känel, Appl. Phys. Lett. **85**, 5673 (2004).

[33] M. C. Xu, Y. Temko, T. Suzuki, and K. Jacobi, J. Appl. Phys. **98**, 083525 (2005).

[34] P. Kratzer, Q. K. K. Liu, P. Acosta-Diaz, C. Manzano, G. Costantini, R. Songmuang, A. Rastelli, O. G. Schmidt, and K. Kern, Phys. Rev. B **73**, 205347 (2006).

[35] G. Costantini, A. Rastelli, C. Manzano, P. Acosta-Diaz, R. Songmuang, G. Katsaros, O. G. Schmidt, and K. Kern, Phys. Rev. Lett. **96**, 226106 (2006).

[36] M. Dähne, H. Eisele, and K. Jacobi, *Atomic Structure of Quantum Dots* in *Growth-related Structures of Semiconductor Nanostructures,* edited by D. Bimberg, Springer, Berlin, to be published.

[37] O. Stier, M. Grundmann, and D. Bimberg, Phys. Rev. B **59**, 5688 (1999).

[38] P. W. Fry, I. E. Itskevich, D. J. Mowbray, M. S. Skolnick, J. J. Finley, J. A. Barker, E. P. O'Reilly, L. R. Wilson, I. A. Larkin, P. A. Maksym, M. Hopkinson, M. Al-Khafaji, J. P. R. David, A. G. Cullis, G. Hill, and J. C. Clark, Phys. Rev. Lett. **84**, 733 (2000).

[39] O. Stier, R. Heitz, A. Schliwa, and D. Bimberg, phys. stat. sol. (a) **190**, 477 (2002).

[40] S. Rodt, A. Schliwa, R. Heitz, V. Türck, O. Stier, R. L. Sellin, M. Strassburg, U. W. Pohl, and D. Bimberg, phys. stat. sol. (b) **234**, 354 (2002).

[41] L. He, G. Bester, and A. Zunger, Phys. Rev. B **70**, 235316 (2004).

[42] G. Bester and A. Zunger, Phys. Rev. B **71**, 045318 (2005).

[43] U. W. Pohl, R. Seguin, S. Rodt, A. Schliwa, K. Pötschke, and D. Bimberg, Physica E **35**, 285 (2006).

[44] F. Hatami, N. N. Ledentsov, M. Grundmann, J. Böhrer, F. Heinrichsdorff, M. Beer, D. Bimberg, S. S. Ruvimov, P. Werner, U. Gösele, J. Heydenreich, U. Richter, S. V. Ivanov, B. Ya. Meltser, P. S. Kop'ev, and Zh. I. Alferov, Appl. Phys. Lett. **67**, 656 (1995).

[45] B. R. Bennett, P. M. Thibado, M. E. Twigg, E. R. Glaser, R. Magno, B. V. Shanabrook, and L. J. Whitman, J. Vac. Sci. Technol. B **14**, 2195 (1996).

[46] P. M. Thibado, B. R. Bennett, M. E. Twigg, B. V. Shanabrook, and L. J. Whitman, J. Vac. Sci. Technol. A **14**, 885 (1996).

[47] F. Hatami, M. Grundmann, N. N. Ledentsov, F. Heinrichsdorff, R. Heitz, J. Böhrer, D. Bimberg, S. S. Ruvimov, P. Werner, V. M. Ustinov, P. S. Kop'ev, and Zh. I. Alferov, Phys. Rev. B **57**, 4635 (1998).

[48] K. Suzuki, R. A. Hogg, K. Tachibana, and Y. Arakawa, Jpn. J. Appl. Phys. **37**, L 203 (1998).

[49] K. Suzuki and Y. Arakawa, J. Crystal Growth **201/202**, 1205 (1999).

[50] J. P. Silveira, J. M. Garcia, and F. Briones, J. Crystal Growth **227**, 995 (2001).

[51] L. Müller-Kirsch, R. Heitz, U. W. Pohl, D. Bimberg, I. Häusler, H. Kirmse, and W. Neumann, Appl. Phys. Lett. **79**, 1027 (2001).

[52] Motlan, E. M. Goldys, and T. L. Tansley, J. Cryst. Growth **236**, 621 (2002).

[53] L. Müller-Kirsch, N. N. Ledentsov, R. Sellin, U. W. Pohl, D. Bimberg, I. Häusler, H. Kirmse, and W. Neumann, J. Crystal Growth **248**, 333 (2003).

[54] X. D. Luo, Z. Y. Xu, Y. Q. Wang, W. X. Wang, J. N. Wang, and W. K. Ge, J. Crystal Growth **247**, 99 (2003).

[55] I. Farrer, M. J. Murphy, D. A. Ritchie, and A. J. Shields, J. Crystal Growth **251**, 771 (2003).

[56] M. Kudo, T. Mishima, S. Iwamoto, T. Nakaoka, and Y. Arakawa, Physica E **21**, 275 (2004).

[57] O. J. Pitts, S. P. Watkins, C. X. Wang, J. A. H. Stotz, T. A. Meyer, and M. L. W. Thewalt, J. Crystal Growth **269**, 187 (2004).

[58] N. Yamamoto, K. Akahane, and N. Ohtani, Physica E **21**, 322 (2004).

[59] T. Nakai, S. Iwasaki, and K. Yamaguchi, Jpn. J. Appl. Phys. **43**, 2122 (2004).

[60] S. Kobayashi, C. Jiang, T. Kawazu, and H. Sakaki, Jpn. J. Appl. Phys. **43**, L662 (2004).

[61] K. Drozdowicz-Tomsia, E. M. Goldys, M. Motlan, H. Zareie, and M. R. Phillips, Appl. Phys. Lett. **86**, 173113 (2005).

[62] G. Balakrishnan, J. Tatebayashi, A. Khoshakhlagh, S. H. Huang, A. Jallipalli, L. R. Dawson, and D. L. Huffaker, Appl. Phys. Lett. **89**, 161104 (2006).

[63] M. Geller, C. Kapteyn, L. Müller-Kirsch, R. Heitz, and D. Bimberg, Appl. Phys. Lett. **82**, 2706 (2003).

[64] M. Hayne, O. Razinkova, S. Bersier, R. Heitz, L. Müller-Kirsch, M. Geller, D. Bimberg, and V. V. Moshchalkov, Phys. Rev. B **70**, 081302 (2004).

[65] E. R. Glaser, B. R. Bennett, B. V. Shanabrook, and R. Magno, Appl. Phys. Lett. **68**, 3614 (1996).

[66] C.-K. Sun, G. Wang, J. E. Bowers, B. Brar, H.-R. Blank, H. Kroemer, and M. H. Pilkuhn, Appl. Phys. Lett. **68**, 1543 (1996).

[67] M. E. Rubin, H. R. Blank, M. A. Chin, H. Kroemer, and V. Narayanamurti, Appl. Phys. Lett. **70**, 1590 (1997).

[68] S. M. North, P. R. Briddon, M. A. Cusack, and M. Jaros, Phys. Rev. B **58**, 12601 (1998).

[69] K. Suzuki, R. A. Hogg, and Y. Arakawa, J. Appl. Phys. **85**, 8349 (1999).

[70] R. Magno, B. R. Bennett, and E. R. Glaser, J. Appl. Phys. **88**, 5843 (2000).

[71] L. Müller-Kirsch, R. Heitz, A. Schliwa, O. Stier, D. Bimberg, H. Kirmse, and W. Neumann, Appl. Phys. Lett. **78**, 1418 (2001).

[72] L. Müller-Kirsch, R. Heitz, A. Schliwa, O. Stier, D. Bimberg, H. Kirmse, and W. Neumann, Appl. Phys. Lett. **78**, 3908 (2001).

[73] L. Müller-Kirsch, A. Schliwa, O. Stier, R. Heitz, H. Kirmse, W. Neumann, and D. Bimberg, phys. stat. sol. (b) **224**, 349 (2001).

[74] Motlan and E. M. Goldys, Appl. Phys. Lett. **79**, 2976 (2001).

[75] M. Hayne, J. Maes, S. Bersier, V. V. Moshchalkov, A. Schliwa, L. Müller-Kirsch, C. Kapteyn, R. Heitz, and D. Bimberg, Appl. Phys. Lett. **82**, 4355 (2003).

[76] Gh. Dumitras and H. Riechert, J. Appl. Phys. **94**, 3955 (2003).

[77] M. Grochol, F. Grosse, and R. Zimmermann, Phys. Rev. B **74**, 115416 (2006).

[78] W. W. Chow, O. Blum Spahn, H. C. Schneider, and J. F. Klem, IEEE J. Quantum Elect. **37**, 1178 (2001).

[79] T. Anan, M. Yamada, K. Nishi, K. Kurihara, K. Tokutome, A. Kamei, and S. Sugou, Electron. Lett. **37**, 566 (2001).

[80] M. Geller, C. Kapteyn, E. Stock, L. Müller-Kirsch, R. Heitz, and D. Bimberg, Physica E **21**, 474 (2004).

[81] A. Marent, M. Geller, D. Bimberg, A. P. Vasi'ev, E. S. Semenova, A. E. Zhukov, and V. M. Ustinov, Appl. Phys. Lett. **89**, 072103 (2006).

[82] M. Geller, A. Marent, T. Nowozin, D. Feise, K. Pötschke, N. Akçay, N. Öncan, and D. Bimberg, Physica E, in print.

[83] M. Geller, A. Marent, and D. Bimberg, *Speicherzelle und Verfahren zum Speichern von Daten*, Deutsche Patentanmeldung Nr. 10 2006 059 110.0 (October 27, 2006).

[84] T. Brown, A. Brown, and G. May, J. Vac. Sci. Technol. B **20**, 1771 (2002).

[85] G. Binnig, H. Rohrer, Ch. Gerber, and E. Weibel, Phys. Rev. Lett. **49**, 57 (1982).

[86] G. Binnig and H. Rohrer, Helv. Phys. Acta **55**, 726 (1982).

[87] J. Tersoff and D. R. Hamann, Phys. Rev. Lett. **50**, 1998 (1983).

[88] G. Binnig and H. Rohrer, Surf. Sci. **152/153**, 17 (1985).

[89] C. J. Chen, *Introduction to Scanning Tunneling Microscopy*, Oxford University Press, New York, 1993.

[90] R. Wiesendanger, *Scanning probe microscopy and spectroscopy: methods and applications*, Cambridge University Press, Cambridge, 1994.

[91] Y. Hasegawa, H. Kiyama, Q. K. Xue, and T. Sakurai, Appl. Phys. Lett. **72**, 2265 (1998).

[92] O. Flebbe, H. Eisele, T. Kalka, F. Heinrichsdorff, A. Krost, D. Bimberg, and M. Dähne-Prietsch, J. Vac. Sci. Technol. B **17**, 1639 (1999).

[93] H. Eisele, O. Flebbe, T. Kalka, and M. Dähne-Prietsch, Surf. Interface Anal. **27**, 537 (1999).

[94] B. Lita, R. S. Goldman, J. D. Phillips, and P. K. Bhattacharya, Appl. Phys. Lett. **75**, 2797 (1999).

[95] N. Liu, J. Tersoff, O. Baklenov, A. L. Holmes, Jr., and C. K. Shih, Phys. Rev. Lett. **84**, 334 (2000).

[96] P. B. Joyce, T. J. Krzyzewski, G. R. Bell, T. S. Jones, S. Malik, D. Childs, and R. Murray, Phys. Rev. B **62**, 10891 (2000).

[97] D. M. Bruls, J. W. A. M. Vugs, P. M. Koenraad, H. W. M. Salemink, J. H. Wolter, M. Hopkinson, M. S. Skolnick, F. Long, and S. P. A. Gill, Appl. Phys. Lett. **81**, 1708 (2002).

[98] J. H. Davies, D. M. Bruls, J. W. A. M. Vugs, and P. M. Koenraad, J. Appl. Phys. **91**, 4171 (2002).

[99] A. Rastelli and H. von Känel, Surf. Sci. **515**, L493 (2002).

[100] A. Lenz, R. Timm, H. Eisele, Ch. Hennig, S. K. Becker, R. L. Sellin, U. W. Pohl, D. Bimberg, and M. Dähne, Appl. Phys. Lett. **81**, 5150 (2002).

[101] F. Montalenti, P. Raiteri, D. B. Migas, H. von Känel, A. Rastelli, C. Manzano, G. Costantini, U. Denker, O. G. Schmidt, K. Kern, and L. Miglio, Phys. Rev. Lett. **93**, 216102 (2004).

[102] J. H. Davies, P. Offermans, and P. M. Koenraad, J. Appl. Phys. **98**, 053504 (2005).

[103] R. Timm, H. Eisele, A. Lenz, T.-Y. Kim, F. Streicher, K. Pötschke, U. W. Pohl, D. Bimberg, and M. Dähne, Physica E **32**, 25 (2006).

[104] A. L. Robinson, Science **229**, 1074 (1985).

[105] R. M. Feenstra, J. A. Stroscio, and A. P. Fein, Surf. Sci. **181**, 295 (1987).

[106] R. M. Feenstra, J. A. Stroscio, J. Tersoff, and A. P. Fein, Phys. Rev. Lett. **58**, 1192 (1987).

[107] R. M. Feenstra and J. A. Stroscio, J. Vac. Sci. Technol. B **5**, 923 (1987).

[108] B. Grandidier, Y. M. Niquet, B. Legrand, J. P. Nys, C. Priester, D. Stiévenard, J. M. Gérard, and V. Thierry-Mieg, Phys. Rev. Lett. **85**, 1068 (2000).

[109] T. K. Johal, R. Rinaldi, A. Passaseo, R. Cingolani, A. Vasanelli, R. Ferreira, and G. Bastard, Phys. Rev. B **66**, 075336 (2002).

[110] T. Maltezopoulos, A. Bolz, C. Meyer, C. Heyn, W. Hansen, M. Morgenstern, and R. Wiesendanger, Phys. Rev. Lett. **91**, 196804 (2003).

[111] G. D. Lian, J. Yuan, L. M. Brown, G. H. Kim, and D. A. Ritchie, Appl. Phys. Lett. **73**, 49 (1998).

[112] M. Kummer, B. Vögeli, and H. von Känel, Mat. Sci. Eng. B **69**, 247 (2000).

[113] A. Hesse, J. Stangl, V. Holý, T. Roch, G. Bauer, O. G. Schmidt, U. Denker, and B. Struth, Phys. Rev. B **66**, 085321 (2002).

[114] F. Ferdos, S. Wang, Y. Wei, A. Larsson, M. Sadeghi, and Q. Zhao, Appl. Phys. Lett. **81**, 1195 (2002).

[115] R. Songmuang, S. Kiravittaya, and O. G. Schmidt, J. Crystal Growth **249**, 416 (2003).

[116] O. Kirfel, E. Müller, D. Grützmacher, and K. Kern, Physica E **16**, 602 (2003).

[117] W. M. McGee, T. J. Krzyzewski, and T. S. Jones, J. Appl. Phys. **99**, 043505 (2006).

[118] A. Lenz, *Atomic structure of capped In(Ga)As and GaAs quantum dots for optoelectronic devices*, PhD thesis, Technische Universität Berlin, to be published.

[119] W. Wu, J. R. Tucker, G. S. Solomon, and J. S. Harris, Jr., Appl. Phys. Lett. **71**, 1083 (1997).

[120] B. Legrand, B. Grandidier, J. P. Nys, D. Stiévenard, J. M. Gérard, and V. Thierry-Mieg, Appl. Phys. Lett. **73**, 96 (1998).

[121] B. Lita, R. S. Goldman, J. D. Phillips, and P. K. Bhattacharya, Appl. Phys. Lett. **74**, 2824 (1999).

[122] H. Eisele, O. Flebbe, T. Kalka anc C. Preinesberger, F. Heinrichsdorff, A. Krost, D. Bimberg, and M. Dähne-Prietsch, Appl. Phys. Lett. **75**, 106 (1999).

[123] N. Liu, H. K. Lyeo, C. K. Shih, M. Oshima, T. Mano, and N. Koguchi, Appl. Phys. Lett. **80**, 4345 (2002).

[124] H. Eisele, *Cross-Sectional Scanning Tunneling Microscopy of InAs/GaAs Quantum Dots*, Wissenschaft und Technik Verlag, Berlin, 2002.

[125] H. Eisele, A. Lenz, Ch. Hennig, R. Timm, M. Ternes, and M. Dähne, J. Crystal Growth **248**, 322 (2003).

[126] D. M. Bruls, P. M. Koenraad, H. W. M. Salemink, J. H. Wolter, M. Hopkinson, and M. S. Skolnick, Appl. Phys. Lett. **82**, 3758 (2003).

[127] A. Lenz, H. Eisele, R. Timm, S. K. Becker, R. L. Sellin, U. W. Pohl, D. Bimberg, and M. Dähne, Appl. Phys. Lett. **85**, 3848 (2004).

[128] Q. Gong, P. Offermans, R. Nötzel, P. M. Koenraad, and J. H. Wolter, Appl. Phys. Lett. **85**, 5697 (2004).

[129] L. Ouattara, A. Mikkelsen, E. Lundgren, L. Höglund, C. Asplund, and J. Y. Andersson, J. Appl. Phys. **100**, 044320 (2006).

[130] C. Çelebi, J. M. Ulloa, P. M. Koenraad, A. Simon, A. Letoublon, and N. Bertru, Appl. Phys. Lett. **89**, 023119 (2006).

[131] A. Lenz, R. Timm, H. Eisele, L. Ivanova, D. Martin, V. Voßebürger, A. Rastelli, O. G. Schmidt, and M. Dähne, phys. stat. sol. (b) **243**, 3976 (2006).

[132] A. Lenz, H. Eisele, R. Timm, L. Ivanova, H.-Y. Liu, M. Hopkinson, U. W. Pohl, and M. Dähne, Physica E, in print.

[133] J. M. Ulloa, C. Çelebi, P. M. Koenraad, A. Simon, E. Gapihan, A. Letoublon, N. Bertru, I. Drouzas, D. J. Mowbray, M. J. Steer, and M. Hopkinson, J. Appl. Phys. **101**, 081707 (2007).

[134] M. Weimer, J. Kramar, and J. D. Baldeschwieler, Phys. Rev. B **39**, 5572 (1989).

[135] M. McEllistrem, G. Haase, D. Chen, and R. J. Hamers, Phys. Rev. Lett. **70**, 2471 (1993).

[136] R. Dombrowski, Chr. Steinebach, Chr. Wittneven, M. Morgenstern, and R. Wiesendanger, Phys. Rev. B **59**, 8043 (1999).

[137] G. J. de Raad, D. M. Bruls, P. M. Koenraad, and J. H. Wolter, Phys. Rev. B **66**, 195306 (2002).

[138] R. M. Feenstra, S. Gaan, G. Meyer, and K. H. Rieder, Phys. Rev. B **71**, 125316 (2005).

[139] Ch. Kittel, *Einführung in die Feskörperphysik*, 14th edition, Oldenbourg, München, 2005.

[140] H. Ibach and H. Lüth, *Festkörperphysik*, 6th edition, Springer, Berlin, 2002.

[141] W. Nolting, *Grundkurs theoretische Physik. Band 5/1: Quantenmechanik*, 6th edition, Springer, Berlin, 2003.

[142] M. Grundmann, J. Christen, N. N. Ledentsov, J. Böhrer, D. Bimberg, S. S. Ruvimov, P. Werner, U. Richter, U. Gösele, J. Heydenreich, V. M. Ustinov, A. Yu. Egorov, A. E. Zhukov, P. S. Kop'ev, and Zh. I. Alferov, Phys. Rev. Lett. **74**, 4043 (1995).

[143] A. Zrenner, J. Chem. Phys. **112**, 7790 (2000).

[144] A. P. Alivisatos, Science **271**, 933 (1996).

[145] T. J. Bukowski and J. H. Simmons, Crit. Rev. Solid State **27**, 119 (2002).

[146] M. Scheffler and R. Zimmermann, editors, *23rd International Conference on the Physics of Semiconductors*, volume 2, World Scientific, Singapore, 1996.

[147] P. Kratzer, C. G. Morgan, and M. Scheffler, Phys. Rev. B **59**, 15246 (1999).

[148] U. W. Pohl, private communication.

[149] Zh. I. Alferov, Sov. Phys. Semicond. **1**, 358 (1967).

[150] Zh. I. Alferov, Yu. V. Zhilyaev, and Yu. V. Shmartsev, Sov. Phys. Semicond. **5**, 174 (1971).

[151] L. L. Chang, L. Esaki, W. E. Howard, R. Ludeke, and G. Schul, J. Vac. Sci. Technol. **10**, 655 (1973).

[152] Zh. I. Alferov, Sov. Phys. Semicond. **11**, 1216 (1977).

[153] M. Yano, Y. Suzuki, T. Ishii, Y. Matsushima, and M. Kimata, Jpn. J. Appl. Phys. **17**, 2091 (1978).

[154] H. Kroemer, Jpn. J. Appl. Phys. **20** Suppl. 20-1, 9 (1981).

[155] M. J. Kelly, *Low-dimensional semiconductors: materials, physics, technology, devices*, Oxford University Press, Oxford, 1995.

[156] R. Steffen, Th. Koch, J. Oshinowo, F. Faller, and A. Forchel, Appl. Phys. Lett. **68**, 223 (1996).

[157] V. A. Shchukin and D. Bimberg, Rev. Mod. Phys. **71**, 1125 (1999).

[158] S. Watanabe, E. Pelucchi, B. Dwir, M. H. Baier, K. Leifer, and E. Kapon, Appl. Phys. Lett. **84**, 2907 (2004).

[159] D. Chithrani, R. L. Williams, J. Lefebvre, P. J. Poole, and G. C. Aers, Appl. Phys. Lett. **84**, 978 (2004).

[160] J. Bauer, D. Schuh, E. Uccelli, R. Schulz, A. Kress, F. Hofbauer, J. J. Finley, and G. Abstreiter, Appl. Phys. Lett. **85**, 4750 (2004).

[161] F. C. Frank and J. H. van der Merwe, P. R. Soc. A **198**, 205 (1949).

[162] M. Volmer and A. Weber, Zeitschrift für physikalische Chemie **119**, 227 (1926).

[163] I. N. Stranski and L. Krastanow, SB Wiener Akademie der Wissenschaften, Klasse IIb **146**, 797 (1938).

[164] O. Madelung, *Semiconductors – Basic Data*, 2nd edition, Springer, Berlin, 1996.

[165] A. G. Cullis, D. J. Norris, M. A. Migliorato, and M. Hopkinson, Appl. Surf. Sci. **244**, 65 (2005).

[166] F. Patella, F. Arciprete, M. Fanfoni, A. Balzarotti, and E. Placidi, Appl. Phys. Lett. **88**, 161903 (2006).

[167] J. Oshinowo, M. Nishioka, S. Ishida, and Y. Arakawa, Appl. Phys. Lett. **65**, 1421 (1994).

[168] F. Heinrichsdorff, A. Krost, M. Grundmann, D. Bimberg, F. Bertram, J. Christen, A. Kosogov, and P. Werner, J. Crystal Growth **170**, 568 (1997).

[169] H. Y. Liu, C. M. Tey, I. R. Sellers, T. J. Badcock, D. J. Mowbray, M. S. Skolnick, R. Beanland, M. Hopkinson, and A. G. Cullis, J. Appl. Phys. **98**, 083516 (2005).

[170] N. N. Ledentsov, *Growth Processes and Surface Phase Equilibria in Molecular Beam Epitaxy*, Springer, Berlin, 1999.

[171] M. A. Herman and H. Sitter, *Molecular beam epitaxy: fundamentals and current status*, 2nd edition, Springer, Berlin, 1996.

[172] M. Henzler and W. Göpel, *Oberflächenphysik des Festkörpers*, 2nd edition, Teubner, Stuttgart, 1994.

[173] L. Däweritz and R. Hey, Surf. Sci. **236**, 15 (1990).

[174] J. E. Northrup and S. Froyen, Phys. Rev. Lett. **71**, 2276 (1993).

[175] S.-H. Lee, W. Moritz, and M. Scheffler, Phys. Rev. Lett. **85**, 3890 (2000).

[176] J. M. Márquez Bertoni, *Struktur von GaAs-Oberflächen und ihre Bedeutung für InAs-Quantenpunkte*, PhD thesis, Technische Universität Berlin, 2000.

[177] Ch. Giesen, A. Szymakowski, S. Rushworth, M. Heuken, and K. Heime, J. Crystal Growth **221**, 450 (2000).

[178] P. Kratzer, E. Penev, and M. Scheffler, Appl. Phys. A **75**, 79 (2002).

[179] E. Penev, S. Stojković, P. Kratzer, and M. Scheffler, Phys. Rev. B **69**, 115335 (2004).

[180] R. Nötzel, J. Temmyo, H. Kamada, T. Furuta, and T. Tamamura, Appl. Phys. Lett. **65**, 457 (1994).

[181] T. Chung, G. Walter, and N. Holonyak, Jr., J. Appl. Phys. **97**, 053510 (2005).

[182] L. Müller-Kirsch, *Metallorganische Gasphasenepitaxie und Charakterisierung von antimonhaltigen Quantenpunkten*, Wissenschaft und Technik, Berlin, 2002.

[183] I. Kaiander, *MOCVD growth of InGaAs/GaAs QDs for long wavelength lasers and VCSELs*, PhD thesis, Technische Universität Berlin, 2006.

[184] G. B. Stringfellow, J. Crystal Growth **128**, 503 (1993).

[185] R. M. Graham, A. C. Jones, N. J. Mason, S. Rushworth, A. Salesse, T.-Y. Seong, G. Booker, L. Smith, and P. J. Walker, Semicond. Sci. Technol. **8**, 1797 (1993).

[186] R. M. Graham, A. C. Jones, N. J. Mason, S. Rushworth, L. Smith, and P. J. Walker, J. Crystal Growth **145**, 363 (1994).

[187] R. Beccard, G. Lengeling, D. Schmitz, Y. Gigase, and H. Jürgensen, J. Crystal Growth **170**, 97 (1997).

[188] C. A. Wang, S. Salim, K. F. Jensen, and A. C. Jones, J. Crystal Growth **170**, 55 (1997).

[189] T. Yang, J. Tatebayashi, S. Tsukamoto, M. Nishioka, and Y. Arakawa, Appl. Phys. Lett. **84**, 2817 (2004).

[190] T.-P. Hsieh, P.-C. Chiu, J.-I. Chyi, N.-T. Yeh, W.-J. Ho, W.-H. Chang, and T.-M. Hsu, Appl. Phys. Lett. **87**, 151903 (2005).

[191] G. Saint-Girons, I. Sagnes, and G. Patriarche, Phys. Rev. B **73**, 045308 (2006).

[192] K. Pötschke, *Antimon-basierte Quantenpunkte*, Diploma thesis, Technische Universität Berlin, 2003.

[193] R. Heitz, F. Guffarth, K. Pötschke, A. Schliwa, D. Bimberg, N. D. Zakharov, and P. Werner, Phys. Rev. B **71**, 045325 (2005).

[194] D. Bimberg, editor, *Growth-related Structures of Semiconductor Nanostructures*, Springer, Berlin, to be published.

[195] I. Kegel, T. H. Metzger, A. Lorke, J. Peisl, J. Stangl, G. Bauer, J. M. García, and P. M. Petroff, Phys. Rev. Lett. **85**, 1694 (2000).

[196] I. Kegel, T. H. Metzger, A. Lorke, J. Peisl, J. Stangl, G. Bauer, K. Nordlund, W. V. Schoenfeld, and P. M. Petroff, Phys. Rev. B **63**, 035318 (2001).

[197] Y. Temko, T. Suzuki, and K. Jacobi, Appl. Phys. Lett. **82**, 2142 (2003).

[198] G. Costantini, C. Manzano, R. Songmuang, O. G. Schmidt, and K. Kern, Appl. Phys. Lett. **82**, 3194 (2003).

[199] N. Saucedo-Zeni, A. Yu. Gorbatchev, and V. H. Méndez-García, J. Vac. Sci. Technol. B **22**, 1503 (2004).

[200] S. O. Cho, Zh. M. Wang, and G. J. Salamo, Appl. Phys. Lett. **86**, 113106 (2005).

[201] G. Biasiol, S. Heun, G. B. Golinelli, A. Locatelli, T. O. Mentes, F. Z. Guo, C. Hofer, C. Teichert, and L. Sorba, Appl. Phys. Lett. **87**, 223106 (2005).

[202] J. M. García, G. Medeiros-Ribeiro, K. Schmidt, T. Ngo, J. L. Feng, A. Lorke, J. Kotthaus, and P. M. Petroff, Appl. Phys. Lett. **71**, 2014 (1997).

[203] B. J. Riel, K. Hinzer, S. Moisa, J. Fraser, P. Finnie, P. Piercy, S. Fafard, and Z. R. Wasilewski, J. Crystal Growth **236**, 145 (2002).

[204] M. C. Xu, Y. Temko, T. Suzuki, and K. Jacobi, Phys. Rev. B **71**, 075314 (2005).

[205] Y. Temko, T. Suzuki, M. C. Xu, K. Pötschke, D. Bimberg, and K. Jacobi, Phys. Rev. B **71**, 045336 (2005).

[206] A. Rastelli and H. von Känel, Surf. Sci. **532**, 769 (2003).

[207] Y. Temko, private communication.

[208] G. Costantini, A. Rastelli, C. Manzano, P. Acosta-Diez, G. Katsaros, R. Songmuang, O. G. Schmidt, H. von Känel, and K. Kern, J. Crystal Growth **278**, 38 (2005).

[209] I. Daruka, J. Tersoff, and A.-L. Barabási, Phys. Rev. Lett. **82**, 2753 (1999).

[210] T. Hammerschmidt, *Growth Simulations of InAs/GaAs Quantum-Dots*, PhD thesis, Technische Universität Berlin, 2006
`http://opus.kobv.de/tuberlin/volltexte/2006/1358/`.

[211] O. Stier, *Electronic and Optical Properties of Quantum Dots and Wires*, Wissenschaft und Technik, Berlin, 2001.

[212] R. Santoprete, B. Koiller, R. B. Capaz, P. Kratzer, Q. K. K. Liu, and M. Scheffler, Phys. Rev. B **68**, 235311 (2003).

[213] S. Lee, O. L. Lazarenkova, P. von Allmen, F. Oyafuso, and G. Klimeck, Phys. Rev. B **70**, 125307 (2004).

[214] S. Tomić, P. Howe, N. M. Harrison, and T. S. Jones, J. Appl. Phys. **99**, 093522 (2006).

[215] N. Moll, M. Scheffler, and E. Pehlke, Phys. Rev. B **58**, 4566 (1998).

[216] A. Lemaître, G. Patriarche, and F. Glas, Appl. Phys. Lett. **85**, 3717 (2004).

[217] P. Offermans, P. M. Koenraad, R. Nötzel, J. H. Wolter, and K. Pierz, Appl. Phys. Lett. **87**, 111903 (2005).

[218] P. D. Quinn, N. R. Wilson, S. A. Hatfield, C. F. McConville, G. R. Bell, T. C. Q. Noakes, P. Bailey, S. Al-Harthi, and F. Gard, Appl. Phys. Lett. **87**, 153110 (2005).

[219] M. A. Migliorato, A. G. Cullis, M. Fearn, and J. H. Jefferson, Phys. Rev. B **65**, 115316 (2002).

[220] E. Steimetz, T. Wehnert, K. Haberland, J.-T. Zettler, and W. Richter, J. Crystal Growth **195**, 530 (1998).

[221] H. Eisele, R. Timm, A. Lenz, Ch. Hennig, M. Ternes, S. K. Becker, and M. Dähne, phys. stat. sol. (c) **0**, 1129 (2003).

[222] L. G. Wang, P. Kratzer, M. Scheffler, and Q. K. K. Liu, Appl. Phys. A **73**, 161 (2001).

[223] R. J. Warburton, C. Schäflein, D. Haft, F. Bickel, A. Lorke, K. Karrai, J. M. García, W. Schoenfeld, and P. M. Petroff, Nature **405**, 926 (2000).

[224] A. Lorke, R. J. Luyken, A. O. Govorov, J. P. Kotthaus, J. M. Garcia, and P. M. Petroff, Phys. Rev. Lett. **84**, 2223 (2000).

[225] A. Lorke, R. Blossey, J. M. Garcia, M. Bichler, and G. Abstreiter, Mat. Sci. Eng. B **88**, 225 (2002).

[226] D. Granados and J. M. García, Appl. Phys. Lett. **82**, 2401 (2003).

[227] P. Offermans, P. M. Koenraad, J. H. Wolter, D. Granados, J. M. García, V. M. Fomin, V. N. Gladilin, and J. T. Devreese, Appl. Phys. Lett. **87**, 131902 (2005).

[228] J.-S. Lee, H.-W. Ren, S. Sugou, and Y. Masumoto, J. Appl. Phys. **84**, 6686 (1998).

[229] B. C. Lee, O. Voskoboynikov, and C. P. Lee, Physica E **24**, 87 (2004).

[230] M. Sztucki, T. H. Metzger, V. Chamard, A. Hesse, and V. Holý, J. Appl. Phys. **99**, 033519 (2006).

[231] H.-S. Ling and C.-P. Lee, J. Appl. Phys. **102**, 024314 (2007).

[232] T. Raz, D. Ritter, and G. Bahir, Appl. Phys. Lett. **82**, 1706 (2003).

[233] J. Sormunen, J. Riikonen, M. Mattila, J. Tiilikainen, M. Sopanen, and H. Lipsanen, Nano Lett. **5**, 1541 (2005).

[234] T. W. Kim, E. H. Lee, K. H. Lee, J. S. Kim, and H. L. Park, Appl. Phys. Lett. **84**, 595 (2004).

[235] J. Cui, Q. He, X. M. Jiang, Y. L. Fan, X. J. Yang, F. Xue, and Z. M. Jiang, Appl. Phys. Lett. **83**, 2907 (2003).

[236] S. W. Lee, L. J. Chen, P. S. Chen, M.-J. Tsai, C. W. Liu, T. Y. Chien, and C. T. Chia, Appl. Phys. Lett. **83**, 5283 (2003).

[237] V. I. Mashanov, H.-H. Cheng, C.-T. Chia, and Y.-H. Chang, Physica E **28**, 531 (2005).

[238] A. O. Govorov, S. E. Ulloa, K. Karrai, and R. J. Warburton, Phys. Rev. B **66**, 081309 (2002).

[239] E. Ribeiro, A. O. Govorov, W. Carvalho, Jr., and G. Medeiros-Ribeiro, Phys. Rev. Lett. **92**, 126402 (2004).

[240] J. A. Barker, R. J. Warburton, and E. P. O'Reilly, Phys. Rev. B **69**, 035327 (2004).

[241] I. Filikhin, V. M. Suslov, and B. Vlahovic, Phys. Rev. B **73**, 205332 (2006).

[242] Y. M. Liu, C. G. Bao, and T. Y. Shi, Phys. Rev. B **73**, 113313 (2006).

[243] A. Schliwa, M. Winkelnkemper, and D. Bimberg, PRB **76**, 205324 (2007).

[244] M. Bayer, A. Kuther, A. Forchel, A. Gorbunov, V. B. Timofeev, F. Schäfer, J. P. Reithmaier, T. L. Reinecke, and S. N. Walck, Phys. Rev. Lett. **82**, 1748 (1999).

[245] U. W. Pohl, K. Pötschke, A. Schliwa, F. Guffarth, D. Bimberg, N. D. Zakharov, P. Werner, M. B. Lifshits, V. A. Shchukin, and D. E. Jesson, Phys. Rev. B **72**, 245332 (2005).

[246] S. Rodt, A. Schliwa, K. Pötschke, F. Guffarth, and D. Bimberg, Phys. Rev. B **71**, 155325 (2005).

[247] G. Bester and A. Zunger, Phys. Rev. B **68**, 073309 (2003).

[248] M. A. Migliorato, D. Powell, S. L. Liew, A. G. Cullis, P. Navaretti, M. J. Steer, M. Hopkinson, M. Fearn, and J. H. Jefferson, J. Appl. Phys. **96**, 5169 (2004).

[249] J.-Y. Marzin, J.-M. Gérard, A. Izraël, D. Barrier, and G. Bastard, Phys. Rev. Lett. **73**, 716 (1994).

[250] M. Grundmann and D. Bimberg, Jpn. J. Appl. Phys. **36**, 4181 (1997).

[251] D. Bimberg, M. Grundmann, N. N. Ledentsov, M. H. Mao, Ch. Ribbat, R. Sellin, V. M. Ustinov, A. E. Zhukov, Zh. I. Alferov, and J. A. Lott, phys. stat. sol. (b) **224**, 787 (2001).

[252] Y. Arakawa, Proc. SPIE **4580**, 179 (2001).

[253] `http://www.ee.ucla.edu/~wu/ee174/images/Bandgap-vs-Lattice%20Constant.jpg`.

[254] U. E. H. Laheld, F. B. Pedersen, and P. C. Hemmer, Phys. Rev. B **52**, 2697 (1995).

[255] R. A. Hogg, K. Suzuki, K. Tachibana, L. Finger, K. Hirakawa, and Y. Arakawa, Appl. Phys. Lett. **72**, 2856 (1998).

[256] B. R. Bennett, R. Magno, and B. V. Shanabrook, Appl. Phys. Lett. **68**, 505 (1996).

[257] B. R. Bennett, B. V. Shanabrook, P. M. Thibado, L. J. Whitman, and R. Magno, J. Crystal Growth **175/176**, 888 (1997).

[258] L. J. Whitman, P. M. Thibado, S. C. Erwin, B. R. Bennett, and B. V. Shanabrook, Phys. Rev. Lett. **79**, 693 (1997).

[259] R. Bożek, A. Babiński, J. M. Baranowski, R. Stępniewski, Z. Klusek, W. Olejniczak, K. Starowieyski, and J. Wróbel, Acta Phys. Pol. A **88**, 974 (1995).

[260] B. M. Kinder and E. M. Goldys, Appl. Phys. Lett. **73**, 1233 (1998).

[261] A. Subekti, M. J. Paterson, E. M. Goldys, and T. L. Tansley, Appl. Surf. Sci. **140**, 190 (1999).

[262] Motlan, K. S. A. Butcher, E. M. Goldys, and T. L. Tansley, Mater. Chem. Phys. **81**, 8 (2003).

[263] Motlan, E. M. Goldys, and L. V. Dao, J. Vac. Sci. Technol. B **20**, 291 (2002).

[264] L. Müller-Kirsch, R. Heitz, U. W. Pohl, D. Bimberg, I. Häusler, H. Kirmse, and W. Neumann, Physica E **13**, 1181 (2002).

[265] L. Müller-Kirsch, U. W. Pohl, R. Heitz, H. Kirmse, W. Neumann, and D. Bimberg, J. Crystal Growth **221**, 611 (2000).

[266] J. Tatebayashi, A. Khoshakhlagh, S. H. Huang, L. R. Dawson, G. Balakrishnan, and D. L. Huffaker, Appl. Phys. Lett. **89**, 203116 (2006).

[267] T. Wang and A. Forchel, J. Appl. Phys. **85**, 2591 (1999).

[268] `http://www.wikipedia.org`.

[269] M. Geller and A. Marent, private communication.

[270] M. Geller, E. Stock, C. Kapteyn, R. L. Sellin, and D. Bimberg, Phys. Rev. B **73**, 205331 (2006).

[271] C. M. A. Kapteyn, M. Lion, R. Heitz, D. Bimberg, C. Miesner, T. Asperger, K. Brunner, and G. Abstreiter, Appl. Phys. Lett. **77**, 4169 (2000).

[272] N. Nuntawong, S. Birudavolu, C. P. Hains, S. Huang, H. Xu, and D. L. Huffaker, Appl. Phys. Lett. **85**, 3050 (2004).

[273] K. Akahane, N. Yamamoto, and N. Ohtani, Physica E **21**, 295 (2004).

[274] H. Y. Liu, M. J. Steer, T. J. Badcock, D. J. Mowbray, M. S. Skolnick, P. Navaretti, K. M. Groom, M. Hopkinson, and R. A. Hogg, Appl. Phys. Lett. **86**, 143108 (2005).

[275] J. M. Ripalda, D. Granados, Y. González, A. M. Sánchez, S. I. Molina, and J. M. García, Appl. Phys. Lett. **87**, 202108 (2005).

[276] C. Y. Jin, H. Y. Liu, S. Y. Zhang, Q. Jiang, S. L. Liew, M. Hopkinson, T. J. Badcock, and E. Nabavi D. J. Mowbray, Appl. Phys. Lett. **91**, 021102 (2007).

[277] J. M. Ulloa, I. W. D. Drouzas, P. M. Koenraad, D. J. Mowbray, M. J. Steer, H. Y. Liu, and M. Hopkinson, Appl. Phys. Lett. **90**, 213105 (2007).

[278] J. A. Stroscio and W. J. Kaiser, editors, *Scanning tunneling microscopy*, Academic Press, San Diego, 1993.

[279] J. A. Kubby and J. J. Boland, Surf. Sci. Rep. **26**, 61 (1996).

[280] R. Young, J. Ward, and F. Scire, Phys. Rev. Lett. **27**, 922 (1971).

[281] G. Binnig, H. Rohrer, Ch. Gerber, and E. Weibel, Appl. Phys. Lett. **40**, 178 (1982).

[282] R. S. Becker, J. A. Golovchenko, D. R. Hamann, and B. S. Swartzentruber, Phys. Rev. Lett. **55**, 2032 (1985).

[283] R. M. Feenstra, W. A. Thompson, and A. P. Fein, Phys. Rev. Lett. **56**, 608 (1986).

[284] R. M. Feenstra and J. A. Stroscio, Phys. Scripta **T19**, 55 (1987).

[285] R. J. Hamers, R. M. Tromp, and J. E. Demuth, Phys. Rev. Lett. **56**, 1972 (1986).

[286] J. E. Demuth, R. J. Hamers, and R. M. Tromp, J. Vac. Sci. Technol. B **5**, 1528 (1987).

[287] D. A. Bonnell, editor, *Scanning tunneling microscopy and spectroscopy: theory, techniques, and applications*, VCH, New York, 1993.

[288] S. Blügel, *Theorie der Rastertunnelmikroskopie, in: Physik der Nanostrukturen, Vorlesungsmanuskripte des 29. IFF–Ferienkurses*, Schriften des Forschungszentrums Jülich, Jülich, 1998
`http://www.fz-juelich.de/iff/staff/Bluegel_S/Lectures/S_Bluegel_lec.html`.

[289] J. Bardeen, Phys. Rev. Lett. **6**, 57 (1961).

[290] J. Tersoff and D. R. Hamann, Phys. Rev. B **31**, 805 (1985).

[291] C. J. Chen, J. Vac. Sci. Technol. A **9**, 44 (1991).

[292] A. J. Heinrich, M. Wenderoth, M. A. Rosentreter, M. A. Schneider, and R. G. Ulbrich, Appl. Phys. Lett. **70**, 449 (1997).

[293] N. D. Jäger, M. Marso, M. Salmeron, E. R. Weber, K. Urban, and Ph. Ebert, Phys. Rev. B **67**, 165307 (2003).

[294] W. Mönch, *Semiconductor Surfaces and Interfaces*, 2nd edition, Springer, Heidelberg, 1995.

[295] H. Lüth, *Surfaces and Interfaces of Solid Materials*, 3rd edition, Springer, Berlin, 1997.

[296] W. J. Kaiser, L. D. Bell, M. H. Hecht, and F. J. Grunthaner, J. Vac. Sci. Technol. A **6**, 519 (1988).

[297] R. M. Feenstra, G. Meyer, F. Moresco, and K. H. Rieder, Phys. Rev. B **66**, 165204 (2002).

[298] V. Voßebürger, *Charakterisierung einzelner Stickstoffatome in der GaAs(110)-Oberfläche*, Diploma thesis, Technische Universität Berlin, 2006.

[299] O. Flebbe, H. Eisele, R. Timm, and M. Dähne, American Institute of Physics Conference Proceedings **696**, 699 (2003).

[300] J. A. Stroscio, R. M. Feenstra, D. M. Newns, and A. P. Fein, J. Vac. Sci. Technol. A **6**, 499 (1988).

[301] R. M. Feenstra, E. T. Yu, J. M. Woodall, P. D. Kirchner, C. L. Lin, and G. D. Pettit, Appl. Phys. Lett. **61**, 795 (1992).

[302] R. M. Feenstra, Phys. Rev. B **50**, 4561 (1994).

[303] P. Mårtensson and R. M. Feenstra, Phys. Rev. B **39**, 7744 (1989).

[304] C. K. Shih, R. M. Feenstra, and P. Mårtensson, J. Vac. Sci. Technol. A **8**, 3379 (1990).

[305] N. D. Lang, Phys. Rev. B **34**, 5947 (1986).

[306] J. A. Stroscio, R. M. Feenstra, and A. P. Fein, Phys. Rev. Lett. **57**, 2579 (1986).

[307] M. Prietsch, A. Samsavar, and R. Ludeke, Phys. Rev. B **43**, 11850 (1991).

[308] R. M. Feenstra, D. A. Collins, D. Z.-Y. Ting, M. W. Wang, and T. C. McGill, Phys. Rev. Lett. **72**, 2749 (1994).

[309] T. J. Krzyzewski, P. B. Joyce, G. R. Bell, and T. S. Jones, Surf. Sci. **517**, 8 (2002).

[310] Y. Sun, S. F. Cheng, G. Chen, R. F. Hicks, J. G. Cederberg, and R. M. Biefeld, J. Appl. Phys. **97**, 053503 (2005).

[311] B. Legrand, J. P. Nys, B. Grandidier, D. Stiévenard, A. Lemaître, J. M. Gérard, and V. Thierry-Mieg, Appl. Phys. Lett. **74**, 2608 (1999).

[312] W. Chen, B. Shin, R. S. Goldman, A. Stiff, and P. K. Bhattacharya, J. Vac. Sci. Technol. B **21**, 1920 (2003).

[313] J.-Q. Lu, H. T. Johnson, V. D. Dasika, and R. S. Goldman, Appl. Phys. Lett. **88**, 053109 (2006).

[314] X.-D. Wang, N. Liu, C. K. Shih, S. Govindaraju, and A. L. Holmes, Jr., Appl. Phys. Lett. **85**, 1356 (2004).

[315] D. M. Bruls, P. M. Koenraad, M. Hopkinson, J. H. Wolter, and H. W. M. Salemink, Appl. Surf. Sci. **190**, 258 (2002).

[316] J. He, R. Nötzel, P. Offermans, P. M. Koenraad, Q. Gong, G. J. Hamhuis, T. J. Eijkemans, and J. H. Wolter, Appl. Phys. Lett. **85**, 2771 (2004).

[317] P. Offermans, P. M. Koenraad, J. H. Wolter, K. Pierz, M. Roy, and P. A. Maksym, Phys. Rev. B **72**, 165332 (2005).

[318] J. M. Ulloa, P. M. Koenraad, E. Gapihan, A. Létoublon, and N. Bertru, Appl. Phys. Lett. **91**, 073106 (2007).

[319] Y. Akanuma, I. Yamakawa, Y. Sakuma, T. Usuki, and A. Nakamura, American Institute of Physics Conference Proceedings **893**, 107 (2007).

[320] C. H. Lin, W. W. Pai, F. Y. Chang, and H. H. Lin, Appl. Phys. Lett. **90**, 063102 (2007).

[321] A. R. Lubinsky, C. B. Duke, B. W. Lee, and P. Mark, Phys. Rev. Lett. **36**, 1058 (1976).

[322] S. Y. Tong, A. R. Lubinsky, B. J. Mrstik, and M. A. Van Hove, Phys. Rev. B **17**, 3303 (1978).

[323] S. Y. Tong, W. N. Mei, and G. Xu, J. Vac. Sci. Technol. B **2**, 393 (1984).

[324] Landolt-Börnstein, Physics of Solid Surfaces, in *Numerical Data and Functional Relationships in Science and Technology,* edited by G. Chiarotti, volume III/24a in *new series*, Springer, Berlin, 1993.

[325] Ph. Ebert, B. Engels, P. Richard, K. Schroeder, S. Blügel, C. Domke, M. Heinrich, and K. Urban, Phys. Rev. Lett. **77**, 2997 (1996).

[326] B. Engels, P. Richard, K. Schroeder, S. Blügel, Ph. Ebert, and K. Urban, Phys. Rev. B **58**, 7799 (1998).

[327] G. J. de Raad, D. M. Bruls, P. M. Koenraad, and J. H. Wolter, Phys. Rev. B **64**, 075314 (2001).

[328] M. A. Rosentreter, M. Wenderoth, N. H. Theuerkrauf, A. J. Heinrich, M. A. Schneider, and R. G. Ulbrich, Phys. Rev. B **56**, 10538 (1997).

[329] N. D. Jäger, Ph. Ebert, K. Urban, R. Krause-Rehberg, and E. R. Weber, Phys. Rev. B **65**, 195318 (2002).

[330] N. D. Jäger, E. R. Weber, K. Urban, and Ph. Ebert, Phys. Rev. B **67**, 165327 (2003).

[331] J. F. Zheng, X. Liu, N. Newman, E. R. Weber, D. F. Ogletree, and M. Salmeron, Phys. Rev. Lett. **72**, 1490 (1994).

[332] M. C. M. M. van der Wielen, A. J. A. van Roij, and H. van Kempen, Phys. Rev. Lett. **76**, 1075 (1996).

[333] C. Domke, M. Heinrich, Ph. Ebert, and K. Urban, J. Vac. Sci. Technol. B **16**, 2825 (1998).

[334] G. Mahieu, B. Grandidier, D. Deresmes, J. P. Nys, D. Stiévenard, and Ph. Ebert, Phys. Rev. Lett. **94**, 026407 (2005).

[335] S. Loth, M. Wenderoth, L. Winking, R. G. Ulbrich, S. Malzer, and G. H. Döhler, Phys. Rev. Lett. **96**, 066403 (2006).

[336] C. Preinesberger, *Rastertunnelmikroskopie an Lanthanidsiliziden auf Si(001)*, Diploma thesis, Technische Universität Berlin, 1998.

[337] T. Kalka, *Aufbau eines Tieftemperatur-UHV-Rastertunnelmikroskops für Ballistische-Elektronen-Emissions-Mikroskopie*, Diploma thesis, Freie Universität Berlin, 1995.

[338] M. Ternes, *Aufbau eines Rastertunnelmikroskops und Untersuchungen an Querschnittsflächen von Halbleiterstrukturen*, Diploma thesis, Technische Universität Berlin, 2001.

[339] R. Timm, *Rastertunnelmikroskopie an Querschnittsflächen von Typ-II Quantentöpfen*, Diploma thesis, Technische Universität Berlin, 2002.

[340] M. Dähne, S. Vandré, C. Preinesberger, S. K. Becker, W. Busse, and T. Kalka, Adv. in Solid State Phys. **41**, 227 (2001).

[341] C. Preinesberger, S. K. Becker, S. Vandré, T. Kalka, and M. Dähne, J. Appl. Phys. **91**, 1695 (2002).

[342] O. Schumann, S. Birner, M. Baudach, L. Geelhaar, H. Eisele, L. Ivanova, R. Timm, A. Lenz, S. K. Becker, M. Povolotskyi, M. Dähne, G. Abstreiter, and H. Riechert, Phys. Rev. B **71**, 245316 (2005).

[343] S. K. Becker, *Selbstorganisierte Lanthanidsilizid-Drähte auf Si(001)*, Diploma thesis, Technische Universität Berlin, 2001.

[344] M. Dähne and T. Kalka, *cm* and *cm32*, IBM Yorktown Heights / Technische Universität Berlin.

[345] S. K. Becker, *CM Utility*^{2}, Version 1.1, © Technische Universität Berlin, AG Dähne, 2001.

[346] Ch. Hennig, *Rastertunnelmikroskopie an Querschnittsflächen von Quantenpunkten auf Vizinalflächen*, Diploma thesis, Technische Universität Berlin, 2002.

[347] A. Lenz, *Rastertunnelmikroskopie an Querschnittsflächen von III-V-Quantenpunkten bei speziellen Wachstumsbedingungen*, Diploma thesis, Technische Universität Berlin, 2002.

[348] L. Ivanova, *Rastertunnelspektroskopie an Halbleiter-Nanostrukturen*, Diploma thesis, Technische Universität Berlin, 2005.

[349] J. Grabowski, *Querschnittsrastertunnelmikroskopische Untersuchung von antimonhaltigen GaAs-Halbleiternanostrukturen*, Diploma thesis, Technische Universität Berlin, 2004.

[350] F. Streicher, *Rastertunnelmikroskopie an Querschnittsflächen von InAs-GaAs-Halbleiterstrukturen*, Diploma thesis, Technische Universität Berlin, 2004.

[351] I. Horcas, R. Fernández, J. M. Gómez-Rodríguez, J. Colchero, J. Gómez-Herrero, and A. M. Baro, Rev. Sci. Instrum. **78**, 013705 (2007).

[352] J. P. Ibe, P. P. Bey, Jr., S. L. Brandow, R. A. Brizzolara, N. A. Burnham, D. P. DiLella, K. P. Lee, C. R. K. Marrian, and R. J. Colton, J. Vac. Sci. Technol. A **8**, 3570 (1990).

[353] A. J. Melmed, J. Vac. Sci. Technol. B **9**, 601 (1991).

[354] A. J. Nam, A. Teren, T. A. Lusby, and A. J. Melmed, J. Vac. Sci. Technol. B **13**, 1556 (1995).

[355] G. S. Kelsey, J. Electrochem. Soc. **124**, 814 (1977).

[356] Y. Nakamura, Y. Mera, and K. Maeda, Rev. Sci. Instrum. **70**, 3373 (1999).

[357] I. Ekvall, E. Wahlström, D. Claesson, H. Olin, and E. Olsson, Meas. Sci. Technol. **10**, 11 (1999).

[358] J. E. Demuth, U. Koehler, and R. J. Hamers, J. Microsc. **152**, 299 (1988).

[359] A.-S. Lucier, H. Mortensen, Y. Sun, and P. Grütter, Phys. Rev. B **72**, 235420 (2005).

[360] E. T. Yu, M. B. Johnson, and J.-M. Halbout, Appl. Phys. Lett. **61**, 201 (1992).

[361] A. R. Smith, S. Gwo, and C. K. Shih, Rev. Sci. Instrum. **65**, 3216 (1994).

[362] `http://sol.physik.tu-berlin.de`.

[363] H. W. M. Salemink and O. Albrektsen, Phys. Rev. B **47**, 16044 (1993).

[364] M. B. Johnson, U. Maier, H.-P. Meier, and H. W. M. Salemink, Appl. Phys. Lett. **63**, 1273 (1993).

[365] H. Kirmse, *Transmissionselektronenmikroskopische Untersuchungen von II-VI-Verbindungshalbleitern unterschiedlicher Dimensionierung*, PhD thesis, Humbold-Universität zu Berlin, 2000.

[366] R. Schneider, H. Kirmse, W. Neumann, F. Heinrichsdorff, A. Krost, and D. Bimberg, Inst. Phys. Conf. Ser. **164**, 31 (1999).

[367] E. Lenz, *In_Berechnung*, Version 1.41, Technische Universität Berlin, AG Dähne, 2004.

[368] Landolt-Börnstein, Semiconductors, in *Numerical Data and Functional Relationships in Science and Technology,* edited by O. Madelung, M. Schulz, and H. Weiss, volume III/17a in *new series*, Springer, Berlin, 1982.

[369] C. Pryor, J. Kim, L. W. Wang, A. J. Williamson, and A. Zunger, J. Appl. Phys. **83**, 2548 (1998).

[370] Ph. Ebert, Surf. Sci. Rep. **33**, 121 (1999).

[371] MaTeck, *Periodic Table of the Elements*, MaTeck GmbH, Juelich, 2004.

[372] M. Pfister, M. B. Johnson, S. F. Alvarado, H. W. M. Salemink, U. Marti, D. Martin, F. Morier-Genoud, and F. K. Reinhart, Appl. Phys. Lett. **67**, 1459 (1995).

[373] K.-J. Chao, C.-K. Shih, D. W. Gotthold, and B. G. Streetman, Phys. Rev. Lett. **79**, 4822 (1997).

[374] S. H. Huang, G. Balakrishnan, A. Khohakhlagh, A. Jallipalli, L. R. Dawson, and D. L. Huffaker, Appl. Phys. Lett. **88**, 131911 (2006).

[375] T. R. Ramachandran, R. Heitz, P. Chen, and A. Madhukar, Appl. Phys. Lett. **70**, 640 (1997).

[376] `http://www.chtm.unm.edu`.

[377] `http://www.sp.phy.cam.ac.uk`.

[378] T. Warming, private communication.

[379] N. W. Ashcroft and N. D. Mermin, *Solid State Physics*, Saunders College, Philadelphia, 1976.

[380] S. G. Kim, S. C. Erwin, B. Z. Nosho, and L. J. Whitman, Phys. Rev. B **67**, 121306 (2003).

[381] J. Steinshnider, M. Weimer, R. Kaspi, and G. W. Turner, Phys. Rev. Lett. **85**, 2953 (2000).

[382] H. A. McKay, R. M. Feenstra, T. Schmidtling, U. W. Pohl, and J. F. Geisz, J. Vac. Sci. Technol. B **19**, 1644 (2001).

[383] R. M. Feenstra, D. A. Collins, and T. C. McGill, Superlattice Microst. **15**, 215 (1994).

[384] J. Harper, M. Weimer, D. Zhang, C.-H. Lin, and S. S. Pei, Appl. Phys. Lett. **73**, 2805 (1998).

[385] J. Steinshnider, J. Harper, M. Weimer, C.-H. Lin, S. S. Pei, and D. H. Chow, Phys. Rev. Lett. **85**, 4562 (2000).

[386] B. Z. Nosho, B. R. Bennett, L. J. Whitman, and M. Goldenberg, J. Vac. Sci. Technol. B **19**, 1626 (2001).

[387] M. Zhong, J. Steinshnider, M. Weimer, and R. Kaspi, J. Vac. Sci. Technol. B **22**, 1593 (2004).

[388] K.-J. Chao, N. Liu, C.-K. Shih, D. W. Gotthold, and B. G. Streetman, Appl. Phys. Lett. **75**, 1703 (1999).

[389] Q. Xie, J. E. Van Nostrand, J. L. Brown, and C. E. Stutz, J. Appl. Phys. **86**, 329 (1999).

[390] B. Z. Nosho, W. Barvosa-Carter, M. J. Yang, B. R. Bennett, and L. J. Whitman, Surf. Sci. **465**, 361 (2000).

[391] M. W. Wang, D. A. Collins, T. C. McGill, and R. W. Grant, J. Vac. Sci. Technol. B **11**, 1418 (1993).

[392] M. W. Wang, D. A. Collins, T. C. McGill, R. W. Grant, and R. M. Feenstra, J. Vac. Sci. Technol. B **13**, 1689 (1995).

[393] N. N. Ledentsov, J. Böhrer, M. Beer, F. Heinrichsdorff, M. Grundmann, D. Bimberg, S. V. Ivanov, B. Ya. Meltser, S. V. Shaposhnikov, I. N. Yassievich, N. N. Faleev, P. S. Kop'ev, and Zh. I. Alferov, Phys. Rev. B **52**, 14058 (1995).

[394] O. J. Pitts, S. P. Watkins, C. X. Wang, V. Fink, and K. L. Kavanagh, J. Crystal Growth **254**, 28 (2003).

[395] I. Farrer, private communication.

[396] A. S. Brown, M. Losurdo, G. Bruno, T. Brown, and G. May, J. Vac. Sci. Technol. B **22**, 2244 (2004).

[397] K. Muraki, S. Fukatsu, Y. Shiraki, and R. Ito, Appl. Phys. Lett. **61**, 557 (1992).

[398] Q. Xie and J. E. Van Nostrand, J. Vac. Sci. Technol. A **17**, 342 (1999).

[399] T. Matsuura, T. Miyamoto, T. Kageyama, M. Ohta, Y. Matsui, T. Furuhata, and F. Koyama, Jpn. J. Appl. Phys. **43**, L605 (2004).

[400] K. Pötschke, L. Müller-Kirsch, R. Heitz, R. L. Sellin, U. W. Pohl, D. Bimberg, N. Zakharov, and P. Werner, Physica E **21**, 606 (2004).

[401] M. Horn-von Hoegen, M. Copel, J. C. Tsang, M. C. Reuter, and R. M. Tromp, Phys. Rev. B **50**, 10811 (1994).

[402] A. Portavoce, I. Berbezier, and A. Ronda, Phys. Rev. B **69**, 155416 (2004).

[403] H. Shimizu, K. Kumada, S. Uchiyama, and A. Kasukawa, Electron. Lett. **36**, 1379 (2000).

[404] J. C. Harmand, L. H. Li, G. Patriarche, and L. Travers, Appl. Phys. Lett. **84**, 3981 (2004).

[405] M. Kudo, T. Nakaoka, S. Iwamoto, and Y. Arakawa, Jpn. J. Appl. Phys. **44**, L45 (2005).

[406] G. E. Franklin, D. H. Rich, A. Samsavar, E. S. Hirschhorn, F. M. Leibsle, T. Miller, and T.-C. Chiang, Phys. Rev. B **41**, 12619 (1990).

[407] M. T. Sieger, T. Miller, and T.-C. Chiang, Phys. Rev. B **52**, 8256 (1995).

[408] M. C. Righi, R. Magri, and C. M. Bertoni, Phys. Rev. B **71**, 075323 (2005).

[409] W. Barvosa-Carter, A. S. Bracker, J. C. Culbertson, B. Z. Nosho, B. V. Shanabrook, L. J. Whitman, H. Kim, N. A. Modine, and E. Kaxiras, Phys. Rev. Lett. **84**, 4649 (2000).

[410] F. Maeda and Y. Watanabe, Phys. Rev. B **60**, 10652 (1999).

[411] J. G. Belk, C. F. McConville, J. L. Sudijono, T. S. Jones, and B. A. Joyce, Surf. Sci. **387**, 213 (1997).

[412] A. Riposan, J. Mirecki Millunchick, and C. Pearson, J. Vac. Sci. Technol. A **24**, 2041 (2006).

[413] J. Mirecki Millunchick, A. Riposan, B. J. Dall, C. Pearson, and B. G. Orr, Surf. Sci. **550**, 1 (2004).

[414] P. Laukkanen, R. E. Perälä, R.-L. Vaara, I. J. Väyrynen, M. Kuzmin, and J. Sadowski, Phys. Rev. B **69**, 205323 (2004).

[415] L. J. Whitman, B. R. Bennett, E. M. Kneedler, B. T. Jonker, and B. V. Shanabrook, Surf. Sci. **436**, L707 (1999).

[416] N. Esser, A. I. Shkrebtii, U. Resch-Esser, C. Springer, W. Richter, W. G. Schmidt, F. Bechstedt, and R. Del Sole, Phys. Rev. Lett. **77**, 4402 (1996).

[417] F. Pulizzi, D. Walker, A. Patanè, L. Eaves, M. Henini, D. Granados, J. M. Garcia, V. V. Rudenkov, P. C. M. Christianen, J. C. Maan, P. Offermans, P. M. Koenraad, and G. Hill, Phys. Rev. B **72**, 085309 (2005).

[418] P. Offermans, P. M. Koenraad, J. H. Wolter, D. Granados, J. M. García, V. M. Fomin, V. N. Gladilin, and J. T. Devreese, Physica E **32**, 41 (2006).

[419] J. Sormunen, J. Riikonen, T. Hakkarainen, M. Sopanen, and H. Lipsanen, Jpn. J. Appl. Phys. **44**, L1323 (2005).

[420] A. Lorke, R. J. Luyken, J. M. Garcia, and P. M. Petroff, Jpn. J. Appl. Phys. **40**, 1857 (2001).

[421] R. Blossey and A. Lorke, Phys. Rev. E **65**, 021603 (2002).

[422] D. Granados, J. M. García, T. Ben, and S. I. Molina, Appl. Phys. Lett. **86**, 071918 (2005).

[423] F. Suárez, D. Granados, M. L. Dotor, and J. M. García, Nanotechnology **15**, S126 (2004).

[424] Y. Aharonov and D. Bohm, Phys. Rev. **115**, 485 (1959).

[425] M. Peshkin and A. Tonomura, *The Aharonov-Bohm Effect,* in: Lecture Notes in Physics, Vol. 340, Springer, Berlin, 1989.

[426] S. Washburn and R. A. Webb, Rep. Prog. Phys. **55**, 1311 (1992).

[427] M. Büttiker, Y. Imry, and R. Landauer, Phys. Lett. **96A**, 365 (1983).

[428] L. P. Lévy, G. Dolan, J. Dunsmuir, and H. Bouchiat, Phys. Rev. Lett. **64**, 2074 (1990).

[429] N. A. J. M. Kleemans, I. M. A. Bominaar-Silkens, V. M. Fomin, V. N. Gladilin, D. Granados, A. G. Taboada, J. M. García, P. Offermans, U. Zeitler, P. C. M. Christianen, J. C. Maan, J. T. Devreese, J. H. Wolter, and P. M. Koenraad, American Institute of Physics Conference Proceedings **893**, 683 (2007).

[430] M. Bayer, M. Korkusinski, P. Hawrylak, T. Gutbrod, M. Michel, and A. Forchel, Phys. Rev. Lett. **90**, 186801 (2003).

[431] M. Peter, K. Winkler, M. Maier, N. Herres, J. Wagner, D. Fekete, K. H. Bachem, and D. Richards, Appl. Phys. Lett. **67**, 2639 (1995).

[432] A. D. Prins, D. J. Dunstan, J. D. Lambkin, E. P. O'Reilly, A. R. Adams, R. Pritchard, W. S. Truscott, and K. E. Singer, Phys. Rev. B **47**, 2191 (1993).

[433] R. M. Feenstra, J. Vac. Sci. Technol. B **21**, 2080 (2003).

[434] D. R. Lide, editor, *CRC Handbook of Chemistry and Physics*, 78th edition, CRC Press, Boca Raton, 1997.

[435] R. M. Feenstra, G. Meyer, and K. H. Rieder, Phys. Rev. B **69**, 081309 (2004).

[436] R. M. Feenstra, private communication.

[437] B. Bansal, High Field Magnet Laboratory, Nijmegen, The Neterlands, private communication.

[438] D. K. Biegelsen, F. A. Ponce, J. C. Tramontana, and S. M. Koch, Appl. Phys. Lett. **50**, 696 (1987).

[439] O. Albrektsen, H. W. M. Salemink, K. A. Mørch, and A. R. Thölen, J. Vac. Sci. Technol. B **12**, 3187 (1994).

[440] T. Kalka, C. Preinesberger, S. Vandré, and M. Dähne-Prietsch, Appl. Phys. A **66**, S1073 (1998).

[441] R. H. Fowler and L. Nordheim, P. Roy. Soc. Lond. A Mat. **119**, 173 (1928).

[442] E. W. Müller and T. T. Tsong, *Field Ion Microscopy, Principles and Applications*, American Elsevier Publishing Company, New York, 1969.

[443] R. Gomer, *Field Emission and Field Ionization,* Harvard Monographs in Applied Science, volume 9, Harvard University Press, Cambridge, 1961.

[444] L. E. Murr, *Electron and ion microscopy and microanalysis, principles and applications*, Marcel Dekker, New York, 1982.

[445] E. W. Müller, Z. Phys. **131**, 136 (1951).

Publications and presentations

Parts of this work have been published in:

- R. Timm, H. Eisele, A. Lenz, S. K. Becker, J. Grabowski, T.-Y. Kim, L. Müller-Kirsch, K. Pötschke, U. W. Pohl, D. Bimberg, and M. Dähne, *Structure and intermixing of GaSb/GaAs quantum dots*, Appl. Phys. Lett. **85**, 5890 (2004).
- R. Timm, J. Grabowski, H. Eisele, A. Lenz, S. K. Becker, L. Müller-Kirsch, K. Pötschke, U. W. Pohl, D. Bimberg, and M. Dähne, *Formation and atomic structure of GaSb nanostructures in GaAs studied by cross-sectional scanning tunnelling microscopy*, Physica E **26**, 231 (2005).
- R. Timm, A. Lenz, J. Grabowski, H. Eisele, and M. Dähne, *A cross-sectional scanning tunneling microscopy study of GaSb/GaAs nanostructures*, Springer Proceedings in Physics **107**, 479 (2005).
- R. Timm, A. Lenz, J. Grabowski, H. Eisele, K. Pötschke, U. W. Pohl, D. Bimberg, and M. Dähne, *Formation and Atomic Structure of GaSb Quantum Dots in GaAs Studied by Cross-Sectional Scanning Tunneling Microscopy*, in: Proceedings of EW-MOVPE XI, ed. by E. Kapon and A. Rudra (Lausanne 2005), p. 39.
- R. Timm, A. Lenz, H. Eisele, L. Ivanova, K. Pötschke, U. W. Pohl, D. Bimberg, G. Balakrishnan, D. L. Huffaker, and M. Dähne, *Onset of GaSb/GaAs quantum dot formation*, phys. stat. sol. (c) **3**, 3971 (2006).

Other publications:

- A. Lenz, R. Timm, H. Eisele, Ch. Hennig, S. K. Becker, R. L. Sellin, U. W. Pohl, D. Bimberg, and M. Dähne, *Reversed truncated cone composition distribution of $In_{0.8}Ga_{0.2}As$ quantum dots overgrown by an $In_{0.1}Ga_{0.9}As$ layer in a GaAs matrix*, Appl. Phys. Lett. **81**, 5150 (2002).
- H. Eisele, A. Lenz, R. Timm, Ch. Hennig, M. Ternes, F. Heinrichsdorff, A. Krost, R. Sellin, U. W. Pohl, D. Bimberg, T. Wehnert, E. Steimetz, W. Richter, and M. Dähne, *Atomic Structure of InAs and InGaAs Quantum Dots Studied by Cross-Sectional Scanning Tunneling Microscopy*, Inst. Phys. Conf. Ser. **171**, P199 (2003).
- O. Flebbe, H. Eisele, R. Timm, and M. Dähne, *Room-Temperature Observation of Standing Electron Waves on GaAs(110) at Surface Steps*, AIP Conf. Proc. **696**, 699 (2003).

- S. K. Becker, J. Grabowski, T.-Y. Kim, L. Amsel, F. Bechtel, N. Tschirner, I. Mantouvalou, A. Lenz, R. Timm, K. Hodeck, F. Streicher, G. Pruskil, H. Eisele, and M. Dähne, *Low Budget UHV STM Built by Physics Students for Use in a Laboratory Exercises Course*, AIP Conf. Proc. **696**, 216 (2003).

- H. Eisele, R. Timm, A. Lenz, Ch. Hennig, M. Ternes, S. K. Becker, and M. Dähne, *Segregation effects during GaAs overgrowth of InAs and InGaAs quantum dots studied by cross-sectional scanning tunneling microscopy*, phys. stat. sol. (c) **0**, 1129 (2003).

- H. Eisele, A. Lenz, Ch. Hennig, R. Timm, M. Ternes, and M. Dähne, *Atomic structure of InAs and InGaAs quantum dots determined by cross-sectional scanning tunnelling microscopy*, J. Crystal Growth **248**, 322 (2003).

- A. Lenz, H. Eisele, R. Timm, S. K. Becker, R. L. Sellin, U. W. Pohl, D. Bimberg, and M. Dähne, *Nanovoids in InGaAs/GaAs quantum dots observed by cross-sectional scanning tunneling microscopy*, Appl. Phys. Lett. **85**, 3848 (2004).

- O. Schumann, S. Birner, M. Baudach, L. Geelhaar, H. Eisele, L. Ivanova, R. Timm, A. Lenz, S. K. Becker, M. Povolotskyi, M. Dähne, G. Abstreiter, and H. Riechert, *Effects of strain and confinement on the emission wavelength of InAs quantum dots due to a $GaAs_{1-x}N_x$ capping layer*, Phys. Rev. B **71**, 245316 (2005).

- R. Timm, H. Eisele, A. Lenz, T.-Y. Kim, F. Streicher, K. Pötschke, U. W. Pohl, D. Bimberg, and M. Dähne, *Structure of InAs/GaAs quantum dots grown with Sb surfactant*, Physica E **32**, 25 (2006).

- A. Lenz, R. Timm, H. Eisele, L. Ivanova, D. Martin, V. Voßebürger, A. Rastelli, O. G. Schmidt, and M. Dähne, *Structural investigation of hierarchically self-assembled GaAs/AlGaAs quantum dots*, phys. stat. sol. (b) **243**, 3976 (2006).

- A. Lenz, H. Eisele, R. Timm, L. Ivanova, H.-Y. Liu, M. Hopkinson, U. W. Pohl, and M. Dähne, *Structure of InAs quantum dots-in-a-well nanostructures*, Physica E, in print.

Contributions at international conferences:

- 12^{th} International Conference on Scanning Tunneling Microscopy/Spectroscopy and Related Techniques (**STM2003**), 21 - 25 July 2003, Eindhoven, The Netherlands:
  Atomic structure and type-II band alignment of GaSb quantum dots in GaAs studied by cross-sectional STM (oral),
  Structural change of InAs quantum dots during GaAs overgrowth studied by (cross-sectional) STM (poster).

- **QD2004** Quantum Dots Conference, 10 - 13 May 2004, Banff, Alberta, Canada:
  Atomic Structure and Type-II Band Alignment of GaSb Quantum Dots in GaAs Studied by Cross-Sectional Scanning Tunneling Microscopy (oral).

- Microscopy of Semiconducting Materials (**MSM XIV**), 11 - 14 April 2005, Oxford, UK:
  Formation, Atomic Structure, and Type-II Band Alignment of GaSb/GaAs Quantum Dots Studied by Cross-Sectional Scanning Tunneling Microscopy (oral).

- 11^{th} European Workshop on Metalorganic Vapour Phase Epitaxy (**EW–MOVPE**), 5 - 8 June 2005, Lausanne, Switzerland:
  Formation and Atomic Structure of GaSb Quantum Dots in GaAs Studied by Cross-Sectional Scanning Tunneling Microscopy (poster).

- International Conference on Modulated Semiconductor Structures (**12 MSS**), 10 - 15 July 2005, Albuquerque, New Mexico, USA:
  Structure of InAs/GaAs Quantum Dots grown with Sb surfactant (poster).

- **EPS** - 21^{st} General Conference of the Condensed Matter Division of the European Physical Society, 26 - 31 March 2006, Dresden, Germany:
  Atomic structure of GaSb/GaAs quantum rings and dots studied by cross-sectional scanning tunneling microscopy (oral).

- 4^{th} International Conference on Quantum Dots (**QD2006**), 1 - 5 May 2006, Chamonix-Mont Blanc, France:
  Growth, Atomic Structure, and Type-II Band Alignment of GaSb/GaAs Quantum Dots and Rings (poster).

- 28^{th} International Conference on the Physics of Semiconductors (**ICPS28**), 24 - 28 July 2006, Vienna, Austria:
  Growth, Atomic Structure, and Electronic Properties of GaSb/GaAs Nanostructures: Quantum Wells, Dots and Rings (oral).

- International Conference on Nanoscience and Technology (**ICN+T2006**), 30 July - 4 August 2006, Basel, Switzerland:
  Local tip-induced band bending at type-II GaSb/GaAs nanostructures studied with cross-sectional scanning tunneling microscopy and spectroscopy (oral).

- Microscopy of Semiconducting Materials (**MSM XV**), 1 - 5 April 2007, Cambridge, UK:
  Growth and atomic structure of GaSb/GaAs quantum dots and rings studied by cross-sectional scanning tunneling microscopy and spectroscopy (oral).

- International Conference on Modulated Semiconductor Structures (**13 MSS**), 15 - 20 July 2007, Genova, Italy: *Growth, atomic structure, and type-II band alignment of GaSb/GaAs nanostructures: Quantum wells, dots, and rings* (poster).

Acknowledgments

I am deeply grateful to many people who have contributed to the success of this work.

First of all, my sincere thanks go to Prof. Mario Dähne for giving me the opportunity to directly "look at the atoms" and for supervising this work. His continuous support at all times, his enthusiasm for physics and teaching, many detailed and fruitful discussions, and his careful proof reading of the manuscript have helped and impressed me far beyond the scope of this thesis.

Prof. Dieter Bimberg is gratefully acknowledged for refereeing this thesis and for his great motivation and support.

Special thanks belong to Dr. Holger Eisele for introducing me into the world of STM and for teaching me much about the details of UHV technology as well as the physics of QDs. I have learned a lot from his knowledge and experience. During all the time of my Diploma and Ph.D. thesis I could benefit from the cooperation with Andrea Lenz, in whom I found an absolutely reliable and loyal colleague, and whith whom I share(d) not only our office, many XSTM experiments, several conferences, and teaching activities, but also a close friendship. Thank you!

I further want to thank Holger, Andrea, and also Lena Ivanova, Jan Grabowski, Vivien Voßebürger, Dominik Martin, and Sebastian Becker for assistance in XSTM measurements, investing sleepless nights and a lot of patience. Even more, I am very grateful to them as well as to Martina Wanke, Kai Hodeck, Angela Berner, and all other members of the Dähne workgroup for a lot of help and encouragement during everyday life, for many great events, and for a working atmosphere that let me really enjoy the time of my Ph.D.

The GaSb QDs studied in this work have been grown by Dr. Lutz Müller-Kirsch and Konstantin Pötschke in the group of Prof. Bimberg, by Dr. Ganesh Balakrishnan in the group of Prof. Diana L. Huffaker, and by Dr. Ian Farrer in the group of Prof. David A. Ritchie. All of them I want to thank for their cooperation in providing the samples. Special thanks also go to Till Warming for the PL data and to Prof. Randall M. Feenstra for his calculations and excellent suggestions on STM contrast and tip-induced band bending. Additionally, I would like to acknowledge Martin Geller for his concern in GaSb QDs and his explanations about the concepts of storage devices, and PD Dr. Udo W. Pohl for his enduring interest in my work and enriching discussions on various aspects of QD growth.

This work profited from funding by the European Commission in the SANDiE Network of Excellence and by projects Da 408/4, Da 408/8, Da 408/13, and SFB 296 of the Deutsche Forschungsgemeinschaft, as well as from a personal grant given by the city of Berlin in the "NaFöG" program.

Finally, I am particularly grateful to my parents, who inspired in me the whish to explore nature, who encouraged me, and who enabled my physics studies. Above all, I thank my wife Bianca for her everlasting support and for every single day.